INFORMATION TO USERS

This manuscript has been reproduced from the microfilm master. UMI films the text directly from the original or copy submitted. Thus, some thesis and dissertation copies are in typewriter face, while others may be from any type of computer printer.

The quality of this reproduction is dependent upon the quality of the copy submitted. Broken or indistinct print, colored or poor quality illustrations and photographs, print bleedthrough, substandard margins, and improper alignment can adversely affect reproduction.

In the unlikely event that the author did not send UMI a complete manuscript and there are missing pages, these will be noted. Also, if unauthorized copyright material had to be removed, a note will indicate the deletion.

Oversize materials (e.g., maps, drawings, charts) are reproduced by sectioning the original, beginning at the upper left-hand corner and continuing from left to right in equal sections with small overlaps.

Photographs included in the original manuscript have been reproduced xerographically in this copy. Higher quality 6" x 9" black and white photographic prints are available for any photographs or illustrations appearing in this copy for an additional charge. Contact UMI directly to order.

UMI®

The Pennsylvania State University

The Graduate School

Department of Materials Science and Engineering

MODELING WELDMENT MACRO AND MICROSTRUCTURE FROM FUNDAMENTALS OF TRANSPORT PHENOMENA AND PHASE TRANSFORMATION THEORY

A Thesis in

Materials Science and Engineering

by

Zhishang Yang

Submitted in Partial Fulfillment
of the Requirements
for the Degree of

Doctor of Philosophy

May 2000

UMI Number: 9966922

UMI®

We approve the thesis of Zhishang Yang.

Date of Signature

_____

Tarasankar DebRoy
Professor of Materials Science and Engineering
Thesis Advisor
Chair of Committee

17 March 2000

_____

Long-Qing Chen
Associate Professor of Materials Science and Engineering
Graduate Program Coordinator for
Materials Science and Engineering

03-20-00

_____

Randall M. German
Brush Chair Professor in Materials

21 Mar 2000

_____

Paul R. Howell
Professor of Metallurgy

3/28/00

_____

Kwadwo Osseo-Asare
Prof. of Metallurgy
In Charge of Graduate Programs in
Metals Science and Engineeering

3/20/00

ABSTRACT

The weldment macro and microstructures were modeled based on the fundamentals of transport phenomena and phase transformation theory. In the present thesis, the study of macrostructure focused on the prediction of the shapes and sizes of the fusion zone (FZ) and the heat affected zone (HAZ). The microstructure investigation included two parts: (1) the phases present and their volume fractions in the FZ and the HAZ, and (2) the grain structure in the HAZ. Two mathematical models were developed in the present thesis: (1) a three dimensional (3D) turbulent heat transfer and fluid flow model, and (2) a 3D Monte Carlo (MC) based grain growth simulation model. The heat transfer and fluid flow model was used to predict the weld geometries and the thermal cycles. The phase transformations during welding were calculated by coupling available phase transformation models with the calculated thermal cycles. The grain growth in the entire HAZ was simulated by coupling the 3D MC model with the 3D heat transfer and fluid flow model.

To check the capabilities of the developed models, several cases were studied, in which the results predicted from modeling were compared with the experimental data. The cases studied included (1) weld metal macro and microstructures of HSLA-100 steel fabricated using gas-metal-arc (GMA) welding, (2) weld metal microstructure of C-Mn steel produced by gas-tungsten-arc (GTA) welding, and (3) macro and microstructures (phase volume fractions and grain structure in HAZ) in the GTA welded commercially pure titanium weldments.

Accurate knowledge of the heat transfer and fluid flow in the weld pool is important for quantitative modeling of weldment macro and microstructures. In the present study, the K - ε turbulence model was incorporated into an existing 3D thermofluid model to consider the effects of turbulence on the fluid flow and heat transfer in the weld pool. The temperature and velocity fields, the weld geometries, and the thermal cycles at various locations in the weldments were calculated from the developed model. Through the present study, it was found that the values of effective viscosity and

effctive thermal conductivity in the weld pools were spatially distributed rather than constants. For both GTA and GMA welding, the computed values of turbulent viscosity and thermal conductivity were much higher than the corresponding molecular values, which indicated that the transport of heat and momentum in the weld pool was significantly aided by turbulence. Thus, previous calculations of heat transfer and fluid flow based on the assumption of laminar flow need to be re-examined. The weld geometries from both GMA welding and GTA welding can be satisfactorily predicted from the present model. Compared to the laminar model, the weld geometries predicted from turbulent model were in much better agreement with the actual weld geometries. The comparison was effectively illustrated in the GTA welded commercially pure titanium case. In addition, the "finger penetration", a unique weld geometric feature in GMA welding, was satisfactorily predicted by the present model in the HSLA-100 steel welds. The thermal cycles can be well predicted from the present 3D turbulent heat transfer and fluid flow model. The predicted cooling rates agreed well with the corresponding experimental data.

To predict the phase transformations during welding, the calculated thermal cycles from the thermal model were coupled with available phase transformation models. For steel welds, Bhadeshia's phase transformation model was used to calculate the time-temperature-transformation (TTT) and continuous-cooling-transformation (CCT) diagrams. The calculated CCT diagrams and cooling rates were then coupled to predict the phases in the weld metal and their volume fractions. In particular, the effects of cooling rates on the weld metal microstructure of the HSLA-100 steel and the effects of chemical composition on the weld metal microstructure of C-Mn steels were investigated in the present study. The HSLA-100 steel welds consisted predominantly of acicular ferrite. Small amounts of allotriomorphic and Widmanstatten ferrites were observed only at high heat inputs. The observed microstructures at different heat inputs can be satisfactorily predicted by coupling the computed cooling rates and CCT diagrams. In the C-Mn steel welds, the phase volume fractions in the welds with different carbon and manganese contents were quantitatively calculated. The phase volume fractions calculated using cooling rate from the heat transfer and fluid flow model were found in

better agreement with the experimental results than those obtained by using the cooling rate from an empirical equation.

The spatial distribution of phases in the weldment of commercially pure titanium was quantitatively predicted by coupling of the calculated thermal cycles at various locations with a phase transformation kinetic model based on a modified JMA equation. The predicted phase boundaries of the $\alpha/(\alpha+\beta)$, $(\alpha+\beta)/\beta$, and the $\beta/$liquid in the titanium weldments were found in good agreement with the real-time experimental results from a unique spatially resolved X-Ray diffraction (SRXRD) technique with synchrotron radiation. The mechanism of the $\alpha \rightarrow \beta$ transition was examined by the comparison of the calculated reaction times from several possible mechanisms with the experimentally determined reaction times. It was found that the $\alpha \rightarrow \beta$ transition was mostly likely controlled by the transport of Ti atoms across the α/β interface.

In the present thesis, the 3D MC model coupled with the 3D heat transfer and fluid flow model was used to predict the grain structure in the entire HAZ of the commercially pure titanium welds. Grain Boundary Migration (GBM) model was used to relate the Monte Carlo simulation step and grid spacing, which were dimensionless quantities in the MC algorithm, to the real time and grain size during welding. A 3D real-time grain structure map in the entire HAZ around the weld pool was established, in which the salient features of the grain growth in the HAZ due to the steep temperature gradients and transient thermal cycles were effectively illustrated. The capability of the 3D MC model for quantitative prediction of grain size spatial distribution in the HAZ was tested in the titanium weldements from four different heat inputs. The calculated grain sizes were found comparable with the corresponding experimental results. In particular, it was found that the grain size gradients in the HAZ varied with locations. At the same distance to the fusion line, the mean grain size on the top surface may be quite different from that on the vertical central plane.

The results presented in this thesis, taken as a whole, indicated that the weldment macro and microstructures can be quantitatively predicted from fundamentals of transport phenomena and phase transformation theory.

TABLE OF CONTENTS

LIST OF FIGURES

LIST OF TABLES

ACKNOWLEDGEMENTS

I would first like to express my deep gratitude to my advisor, Dr. Tarasankar DebRoy, for his patient and expert guidance throughout this research. I would also like to thank Drs. Longqing Chen, Randall M. German, and Paul Howell for time and valuable advice while serving as my thesis committee. I am very grateful to Dr. H. K. D. H Bhadeshia for allowing me to use his phase transformation model. Many thanks to Dr. John W. Elmer at Lawrence Livermore National Laboratory for providing experimental results for investigation of commercially pure titanium. I very appreciate Dr. Kamlesh Mundra for his help in heat transfer and fluid flow simulation and Dr. Suresh Babu for his discussion on microstructure modeling. My thanks to my colleagues Tao Hong, Yang Liu, Mario Pastor, Todd Palmer, Sarang Sista, Hari Venugopalan, and Hailiang Zhao for their help during my study at Penn State.

I am deeply indebted to my wife, Li Liu, and my lovely twin sons, Mike and Jack, for their cooperation during my Ph. D. study. I very appreciate my mother- and father-in-law, Lijing Liu and Guoliang Liu, and my parents, Shulan Luo and Qiong Yang, for their support, encouragement, and many other important contributions such as taking care of my kids during my study.

CHAPTER 1

INTRODUCTION

1.1 General Background

During fusion welding process, the use of an intense heat source results in rapid heating of the material, its melting, and solidification. In the weld pool, the heat transfer and fluid flow affect temperature fields and thermal cycles which, in turn, affect the macro- and microstructures in the weld metal. In the solid region around the weld pool, the thermal cycles may lead to solid state phase transformations and changes in the grain structure. The kinetics of phase transformations and grain growth vary across the weldment and are functions of both the heating and cooling rates as well as the maximum temperatures attained during welding. In the present thesis, macrostructure specifically means the shapes and sizes of the fusion zone (FZ) and the heat affected zone (HAZ). The microstructure mainly focuses on two parts: (1) the phases present and their volume fractions in the FZ and the HAZ, and (2) the grain sizes and their spatial distribution in the HAZ. Since the integrity and properties of a weldment are directly related with its macro and microstructures,[1-3] understanding the development of macro and microstructures in the weldment is very important.

For a given material, knowledge of the temperature field and the thermal cycles at various locations in the weldment is a prerequisite to understand the development of weldment macro and microstructures.[1-3] Due to the high temperatures, intense plasma arc environment, and small weld pool area, measurement of temperature field and thermal cycles in the weld pool remains a major challenge. Mathematical modeling provides a recourse to address this problem. In recent years, mathematical modeling of transport phenomena in the weld pool has provided detailed insight about the welding processes.[1-28] Based on modeling heat transfer and fluid flow in the weld pool, significant progress has been made in understanding the development of weld pool shape and size,[1-24] cooling rate,[19,20] and the concentration of volatile alloying elements from the weld pool.[25,26]

However, until now very little research has been done to use the accurate heat transfer and fluid flow calculation to quantitatively understand the development of the macro- and microstructure in the weldment. Efforts to quantitatively model the development of weldment microstructures,[20] inclusion characteristics,[27] vaporization of alloying elements from the weld pool,[26,27] and concentrations of dissolved gases in the weld metal[19,28] starting from transport phenomena are just beginning.

Accurate prediction of the weld geometry and the thermal cycles in the weldment requires a comprehensive understanding of heat transfer and fluid flow in the weld pool. In the past two decades, the importance of convective heat transfer in the weld pool has been recognized and the different driving forces responsible for the fluid motion, such as surface tension gradient, electromagnetic, and buoyancy forces have been investigated in detail by mathematical modeling. In most previous research, the nature of the flow in the weld pool was assumed to be laminar. However, recent experimental observations[29] and theoretical calculations[22,23] have indicated that, in many cases, the fluid flow in the weld pool is turbulent rather than laminar. Some initial efforts[22,23] have been undertaken in the modeling of heat transfer and fluid flow in the weld pool in two dimensions considering turbulent flow. These initial efforts have demonstrated that accurate prediction of the temperature and velocity fields in the weld pool, as well as the weld pool geometry must consider turbulence effects.

Previous efforts to model turbulence in weld pool[22,23] were limited to two dimensions. These calculations cannot provide a full description of the heat transfer and fluid flow in the weld pool. Furthermore, three dimensional temperature fields and thermal cycles are needed for realistic modeling of microstructural evolution. Therefore, a three dimensional turbulent thermofluid model is essential for achieving realistic simulation of heat transfer and fluid flow in the weld pool as well as microstructural evolution in the weldment.

During welding, various solid state transformations occur in both the FZ and the HAZ. The extents of these transformations depend on the chemical compositions of the

material and the thermal cycle. The solid state transformations that occur during welding can be grouped into four categories:[30] (1) phase changes involving diffusional transformation, (2) phase changes involving displacive transformation, (3) spinodal decomposition, and (4) solid state processes such as grain growth, coarsening, and solute redistribution. The above transformations may occur concurrently and interact with each other due to the complicated thermal cycles involved during welding process. The ability to model weldment microstructure relies on a deep understanding of phase transformation theory governing the phase changes and the thermal cycles. In the past decade, considerable progress has been made in the prediction of weldment microstructure in both the FZ and the HAZ. Some phase transformation models have been established in an effort to predict microstructures in the FZ and the HAZ of steel welds.[31-37] However, thermal cycles at various locations of the weldment are necessary for their application.

The grain growth phenomenon in the HAZ is complicated due to the steep temperature gradients and rapid thermal cycling in this region. Near the fusion line, the atomic mobility may vary even across a single grain considering the steep temperature gradients and very coarse grains at this region. This phenomenon can not be simulated by the classical analytical equation for grain growth,[42] in which a constant temperature or average thermal cycle is assumed in a single grain. In the past several years, efforts have been made to apply Monte Carlo (MC) technique to simulate grain growth in the weld HAZ.[38-41] The advantage to apply this technique to simulate grain growth in the HAZ is that it can provide not only grain growth kinetics but also grain topological information.

Previous simulations of the grain growth in the HAZ[38-41] were limited in two dimensions. Considering the significant change of local thermal and topological environment within the HAZ, simulation of grain growth in two dimensions is not sufficient for understanding grain growth occurring in three dimensional environment. For a realistic simulation, a three dimensional MC model considering spatial variations of temperature and thermal cycles in the whole region of the HAZ around the weld pool is needed.

In short, the development of weldment macro- and microstructures are governed by various physical processes. In order to obtain accurate predictions of the weld geometry and thermal cycles in the weldment, turbulent heat transfer and fluid flow in the weld pool should be considered in three dimensions in the development of a thermal model. Due to the steep temperature gradients and rapid thermal cycles during welding, accurate knowledge of the thermal cycles at various locations of the weldment is a prerequisite for modeling welding induced phase transformations and grain growth.

1.2 Objectives

The overall objective of this study is to seek a quantitative understanding of the development of weldment macrostructure, i.e., the geometry of the FZ and the HAZ, and microstructure, i.e., the phases present in the FZ and the HAZ, the volume fractions of the phases, and the grain structure in HAZ, from the fundamentals of transport phenomena and phase transformation theory. To achieve this objective, comprehensive mathematical models will be developed and the model predictions will be compared with experimental data.

In particular, two mathematical models will be developed in the present thesis: (1) a three-dimensional, turbulent heat transfer and fluid flow model for prediction of the weld geometry and the thermal cycles in the weldment, and (2) a three dimensional Monte Carlo model for simulation of grain growth in the whole HAZ. The heat transfer and fluid flow model will be coupled with new/or available phase transformation models and the Monte Carlo model for quantitative prediction of welding induced phase transformations and grain growth, respectively. The cases to be studied in the present thesis are: (1) weld metal macro and microstructures of HSLA-100 steel fabricated using gas-metal-arc (GMA) welding, (2) weld metal microstructure of C-Mn steel produced by gas-tungsten-arc (GTA) welding, and (3) macro and microstructures (phase volume fractions and grain structure in HAZ) in the GTA welded commercially pure titanium weldments.

1.3 Thesis Structure

The thesis consists of six chapters. Chapter 1 describes the subject matter, objective, and contents of the thesis. In chapter 2, the background materials necessary for simulation of heat transfer and fluid flow in the weld pool, phase transformations in the FZ and the HAZ, and grain growth in the HAZ, are critically reviewed. In chapter 3, the models developed in the present study, the 3D turbulent heat transfer and fluid flow model and the 3D Monte Carlo (MC) model, are described. The procedures for applying these models for the prediction of the weldment macro- and microstructures are also presented in this chapter.

In chapter 4, the macro- and microstructures in the weldments of low alloy steels (e.g. HSLA-100 steel and C-Mn steels) are modeled. The special weld geometry from GMA welding, "finger penetration", is predicted by the heat transfer and fluid flow model. The weld metal microstructures are predicted by coupling the calculated thermal cycles from the heat transfer and fluid flow model with an available, well tested phase transformation model.[31-33] In particular, the effect of cooling rate on the weld metal microstructure of HSLA-100 steel and the effect of chemical composition on the C-Mn steel weld metal microstructure are calculated. The calculated weld geometries, thermal cycles, and phase volume fractions are compared with corresponding experimental results.

In chapter 5, the macro and microstructures in the weldments of commercially pure titanium are investigated. The temperature field and thermal cycles necessary for prediction of the macro and microstructures are calculated from the heat transfer and fluid flow model. The microstructural investigation in this chapter is focused on the HAZ. A modified Johnson-Mehl-Avrami (JMA) equation[45] is used to describe the phase transformation kinetics under non-isothermal conditions in the HAZ. The calculated thermal cycles at various locations are incorporated into the modified JMA equation to predict the spatial phase distribution in the HAZ. The predicted phase distributions are compared with real-time experimental results of Elmer et al.[43-44] To simulate the grain growth in the whole HAZ, the 3D MC model is coupled with the 3D heat transfer and

fluid flow model. Systematic welding experiments were conducted by our collaborators in Lawrence Livermore National Laboratory to check the capability of the MC model. The computed spatial distribution of grain size was compared with the experimental results under various welding conditions.

Concluding remarks of the present thesis are made in chapter 6.

1.4 References

1. S. A. David and T. DebRoy: *Science*, **257**, 497 (1992).

2. T. DebRoy and S. A. David: Review of Modern Physics, **67**, 85 (1995).

3. S. A. David, T. DebRoy and J. M. Vitek: MRS BULLETIN, **1**, 29 (1994).

4. D. R. Atthey: *J. Fluid Mech.*, **98**, 787 (1980).

5. G. M. Oreper, T. W. Eager, and J. Szekely: *Weld. J.*, **62**, 307s (1983).

6. G. M. Oreper and J. Szekely: *J. Fluid Mech.*, **147**, 53 (1984).

7. M. C. Tsai and S. Kou: *Numerical Heat Transfer*, Part A, **17**, 73 (1990).

8. M. C. Tsai and S. Kou: *Weld. J.*, **69**, 241s (1990).

9. M. C. Tsai and S. Kou: *Intl. J. for Numerical Method in Fluids*, **9**, 1503 (1989).

10. S. Kou and Y. H. Wang: *Metall. Trans. B*, **17A**, 2271 (1986).

11. S. Kou and Y. H. Wang: *Weld. J.*, **65**, 63s (1986).

12. T. Zacharia, S. A. David, J. M. Vitek, and T. DebRoy: *Weld. J.*, **68**, 499s (1989).

13. T. Zacharia, S. A. David, J. M. Vitek, and H. G. Krauss: *Metall. Trans. B*, **22B**, 243 (1991).

14. T. Zacharia, S. A. David, J. M. Vitek, and T. DebRoy:. *Metall. Trans. B.*, **21B**, 600 (1990).

15. A. J. Paul and T. DebRoy: *Metall. Trans. B*, **19B**, 851 (1988).

16. K. Mundra, T. DebRoy, and K. Kelkar: *Numerical Heat Transfer*, Part A, **29**, 115 (1996).

17. K. Mundra, T. DebRoy, T. Zacharia, and S. A. David: *Weld. J.*, **71**, 313s (1992).

18. W. Pitscheneder, T. DebRoy, K. Mundra, and R. Ebner: *Weld. J.*, **75**, 71s (1996).

19. K. Mundra, J. M. Blackburn, and T. DebRoy: *Science and Technology of Welding and Joining*, **2**, 174 (1997).

20. K. Mundra, T. DebRoy, S. S. Babu, and S. A. David: *Weld. J.*, **76**, 163s (1997).

21. K. C. Tsao and C. S. Wu: *Weld. J.*, **67**, 70s (1988).

22. R. T. C. Choo and J. Szekely: *Weld. J.*, **73**, 25s (1994).

23. K. Hong, D. C. Weckman, and A. B. Strong: *Trends in Welding Research*, ed. by H. B. Smartt, J. A. Johnson and S. A. David, p. 399, ASM INTERNATIONAL, Materials Park, OH (1996).

24. C. Chan, J. Mazumder, and M .M. Chen: *Metall. Trans. A*, **15A**, 2175 (1984).

25. A. Block-Bolten and T. W. Eager: *Metall. Trans. B*, **15B**, 461 (1984).

26. P. A. A. Khan and T. DebRoy: *Metall. Trans. B*, **15B**, 641 (1984).

27. T. Hong, W. Pitscheneder, and T. DebRoy: *Science and Technology of Welding and Joining*, **3**, 33 (1998).

28. T. A. Palmer and T. DebRoy: *Science and Technology of Welding and Joining*, **3**, 190 (1998).

29. M. Malinowski-Brodnicka, G. denOuden, and W. J. P. Vink: *Weld. J.*, **69**, 52s (1990).

30. S. A. David and S. S. Babu: in *Mathematical Modelling of Weld Phenomena 3*, ed. by H. Cerjak and H. K. D. H. Bhadeshia, p. 151, Institute of Materials (1997).

31. H. K. D. H. Bhadeshia and L. -E. Svensson: in *Mathematical Modeling of Weld Phenomena*, ed. by H. Cerjak and K.E. Easterling, p. 109, Institute of Materials (1993)..

32. H. K. D. H. Bhadeshia: in *'Recent Trends in Welding Science and Technology'*, ed. by S. A. David and J. M. Vitek, p. 189, ASM INTERNATIONAL, Materials Park, OH (1990).

33. H. K. D. H. Bhadeshia, L. -E. Svensson, and B. Gretoft: *Acta metall.*, **33**, 1271 (1985).

34. Ashby and K. E. Easterling: *Acta metall.*, **30**, 1969 (1982).

35. J. C. Ion, K. E. Easterling, and M. F. Ashby: *Acta metall.*, **32**, 1949 (1984).

36. D. F. Watt, L. Coon, M. Bibby, J. Goldak, and C. Henwood: *Acta metall.*, **36**, 3029 (1988).

37. L. Coon and D. F. Watt: in *Computer Modeling of Fabrication Processes and Constitutive Behaviour of Materials*, ed. by J. Too, p. 467, CANMET, Ottawa (1987).

38. J. Gao and R. G. Thompson: *Acta Metall.*, **44**, 4565 (1996).

39. J. Gao, R. G. Thompson, and Y .Cao: *Trends in Welding Research*, ed. by H. B. Smartt, J. A. Johnson and S. A. David, p. 199, ASM INTERNATIONAL, Materials Park, OH (1996).

40. B. Radhakkrishnan and T. Zacharia: *Metall. Trans. A*, **26A**, 167 (1995).

41. A. Wilson, R. P. Martukanitz, and P. Howell: published in the 5th International Conference on Trends in Welding Research, ed. by J. M. Vitek, S. A. David, J. A. Johnson, H. B. Smart, and T. DebRoy, p. 161, Pine Mountain, GA (1998).

42. J. E. Burke and D. Turnbull: *Prog. Met. Phys.*, **3**, 220 (1952).

43. J. W. Elmer, Joe Wong and Thorsten Ressler: *Metall. Mater. Trans. A*, **29A**, 2761 (1998).

44. J. W. Elmer, Joe Wong, M. Fröba, P. A. Waide and E. M. Larson: *Metall. Mater. Trans. A*, **27A**, 775 (1996).

CHAPTER 2

BACKGROUND

The overall objective of the present thesis is to quantitatively predict weldment macro- and microstructures starting from transport phenomena. The heat transfer and fluid flow in the weld pool not only determine the geometries of the FZ and the HAZ but also significantly affect the thermal cycles in these regions, which in turn determine weldment microstructural evolution.[1-3] Experimental determination of temperature profile and fluid field in the weld pool is extremely difficult due to the small weld pool size, the extreme temperatures involved and the presence of the welding arc. Mathematical modeling provides a recourse to overcome these difficulties. Accurate calculation of heat transfer and fluid flow in the weld pool is thus essential for quantitative prediction of macro- and microstructural evolution in the weldment during fusion welding.

In recent years, several comprehensive phase transformation models[51-53,65-68,94] have been developed to predict weldment microstructural evolution by accounting for the characteristics of reactions and transformations involved in welding process. However, these phase transformation models can not be applied to welding process unless the thermal cycles at various locations in the weldment are known. The ability to model weldment microstructural evolution relies on comprehensive phase transformation theory and accurate thermal cycles. Coupling these phase transformation models with the calculated thermal cycles from reliable thermal models is an important approach to quantitatively predict the phase transformations and the resulting phase volume fractions in the weldment.

Significant grain growth often coours in the HAZ due to high temperatures that the solid material in this region experiences. The grain growth in the HAZ occurs under steep temperature gradients and transient thermal cycles. Knowledge of the thermal cycles at various locations is critical for quantitative prediction of grain growth in the HAZ. In recent years, Monte Carlo (MC) based grain growth simulation technique has been used to simulate the grain growth in the HAZ.[104-107] The MC technique can provide

not only grain growth kinetics but also microstructural information. The MC technique is particularly attractive in simulation of grain growth in the HAZ, because the temperature dependence of grain boundary migration can be effectively simulated by this technique.

The purpose of this chapter is to critically review the background materials necessary for the research in the present thesis. The subject matter is classified into three categories: (1) transport phenomena in weld process, (2) modeling steel weldment microstructure, and (3) simulation of grain growth in the weld HAZ.

2.1 Transport Phenomena in Welding Processes

The interaction of the heat source with the material during welding is a complex physical phenomenon. Experimental study of the fluid flow and heat transfer in the weld pool has been generally limited to the measurement of surface temperatures and velocities.[24-32] Direct measurement of the temperatures inside the weld pool by using thermocouples is difficult because of the very high temperatures in the weld pool. This method is also inappropriate due to the errors resulting from thermal loading caused by the presence of the wire in the small weld pool.[29] Thus, various indirect measurement methods[24-30] have been developed in an effort to measure the weld pool surface temperatures. These methods include narrow band infrared pyrometry,[24,25] infrared thermographic cameras,[26,27] fiber optical thermographic sensing,[28] and optical spectral radiometric/laser reflectance.[29,30] As pointed out by Kraus,[29] most of these methods entails a high degree uncertainty due to many assumptions need to be made with respect to the dependency of emissivity on temperature, the associated angle, and the wavelength. In addition, the presence of plasma environment during the arc welding processes can also result in some additional errors. Currently, the non-contact techniques for the measurement of weld pool surface temperatures are still evolving. The measurement of flow velocities in the small and intensely heated weld pool is even more difficult. This task becomes more challenging considering the intense arc and plasma

over the weld pool. Very few data have been reported on the measurement of velocities in the weld pool.[31, 32]

Considering the difficulties existed in experimental measurements, mathematical modeling has become an alternative approach to study the fluid flow and heat transfer in the weld pool. Mathematical modeling can not only avoid the difficulties associated with the experimental measurements but also provide quantitative fundamental understanding of heat transfer and fluid low inside the weld pool. In recent years significant progress have been made in understanding of heat transfer and fluid flow in the weld pool by mathematical modeling.[4-23] In this section. the fundamental principles involved in the heat transfer and fluid flow in the weld pool and previous work in this field are presented.

2.1.1 Energy Transfer from Heat Source to Workpiece

The size and shape of a weld pool resulting from GTA or GMA welding process depend on: (a) the magnitude of the total energy input, (b) the spatial distributions of the energy inputs, and (c) the way the energy is dissipated in the workpiece. The total heat input into the weld is determined by the power supplied by the heat source and the arc efficiency. which is a function of shielding gas. wire feed rate, arc length. electrode diameter. etc. During GTA welding, the radiation from the arc provides the entire heat for welding. During GMA welding, the total heat into the weld is divided between the arc and the sensible heat carried by the molten droplets. Quantitative knowledge of the fraction due to heat from arc (f_a) and that from the molten droplets (f_d) in GMA welding is important. For example. the fraction of heat from molten droplets has significant effect on the shape and size of the "finger penetration", which is a unique geometric feature in GMA welding. Typical values of f_a and f_d in GMA welding reported in some experiments[33-35] are listed in Table 2.1. From the data in Table 2.1, it can be observed that the values of f_a and f_d vary largely depending on the welding conditions. Thus, quantitative information on the values of f_a and f_d should be based on the specified welding conditions.

Table 2.1: Heat transfer efficiency and energy partitioning in GMA welding

Welding conditions	total efficiency η (%)	f_α (%)	f_d (%)	References
Stationary plasma GMA; I = 100~300 A; VI = 4~8 (kW); Ar + 7 % CO2	71	76	24	Ref. 33
Pulsed current GMA; heat input = 0.5~5 kJ/mm Ar + 5 % CO2	60 ~70	38	62	Ref. 34
GMA welding I = 193~132 A. V = 32~36 V welding speed = 7.5~12.8 mm/s Ar + 2 % O2	85	53	47	Ref. 35

The distribution of heat flux input to the surface of the weld pool from the arc has a direct influence on the weld pool geometry. Gaussian distribution of the heat input has been widely used for modeling heat distribution in GTA welding.[4-22] Two types of Gaussian distributions have been reported in the literature for modeling the heat distribution. One is the classical Gaussian distribution of heat input, which was first proposed by Pavelic et al[131] and has been extensively in the simulation of heat flow during welding.[7-19] The other is a modified equation based on experimental results.[36,37] The classical Gaussian distribution of heat input can be expressed as: [7-19,131]

$$q(r) = \frac{3\eta VI}{\pi R^2} \exp\left(\frac{-3r^2}{R^2}\right)$$

(2.1)

where q(r) is the heat flux. η is the arc efficiency, V is the welding voltage. I is the current. r is the distance between a specified location and the heat source, and R is the radius of the arc. Based on experimental results, Tsai et al[36] and Smartt et al[37] modified some parameters in the classical equation to model heat distribution in GTA welding. The modified distribution is expressed as:

$$q(r) = \frac{\eta VI}{2\pi\sigma^2} \exp\left(\frac{-r^2}{2\sigma^2}\right)$$

(2.2)

where symbols q(r), η, V, I, and r have the same meanings as those defined above for equation (2.1). Instead of the arc radius, the symbol of σ, called as distribution parameter,

is used in the modified equation. The distribution parameter is determined by arc length, current, and electrode tip angle.[36,37] For example, the reported value of the Gaussian distribution parameter increases from 1.5 mm to 3.6 mm as the arc length increases from 2 mm to 9 mm for a 100 A arc. This modified Gaussian distribution of heat has also been used in modeling GTA welding process.[5,6,20,22] No systematic experimental measurements have been made for heat distribution during GMA welding. Both the classical and the modified Gaussian heat flux distributions have also been used to model GMA welding process.[20, 38-41]

2.1.2 Fluid Motion and Driving Forces

The significant effect of the fluid flow in the weld pool on heat transfer has been recognized in recent years.[4-23] During arc welding, the fluid flow in the weld pool is driven by a combination of several forces such as surface tension, electromagnetic, buoyancy forces, and the impinging and dragging force of the arc plasma. During GMA welding, there is an additional force due to the impact of metal droplets. Since the impinging and dragging force of the arc plasma stream becomes important only at very high welding currents,[126] for example in excess of 500A. The flow pattern and the resulting weld pool geometry driven by the different forces are schematically shown in Fig. 2.1.

The buoyancy force is caused by the density variations due to the temperature gradients within the weld pool. The variations of density in the weld pool induces the fluid rising in the hotter, less-dense region and sinking in the cooler and denser region, as shown in Fig. 2.1(a). The buoyancy force can be expressed as:[10,16]

$$F_b = \rho g \beta (T - T_{ref})$$ (2.3)

where ρ is the density of liquid metal, g is the acceleration of gravity, β is the thermal expansion coefficient, and T_{ref} is any arbitrarily selected reference temperature.
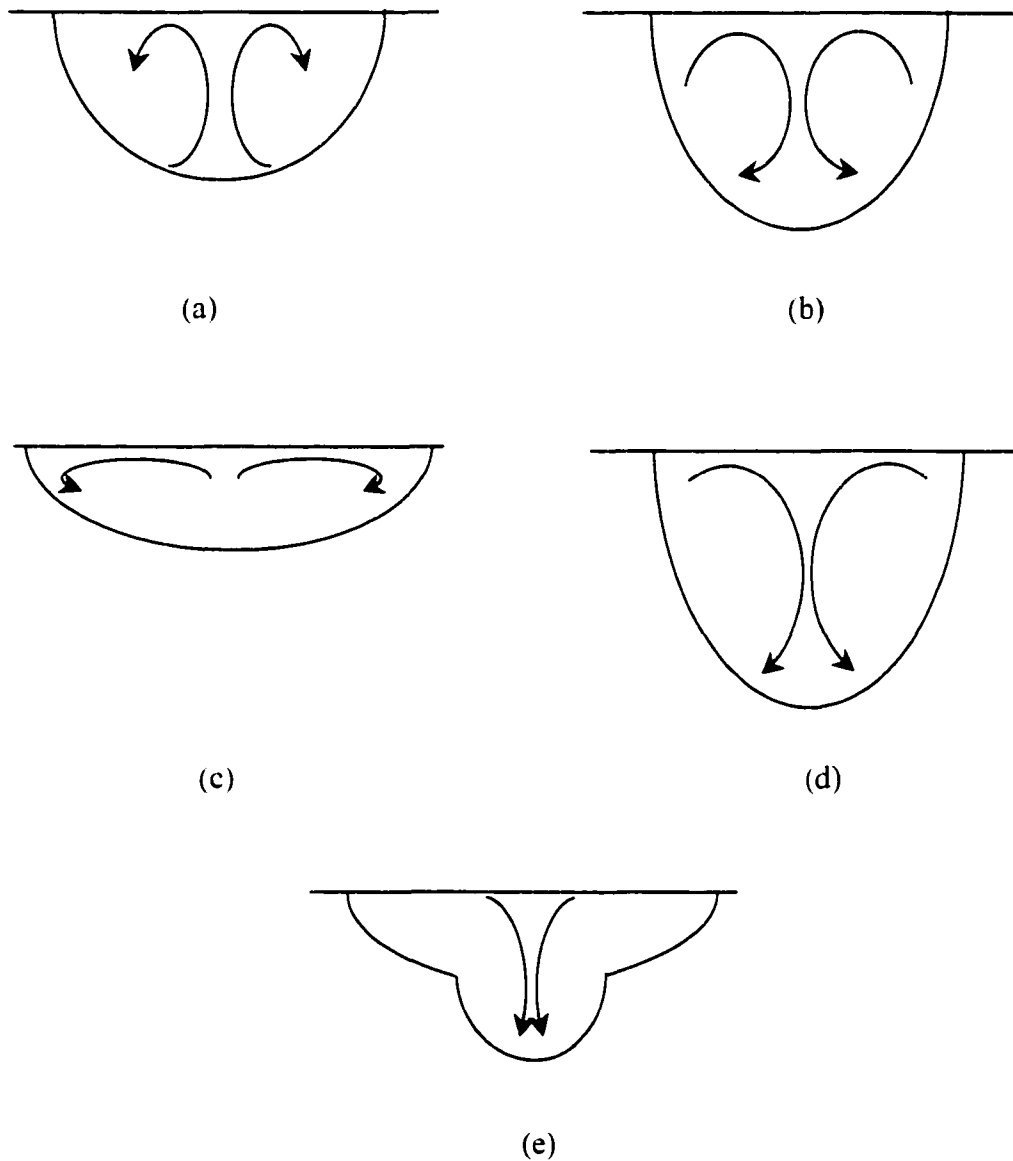
Fig. 2.1: Schematic fluid flow profiles produced by various driving forces. (a) fluid driven by buoyancy force; (b) fluid motion driven by electromegnetic force; (c) fluid driven by surface tension gradeint with $\partial\gamma/\partial T < 0$; (d) fluid driven by surface tension gradeint with $\partial\gamma/\partial T > 0$; (e) impact force from metal droplet during GMA welding.

The electromagnetic force is generated by the interaction of the diverging current and the self induced magnetic field. This electromagnetic force is also called the Lorentz force, which in weld pool is a force radially inwards and downwards. The Lorentz force pulls the liquid metal toward the center along the surface and pushes it down to the bottom of the weld pool, as shown in Fig. 2.1(b). The electromagnetic force can be expressed as:[10,16]

$$F_{em} = J \times B \qquad (2.4)$$

where J is the current density vector and B is the magnetic flux vector. The procedure for calculation of the electromagnetic force in the weld pool is available in the literature.[10,11]

The variation of surface tension at the surface of the weld pool generates a shear stress. The spatial gradient of surface tension is a stress, known as the Marangoni stress. This stress may arise due to variations of both temperature and composition, which can be expressed as:

$$\tau = \frac{d\gamma}{dT}\frac{dT}{dy} + \frac{d\gamma}{dC}\frac{dC}{dy} \qquad (2.5)$$

where τ is the shear stress due to temperature gradient, γ is the interfacial tension, T is the temperature, C is the concentration of surface active element, and y is the distance along the surface from the axis of the heat source. In most cases, the difference in surface tension is due to the temperature variation at the weld pool surface. Sahoo et al.[42] proposed a model for the temperature coefficient of surface tension in binary alloy systems with some surface active elements. From the analysis of the available data in Fe-O, Fe-S, Fe-Se, Cu-O, Cu-S, Cu-Se, Cu-Te, Ag-O, and Sn-Te systems, it was found that the interfacial tension in these systems could be satisfactorily described by a formalism based on the combination of Gibbs and Langmuir adsorption isotherms. The temperature coefficient of surface tension, $d\gamma/dT$, in a binary alloy containing surface active element can be expressed as a function of both temperature and chemical composition:[42]

$$\frac{d\gamma}{dT} = -A - R\Gamma_s \ln(1 + Ka_i) - \frac{Ka_i}{(1 + Ka_i)} \frac{\Gamma_s(\Delta H^\circ - \Delta \overline{H}_i^M)}{T} \qquad (2.6)$$

where A is the negative value of $d\gamma/dT$ for pure metal, Γ_s is the surface excess at saturation, K is the adsorption coefficient, a_i is the activity of species i in the solution, ΔH° is the standard heat of adsorption, and $\Delta \overline{H}_i^M$ is the partial molar enthalpy of mixing of species i in the metal. The temperature coefficient of surface tension, $d\gamma/dT$, for pure metal is negative. Thus, the surface tension is low at the center of the weld pool and is high near the weld pool edge, which will cause an outward flow and consequently a wide and shallow weld pool, as shown in Fig. 2.1(c). For an alloy with a significant amount of surface active element such as sulfur or oxygen, the temperature coefficient of surface tension, $d\gamma/dT$, may be positive, which will cause an inward flow and consequently a narrow and deep weld pool, as shown in Fig. 2.1(d).

In addition to the above forces, the molten droplets transferred from the consumable electrode to the weld pool can carry significant kinetic energy into the weld pool during GMA welding. This force can cause an increased penetration in the middle of the weld pool and make the "finger penetration" weld pool shape, as shown in Fig. 2.1(e).

2.1.3 Estimation of Scaling and Order of Magnititude

In order to understand the heat transfer and fluid flow behavior in the weld pool, it is useful to examine certain dimensionless numbers. These dimensionless numbers characterize the relative importance of different heat transfer mechanisms and the relative importance of the driving forces for metal flow in the weld pool.

2.1.3.1 Relative importance of heat transfer by conduction and convection in the weld pool

The heat in the weld pool is transported by the combination of convection and conduction mechanisms. The relative importance of convection and conduction in the overall transport of heat in the weld pool can be assessed from the value of the Peclet number, Pe, which is given by:

$$Pe = \frac{u\rho C_p L_R}{k} \tag{2.7}$$

where u is the velocity, ρ is the density, C_p is the specific heat at constant pressure, L_R is the characteristic length, and k is the thermal conductivity of the melt. When Pe is large, which in physical terms means large melt velocity, large weld-pool, and poor thermal conductivity, then the convective effects, i.e. the weld pool circulation will markedly affect the heat transfer. In contrast, the effect of heat dissipation by conduction mechanism is negligible. For example, in the welding of steel, typical velocity in the weld pool is 0.2 m/s, the density is 7200 kg/m^3, the specific heat is 754 J/kg·K, the weld depth is 0.005 m, the thermal conductivity is 25 W/m·K, and the corresponding value of Pe is found to be 217.2. Under most welding conditions, the heat in the weld pool is predominantly transported by convection, and the reported Peclet number values are much larger than unity.[5, 16-19]

Another important dimensionless parameter, Prandtal number (Pr), is used for judging the relative importance of the viscous diffusivity and thermal diffusivity in heat dissipation. The Prandtal number, Pr, is expressed as:

$$Pr = \frac{\nu}{\alpha} = \frac{C_p \mu}{k} \tag{2.8}$$

where ν is the viscous diffusivity, α is the thermal diffusivity, C_p is the specific heat at constant pressure, μ is the viscosity, and k is the thermal conductivity. From equation (2.8), it is obvious that the Prandtal number is actually a combination of material physical property for laminar flow. For example, in the steel weld pool,[2, 16] the specific heat is 754 J/kg·K, the viscosity is 0.006 kg/m·s, the thermal conductivity is 25 W/m·K, and the value of Pr is 0.181. In contrast, in the aluminum weld pool,[144, 145] specific heat is 896 J/kg·K, the viscosity is 0.007 kg/m·s, the thermal conductivity is 107.8 W/m·K, and the value of Pr is only 0.058. Compared with the value of Pr for the steel weld pool, the lower value of Pr in the aluminum weld pool indicates that less heat will be dissipated by viscous diffusivity due to large thermal conductivity of aluminum. As an extension of the Prandtal number, turbulent Prandtal number, Pr_t, has been introduced to describe the heat dissipation mechanism in turbulent flow.[21, 22, 139, 140] The turbulent Prandtal number is very

important for turbulent heat transfer and fluid flow calculations, in which the turbulent thermal diffusivity is not known priori and obtained from turbulent viscous diffusivity by the Prandtal number.[21,22] For steel and aluminum, the turbulent thermal conductivity can be related to the turbulent viscosity by the turbulent Prandtl number,[139,140] $Pr_t = C_p\mu_t/k_t = 0.9$.

2.1.3.2 Relative importance of driving forces in the weld pool

Several dimensionless numbers have been used in the literature to determine the relative importance of different driving forces in the weld pool, which are summarized in Table 2.2. The relative importance of the driving forces in the weld pool, i.e., the surface tension gradient force, electromagnetic force, and buoyancy force, can be judged by the combination of the dimensionless numbers listed in Table 2.2. For example, the ratio of buoyancy force to surface tension gradient force can be expressed as:

$$R_{b/s} = \frac{Gr}{M_a} \qquad (2.9)$$

where Gr is Grashof number, which is the ratio of buoyancy force to viscous force, and Ma is surface tension Reynolds number, which is the ratio of surface tension gradient force to viscous force. The ratio of buoyancy force to electromagnetic force can be expressed as:

$$R_{b/m} = \frac{Gr}{R_m} \qquad (2.10)$$

where R_m is magnetic Reynold's number, which is the ratio of electromagnetic force to viscous force. The ratio of surface tension gradient force to electromagnetic force can be expressed as:

$$R_{s/m} = \frac{M_a}{R_m} \qquad (2.11)$$

where Ma is surface tension Reynolds number and where R_m is magnetic Reynold's number.

To estimate the relative importance of these driving forces, typical parameters for GTA welding of steel, presented in Table 2.3, were used. The characteristic length for calculation of Grashof number is determined following the classical example given in a

Table 2.2: Dimensionless numbers for describing the relative importance of different forces

Dimensionless number	Description
Reynolds number, $Re = \dfrac{\rho u L_R}{\mu}$	Ratio of inertial force to viscous force
Grashof number, $Gr = \dfrac{g\beta l^3 \Delta T \rho^2}{\mu^2}$	Ratio of buoyancy to viscous force
Magnetic Reynold's number, $R_m = \dfrac{\rho \mu_m I^2}{4\pi^2 \mu^2}$	Ratio of electromagnetic force to viscous force
Surface-tension Reynolds number, $Ma = \dfrac{\rho L_R \Delta T \frac{\partial \gamma}{\partial T}}{\mu^2}$	Ratio of surface tension gradient force to viscous force

* The meanings of the symbols in these dimensionless numbers are given in Table 2.3.

Table 2.3: Typical parameters for calculation of the dimensionless numbers

Thermal expansion coefficient, β	1.0×10^{-4} K^{-1}
Gravitational acceleration, g	9.8 m/s^2
Density, ρ	7100 kg/m^3
Magnetic permeability, μ_m	1.26×10^{-6} N/A^2
Viscosity, μ	6.0×10^{-3} kg/m-s
Surface-tension temperature coefficient, $\partial \gamma / \partial T$	-4.3×10^{-4} N/m-K
Characteristic length of the weld pool, L_R	0.005 m
Characteristic length for calculation of Grashof number, l	0.00125 m
Average velocity in the weld pool, u	0.05 m/s
Temperature gradient, ΔT	600 K
Current, I	100 A
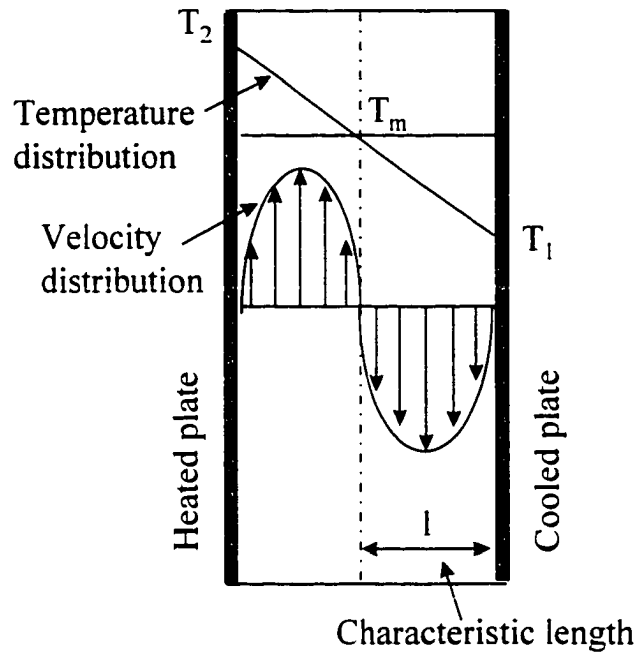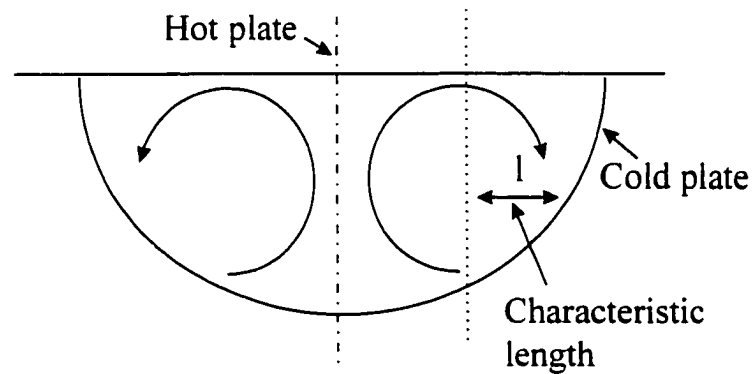
Fig.2.2: (a) Definition of characteristic length for free convection between two vertical plates with different temperatures.[123] (b) Definition of characteristic length for convection due to buoyancy force in the weld pool.

standard text book by Bird, Stewart, and Lightfoot,[123] as shown in Fig. 2.2(a). In their example, free convection between two vertical plates with different temperatures was studied. The convection due to buoyancy force in the weld pool can be treated in a similar way as shown in Fig. 2.2(b). The central region has higher temperature than the side of the weld pool which is at the solidus temperature of the alloy. Due to the density difference, the hot liquid metal will rise in the middle of the weld pool and sink in the relatively cooler region near the sides. Considering the characteristics of buoyancy in the weld pool, the characteristic length for the calculation of Grashof number in the weld pool can be approximately taken as one eighth of the width of the weld pool, as shown in Fig. 2.2(b).

The calculated values of the dimensionless numbers are given in Table 2.4. Compared to surface tension gradient force, the buoyancy force is negligible since the value of the dimensionless number $R_{b/s}$ is very small (0.0063). In contrast, the electromagnetic force is comparable with the surface tension gradient force. The value of $R_{s/m}$ under this condition (100A) is 3.97, which means that the surface tension gradient force is larger than the electromagnetic force. However, this situation may change if the welding current increases. For example, if the currents are taken to be 200 A and 300 A and other parameters remain unchanged, the corresponding values of $R_{s/m}$ will be 0.99 and 0.44, respectively. This means that the electromagnetic force can be the dominant force in the weld pool at high welding currents.

2.1.3.3 Estimation of Velocity in the Weld Pool

As suggested by DebRoy and David,[2] the order of the maximum velocity of the flow driven by the surface tension gradient can be approximated by the following expression:

$$u_m^{3/2} \approx \frac{d\gamma}{dT} \frac{dT}{dy} \frac{W^{1/2}}{0.664 \rho^{1/2} \mu^{1/2}}$$

(2.12)

where γ is surface tension, T is temperature, y is the distance along the surface from the axis of the heat source, W is the width of the weld pool, ρ is the density of the liquid metal, and μ is the viscosity. Assuming typical values of physical properties and weld

Table 2.4 Calculated values of the dimensionless numbers from parameters in Table 2.3

Dimensionless number	values
Reynolds number, Re	2958
Grashof number, Gr	1.61×10^3
Magnetic Reynold's number, R_m	6.30×10^4
Surface-tension Reynolds number, Ma	2.54×10^3
Dimensionless number, $R_{b/s}$	0.0063
Dimensionless number, $R_{b/m}$	0.025
Dimensionless number, $R_{s/m}$	3.97

pool dimensions in equation (2.12), a maximum velocity of 62 cm/s was obtained in the weld pool.[2] The magnitude of this calculated velocity is comparable with the experimentally determined value. In a series of experimental studies in GTA welding by Heiple et al.,[32] surface velocities of the order of 100 cm/s were measured and complete reversal of the direction of fluid flow and a marked change in weld pool geometry were observed due to small changes in surface active elements such as sulphur and oxygen. It was concluded that the marangoni force was the most dominant of all forces driving fluid flow in the weld pool from GTA welding using 150 A current.

If the surface tension gradient is not considered, the maximum velocities can be much smaller. For example, the maximum velocity due to buoyancy can be approximated by the following expression: [44]

$$u_m \approx \sqrt{g\beta\Delta Td} \qquad (2.13)$$

where g is the acceleration due to gravity, β is the coefficient of the volume expansion, ΔT is the temperature difference, and d is the depth. For the values of $\Delta T = 600$ °C, g =981 cm/s^2, $\beta = 3.5 \times 10^{-5}$/°C, and d = 0.5 cm, the calculated value of um from equation (2.13) was found to be[2] 3.2 cm/s. In the case of electromagnetically driven flow in the weld pool, the velocity values reported in the literature[45] were around 20 cm/s at a welding current of 100 A. The magnitude of the velocities from both buoyancy and

electromagnetic forces in the weld pool are usually much smaller than those resulting from surface tension gradient force.

2.1.4 Calculation of Convective Heat Transfer in the Weld Pool

Attempts to understand transport phenomena in fusion welding process date back to the 1940's. However, up to the early 1980's, efforts in calculating heat transfer during welding were mostly limited to pure conduction heat transfer. One of the initial efforts to model fluid flow in the weld pool was made by Atthey[4] to understand the effect of fluid flow pattern on the heat transfer inside the weld pool during stationary GTA welding. The principle driving force considered was electromagnetic force and the flow pattern with 100 A current was calculated in an isothermal hemispherical pool of known shape and size. The corresponding peclet number, Pe, was found to be much larger than unity (10<Pe<70). Thus, it was concluded that convection was the dominant mode of heat transfer in the weld pool. However, another important driving force, surface tension was ignored in his calculation and the fluid flow calculation was not coupled with thermal calculation in his model.

Oreper, Szekely and Eagar,[5] and Oreper and Szekely[6] modeled heat transfer and fluid flow model in the weld pool in two dimensions. In their model, the driving forces in the GTA weld pool such as the surface tension, electromagnetic, and buoyancy forces were considered. It was found that surface tension and electromagnetic forces dominate the flow behavior in the weld pool. The surface tension driven flows were found to be very effective in dissipation of the incident energy flux on the pool surface. They[5] found that the surface tension may produce quite high surface velocities. With welding current being 100 A, the calculated maximum velocity was found to be 83.8 cm/s by considering surface tension gradient force. In contrast, the calculated velocity was only 4.5 cm/s without considering surface tension gradient force. They found that both surface tension gradient and electromagnetic forces can have profound effect on the weld pool shape.[5]

The initial modeling efforts stimulated a great deal of interest in studying transport phenomena in the weld pool by mathematical modeling. Since then,

considerable efforts have been made in understanding the fluid flow and heat transfer in the weld pool. Tsai and Kou[7-9] modeled separately the effects of buoyancy, electromagnetic, and surface tension on the heat transfer and flow patterns in the weld pool for stationery GTA welding. Kou and Wang[10,11] developed a comprehensive model to calculate temperature distributions in moving weld pools where the convection was driven by surface tension, electromagnetic, and buoyancy forces. The convection patterns and the weld penetrations due to individual driving forces were demonstrated separately to show distinct differences among themselves and at the same time to explain those due to the combined driving forces. Two circulation loops were predicted in the weld pool for the surface tension temperature coefficient, $\partial\gamma/\partial T = -0.35\times10^{-3}$ kg/s^2·K. The outward Marangoni flow dominated near the weld pool surface and another downward circulation in the bulk of weld pool was induced by electromagnetic force.

In the last two decades, considerable efforts have been made at Penn State in understanding heat transfer and fluid flow in the weld pool by mathematical modeling. Starting from the calculations of temperature and velocity fields in the weld pool, the weld pool geometry,[12,14,15,18,19] vaporization of alloying elements,[15,129,132-135] weld metal microstructure,[15,128] inclusion characteristics,[136] and concentrations of dissolved gases in the weld metal[19,130,137] have been systematically investigated by comprehensive mathematical modeling combined with critical experiments. Since the 3D turbulent heat transfer and fluid flow proposed in the present investigation is mainly based on previous investigations at Penn State, a review of the previous work at Penn State is given below.

The 3D heat transfer and fluid flow model[16] now available at Penn State has been developed and refined through the past 15 years. The model was initially established for two dimensional calculations and was applied in some simple material systems such as pure iron.[14,15] Up to date, the model has been used to calculate the weld geometries in the weldments of pure iron,[14,15] stainless steel,[12,13,17,18] low alloy steels,[19] aluminum alloys,[142] and commercially pure titanium[143] fabricated by different welding processes. Paul and DebRoy[15] calculated the heat transfer and fluid flow in the weld pool of pure iron and pure iron doped with sulfur fabricated by laser welding. The weld pool geometry

and the secondary dendrite arm spacing of the solidified structure were predicted based on the calculated temperature profiles and cooling rates. No electromagnetic force exists during laser welding and surface tension gradient force is the dominant driving force in the weld pool. As shown in Fig. 2.3, the ratio of depth to width in the pure iron weld pool was found to be much smaller than that in the pure iron doped with sulfur. This is because the surface tension temperature coefficient in pure iron is negative, which results in an outward flow on the surface of the weld pool, while that in pure iron containing sulfur is positive, which causes an inward flow on the surface. The theoretically predicted weld pool geometry and the secondary dendrite arm spacing were comparable with corresponding experimental results.

Zacharia et al.[12,13] developed a model to quantitatively understand the influence of the heat transfer and fluid flow in the transient development of the weld pool of 304 stainless steel fabricated by GTA and laser welding. In their work, the coefficient of surface tension was taken as a function of both temperature and sulphur concentration based on a the model proposed by Sahoo et al.[42] It was found that the spatial variation of surface tension dominated the fluid flow patterns and controlled the development of the weld pool. It was shown that the weld penetration and the aspect ratio were not determined solely on the basis of level of surface active elements but rather due to a combination of the level of surface active elements and the temperature distribution at the weld pool surface. Good agreement was achieved between the predictions of the model and experimental observations with respect to the shape and size of the weld pool as shown in Fig. 2.4.

Mundra et al.[17] examined the effects of thermophysical properties on the heat transfer and fluid flow in the weld pool. Fig. 2.5 shows some of the calculated results from the model. The effects of thermal diffusivity of liquid metal are shown in Fig. 2.5 (a). The role of this parameter can be understood by the way it influences the heat distribution in the pool. High value of k/C_p means that there is less resistance to the heat flow in the weld pool and the heat absorbed at the surface reaches the liquid/solid

(b)
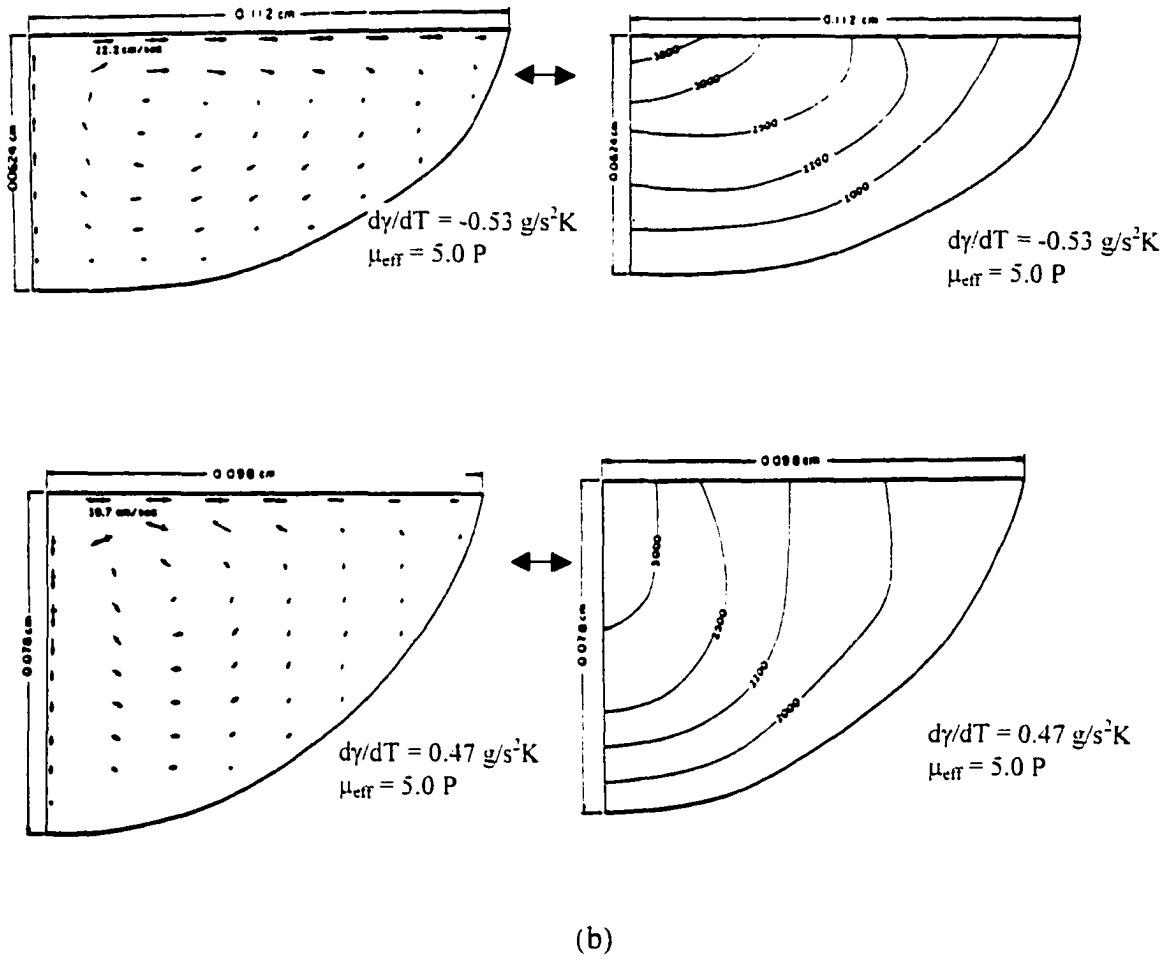
Fig. 2.3: Comparion of the calculated temperature field, velocity field, and the resulting geometry of the weld pool in the pure iron and the pure iron doped with sulfur.[14]

6.0 —
5.5 —
5.0 —
4.5 —
4.0 —
3.5 —   500 μm
3.0 —

Y-AXIS (MM)

3000 K 2800 K 2600 K 2400 K 2200 K 2000 K 1800 K

— 0.1 M/S

-4.0   -3.0   -2.0   -1.0   0.0   1.0   2.0   3.0   4.0

X-AXIS (MM)

(a)

edges in detail by using continum field model.

6.00 —
5.98 —
5.96 —
5.94 —
5.92 —
5.90 —
5.88 —
5.86 —
5.84 —
5.82

Y-AXIS (MM)

— 0.1 M/S

-0.25   -0.20   -0.15   -0.10   -0.05   0.00   0.05   0.10   0.15   0.20   0.25

X-AXIS (MM)
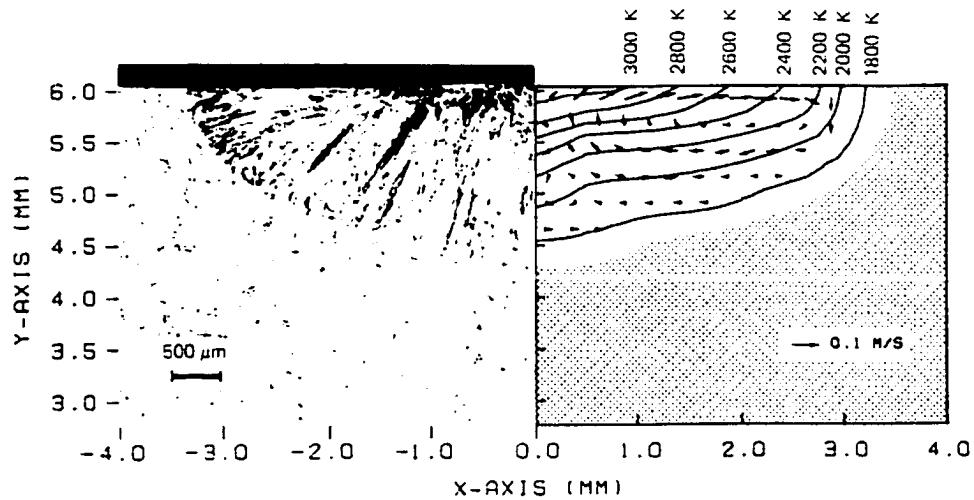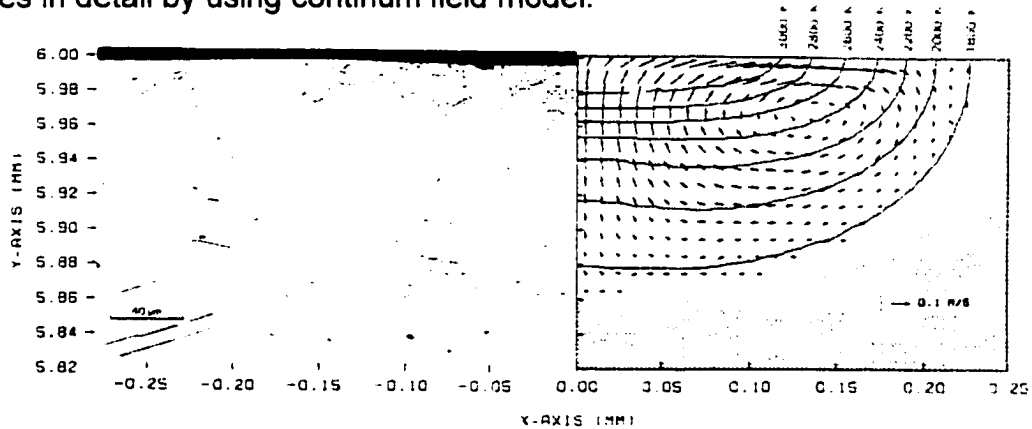
(b)

Fig. 2.4: Comparison of the calculated and experimentally observed weld fusion zone geometry of 304 stainless steel (90 ppm sulfur) from different weld processes.[12] (a) GTA welding, current 150 A, and voltage 14 V; (b) laser welding, 500 W, and absorptivity 0.15.
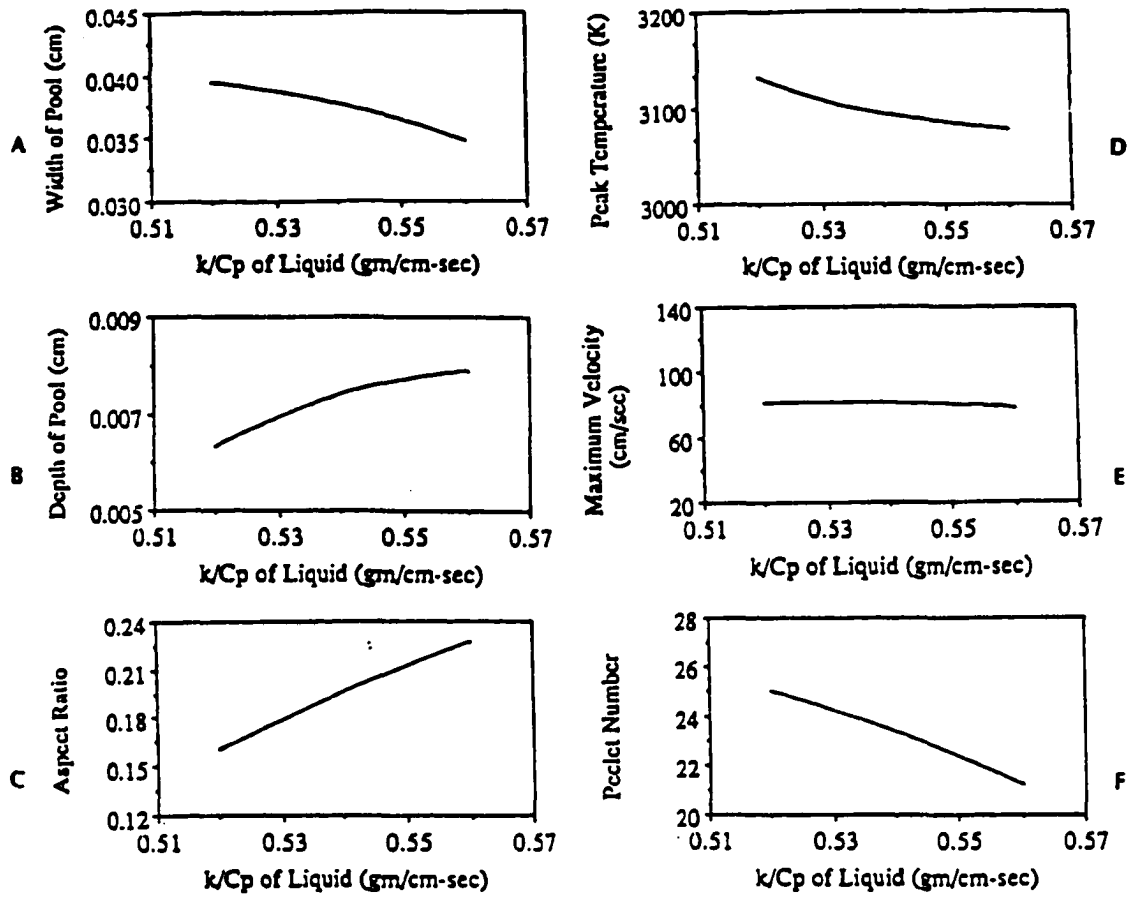
Fig. 2.5: (a) Effects of k/C_p of liquid on: A - width; B - depth; C - aspect ratio of the weld pool; D - peak temperature; E - maximum velocity; F - the Peclet number for heat transfer.[17]
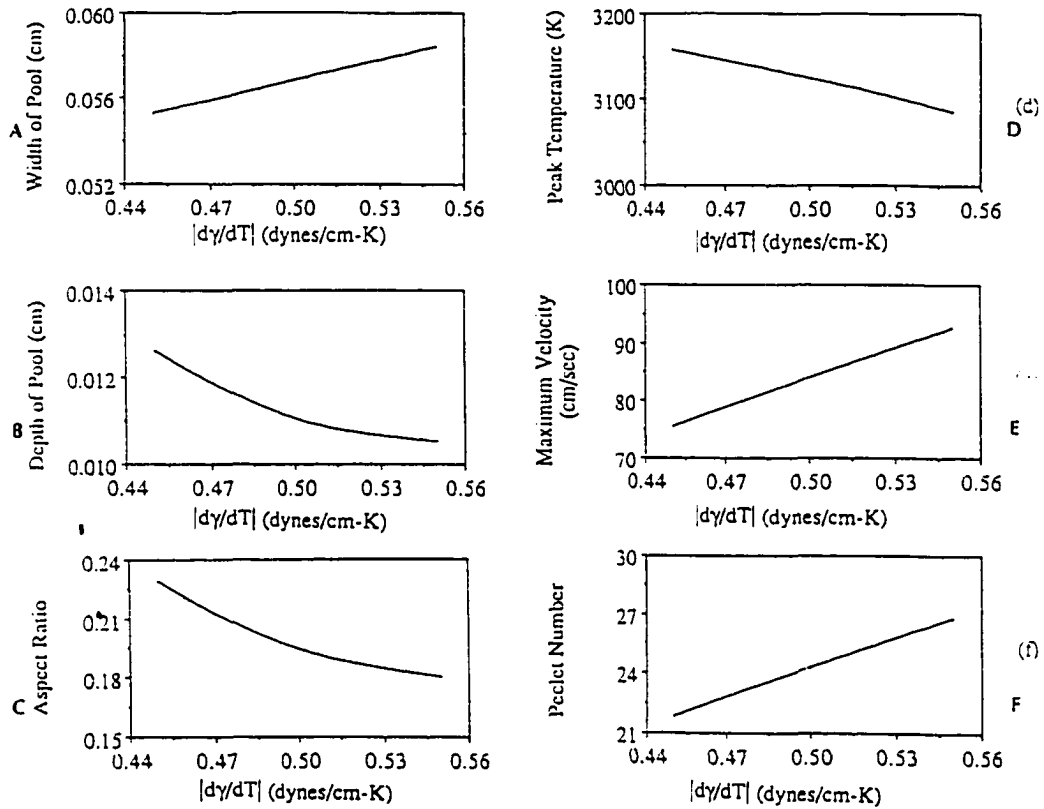
Fig. 2.5(b): Effects of dγ/dT of liquid on: A - width; B - depth; C - aspect ratio of the weld pool; D - peak temperature; E - maximum velocity; F-the Peclet number for heat transfer.[17]

interface easily. As a result, lower peak temperature and smaller weld pool are obtained as the value of k/C_p increases. The effects of surface tension temperature coefficient, $d\gamma/dT$, on the weld geometries, peak temperature, and maximum velocity are presented in Fig. 2.5(b). An increase in $d\gamma/dT$ results in an increased shear stress and surface velocities. Since the value of $d\gamma/dT$ for pure iron is negative, the liquid metal flows from interface easily. As a result, lower peak temperature and smaller weld pool are obtained as the value of k/C_p increases. The effects of surface tension temperature coefficient, $d\gamma/dT$, on the weld geometries, peak temperature, and maximum velocity are presented in center to outside on the top surface. Consequently, the width of the pool increases with the value of $d\gamma/dT$ and the depth of the pool decreases for a given heat input.

More recently, Mundra et al.[16] developed a 3D model to calculate the heat transfer and fluid flow in the weld pool. The weld pool shape and size of over two hundred laser spot welds[18] fabricated at various heat inputs were satisfactorily predicted by the model. Fig. 2.6 shows the comparison of the predicted weld geometries for the steels with different sulfur contents with the corresponding experimental results at various heat inputs. When the laser power was low (1900 W), the weld pool geometries were similar in the two steels containing 20 and 150 ppm sulfur. In contrast, when the laser power was higher (3850 W or 5200 W), the weld geometry showed a pronounced dependence on the concentration of sulfur. At higher laser power, much deeper penetration was obtained in the welds with 150 ppm sulfur than those with 20 ppm sulfur. The phenomena observed can be explained by considering the relative importance of convective and conductive heat transfer in the weld pool. When the laser power was 1900 W, the values of the Peclet number (Pe) in both welds were found to be less than unity. This means that conductive heat transfer was more important than convective heat transfer at this heat input. Thus, the effect of sulfur content on surface tension and the resulting weld geometries was insignificant. However, much larger values of the Peclet number were found (>200) at high laser power (3850 W and 5200 W), which indicated that convective heat transfer was dominant in the weld pool. As a result, the effect of sulfur on the weld pool geometries was pronounced.
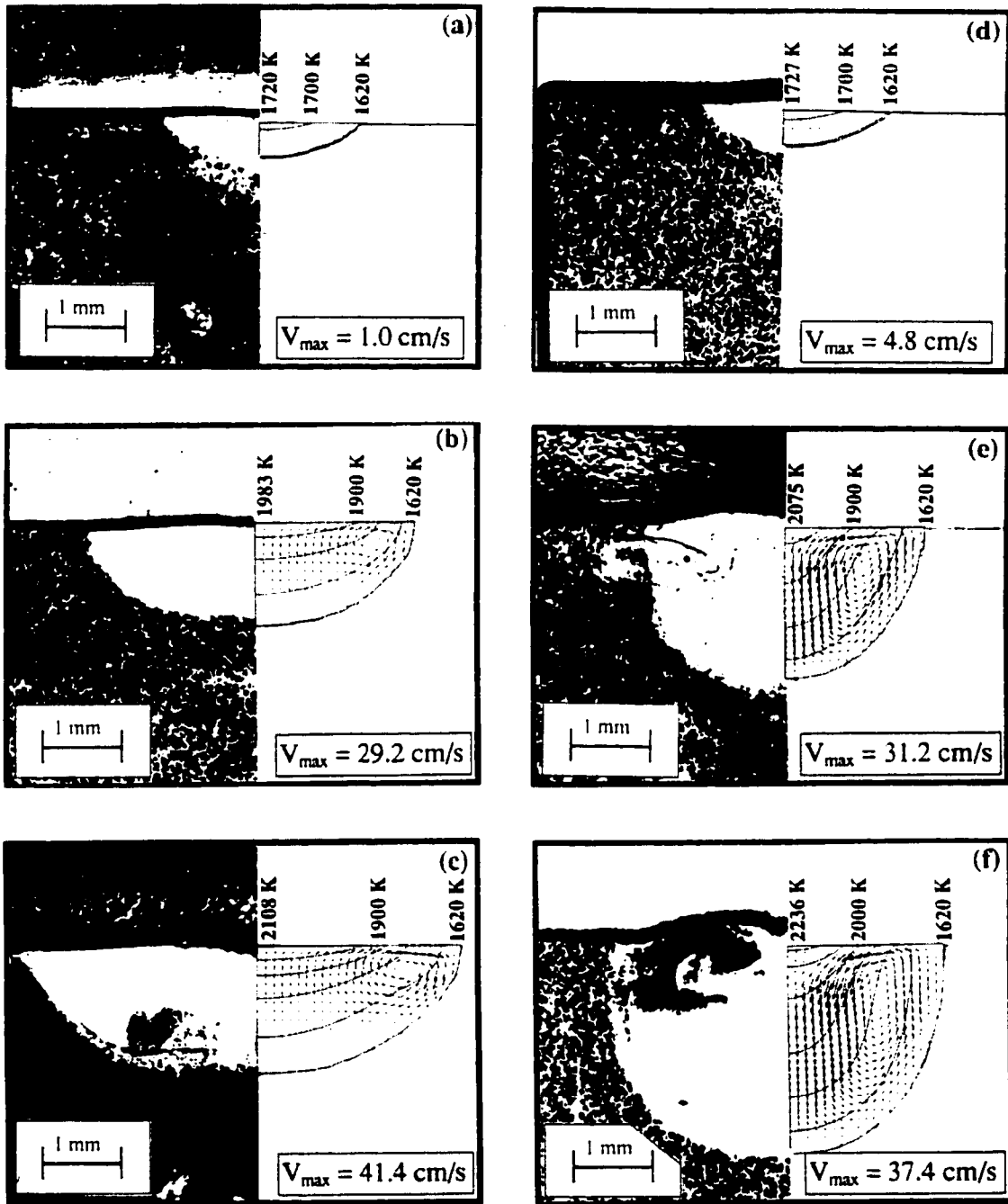
Fig. 2.6: Comparison[18] of the calculated and experimentally observed weld pool geometries for the steel containing 20 ppm sulfur for laser powers of (a) 1900 W, (b) 3850 W and (c) 5200 W and for the steel containing 150 ppm sulfur for laser powers of (d) 1900 W, (e) 3850 W and (f) 5200 W.

To assess the model, the calculated temperature fields from the model have been compared with the experimental results. Fig. 2.7 shows a comparison of the calculated temperature fields at the weld pool surface with the temperature fields which were measured with thermo-camera during laser welding experiments.[127] It can be observed that the predicted temperature fields agree well with the experimental results. The calculated peak temperatures are consistent with the measured values within the experimental uncertainty. The model was also used to predict the weld geometries and cooling rates in low alloy steels from GMA welding. The predicted results were found in good agreement with the corresponding experimental results.[19]

In addition to the weld geometry prediction, much efforts have been made at Penn State to model the alloying element vaporization,[15,129,132-135] concentrations of dissolved gases in the weld metal,[19,130,137] and inclusion characteristics in the weld metal.[136] Quantitative understanding of the loss of alloying elements from weld pools involves numerical solution of the conservation equations of mass, momentum, and transitional kinetic energy of the vapor molecules near the weld pool surface. Furthermore, the weld pool surface temperature distribution is also critical for the vaporization rate calculations. DebRoy et al.[135,129] developed a comprehensive mathematical model to calculate the vaporization of pure metals and the loss of alloying elements from stainless steel weld pools. In the model, the velocity distribution functions were used in the conservation equations to determine the rates of vaporization from and the rates condensation on the weld pool surface due to a total pressure gradient at the pool surface. Compared to the vaporization rates calculated from the Langmuir equation, the rates predicted from the model were found much closer to the experimentally determined values for both pure iron and titanium.[135]

Based on calculation of heat transfer and fluid flow in the weld pool, significant progress has also been made at Penn State in understanding of hydrogen and nitrogen distribution in the weld metal. A model to calculate heat transfer, fluid flow, and hydrogen concentration in the weldment in three dimensions has been applied to predict hydrogen concentration in the weldment of GMA welded steels.[19] The predicted trend of

(a) 4800 W   (b) 3200 W
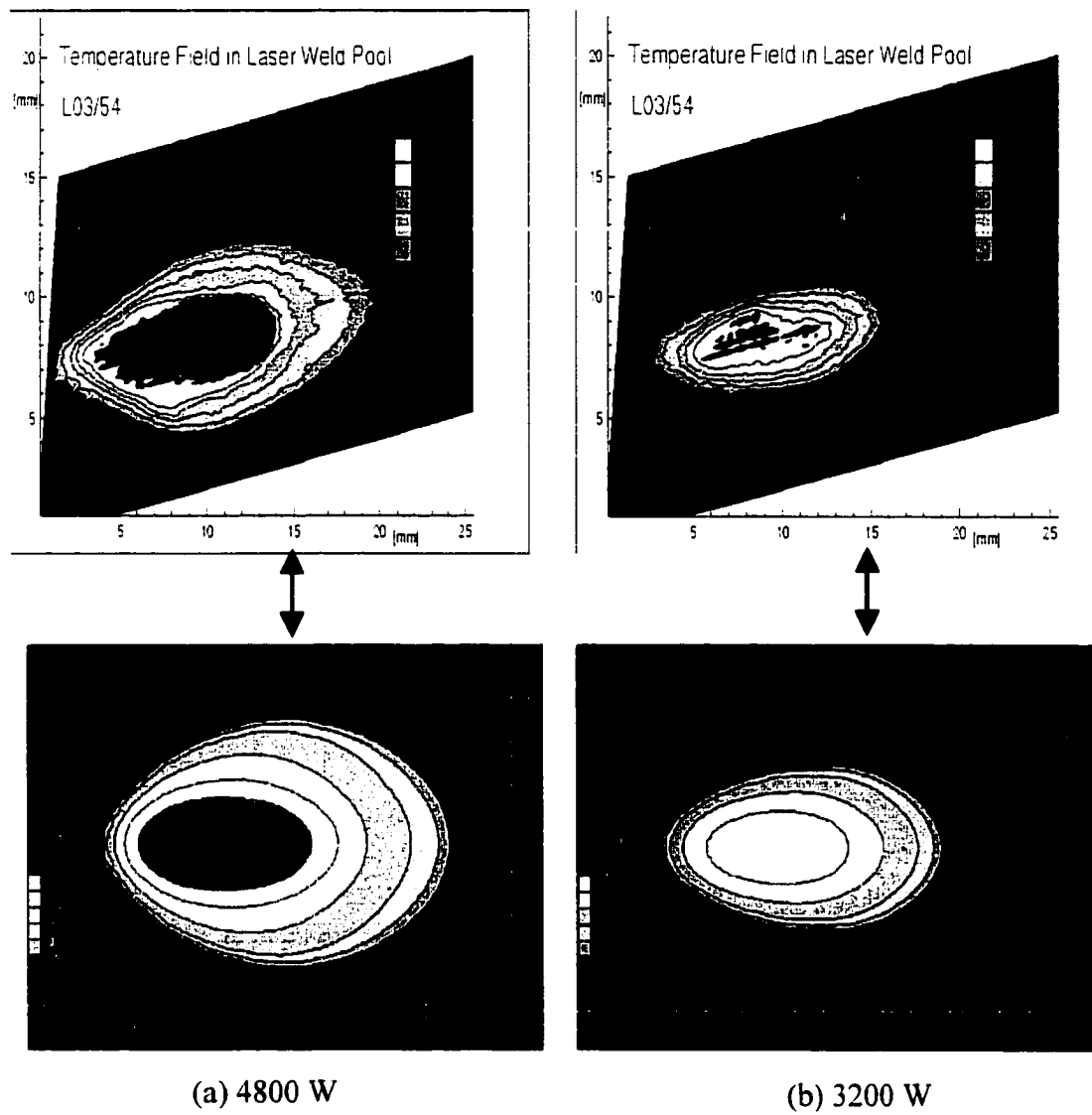
Fig. 2.7: Comparison of calculated and experimentally measured temperature fields at different powers during laser welding.[127]

the hydrogen content in the weldment under the investigated conditions was consistent with experimental observation. To calculate the nitrogen dissolution in the weld metal. Mundra and DebRoy[137] proposed a model in which the concentration of atomic nitrogen in the plasma was assumed higher than what would be expected in equilibrium with diatomic nitrogen at the temperatures of the weld pool surface. To understand the partition of nitrogen between the weld metal and its plasma environment, both mathematical modeling and physical modeling experiments were made by Palmer and DebRoy.[130] The observed nitrogen concentrations in the pure iron weld metals could be explained by calculated results from the modeling.[130]

Recently. the calculation of heat transfer and fluid flow in the weld pool has also provided a basis for modeling inclusion growth in the weld pool. Inside the weld pool. molten liquid undergoes vigorous circulation resulting from buoyancy, surface tension, and. when electric current is used, electromagnetic forces. It is the specifics of the time-temperature histories experienced by the inclusions that affect their composition and size distribution. Hong et al.[136] modeled the inclusion formation in the weld pool by considering their path. temperature history, velocities, and oxygen diffusion kinetics during arc welding. The predicted size distribution of the inclusions was comparable with the corresponding experimental results.

The agreement between the calculated and experimentally determined values of weld geometry and other parameters for various welding conditions justify the validity of the calculations using the 3D heat transfer and fluid flow model now available at Penn State. However, it should be recognized that the calculation of heat transfer and fluid flow in this previous model was performed using enhanced viscosity and thermal conductivity in most cases. For improved understanding of the heat transfer and fluid flow in the weld pool, a detailed turbulence model is needed to compute effective viscosity and thermal conductivity distributions in the weld pool.

2.1.5 Turbulent Heat Transfer and Fluid Flow in the Weld Pool

Many existing weld pool models have implicitly assumed laminar flow in the weld pool for simplicity. However, recently, both experimental observations[49] and theoretical calculations[21,22] in GTA welding have indicated that the fluid flow in the weld pool is turbulent in nature. Malinowski-Brodnicka et al.[49] measured the flow velocity in AISI 310 stainless steel weld pools and found that the Reynolds number was about 3,000. Comparing this value to the classical critical Reynolds number for transition from laminar to turbulent flow in pipes (Re=2,100), the flow in the AISI 310 weld pools was concluded to be turbulent.[49] As discussed earlier, both experimental measurement[32] and theoretical calculations[2,5,10,11,15] showed the maximum velocity in the weld pool is in the order of 50 cm to 100 cm/s. On a fundamental basis, the large shear rate associated with such high free surface velocity in small weld pools leads to turbulent fluctuations.

Some previous calculations recognized turbulent nature of the flow in the weld pool and modeled the turbulent effects of heat transfer and fluid flow by using enhanced viscosity and thermal conductivity.[16-19,47] The predicted shape and size of the weld pool were found to be much closer to experimental results by adopting these enhanced viscosity and thermal conductivity.[16-19,47] However, in these calculations the necessary values of the enhanced viscosity and thermal conductivity were selected arbitrarily and not from fundamental principles. In contrast, turbulent viscosity and thermal conductivity are commonly used in computational fluid dynamics to account for turbulence.[50] In the turbulent viscosity concept, the energy dissipation due to turbulence is accounted for by locally increasing the viscosity according to various schemes, i.e. the effective viscosity is the sum of the molecular viscosity and the turbulent viscosity, where the molecular viscosity is a physical property of the fluid, and the turbulent viscosity is a system property which depends on the nature of the flow in a given system. Likewise, the effective thermal conductivity is the sum of the molecular value and the turbulent value.

Choo and Szekely[21] considered turbulence in the calculation of heat transfer and fluid flow in the weld pool in a two dimensional model, in which the K-ε turbulence
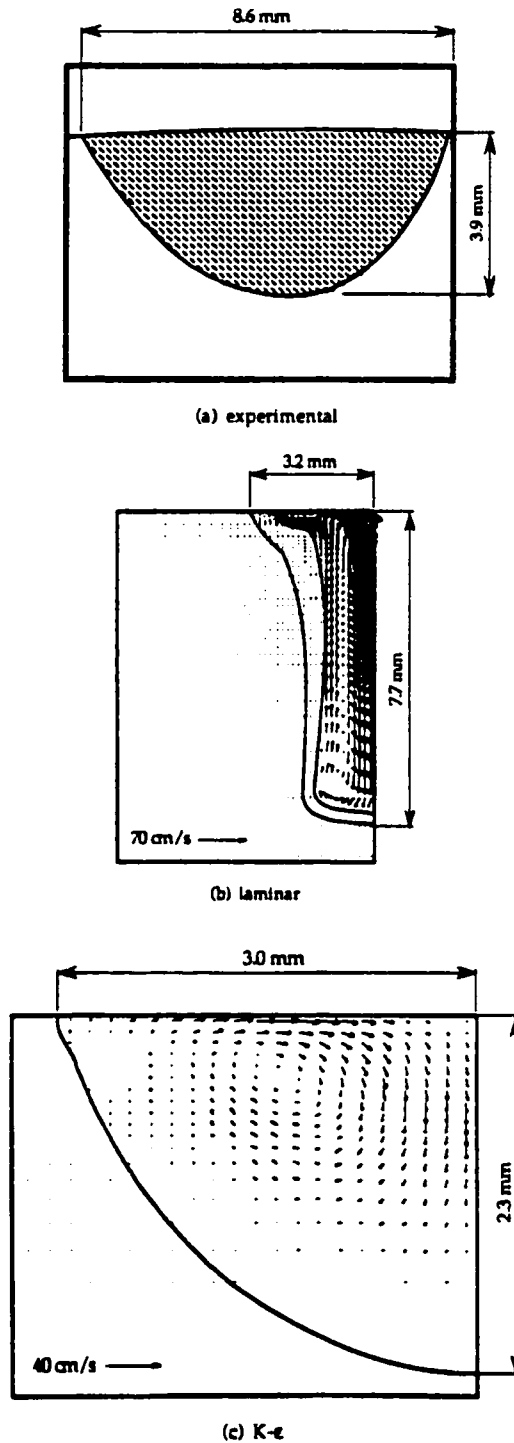
Fig. 2.8: Comparison of weld pool shapes from (a): experimental results; (b): numerical results based on laminar model; (c): numerical results based on K - ε turbulence model. Welding conditions: GTA welding of 304 stainless steel, 100A, 13.2V.[21]

model[50] was adopted. The flow in AISI 304 stainless weld pools from stationary GTA welding was simulated by a turbulence model. The calculated geometries from both laminar and turbulent models were compared with the experimental geometry as shown in Fig. 2.8. They[21] found that the calculated weld pool geometries from turbulence model were in much better agreement with experimental measurements than those from laminar model.

More recently, Hong, Weckman, and Strong[22] incorporated K-ε turbulence model in their weld thermo-fluid model, in which the free surface of the weld pool and wall function boundary for the solid-liquid interface were considered by using a dynamic grid-remapping technique. The temperature distributions and flow patterns in the weld pool from their laminar and turbulent models were compared in Figs. 2.9 and 2.10, respectively. It was found that the depth of the weld pool, the peak temperature, and the maximum velocity were reduced due to consideration of turbulent heat transfer and fluid flow. As shown in Fig. 2.10 (c), the values of dimensionless viscosity μ_t/μ are much larger than unity in the weld pool, which indicates that strong turbulence exists in the weld pool. The predicted width, depth, and the width to depth ratio of the weld pool from both laminar and turbulent models were compared with the corresponding experimental results in Fig. 2.11. It is obvious that the predicted results from the turbulent model is in much better agreement with the observed results than those obtained from the laminar model. Based on these results, they concluded that the influence of turbulence on the final weld pool shape and size was significant in the GTA welding of AISI 304 stainless.

The weld models discussed above[21,22] have demonstrated that heat transfer and fluid flow in the weld pool are turbulent. The results from these models suggested that accurate predictions of the weld pool geometry as well as the thermal histories in the weldment can only be possible if effects of turbulence are modeled. However, these previous turbulent calculations were only limited in two dimensions for modeling of stationary GTA welding. The two dimensional calculation can not provide a full description of the heat transfer and fluid flow in the weld pool. For example, it does not provide the spatial distribution of temperatures and the variation of the thermal cycles at various locations in the whole weldment.
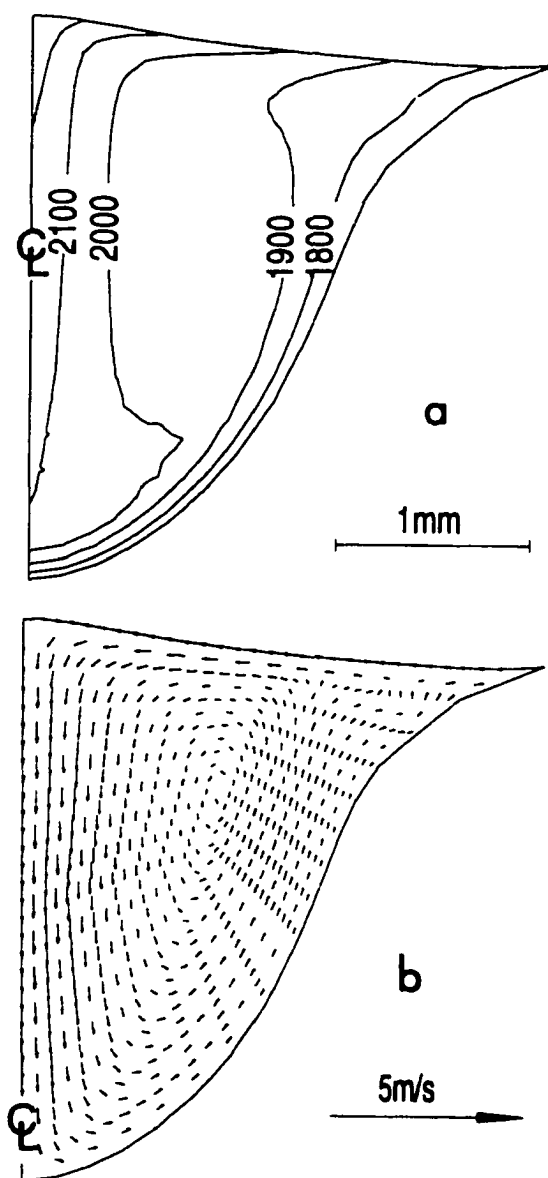
Fig. 2.9: Calculated temperature and velocity fields in 0.015 wt%S AISI 304 stainless steel from laminar model: (a) Tempertures (K) (Tmax = 2,345 K); (b) flow pattern (Vmax =0.59 m/s). Welding conditions: GTA, 120A, 9.2V.[22]
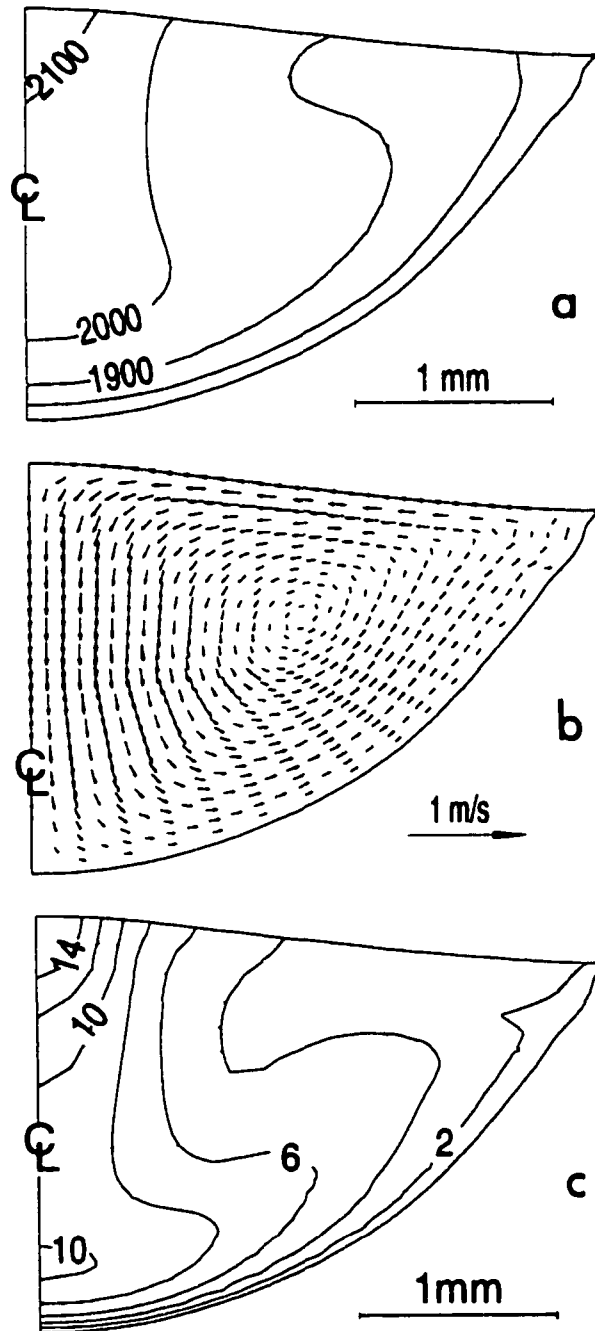
Fig. 2.10: Calculated temperature and velocity fields in 0.015 wt%S AISI 304 stainless steel from turbulent model: (a) Tempertures (K) (Tmax = 2,146 K); (b) flow pattern (Vmax = 0.27 m/s); (c) dimensionless viscosity, μ_t/μ, (max = 16). Welding conditions: GTA, 120A, 9.2V.[22]
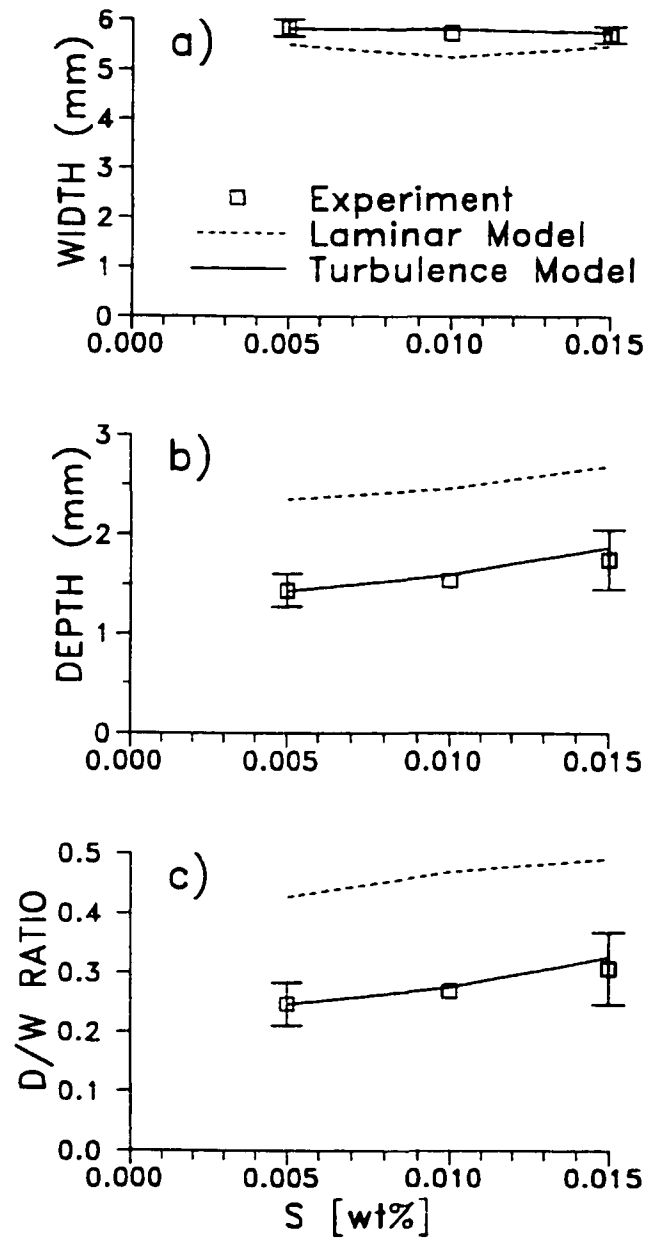
Fig. 2.11: Comparison of the calculated geometries from both laminar and turbulent model with experimental data: (a) width; (b) depth; (c) d/w ratio. Welding conditions: GTA. 120A. 9.2V.[22]

2.1.6 Summary of Modeling Heat Transfer and Fluid Flow in Weld Pool

Accurate prediction of temperature and velocity fields, weld pool geometry, and the thermal cycles in the weldment needs to consider convective heat transfer in the weld pool. Appropriate modeling of fluid motion in the weld pool needs to account for the combination of driving forces such as surface tension gradient force, electromagnetic force, and buoyancy force. During GTA welding process, surface tension gradient induced force is the dominant driving force in most cases. Electromagnetic force is significant only at high welding currents. Buoyancy force is usually negligible.

Accurate predictions of the weld geometry and thermal cycles in both GTA and GMA welding processes need to consider turbulent heat transfer and fluid flow in the weld pool. Knowledge of local values of effective thermal conductivity and viscosity in the weld pool is necessary for calculation of heat transfer and fluid flow in the weld pool. The widely used K-ε turbulence model can be used to calculate these quantities.

The existing weld models incorporating rigorous turbulence calculations[21,22] were only limited in two dimensions for the modeling of stationary GTA welding. The two dimensional calculation cannot provide a full description of the heat transfer and fluid flow in the weld pool. However, accurate thermal cycles at various locations are necessary for the prediction of phase transformations and grain growth in the weldment. In addition, moving heat sources are used in most welding processes. Therefore, a three dimensional model considering turbulent heat transfer and fluid flow in the weld pool with a moving heat source is essential for achieving a realistic simulation of weld pool behavior.

2.2 Modeling Steel Weldment Microstructure

Modeling of steel weldment microstructure requires understanding of the phase transformation kinetics and the thermal cycles in the material. The thermal cycles can be obtained from reliable mathematical models by comprehensive modeling of heat transfer and fluid flow during welding, which has been discussed in the previous section. In recent years, several phase transformation models have been developed for modeling microstructure in steel welds[51-53] and HAZ.[65-68] Coupling these phase transformation models with the calculated thermal cycles from a reliable thermal model is essential for quantitative understanding of steel weldment microstructure.

Considering the complexities of the phase transformation mechanisms in steels and the existing controversies in this field, the review given here is not intended to cover all of the topics. Consequently, the aim of this critical review is to provide the background material necessary for quantitative understanding of phase transformations in low alloy steel weldments with emphasis on models based on phase transformation thermodynamics and kinetics. In this section, the widely used three phase transformation models for prediction of weldment microstructure in low alloy steels are reviewed. The model developed by Ion, Ashby, and Easterling[65,66] and the model developed by Watt et al[67,68] are valid for prediction of microstructure in the HAZ. The model developed by Bhadeshia et al.[51-55] is valid for the calculation of microstructures of the fusion zone. Specifically, the phase transformation model developed by Bhadeshia et al.[51-55] is described in detail, because this model will be combined with the calculated cooling rates from our 3D heat transfer and fluid flow model to predict the microstructural evolution in low alloy steel welds.

2.2.1 Classification of Steel Weld Metal Microstructure

Calculation of microstructure needs a detailed description of each phase. For a meaningful classification of the different features in a microstructure, the various phases and microconstituents should be identified by using a system of nomenclature that is both widely accepted and well understood. In wrought steels, this need has been satisfied to a large degree by the Dube scheme,[58] in which various ferrites are classified according to their morphologies. Four well defined ferrite morphologies recognized by Dube and later extended by Aaronson[59] are: grain boundary allotriomorphs, Widmansttaten side plates or laths, intragranular idiomorphs, and intragranular plates. In the present investigation, the classification of ferrites adapted is based on the mechanisms of phase transformations[51-53] in the weld metal rather than from morphological observations. From phase transformation point of view, the major components in the weld metal of low alloy steels include allotriomorphic ferrite (α), Widmanstatten ferrite (α_w), and acicular ferrite(α_a). There may also be some microphases composed of martensite (α'), retained austensite (γ') or degenerate pearlite (P). It can be noted that this classification of ferrite in the weld metal is consistent with the morphological classification proposed by Dube,[58] although the notations are somewhat different. Acicular ferrite does not figure in the Dube scheme because it is rarely observed in wrought steels. Fig. 2.12(a) and (b) show the typical morphologies of the major microstructural components in the weld metal as well as typical phases in the HAZ of low alloy steels.

Allotriomorphic ferrite (α) is the first phase to form on cooling austenite below the Ae3 temperature, i.e. the phase boundary of $\gamma/(\alpha+\gamma)$. It nucleates at the columnar austenite grain boundaries and then thicken at a rate controlled by the diffusion of carbon in the austenite ahead of the transformation interface.[51-54] The grain boundary allotriomorphs have curved boundaries with the austenite. "Allotriomorphic" means a "particle of a phase that does not have a regular external shape".

Secondary Widmanstatten ferrite (α_w) nucleates at the allotriomorphic ferrite/austenite boundaries and grows as sets of parallel plates separated by thin regions
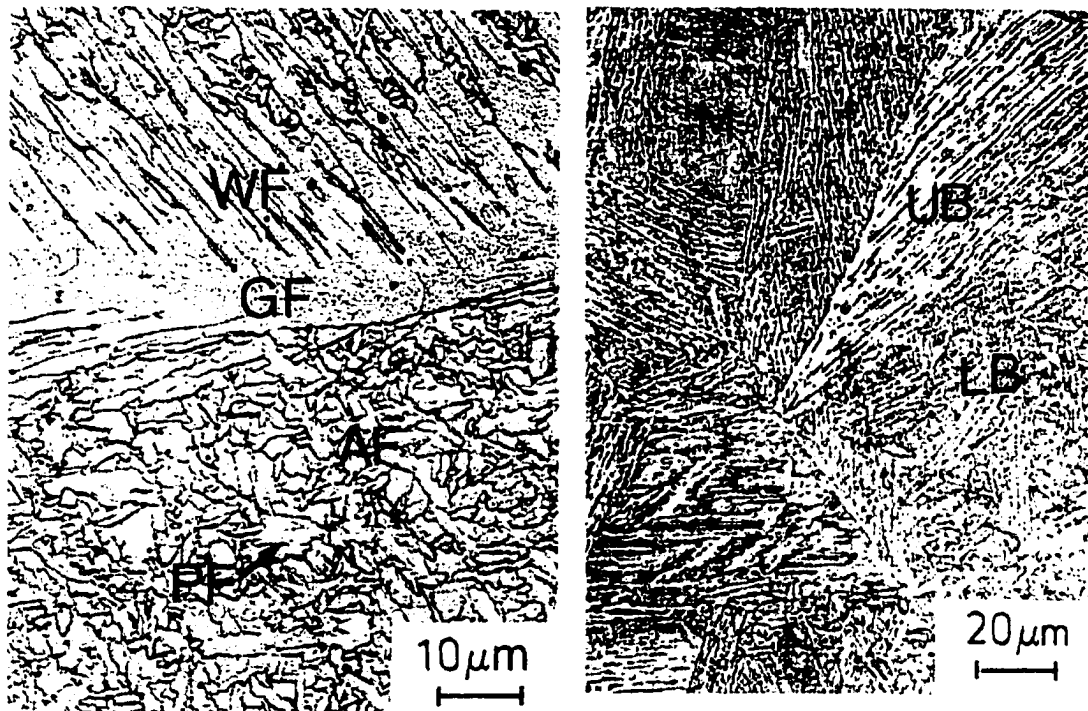
Fig.2.12: Major microstructural components in the weld metal of low alloy steels; The term GF, WF, AF, and PF refer to grain boundary ferrite (allotriomorphic ferrite), Widmansatten ferrite, acicular ferrite (intragranular plates), and polygonal ferrite (idiomorphic ferrite), respectively. (b): Major microstructural components in the HAZ of low alloy steels; The term UB, LB, and M refer to upper banite, lower banite, and martensite, respectively.[60]

of austenite, the latter subsequently being retained at ambient temperature or transformed to martentiste and/or pearlite. This Widmanstatten ferrite and its associated microphases are sometimes referred[61] as "ferrite with aligned martensite-austenite carbide". Primary Widmansatten ferrite can nucleate directly from austenite boundaries, although its mechanism of formation is identical to that of secondary Widmanstatten ferrite.[1-3]

Acicular ferrite (α_a) is a phase most commonly observed in low alloy steel weld deposits. The term "acicular" means shaped and pointed like a needle. It is now generally recognized that the acicular ferrites are thin, lenticular plates with three dimensional morphology. Although many efforts have been made in recent years, as shown in the review papers,[62-64] the transformation mechanism of acicular ferrite is still uncertain. However, it has been generally recognized that acicular ferrite nucleates intragranularly at inclusions within the large austenite grains. The presence of acicular ferrite can significantly improve the toughness of weld deposits because of its chaotic microstructure, which deflects the propagation of cleavage cracks.[51-53]

Microphases in this thesis means the transformation structures resulting from carbon enriched retained austenite in low alloy steels. It might include martensite, retained austenite, bainite, and degenerate pearlite.

2.2.2 Modeling Steel Wledment Microstructure in the HAZ

2.2.2.1 Ion - Easterling - Ashby Model

Ion, Easterling and Ashby[65,66] developed a model to calculate austenite grain growth, precipitate dissolution and coarsening, and the volume fractions of various phases (martentsite, bainite, ferrite, and pearlite) in the HAZ. The algorithm for calculation of grain growth in the HAZ in the model will be discussed later in section 1.3.2. In this section, only the method for calculation of phase transformation due to austenite decomposition is presented. The model used the data of Inagaki and Sekiguchi[138] who constructed continuous cooling transformation (CCT) diagrams for a wide range of structural steels. The CCT diagrams were established based on an

austenitizing temperature of 1350 °C, which represents the part of the HAZ fairly close to the fusion line. The phase volume fractions are determined by the time necessary for cooling from 1073 to 773 K (Δt) and the carbon equivalent of the steel (C_{eq}). The value of Δt in the model was calculated by a modified Rosenthal equation.[65] An example for typical microstructure vs. Δt is given in Fig. 2.13. Two specific cooling times are considered in the model to give a 50% martensite/50% bainite structure, $\Delta t_{1/2}^{m}$, and a 50% bainite/50% ferrite or pearlite structure, $\Delta t_{1/2}^{b}$. The influence of the alloying elements on these critical cooling times is related to the carbon equivalent of the steel (C_{eq}) by the empirical equations:[77]

$$\log\Delta t_{1/2}^{m} = 8.79\ C_{eq} - 1.52 \qquad (2.12.a)$$

$$\log\Delta t_{1/2}^{b} = 8.84\ C_{eq} - 0.74 \qquad (2.12.b)$$

where $\Delta t_{1/2}^{m}$ and $\Delta t_{1/2}^{b}$ have units of seconds and C_{eq} is measured in wt%.

In the model, the volume fractions of ferrite and pearlite are not distinguished and are expressed by a form of the Johnson-Mehl equation:[72]

$$V_{fp} = 1 - e^{-0.69\left(\frac{\Delta t}{\Delta t_{1/2}}\right)^{n}} \qquad (2.13)$$

where V_{fp} is the volume fraction of ferrite/pearlite after a time Δt (characterizing the cooling part of the weld thermal cycle). $\Delta t_{1/2}$ is the time required for half the transformation to occur. n is a value depending on the nucleation sites (it takes the value 3 for random nucleation, 2 for nucleation on grain edges, and 1 for nucleation on grain corners). The parameter, -0.69, taken in equation (2.13) corresponds to 50% transformation, i.e., exp(-0.69)=0.5.

Similar expressions were developed for the volume fractions of bainite and martensite, which are formed from the untranformed austenite during subsequent cooling. The volume fractions of bainite and martensite are expressed as:
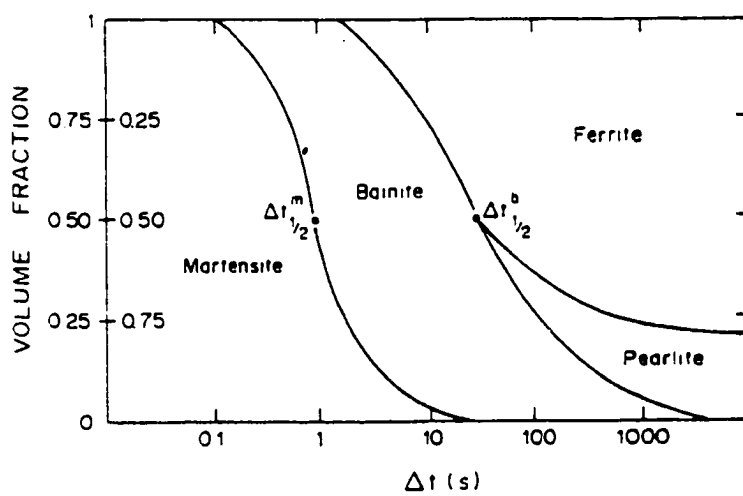
2.13: Typical microstructure vs. Δt diagrm for structural steels.[138]

$$V_m = e^{-0.69\left(\frac{\Delta t}{\Delta t^m_{1/2}}\right)^2}$$ (2.14)

$$V_b = e^{-0.69\left(\frac{\Delta t}{\Delta t^b_{1/2}}\right)^2} - V_m$$ (2.15)

where V_b and V_m are the volume fractions of bainite and martensite, respectively.

The advantage of Ion-Easterling-Ashby model is that microstructural diagrams can be established. from which the austenite grain size. the extent of the dissolution of the precipitates. and the amount of martensite in the HAZ can be directly read. The calculation of grain growth in the model will be introduced later in section 2.3.2. One typical HAZ microstructural diagram is shown in Fig. 2.14. This HAZ microstructural diagram provides an overall picture of the effect of various welding processes on microstructure in the HAZ. The calculated results have been correlated with actual welding experiments. However. the transformation rates for ferrite/pearlite. bainite. and martensite are approximated by using an empirical formula based on the carbon equivalent index.
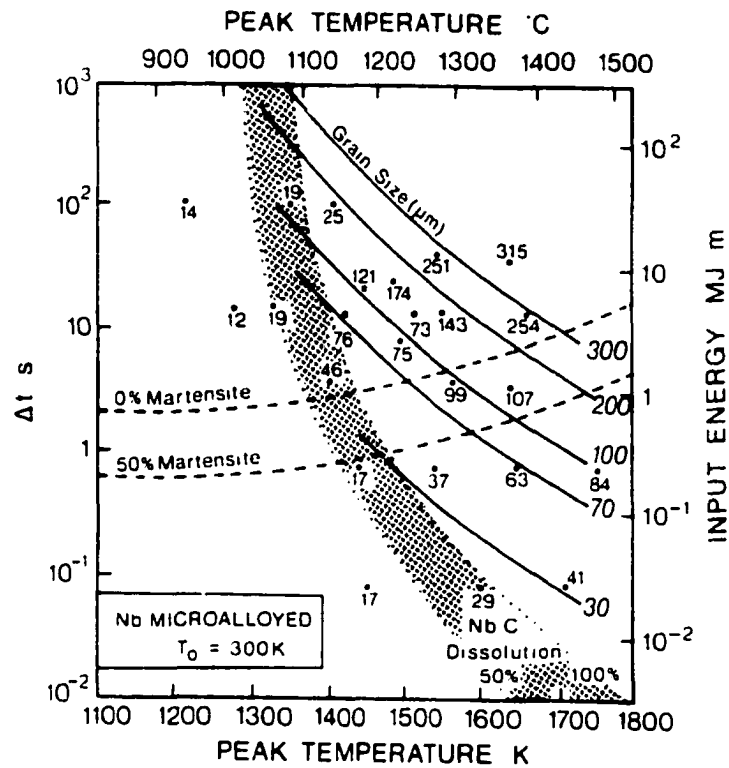
Fig. 2.14: A HAZ microstructural diagram for Nb-microalloyed steel. Experimental data are shown in points in the diagram. Alloy composition (wt%): 0.12C, 0.16Si, 0.91Mn, 0.002P, 0.005S, 0.04Al, 0.021Nb, 0.011N. The full lines are contours of constant grain size (3D prior austenite). The broken lines show the volume fraction of martensite. The shaded area region shows the extent of dissolution of the carbide particles.[66]

2.2.2.2 Model by Watt et al.

Watt et al.[67,68] developed a model to calculate the volume fractions of the phases in the HAZ based on an algorithm developed by Kirkaldy et al.,[69-71] which was originally developed for predicting the hardenability of low alloy steels. Watt et al.[67,68] combined Kirkaldy's algorithm with a suitable model of heat transfer in the weld HAZ to predict the microstructural development in the weld HAZ. The required inputs for this model are the eutectoid temperature (Ae_1), the solidus temperature of the $(\alpha+\gamma)/\gamma$ phase boundary (Ae_3), the ferrite solubility temperature as a function of carbon (F_S), the bainite start temperature (B_S), and the martensite start temperature (M_S). In the model, these inputs are empirically calculated from the composition of the alloy. A set of equations were developed to model each of the daughter products from austenite decomposition process. These equations assume that a single continuous function can describe both nucleation and subsequent growth for each of the daughter phases. According to Kirkaldy et al.,[69-71] the general reaction rate for each reaction can be expressed as:

$$\frac{dX}{dt} = B(G,T)X^m(1-X)^p \qquad (2.16)$$

where X is the volume fraction of the daughter product. B is an effective rate coefficient which depends on T, the temperature, and G, the austenite grain size. The semi-empirical coefficients. m and p, are set to less than one to assure convergence in a form that is derived from a point nucleation and impingement growth model.[78] The rate coefficient includes the effect of grain size on the density of nucleation sites. It also includes the amount of austenite supercooling, and the effect of alloying elements and temperature on diffusion. Based on the general reaction rate equation, the reaction rates for various products are determined by considering the corresponding phase transformation characteristics.

The form of the austenite decomposition equations in their model has its basis in the theory of reaction kinetics. The empirical factors used in the equations have been accumulated over 200 different steel compositions to produce a good fit to their TTT and CCT diagrams. The model has been combined with a finite element heat transfer model to predict the HAZ microstructure.[79] The predicted microstructure was found to be

comparable with the experimental results. However, like Ion-Easterling-Ashby model, no distinction has been made between allotriomorphic ferrite and Widmanstatten ferrite in this model. In addition, the reaction kinetic arguments on which the model are based are not universally accepted.[80,81] In particular, the assumption that the nucleation and subsequent growth can be treated as a single continuous function may not be valid. For example, it has been argued[80,81] that it is necessary to separate the nucleation kinetics from the growth rate processes, with the additivity principle only applicable to the latter. As a result, an incubation time should be included before growth equations are applied.

The two models described above are used for prediction of the microstructural development in the HAZ. This is mainly because many of the empirical constants in these two models were obtained by fitting the experimental data (e.g. experimentally determined TTT and CCT diagrams) into the classical kinetic equations. These experimental TTT and CCT diagrams were normally established under the condition that the chemical composition within the prior austenite grains is uniform. Therefore, the algorithms obtained from using these data may not be suitable for the prediction of microstructural development in the weld metal, in which significant solute segregation exists in the prior austenite grains due to nonequilibrium solidification.

2.2.3 Model Developed by Bhadeshia et al.

Based on thermodynamics and phase transformation kinetics, Bhadeshia et al[51-53] developed a comprehensive model for the decomposition of austenite in the low alloy steel weld metal. In this model, the phase transformation mechanisms for the various microconstituents, the multicomponent phase diagram, and non-equilibrium cooling conditions have been considered in predicting the microstructural development in the weld metal. The phase boundaries, time-temperature-transformation (TTT) diagram and continuous-cooling-transformation (CCT) diagram in low alloy steel can be calculated from this model. The volume fractions of various phases are calculated based on their corresponding phase transformation mechanisms. Since this model will be coupled with

our 3D heat transfer and fluid flow model to predict the microstructural evolution in the weld metal of low alloy steels, the physical principles and algorithm in this model is described in this section in detail.

2.2.3.1 Microstructural Evolution in the Weld Metal

The microstructural evolution in the weld metal of low alloy steel is schematically shown in Fig. 2.15. The final weld metal microstructure is dominantly determined by the austenite decomposition process within the temperature range from 1073 to 773 K. During cooling of the weld metal, allotriomorphic ferrite is the first phase to form from the decomposition of austenite in low alloy steels. It nucleates at the austenite grain boundaries and grows by a diffusional mechanism. As the temperature decreases, diffusion becomes sluggish and displacive transformation is kinetically favored. At relatively low undercoolings, plates of Widmanstatten ferrite forms by a displacive mechanism. At further undercoolings, bainite nucleates by the same mechanism as Widmanstatten ferrite and grows in the form of sheaves of small platelets. Acicular ferrite nucleates intragranularly at inclusions and is assumed to grow by the same mechanism as bainite in the present model.[51-53,55] The morphology of acicular ferrite differs from that of conventional bainite because the former nucleates intragranularly at inclusions and within large austenite grains, while the latter nucleates initially at austenite grain boundaries and grows by the repeated formation of subunits to generate the classical sheaf morphology.

2.2.3.2 Assumptions in the Model

Knowledge of the prior austenite grain size is the prerequisite for quantitative calculation of the subsequent ferrite phase volume fractions during austenite decomposition. In low-alloy steel welds, solidification begins with the epitaxial nucleation and growth of δ-ferrite at the fusion boundary. The large temperature gradients at the solid-liquid interface ensures that solidification proceeds with a cellular front,[85] the final δ-ferrite grains are thus in columnar shape with their major axes lying along the direction of maximum heat flow. In the model, the morphology of the austenite
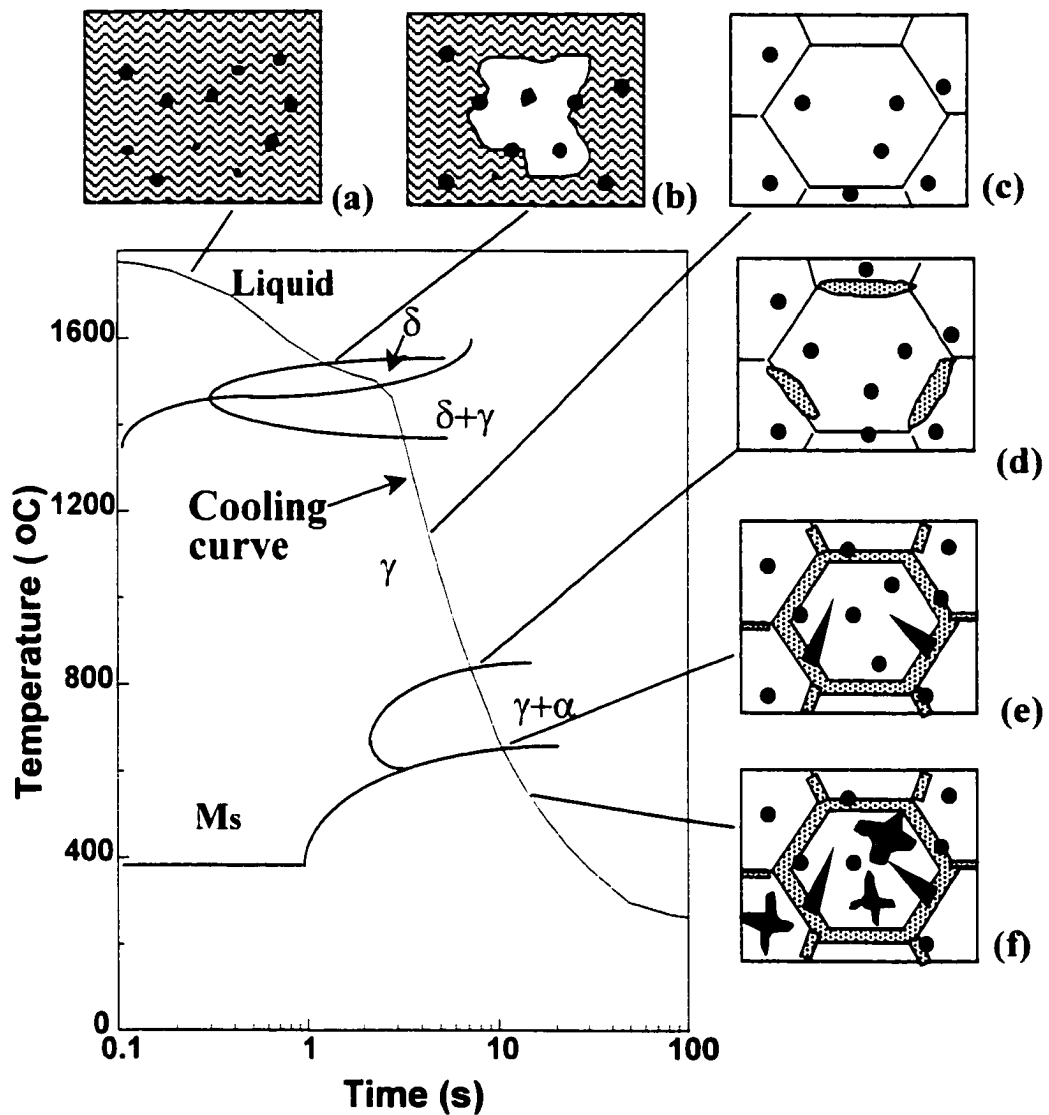
Fig. 2.10: Schematic diagram for microstructural evolution in low alloy steels: (a) inclusion formation; (b) δ-ferrite formation; (c) austenite formation; (d) allotriomorphic ferrite formation; (e) Widmanstatten ferrite formation; and (f) acicular ferrite/bainite formation (adapted from Bhadeshia).[55]

grains is represented as a uniform, space-filling array of hexagonal prisms with its length "c" and cross-section side length "a". The c-axes of the prisms are parallel to the direction of maximum heat flow. The value of side length "a" can be calculated from the mean lineal intercept in the direction normal to the major axes of the austenite grains as following:[51-53]

$$a = \frac{2\overline{L}_t}{\pi \cos(30^\circ)} \tag{2.17}$$

where $\overline{L}_t$ is the mean lineal intercept in the direction normal to the major axes of the austenite grains. The value of $\overline{L}_t$ can be either measured on a transverse section of the weld experimentally or estimated from empirical formula,[51] which is established by regression of numerous experimental results. The mean intercept of the columnar austenite grain size can be approximated from empirical formula as:

$$\overline{L}_t(\mu m) = 64.5 - 445.8(wt\%C) + 139(wt\%Si) - 7.6(wt\%Mn) + 16(\text{heatinput}, kJ / mm) \tag{2.18}$$

Another important assumption in the model is that "Paraequilibrium" assumed in the calculation of phase transformations. "Paraequilibrium" is a constrained phase equilibrium when a phase change is so rapid that one or more components cannot redistribute within the phase in the available time scale.[51,54,55,86] For transformation in steels, the diffusion coefficients of substitutional and interstitial components differ significantly. It is possible that the sluggish substitutional alloying elements may not have sufficient time to redistribute during the transformation of austenite to ferrite under some circumstances, even though carbon may partition into austenite.[51,54,55,86] In the model, "paraequilibrium" is assumed at the γ/α boundary.[51-53] Under the "paraequilibrium" condition, the substitutional solute/iron atom ratio remains constant everywhere. Since carbon is a fast diffusing species in iron, it can partition to an extent which allows it to achieve local (para) equilibrium at the interface.

Considering the rapid cooling rates involved, it is reasonable to assume paraequilibrium in the weld metal under welding condition. Under this assumption, the carbon concentration in austenite ($x^{\gamma\alpha}$) and that in the ferrite ($x^{\alpha\gamma}$) at the interface can be determined from a calculated multicomponent phase diagram. Then the diffusion-controlled growth rate for ferrite can be calculated using the theory relevant to Fe-C alloys by substituting the carbon concentrations in austenite ($x^{\gamma\alpha}$) and that in the ferrite ($x^{\alpha\gamma}$) at the interface.

2.2.3.3 Calculation of TTT and CCT diagrams

Time-temperature-transformation (TTT) diagrams are very useful in representing the transformation characteristics and revealing the effects of alloying elements on the transformation kinetics. For the decomposition of austenite in steel, most diagrams can be classified into two C curves, the one at higher temperatures representing reconstructive transformation to ferrite or pearlite, and that at lower temperatures representing displacive reactions such as Widmanstatten ferrite and banite.[51-53,55,87] The Martensite start temperature is generally represented as a horizontal line parallel to the time axis.[55] The characteristics of C curves are usually attributed to the balancing contributions from the driving force and the diffusion processes. The combined effects of these two factors determine the overall reaction kinetics. The driving force is small in the vicinity of the transformation start temperature and increases with undercooling whereas diffusion becomes increasingly sluggish as the temperature is reduced.

Time-temperature-transformation (TTT) curves in the model are calculated based on the thermodynamic method developed by Bhadeshia.[87] The method includes the calculation of two separate C curves representing the initiation of diffusional and displacive transformations, respectively. The position of the curves in the time/temperature domain are determined using a semi-empirical thermodynamic approach capable of considering C, Mn, Si, Ni, Cr, Mo and V in any combination, as long as the alloying elements remain in solid solution in the austenite. The upper C curves, or diffusional curves, refer to the time taken for the initiation of the allotriomorphic ferrite

or of the pearlite transformation. The lower or shear C curves refer to the initiation of displacive transformations, such as the Widmanstatten ferrite and bainite reactions. In the model, it is assumed that the lower C curve also describes the formation of acicular ferrite.[51-53, 55]

Based on Russell's expression for incubation time during nucleation,[82,83] Bhadeshia developed a thermodynamic method to calculate the incubation times for both reconstructive and displacive transformations in low alloy steels by the following expression: [84]

$$\tau = T^a \cdot \left(\Delta G_{max}\right)^b \cdot \exp\left\{\frac{c}{T}\right\} \cdot d \qquad (2.19)$$

where τ is the incubation time for a transformation. T is the absolute temperature. ΔG_{max} is the maximum driving force for nucleation. the symbols of a, b, c and d are constants. The details of calculation of ΔG_{max} and determination of constants a, b, c and d are given in references 84 and 87.

Although the general theory of transformation kinetics is largely confined to isothermal reactions, some efforts have been made to predict the non-isothermal transformation behavior from their isothermal transformation curves.[89] Scheil additive rule[90] can be used to calculate CCT diagram from the corresponding TTT diagram. In this procedure, the total time to reach a specified stage of transformation is obtained by adding the fractions of the time to reach this stage isothermally until the sum reaches unity. The additive rule can be expressed as: [89]

$$\int_0^t \frac{dt}{t_a(T)} = 1 \qquad (2.20)$$

where $t_a(T)$ is the incubation time to a specified stage on a TTT diagram for isothermal reactions. t is the time to that stage for the non-isothermal reactions, and dt is the time interval spent by the sample at temperature T. In the present weld model, the calculated TTT diagram is transformed to CCT diagram based on Scheil additive rule.[91]

2.2.3.4 Calculation of Phase Volume Fractions

For quantitative phase volume fraction calculation, the austenite grain is assumed to be hexagonal in cross section with prism length a, as shown in Fig. 2.16. When the weld metal cools to a temperature below Ae3, the austenite (γ) transforms to layers of allotriomorphic ferrite (α) which grows by a diffusional transformation mechanism. The start temperature for $\gamma \rightarrow \alpha$ is determined by using the additive reaction rule. By this way, the cooling rate and the computed TTT diagram for the alloy are considered for the calculation of allotriomorphic ferrite phase volume fractions. The cross-over point of the two C curves is set to be the complete temperature for $\gamma \rightarrow \alpha$ reaction below which displacive transformations are assumed to be kinetically favored, so that the growth of α ceases and gives way to displacive transformations. The α layers are assumed to grow by a paraequilibrium mechanism, at a rate controlled by the diffusion of carbon in the γ ahead of the moving α/γ interface.. The thickness of the α layer (q) can thus be related to the square root of time via the one dimensional thickening rate constant (α_1) as following: [51-53]

$$q = \int_{t_h}^{t_1} 0.5\alpha_1 t^{-0.5} dt \qquad (2.21)$$

where q is the thickness of the α layer. t_h is the starting time of the transformation. t_1 is the finishing time of the transformation, and α_1 is the one-dimensional parabolic thickening rate constant, obtained by solving the following equation based on mass balance: [51-53]

$$\frac{2(\overline{D}/\pi)^{1/2}(x^{\gamma\alpha} - \overline{x})}{(x^{\gamma\alpha} - x^{\alpha\gamma})} = \alpha_1 \exp\left\{\frac{\alpha_1^2}{4\overline{D}}\right\} \mathrm{erfc}\left\{\frac{\alpha_1}{2\overline{D}^{1/2}}\right\} \qquad (2.22)$$

where $x^{\gamma\alpha}$ and $x^{\alpha\gamma}$ are the paraequilbrium carbon concentration in austenite and ferrite respectively at the interface (obtained using a calculated multicomponent phase diagram), $\overline{x}$ is the average carbon concentration in the alloy and $\overline{D}$ is a weighted average diffusivity[53,54] of carbon in austenite.
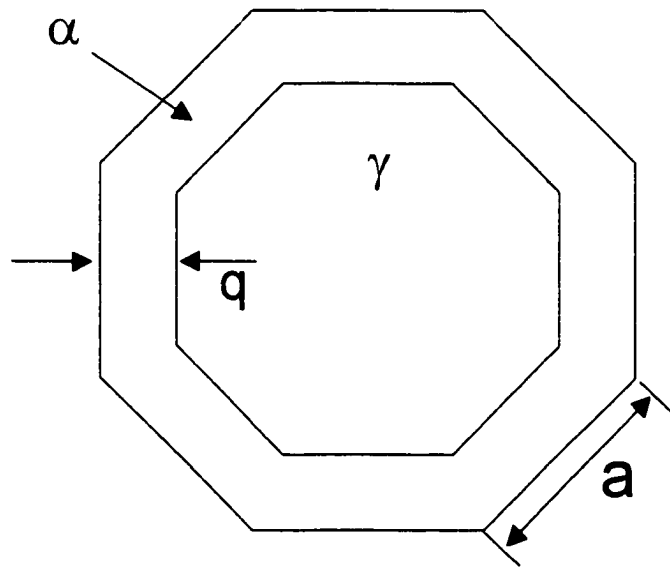
Fig. 2.16: Assumed shape of an austenite grain; γ = Austenite. α = Allotriomorphic ferrite. q = thickness of α, a = side length of hexagonal austenite grain.

Based on the area that allotriomorphic ferrite occupies in the hexagonal cross section of austenite grain, as shown in Fig. 2.16, the volume fraction of allotriomorphic ferrite can be calculated as: [51-53]

$$V_\alpha = \left[2q \tan\{30^\circ\}\left(2a - 2q \tan\{30^\circ\}\right) \right] / a^2 \tag{2.23}$$

where q is the thickness of the α layer and a is the prism length of the hexagonal cross section of austenite grain.

The Widmanstatten ferrite consists of mutually accommodating plates with slightly different habit plane indices. In the model, the shape of the plate is approximated by a thin wedge with its length in the major growth direction, growth in the other two dimensions soon becoming stifled by impingement with the diffusion fields of nearby plates in a packet. [51-53] The lengthening rate G of Widmanstatten ferrite is estimated using the theory developed by Trivedi for the paraequilibrium diffusion-controlled growth. [93] Widmanstatten ferrite grows at a constant rate due to its shape as long as soft-impingement (overlap of diffusion fields) does not occur. This is unlike the case for allotriomorphic ferrite, in which the growth rate progressively slows down due to the build up of carbon ahead of the interface. Based on the area that Widmanstatten ferrite occupied in the hexagonal cross section of austenite grain after the formation of the allotriomorphic ferrite, the volume fraction of Widmanstatten ferrite is calculated by: [51-53]

$$V_w = C_4 G \left(2a - 4q \tan\left(30^\circ\right) t_2^2 / (2a)^2 \right) \tag{2.24}$$

where C_4 is a constant independent of alloy composition, G is the lengthening rate of Widmanstatten ferrite, a is the prism length of the hexagonal cross section of austenite grain, q is the thickness of the α layer, and t_2 is the time available for the formation of Widmanstatten ferrite. From equation (2.24), it can be noted that the V_w depends not only the austenite grain size (a) but also on the thickness of the layer of the allotriomorphic ferrite (q) which formed earlier.

Acicular ferrite forms at a temperature range where reconstructive transformations become relatively sluggish and displacive reactions dominate. This transformation has not been studied from a fundamental point of view in great depth, so

there are no models available to calculate the volume fraction of acicular ferrite (V_a) from first principles. However, for many low alloy steel welds it is possible to calculate V_a via the equation based on mass conservation:[51-53]

$$V_a = 1 - V_\alpha - V_W - V_m \qquad (2.25)$$

where V_m is the volume fraction of microphases, which can be estimated as in Bhadeshia et al.[51-52] The method works well for numerous welds, but fails when the primary microstructure consists of just acicular ferrite and martensite.[89]

Bainite is assumed to form by displacive mechanism in the present weld model.[51-55] In displacive mechanism, bainite ferrite grows without diffusion, with the carbon being partitioned into the residual austenite immediately after the growth event.[51-55] Such a mechanism can explain the "incomplete reaction phenomena",[51,55,91] which can not be explained by reconstructive mechanism. The "incomplete reaction phenomena" is that reaction from austenite to banite stops well before austenite achieves its paraequilibrium carbon concentration as given by the Ae_3' curve on the phase diagram as shown in Fig. 2.17. In fact, it stops when the carbon concentration of the residual austenite approaches the T_0 curve, which describes the locus of all points on the phase diagram where austenite and ferrite of the same composition have identical free energies.[55,91] For bainite, whose growth is accompanied by an invariant - plane strain shape deformation, the strain energy of transformation is about 400 J/mol, and T_0 curve as modified to account for this stored energy is called the T_0' curve.[55, 91]

As the austenite becomes progressively enriched with carbon, a stage is eventually reached when it is thermodynamically impossible for further bainite to grow by diffusionless transformation. At this stage, the composition of the austenite is given by the T_0' curve of the diagram.[55,91] Based on the T_0 concept, a method of estimating the limiting volume fractions is established.[55,91] In this method, it assumes that isothermal reaction is permitted for a time period t_c which is long enough to permit the volume fraction of bainitic ferrite reach its limiting value. The microstructure after isothermal transformation (at T_i) in the upper bainite transformation range followed by cooling to ambient temperature (T_A) consists of bainite ferrite, carbon enriched retained austenite
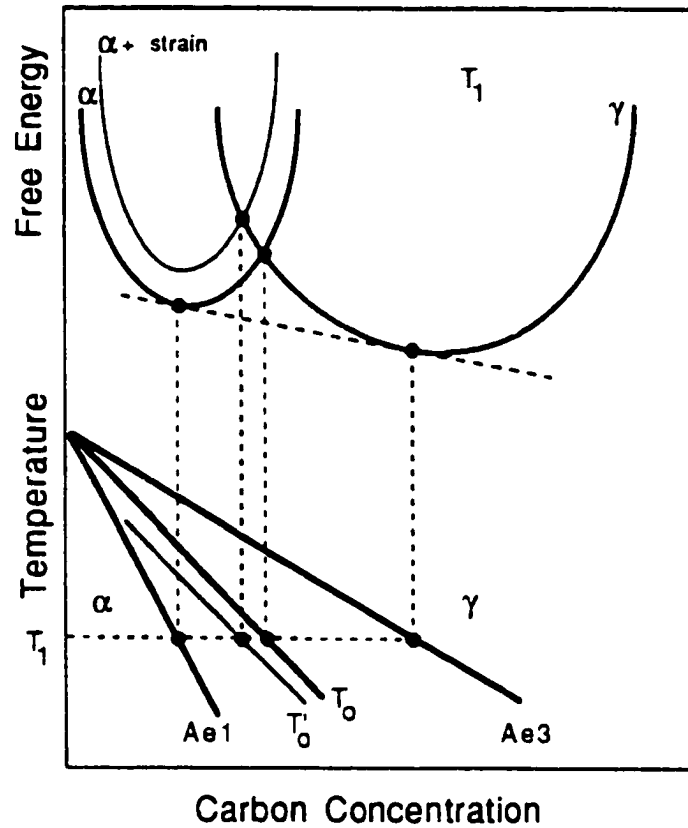
Fig. 2.17: Schematic illustration of the origin of the T_0 curve on the phase diagram. The T'_0 curve incorporates a strain energy term for the ferrite. illustrated on the diagram by raising the free energy curve for ferrite by an appropriate quantity.[55]

and untempered martensite. At temperature T_i, the bainite reaction will cease when the carbon concentration of the residual austenite (x_γ) approaches the T_0 curve. In the model, the volume fraction of bainite ferrite (V_B) is given by a lever rule applied to the Ae_1' and T_0 curves: [85]

$$V_B = \left(x_{T_0} - \bar{x}\right) / \left(x_{T_0} - x_{\alpha\gamma} - x_c\right)$$ (2.26)

where $x_{\alpha\gamma}$ is the paraequilibrium carbon concentration of the bainite ferrite. $\bar{x}$ is the average carbon concentration of the alloys and x_c is the amount of carbon which is tied up as carbides within the bainitic ferrite.

When cooling to ambient temperature, some of the residual austenite may transform to martensite with the remiander being retained. The martensite - start temperatures (Ms) of the residual austenite can be estimated by assuming that its carbon concentration is X_{T_0}. In the model, the amount of martensite V_α. is calculated by an empirical formula: [92]

$$V_{\alpha'} = \left(1 - V_M\right)\left[1 - \exp\left\{-0.011\left(M_s - T_A\right)\right\}\right]$$ (2.27)

It should be noted that the method in the model only permits the calculation of the volume fraction of all the phases when dealing with upper bainite. For lower bainite, the calculations are not yet possible because no method exists for predicting x_c. The method also assumes that the partitioned carbon is distributed homogeneously within the residual austenite.

2.2.3.5 Calculation of Cooling Rates

The weld metal microstructural evolution in low alloy steels is determined by both chemical composition and cooling rates within austenite decomposition range (1073 - 773 K). Thus, accurate knowledge of cooling rates within austenite decomposition range is a prerequisite for quantitative calculation of weld metal microstructure. The cooling rates in the weld metal of low alloy steels are mainly determined by the heat input, preheat or interpass temperature, and the geometry of weldment.

An empirical equation has been established by Svensson et al.[141] to predict the cooling rates within the austenite decomposition range (1073 - 773 K) in the weld metal of low alloy steel. The empirical equation was established by regression of experimental results and expressed as: [141]

$$\frac{dT}{dt} = \frac{C_1(T - T_i)^{C_2}}{q\eta}$$

(2.28)

where T is temperature, t is time, Q is the energy input per unit length, η is the energy transfer efficiency, T_i is interpass temperature, C_1 and C_2 are adjustable constants determined by the welding process and the geometry of the weldment. The cooling rates calculated from this empirical equation has been coupled with Bhadeshia's phase transformation model to predict phase transformations in the weld metal of low alloy steels.[14] It was found that the predicted results were comparable with experimental results.

However, the constants C_1 and C_2 in equation (2.28) have to be determined for each set of experimental conditions for best results. When some conditions change (e.g. the welding process, geometry shape and size of the sample), new values of C_1 and C_2 have to be determined from experimental data. Furthermore, the empirical equation assumes that C_1 and C_2 are independent of locations in the fusion zone. Therefore, the cooling rates obtained from this equation can not be used to predict either the spatial variation of microstructure within the fusion zone or the changes in the microstructure resulting from a wide variety of welding processes and welding conditions.

2.2.4 Summary of Modeling Phase Transformations in Steel Weldments

The final microstructure in the weld metal of low alloy steels is mainly determined by the austenite decomposition process within the temperature range from 1073 to 773 K. Different daughter phases (e.g. allotromorphic ferrite, Widmanstatten ferrite, acicular ferrite, bainite, and martensite) are expected in the weld metal, since

various transformations may occur during austenite decomposition. The extents of the phase transformations and the resulting phase volume fractions depend on both chemical composition and the cooling rate. Thus, the ability to model weld metal microstructure relies on a deep understanding of phase transformation theory governing the phase changes and the cooling rate that the material experiences.

Modeling of steel weldment microstructure has now reached a level where it is possible to quantitatively predict the effects of welding variables such as chemical composition on the phase volume fractions in the weld metal for many steels. However, phase transformation models can not be applied to welding process unless the thermal cycles are known. In the weldment, the thermal cycles vary with location and are dependent on welding conditions. Accurate knowledge of thermal cycles is a prerequisite for quantitative calculation of the phase transformations. Empirical equations for calculation of cooling rate in the weldment are not flexible to consider either the weldment geometry or the welding variables. Furthermore, such an approach can not calculate the thermal cycles at various locations. In contrast, comprehensive heat transfer and fluid flow models can be used to predict thermal cycles for various weldment geometries under different welding conditions at all locations within the weldment. Thus, coupling of a phase transformation model with the calculated thermal cycles from a comprehensive thermal model is attractive for the prediction of the weld metal microstructural evolution in low alloy steels.

2.3 Simulation of Grain Growth in the HAZ

2.3.1 Grain Growth Kinetics

The driving force for grain growth results from the decrease in total grain boundary energy which accompanies reduction in total grain boundary area.[108-110] Two types of grain growth phenomena have been distinguished: normal growth and abnormal growth. In the normal grain growth, the microstructure exhibits a uniform increase in

grain size and the normalized grain size distribution function is invariant with time.[109-110] The abnormal grain growth is characterized by the growth of just few grains to very large size. These grains grow by consuming the surrounding grains, until the fine grains are entirely replaced by a few coarse grains. Abnormal grain growth usually occurs when normal grain growth is impeded by second phase particles.[119] In the present thesis, only the normal grain growth phenomenon is studied.

The normal grain growth phenomenon has been extensively investigated because of the importance of its resulting microstructure in controlling the physical and mechanical properties of the polycrystalline materials. In a classical paper of the early 1950s, Burke and Turnbull[108] deduced a parabolic relationship for grain growth kinetics under isothermal conditions. The migration of a grain boundary was modeled as occurring by atom transport across the boundary under a pressure due to surface curvature. The surface curvature forces were considered on an isolated section of boundary. The boundary tends to migrate towards its center of curvature as this reduces the area of boundary and hence the energy associated with it. Several assumptions were made in his derivation: (1) the radius of curvature, r, is proportional to the mean grain radius of grains, R: (2) the grain boundary migration velocity is proportional to dR/dt: (3) the grain boundary free energy, γ, is independent of grain size and time: (4) the mean driving force is proportional to $2\gamma/R$. Based on the above assumptions, Burke and Turnbull[108] derived a parabolic relation to describe the grain growth kinetics:

$$\overline{D}^2 - \overline{D_0}^2 = Kt \tag{2.29}$$

where $\overline{D}$ is the mean grain size at time t. $\overline{D_0}$ is the initial mean grain size, and K is a kinetic constant. After the theory proposed by Burke and Turnbull,[108] other theories[109-113] were proposed to predict the time-dependence of average grain size and size distribution by analytical models. Most these analytical theories also predict a parabolic growth law. In equation (2.29), the grain growth exponent is 2, which is the theoretical limit for grain growth exponent. However, the experimentally determined grain growth exponent values have been reported to vary from 2 to 4 for pure metals. The deviation of the experimental values from theoretical prediction has been attributed to the presence of additional factors

not considered in the analytical models. These additional factors include solute drag, impurity segregation, anisotropies, second particles, and simplified geometry and topologies.

2.3.2 Analytical Calculation of Grain Growth in the HAZ

The grain growth in the weld HAZ occurs under the steep temperature gradients and transient thermal cycles. Analytical equations have been extensively used for the calculation of grain size in the HAZ.[65,66,95,96] One popular analytical method was proposed by Ashby et al[65,66] to simulate grain growth in the HAZ based on the idea of integrating the parabolic grain growth kinetic equation over the weld thermal cycles.

Assuming that grain growth is diffusion controlled, driven by grain boundary energy, and requires no nucleation, then the extent of transformation depends on the integrated number of diffusive jumps during the weld thermal cycle. The austenite grain growth in the HAZ can be calculated by a kinetic equation as: [65,66]

$$g^2 - g_0^2 = k_1 \left\{ \int_0^\infty e^{-\frac{Q}{RT(t)}} dt \right\}$$ (2.30)

where g is the grain size after time t, g_0 is the initial grain size, k_1 is a kinetic constant, Q is the activation energy for grain growth, T(t) is the temperature varying with time, and R is the gas constant. For a specified material, the values of k_1 and Q need to be determined from experiments. The term in the bracket of equation (2.29) is the "kinetic strength" of the cycle, J, which is defined as:[65,66]

$$J = \int_0^\infty e^{-\frac{Q}{RT(t)}} dt$$ (2.31)

where Q is the activation energy for process concerned (e.g. grain growth, precipitation or coarsening of particles, etc.), T(t) is the temperature varying with time, and R is the gas constant.

The calculated results from equation (2.30) with experimentally determined k_1 and Q can provide some quantitative information as well as insights about the effects of the welding parameters on the grain growth in the HAZ. However, the evolution of grain structure depends on the orientations of the grains, the coordinates of the grain boundary network, and the driving forces of the boundary migrations. The general analytical equation can not account for all these factors in combination. This difficulty is further enhanced by the steep temperature gradient and transient thermal cycling in the HAZ. For example, some special phenomena for grain growth in the HAZ such as "thermal pinning" can not be predicted by analytical calculations.[95,97] In contrast, numerical mathematical models based on the basic principles of grain growth phenomena, such as Monte Carlo based grain simulation technique, have the capability to effectively model not only grain growth kinetics but also the topological evolution of the grain structure.

2.3.3 Simulation of Grain Growth by Monte Carlo (MC) Technique

2.3.3.1 Simulation Methodologies of Monte Carlo (MC) Technique

The simulation methodologies of MC technique have been given in detail in the literature[98-104] and are briefly described here. A computer image of the polycrystalline microstructure is first created by mapping the continuum grain structure onto a discrete lattice. This is accomplished by dividing the material into small area (2D) or volume (3D) elements, and placing the center of these elements onto the lattice points. The lattice can be triangular or square in two dimensions, and simple cubic in three dimensions. Each of the grid points will be assigned a random orientation number between 1 and Q, where Q is the total number of grain orientations. A grain boundary segment is defined to lie between two sites of unlike orientation as shown in Fig. 2.18. In other word, two adjacent grid points having the same orientation number are considered to be a part of the same grain; otherwise they belong to different grains. The grain boundary energy is specified by defining an interaction between nearest neighbor lattice sites. The local interaction energy is calculated by the Hamiltonian:
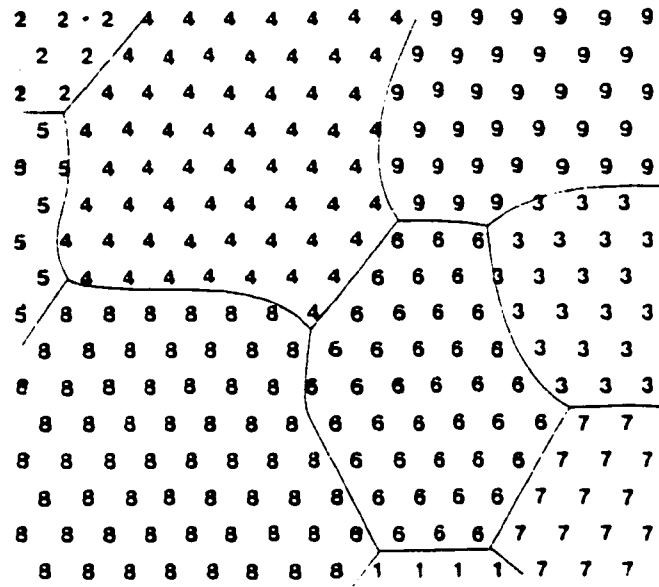
Fig. 2.18: Sample microstructure on a triangular lattice where the integers
Denote orientation and the lines represent grain boundaries.[98]

$$E = -J \sum_{j=1}^{nn} (\delta_{S_i S_j} - 1) \qquad (2.32)$$

where J is a positive constant which sets the scale of the grain boundary energy, δ is the Kronecker's delta function, S_i is the orientation at a randomly selected site i, and S_j are the orientations of its nearest neighbors. The sum is taken over all nearest neighbor sites (nn). The nearest neighbor pairs contribute J to the system energy when they are of unlike orientation and zero otherwise.

The kinetics of grain boundary migration are simulated by selecting a site randomly and changing its orientation to one of the nearest neighbor orientations based on energy change due to the attempted orientation change. The probability of orientation change is defined as:

$$p = 1 \qquad \text{for} \qquad \Delta E \leq 0 \qquad (2.33)$$

$$p = \exp(-\Delta E / k_B T) \qquad \text{for} \qquad \Delta E > 0 \qquad (2.34)$$

where ΔE is the change of energy due to the change of orientation. k_B is the Boltzman constant. and T is the temperature. Successful transitions at the grain boundaries t_o orientations of nearest neighbor grains thus corresponds to boundary migration.

2.3.3.2 Relation between MC Simulation Step and Real Time

One critical issue to apply the MC technique to a real metallurgical phenomenon is to establish the relation between the MC simulation step (t_{MCS}) and real time-temperature. Depending on the nature of the problem. different methods[97,105-107] have been used to convert real time to the MC simulation step. These methods can be classified into:[105,106] Atomistic Model, Grain Boundary Migration (GBM) Model, and Experimental Data Base (EDB) Model.

Atomistic model

In the atomistic model, the grid points in the simulated domain are treated as atoms. The MC simulation step is correlated to atomic diffusion across grain boundary and connected to real time-temperature by the following relationship:

$$t_{MCS} = v \times \exp\left(-\frac{Q}{RT}\right)t \tag{2.35}$$

where t_{MCS} is the MC simulation step, v is the atomic vibration frequency, Q is the activation energy for grain growth, R is the gas constant, T is temperature, and t is real time. To apply equation (2.35) for grain growth in the HAZ, the experienced temperature - time curve at a location of the HAZ is divided into many short intervals. The temperature in each time interval is assumed to be constant. The MC simulation step for a transient thermal cycle is thus obtained by summation of the MC simulation step at each time interval, which can be expressed as:

$$t_{MCS} = \sum_{i=1}^{m} v \times \exp\left(-\frac{Q}{RT_i}\right) \times \Delta t_i \tag{2.36}$$

where T_i is the average temperature within the time interval Δt_i, and m is the number of the time intervals. Because of the small size of the atoms and the limitation of computer resource, the atomistic model can only be used to simulate grain growth in the structure with small assemblies of atoms such as nanocrystals. To simulate grain growth associated with large grain size, the Grain Boundary Migration (GBM) model and Experimental Data Base (EDM) model can be used. In these two models, the grid points are treated as a block of physical area (in 2D) or volume (in 3D) in the material.

Grain Boundary Migration (GBM) Model

Grain boundary migration reduces number of grains, thereby increasing the mean grain size and reducing the total grain boundary energy. Assuming that grain growth is controlled by atomic diffusion across the grain boundary, driven by grain boundary energy, and requiring no nucleation, the grain boundary migration velocity (v) can be expressed as:[119]

$$v = \frac{AZvV_m^2}{N_aRT} \times \exp\left(\frac{\Delta S_a}{R}\right) \times \exp\left(-\frac{Q}{RT}\right) \times \frac{2\gamma}{r} \tag{2.37}$$

where A is the accommodation probability, Z is the average number of atoms per unit area at grain boundary, v is the atomic vibration frequency, V_m is the atomic molar volume, N_a is Avagadro's number, ΔS_a is the activation entropy, Q is the activation

energy for grain growth, g is the grain boundary energy, T is the absolute temperature, and R is the gas constant. The following assumptions are made in the model:

(1) The mean radius of curvature (r) of all the grain boundaries is equal to the mean intercept of grains (L).

(2) The velocity of grain boundary migration is related to the growth rate by the following relationship:

$$v = \frac{d(L/2)}{dt} = \frac{1}{2} \times \frac{dL}{dt}$$ (2.38)

(3) The atomic vibration frequency (v) is related to temperature as:

$$v = \frac{kT}{h} = \frac{RT}{N_a h}$$ (2.39)

where h is Planck's constant and k is Boltzmann's constant.

Based on the above assumptions, the isothermal grain growth kinetics can be deduced as:

$$L^2 - L_0^2 = \left\{ \frac{4\gamma AZV_m^2}{N_a^2 h} \times \exp(\frac{\Delta S_a}{R}) \right\} \times \exp\left(\frac{-Q}{RT}\right) \times t$$ (2.40)

where L is the average grain size at time t and L_0 is the initial average grain size. On the other hand, through the MC simulation, an empirical relation between the simulated grain size and the MC simulation time can be obtained as:[105, 106]

$$L = K_1 \times \lambda \times (t_{MCS})^{n_1}$$ (2.41)

where L is the dimensionless simulated grain size measured by mean grain intercepts, λ is the discrete grid point spacing in MC technique, t_{MCS} is MC simulation time or MC simulation iteration steps, K_1 is the simulated kinetic constant, and n_1 is the simulated value of the inverse of the grain growth exponent. Both K_1 and n_1 are the model constants, which are obtained by regression analysis of the data generated from MC simulation. Equating the mean grain intercept of equation (2.40) to that of equation (2.41) and integrating t_{MCS} over the entire thermal cycle, the t_{MCS} for simulation of grain growth in the HAZ can be expressed as:

$$(t_{MCS})^{2n_2} = \left(\frac{L_0}{K_1\lambda}\right)^2 + \frac{1}{(K_1\lambda)^2}\left\{\frac{4\gamma A Z V_m^2}{N_a^2 h} \times \exp\left(\frac{\Delta S_a}{R}\right)\right\} \times \sum_{i=1}^{m}\left[\Delta t_i \times \exp(-\frac{Q}{RT_i})\right] \quad (2.42)$$

Through equation (2.42), the Monte Carlo simulation step for a non-isothermal process can be related with its temperature-time history.

When the isothermal grain growth data for a given material are insufficient, the GBM model is a good approach for grain growth simulation. However, the physical properties of the material must be available. Strictly speaking, the GBM model is only valid for pure materials. This is because the value of grain growth exponent is assumed to be 2.0 in the model, as given in equation (2.40). As discussed earlier, this ideal value (2.0) was theoretically derived and was only suitable for very pure material at high temperatures, in which the effects of solute drag, impurity segregation, and second particles on grain growth can be ignored. Thus, for metals with relatively high content of impurities or alloys, the experimental data based (EDB) model should be used, in which sufficient kinetic data for isothermal grain growth at different temperatures are needed.

Experimental Data Base (EDB) Model

Based on the data from isothermal grain growth experiments, a relation can be established between the grain size (L), temperature (T) and holding time (t), which can be expressed as:

$$L^n - L_0^n = K \times t \times \exp(-\frac{Q}{RT}) \quad (2.43)$$

As shown in equation (2.41), the relation between the grain size and the t_{MCS} can also be established by Monte Carlo simulation at constant temperature. Combining equations (2.41) and (2.43), the relation between the t_{MCS} for the isothermal grain growth and the real time temperature can be established as:

$$(t_{MCS})^{n \times n_1} = \left(\frac{L_0}{K_1\lambda}\right)^n + \frac{K}{(K_1\lambda)^n} \times t \times \exp(-\frac{Q}{RT}) \quad (2.44)$$

Similarly, the temperature-time curve in the HAZ needs to be divided into many intervals and each step is assumed to be isothermal. Equation (2.44) can then be transformed into:

$$(t_{MCS})^{n \times n_i} = \left(\frac{L_0}{K_1 \lambda}\right)^n + \frac{K}{(K_1 \lambda)^n} \times \sum_{i=1}^{m} \left[\Delta t_i \times \exp(-\frac{Q}{RT_i})\right] \qquad (2.45)$$

In equation (2.45), the Monte Carlo simulation step is related with real time-temperature history based on available isothermal grain growth kinetic data n and K.

2.3.3.3 Previous MC Simulation of Grain Growth in the HAZ

In recent years, some efforts have been made to apply MC technique in simulation of grain growth in the HAZ. Gao et al.[105,106] simulated the grain structure in the HAZs of different welds by using MC technique in two dimensions. The materials investigated were nanocrystalline nickel thin film, aluminum plate, and 0.5Cr-Mo-V steel. Depending on the material systems investigated, different kinetic models as described in the previous section (e.g. Atomistic Model, GBM model, and EDB model) were applied in establishing the relation between the MC step, t_{MCS}, and the real time-temperature. It was found that the Monte Carlo based simulation technique can be successfully used in simulating normal grain growth in the presence of thermal gradients as in the HAZ of welds. When the isothermal grain growth data were available such as 0.5Cr-Mo-V steel, good results were obtained from the experimental data based model. For the case where experimental data were insufficient but data on physical properties were available such as pure aluminum plate, the grain boundary migration model was used as an alternative to simulate grain growth.

Monte Carlo based model have also been used to predict the "thermal pinning" phenomena in the HAZ.[97] This phenomena was first observed by Alberry[95] in the weld HAZ of a 0.5 Mo-Cr-V steel. In comparing the grain growth in the HAZ of real welds with that in simulated specimen by bulk heating, Alberry[95] found that the grain size in simulated specimen was larger than that in the HAZ of a weld when comparison was made on the basis of a similar thermal cycle. A possible explanation of this observation is the phenomenon of "thermal pinning", which can be attributed to the presence of steep

temperature gradients in a weld HAZ. This effect has been disregarded in the analytical analysis,[65,66,95,96] but it can be easily included in Monte Carlo technique.[97] Radhakrishnan et al.[97] have demonstrated that the retarded grain growth kinetics due to the presence to steep temperature gradient can be simulated by using MC technique as shown in Fig. 2.19. This figure shows the kinetics of grain growth at a specified location in the HAZ (120 μm from the fusion line) and the kinetics for bulk heating using an identical thermal cycle. It can be observed that the grain growth kinetics at the specified location in the HAZ was lower than that for bulk heating which experienced an identical thermal cycle.

Although the thermal pinning phenomenon can be simulated by the MC technique. the magnitude of the pinning effect predicted by the MC simulations[97] was found to be still significantly lower than that in the actual weld HAZ. In other word. the predicted grain size from MC simulation was still larger than that in the actual weld HAZ. even though the thermal pinning phenomenon had been modeled. This indicated that there was an additional inhibition effect except for the "thermal pinning". The formation of the grain boundary liquid is believed to be responsible for this additional pinning.[97,107] The liquid in the HAZ may be formed by different mechanisms. The grain boundary liquid can be formed by the sub-solidus liquidation caused by the presence of soluble second particles[97,107,120,121] or by intergranular penetration of liquid and/or solute from the fusion zone along grain boundaries in the HAZ.[97] The dominance of one mechanism over another depends on the system investigated.

The grain boundary liquidation can occur in the HAZ above the solidus temperature and the grain growth in the HAZ can be significantly retarded due to the presence of liquid at grain boundaries.[97] Abnormal grain size distribution can result from grain boundary liquidation. In analyzing the grain size distribution in the HAZ of maraging steels. Pepe et al.[120,121] found that the average grain diameter was 54 μm at the location of 100 μm from the fusion line and only 48 μm at the fusion line. Similar trend of grain size distribution was observed in the experiments by Wilson et al..[107] in which
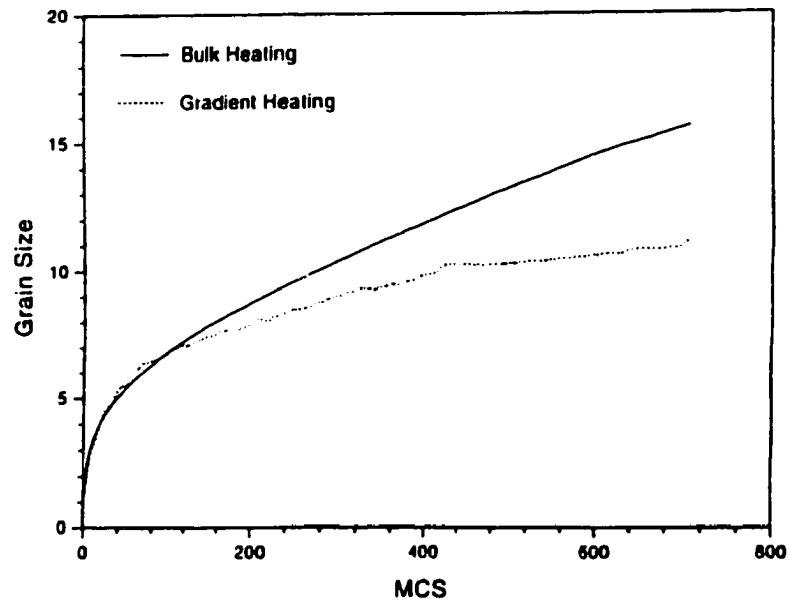
Fig. 2.19: MC simulated grain growth kinetics at the 120 μm location from the fusion line in the HAZ and for the bulk heating using identical thermal cycle.[97]

the grain size distribution in the HAZs of the HSLA-80 and HSLA-100 welds were analyzed systematically. Significant reductions in grain size in the vicinity of the fusion line were observed. The pinning effect due to the liquidation of grain boundary has been simulated using MC technique by Radhakrishnan et al.[97] and Wilson et al.[107] Since the grain growth was assumed completely pinned by the grain boundary liquid, the corresponding portion of the thermal cycle was not considered in the calculation of the Monte Carlo simulation step, t_{MCS}, in the simulations. Thus, the t_{MCS} value and the simulated grain size near the fusion line decreases as the liquidus temperature decreases, as shown in Figs. 2.20 and 2.21, respectively. In this way, the effect of grain boundary liquidation on grain growth can be simulated by the MC technique.
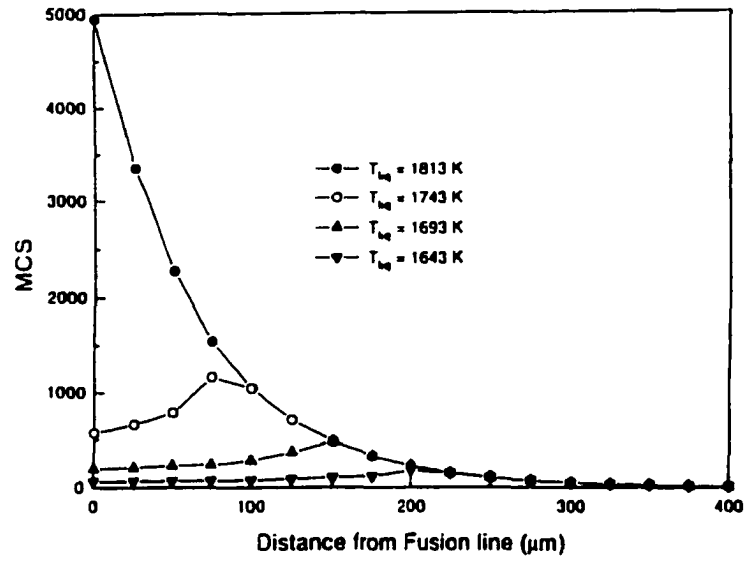
Fig. 2.20: The Monte Carlo simulation steps. MCS. used for considering the pinning due to grain boundary liquidation.[97]
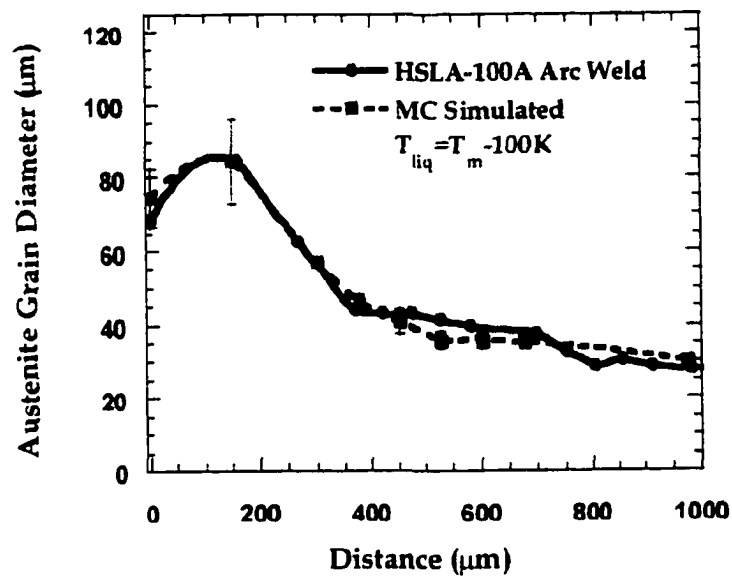
Fig. 2.21: Austenite grain size distribution for experimental HSLA-100 arc weld and MC simulated HAZ considering the pinning due to grain boundary liquidation.[107]

2.3.4 Summary of Simulation of Grain Growth in HAZ

Due to the steep temperature gradient and transient thermal cycles in the HAZ, it is difficult to use experimental methods alone to study the complicated grain growth phenomena in this region. Theoretical calculations by using analytical equation can provide quantitative kinetic information on the grain growth in the HAZ. However, the general analytical equation can not account for many important factors that determine the topological evolution of the grain structure such as the orientations of the grains and the coordinates of the grain boundary network. In contrast, MC technique based grain growth simulation method has the capability to provide both microstructural and kinetic information. MC simulation technique is particularly attractive for studying grain growth in the HAZ with steep temperature gradient because the spatial variation of grain boundary mobility can be automatically incorporated into the algorithm. In the MC algorithm, the grains are subdivided into many discrete small units which then have individual mobilities assigned depending on the local temperature. Some special phenomena for grain growth in the HAZ such as "thermal pinning" can be well predicted by the MC based grain simulation technique.

Previous simulations of the grain growth in the HAZ were limited in two dimensions. Considering the significant change of local thermal and topological environment within the HAZ, simulation of grain growth in two dimensions is not sufficient for real grain growth occurring in three dimensional environment. Furthermore, the two dimensional simulation can not provide a full description of the grain growth phenomena in the HAZ. Some unique features of grain growth in the HAZ are ignored in the two dimensional calculations. For example, the width of the HAZ usually varies with the location in the actual weldment. This temperature dependence of width variation was ignored in the previous two dimensional simulations. For a more realistic simulation, a three dimensional MC model considering spatial variations of temperature and thermal cycles in the whole region of the HAZ around the weld pool is needed. Accurate knowledge of thermal cycles at various locations is essential for simulation of grain growth in the HAZ considering the steep temperature gradient in this region.

2.4 SUMMARY

The development of weldment macro- and microstructures is governed by various physical processes Modeling of weldment maco- and microstructures needs to address the physical processes occurring at the macroscopic scale (heat transfer and fluid flow), as well as those occurring at the microscopic scale (phase transformations and grain growth). [122]

In order to obtain accurate predictions of the weld geometry and the thermal cycles in the weldment, turbulent heat transfer and fluid flow in the weld pool should be considered in the development of a thermal model. The existing turbulent weld models are limited to two dimensions. The two dimensional calculations cannot provide a full description of the heat transfer and fluid flow in the weld pool. In addition, two dimensional simulation cannot predict the thermal cycles at various locations in the whole weldment, which is a prerequisite to quantitatively predict phase transformations and grain growth in the weldment. Therefore, a 3D model considering turbulent heat transfer and fluid flow is essential for achieving realistic simulation and obtaining complete information.

Phase transformation models that consider the characteristics of the welding process are now available for a quantitative prediction of welding-induced phase transformations. To apply these phase transformation models in prediction of weldment microstructure, accurate knowledge of the thermal cycles at various locations of the weldment is needed. Coupling the available phase transformation models with thermal cycles calculated from a comprehensive heat transfer and fluid flow model will be an effective approach for quantitative calculation of phase transformations during welding.

The Monte Carlo based grain growth simulation technique can provide not only grain growth kinetics, but also detailed microstructural information. Furthermore, it can effectively simulate the unique grain structure in the HAZ, where steep temperature gradient and transient thermal cycles exist. Knowledge of the steep temperature gradient and the thermal cycles at various locations in the HAZ is a key factor for quantitative prediction of grain growth in this region. For a realistic simulation, a three dimensional

MC model needs to be established and coupled with a three dimensional thermal model. By this way, the effect of the spatial variation of the thermal cycles on the grain growth in the HAZ can be effectively simulated.

2.5 References:

1. S. A. David and T. DebRoy: *Science*, **257**, 497 (1992).

2. T. DebRoy and S. A. David: Review of Modern Physics, **67**, 85 (1995).

3. S. A. David, T. DebRoy and J. M. Vitek: MRS BULLETIN, **1**, 29 (1994).

4. D. R. Atthey: *J. Fluid Mech.*, **98**, 787 (1980).

5. G. M. Oreper, T. W. Eager, and J. Szekely: *Weld. J.*, **62**, 307s (1983).

6. G. M. Oreper and J. Szekely: *J. Fluid Mech.*, **147**, 53 (1984).

7. M. C. Tsai and S. Kou: *Numerical Heat Transfer*, Part A, **17**, 73 (1990).

8. M. C. Tsai and S. Kou: *Weld. J.*, **69**, 241s (1990).

9. M. C. Tsai and S. Kou: *Intl. J. for Numerical Method in Fluids*, **9**, 1503 (1989).

10. S. Kou and Y. H. Wang: *Metall. Trans. B*, **17A**, 2271 (1986).

11. S. Kou and Y. H. Wang: *Weld. J.*, **65**, 63s (1986).

12. T. Zacharia, S. A. David, J. M. Vitek, and T. DebRoy: *Weld. J.*, **68**, 499s (1989).

13. T. Zacharia, S. A. David, J. M. Vitek, and T. DebRoy:. *Metall. Trans. B.*, **21B**, 600 (1990).

14. A. Paul and T. DebRoy: Advances in Welding Science and Technology, ed. by S. A. David, p. 29. ASM INTERNATIONAL, Materials Park, OH (1986).

15. A. J. Paul and T. DebRoy: *Metall. Trans. B.* **19B**, 851 (1988).

16. K. Mundra, T. DebRoy, and K. Kelkar: *Numerical Heat Transfer*, Part A, **29**, 115 (1996).

17. K. Mundra, T. DebRoy, T. Zacharia, and S. A. David: *Weld. J.*, **71**, 313s (1992).

18. W. Pitscheneder, T. DebRoy, K. Mundra, and R. Ebner: *Weld. J.*, **75**, 71s (1996).

19. K. Mundra, J. M. Blackburn, and T. DebRoy: *Science and Technology of Welding and Joining*, **2**, 174 (1997).

20. K. C. Tsao and C. S. Wu: *Weld. J.*, **67**, 70s (1988).

21. R. T. C. Choo and J. Szekely: *Weld. J.*, **73**, 25s (1994).

22. K. Hong, D. C. Weckman, and A. B. Strong: *Trends in Welding Research*, ed. by H. B. Smartt, J. A. Johnson and S. A. David, p. 399, ASM INTERNATIONAL, Materials Park, OH (1996).

23. C. Chan, J. Mazumder, and M .M. Chen: *Metall. Trans. A*, **15A**, 2175 (1984).

24. D. A. Schauer, W. H. Giedt, and S. M. Shintaku: *Weld. J.*, **57**, 127s (1978).

25. W. H. Giedt, X. Wei, S. Wei: *Weld. J.*, **63**, 376s (1984).

26. W. E. Lukens and R. A. Morris: *Weld. J.*, **61**, 27s (1982).

27. W. Pitscheneder, R. Ebner, T. Hong, T. DebRoy, K. Mundra and R. Benes: Experimental and numerical investigation of transport phenomena in conduction mode weld pools. In mathematical modeling of weld phenomena 4, p. 4, 1998.

28. J. D. Boillot, P. Cielo, and G. Begin, C. Michel, M. Lessard: *Weld. J.*, **64**, 209s (1985).

29. H. G. Kraus: *Weld. J.*, **66**, 353s (1987).

30. H. G. Kraus: *Weld. J.*, **68**, 84s (1989).

31. C. R. Heiple and J. R. Roper: *Weld. J.*, **60**, 143s (1981).

32. C. R. Heiple and J. R. Roper: *Weld. J.*, **61**, 97s (1982).

33. W. G. Essers and R. Walter: *Weld. J.*, **60**, 38s (1981).

34. G. L. Allum and L. Quintino: *Metal Construction*, 314R (1985).

35. A. D. Watkins, H. B. Smartt, and C. J. Einerson: Advances in Welding Science and Technology, ed. by S. A. David and J. M. Vitek, p. 19, ASM INTERNATIONAL, Materials Park, OH (1989).

36. N. S. Tsai and T. W. Eager: *Metall. Trans. B*, **16B**, 841 (1985).

37. H. B. Smartt, J. A. Stewart, and C. J. Einerson: in "85 ASM International Welding Congress; paper no. 8511-011, Toronto, Canada, Oct. 1985.

38. E. Pardo and D. C. Weckman: *Metall. Trans. B*, **20B**, 937 (1989).

39. T. Tekriwal and J. Mazumder: *Weld. J.*, **67**, 150s (1988).

40. C. S. Wu and L. Dorn: in *Mathematical Modelling of Weld Phenomena 3*, ed. by H. Cerjak and H. K. D. H. Bhadeshia, p. 898, Institute of Materials (1997).

41. J. -W. Kim and S. -J. NA: *Transaction of the ASME*, **116**, 78 (1994).

42. P. Sahoo, T. DebRoy, and M. J. McNallan: *Metall. Trans. B*, **19B**, 483 (1988).

43. T. Zacharia, S. A. David, J. M. Vitek, and T. DebRoy: *Weld. J.*, **68**, 510s (1989).

44. J. Szekely: *Advances in Welding Science and Technology*, ed. by S. A. David, p. 3, ASM INTERNATIONAL, Materials Park, OH (1989).

45. Y. H. Wang and S. Kou: *Advances in Welding Science and Technology*, ed. by S. A. David, p. 65, ASM INTERNATIONAL, Materials Park, OH (1989).

46. A. D. Brent, V. R. Voller, and K. J. Reid: *Numerical Heat Transfer*, **13**, 297 (1988).

47. H. Davis: *"Numerical Modelling of Weld Pool Convection in Gas Metal Arc Welding"*, Ph.D. Thesis, University of Adelaide, Australia, September, 1995.

48. D. N. Shackleton and W. Lucas: *Weld. J.*, **53**, 537s (1974)..

49. M. Malinowski-Brodnicka, G. denOuden, and W. J. P. Vink: *Weld. J.*, **69**, 52s (1990).

50. B. E. Launder and B. D. Spalding: *Mathematical Models of Turbulence*, Academic Press, New York, N.Y, 1972.

51. H. K. D. H. Bhadeshia and L. -E. Svensson: in *Mathematical Modeling of Weld Phenomena*, ed. by H. Cerjak and K.E. Easterling, p. 109, Institute of Materials (1993)..

52. H. K. D. H. Bhadeshia: in *'Recent Trends in Welding Science and Technology'*, ed. by S. A. David and J. M. Vitek, p. 189. ASM INTERNATIONAL, Materials Park, OH (1990).

53. H. K. D. H. Bhadeshia, L. -E. Svensson, and B. Gretoft: *Acta metall.*, **33**, 1271 (1985).

54. H. K. D. H. Bhadeshia: *Progress in Materials Science*, **29**, 321 (1985).

55. H. K. D. H. Bhadeshia: *Bainite in Steels*, Institute of Materials (1992).

56. W. F. Savage, C. D. Lundin, and A. H. Aaronson: *Weld. J.*, **44**, 175 (1965).

57. G. J. Davies and J. G. Garland: *Int. Metallurgical Rev.*, **20**, 83 (1975).

58. C. A. Dube, H. I. Aaronson, and R. F. Mehl: *Rev. Met.*, **55**, 201 (1958).

59. H. I. Aaronson: in *Decomposition of Austenite by Diffusional Processes*, ed. by V. F. Zackay and H. I. Aaronson, p. 387, Wiley, New York (1962).

60. Oystein Grong: *Metallurgical Modelling of Welding*, p. xx, Institute of Materials (1994).

61. D. J. Abson and R. E. Dolby: A Scheme for quantitative description of ferritic weld metal microstructures. IIW document IX-J-29-80.

62. O. Grong and D. K. Matlock: *Int. Met. Rev.*, **31**, 27 (1986).

63. D. J. Abson and R. J. Pargeter: *Int. Met. Rev.*, **31**, 141 (1986).

64. H. K. D. H. Bhadeshia: in *Phase Transformation '87*, ed. by G. W. Lorrimer, p. 309, Institute of Metals, London (1988).

65. Ashby and K. E. Easterling: *Acta metall.*, **30**, 1969 (1982).

66. J. C. Ion, K. E. Easterling, and M. F. Ashby: *Acta metall.*, **32**, 1949 (1984).

67. D. F. Watt, L. Coon, M. Bibby, J. Goldak, and C. Henwood: *Acta metall.*, **36**, 3029 (1988).

68. L. Coon and D. F. Watt: in *Computer Modeling of Fabrication Processes and Constitutive Behaviour of Materials*, ed. by J. Too, p. 467, CANMET, Ottawa (1987).

69. J. S. Kirkaldy and D. Venugopalan: in *Phase Transformations in Ferrous Alloys*, ed. by A. R. Marder and J. I. Goldenstein, p. 125, Am. Inst. Min. Engrs, Philadephia, PA (1984).

70. J. S. Kirkaldy and R. C. Sharma: *Scripta metall.*, **16**, 1193 (1982).

71. J. S. Kirkaldy: *Metall. Trans.*, **4**, 2327 (1973).

72. W. A. Johnson and R. F. Mehl: *Trans. Am. Inst. Min. Engrs*, **136**, 416 (1939).

73. M. Avrami: *J. Chem Phys.*, **9**, 177 (1941).

74. I. M. Lifshitz and V.V. Slyozov: J. Phys. Chem., **19**, 35 (1961).

75. C. M. Wagner: Z. Electrochem., **65**, 581 (1961).

76. M. Inagaki and H. Sekiguchi: *Trans. Natn. Res. Inst. Metals*, Japan, **2**, 102 (1960).

77. International Institute of Welding Doc. IIS/IIW-382-71, "Guide to the Weldability of C-Mn Steels and C-Mn Microalloyed Steels" (1971).

78. J. W. Cahn: *Acta metall.*, **4**, 572 (1956).

79. C. Henwood, M. Bibby, J. Goldak, and D. F. Watt: *Acta metall.*, **36**, 3029 (1988).

80. M. B. Kuban, R. Jayaraman, E. B. Hawbolt, and J. K. Brimacombe: *Metall. Trans.*, **17A**, 1493 (1986).

81. E. B. Hawbolt, B. Chau and J. K. Brimacombe: *Metall. Trans.*, **14A**, 1803 (1983).

82. K. C. Russell: *Acta metall.*, **16**, 761 (1968).

83. K. C. Russell: *Acta metall.*, **17**, 1123 (1969).

84. H. K. D. H. Bhadeshia: *Document of "Weld Microstructure Program"*, Department of Mat. Sci and Metallurgy, University of Cambridge, UK, unpublished.

85. F. A. Calvo, K. P. Bently, and R. G. Baker: *Studies of the Welding Metallurgy of Steels*, p. 71, BWRA, Abingdon, Cambridge (1963).

86. A. Hultgern: *Jernkontorets Ann.*, **136**, 403 (1951).

87. H. K. D. H. Bhadeshia: *Metal Science*, **16**, 159 (1982).

88. M. Cohen: *Trans. ASM*, **28**, 53 (1940).

89. J. W. Christian: *The Theory of Transformations in Metals and Alloys*, Edition 1, p. 492, Pergamon, Oxford (1965).

90. E. Scheil: *Arch. Eisenhuttenwesen*, **12**, 565 (1935).

91. M. Takahashi and H. K. D. H. Bhadeshia: *Materials Transactions, JIM,* **32,** 689 (1991).

92. P. P. Koistinen and R. E. Marburger: *Acta metall.,* **7,** 59 (1959).

93. R. Trivedi: *Metall. Trans.,* **1,** 921 (1970).

94. B. Buchmayr and H. Cerjak: *Weld Quality: Role of Computers,* Pergamon Press, Oxford, 43 (1988).

95. P. J. Alberry, B. Chew, and W. K. C. Jones: *Metals Technology,* **4,** 317 (1977).

96. R. P. Martukanitz, P. R. Howell, and W. A. Pratt: *International Trends in Welding Science and Technology,* ed. by S. A. David and J. M. Vitek, p. 271, ASM INTERNATIONAL, Materials Park, OH (1993).

97. B. Radhakkrishnan and T. Zacharia: *Metall. Trans. A,* **26A,** 2123 (1995).

98. M. P. Anderson, D. J. Srolovitz, G. S. Grest, and P. S. Sahni: *Acta Metall.,* **32,** 783 (1984)

99. D. J. Srolovitz, M. P. Anderson, P. S. Sahni, and G. S. Grest: *Acta Metall.,* **32,** 793 (1984).

100. A. D. Rollett, D. J. Srolovitz, M. P. Anderson: *Acta. Metall.,* **37,** 1227 (1989).

101. M. P. Anderson, G. S. Grest, and D. J. Srolovitz: *Phil. Mag. B,* **59,** 293 (1989).

102. Y. Saito and M. Enomoto: *ISIJ International,* **32,** 267 (1992).

103. Y. Saito: *ISIJ International,* **38,** 559 (1998).

104. B. Radhakkrishnan and T. Zacharia: *Metall. Trans. A,* **26A,** 167 (1995).

105. J. Gao and R. G. Thompson: *Acta Metall.,* **44,** 4565 (1996).

106. J. Gao, R. G. Thompson, and Y .Cao: *Trends in Welding Research,* ed. by H. B. Smartt, J. A. Johnson and S. A. David, p. 199, ASM INTERNATIONAL, Materials Park, OH (1996).

107. A. Wilson, R. P. Martukanitz, and P. Howell: published in the 5th International Conference on Trends in Welding Research, ed. by J. M. Vitek, S. A. David, J. A. Johnson, H. B. Smart, and T. DebRoy, p. 161, Pine Mountain, GA (1998).

108. J. E. Burke and D. Turnbull: *Prog. Met. Phys.,* **3,** 220 (1952).

109. M. Hillert: *Acta metall.,* **13,** 227 (1965).

110. P. Feltham: *Acta metall.,* **5,** 97 (1957).

111. F. N. Rhines and K. R. Craig, *Metall. Trans. A,* **5A,** 413 (1974).

112. N. Rivier: *Phil. Mag. B,* **47,** L45 (1983).

113. I-Wei, Chen, *Acta Metall.* **35,** 1723 (1987).

114. E. L. Holmes and W. C. Winegard: *Acta metall.*, **7**, 411 (1959).

115. J. P. Drolet and A. Galibois: *Acta metall.*, **16**, 1387 (1968).

116. G. F. Bolling and W. C. Winegard: *Acta metall.*, **6**, 283 (1958).

117. H. Hu: *Can. Metall. Q.*, 13, 275 (1974).

118. P. Gordon and T. A. E. Bassyoni: *Trans. Am. Inst. Min. Engrs*, **233**, 391 (1965).

119. D. A. Porter and K. E. Easterling: *Phase Transformation in Metals and Alloys*, Chapman & Hall, 1992.

120. J. J. Pepe and W. F. Savage: *Weld. J.*, **46**, 411s (1967).

121. J. J. Pepe and W. F. Savage: *Weld. J.*, **49**, 545s (1970).

122. S. A. David and S. S. Babu: in *Mathematical Modelling of Weld Phenomena 3*, ed. by H. Cerjak and H. K. D. H. Bhadeshia, p. 151, Institute of Materials (1997).

123. R. B. Bird, W. E. Stewart, and E. N. Lightfoot: Transport Phenomena, p. 298, John Wiley & Sons, Inc. (1960).

124. J. W. Christian: *The Theory of Transformations in Metals and Alloys*, Edition 1, p. 492, Pergamon, Oxford (1965).

125. K. Hong: "A Comprehensive Thermo-Fluids Model of Arc Welding Process", Ph.D. Thesis, University of Waterloo, Canada, 1996.

126. M. L. Lin and T. W. Eager: *Weld. J.*, **64**, 163s (1985).

127. W. Pitscheneder, R. Ebner, T. Hong, T. DebRoy, K. Mundra and R. Benes: Experimental and numerical investigation of transport phenomena in conduction mode weld pools. In mathematical modeling of weld phenomena 4, p. 4, 1998.

128. K. Mundra, T. DebRoy, S. S. Babu, and S. A. David: *Weld. J.*, **76**, 163s (1997).

129. K. Mundra and T. DebRoy: *Weld. J.*, **72**, 1s (1993).

130. T. A. Palmer and T. DebRoy: *Science and Technology of Welding and Joining*, **3**, 190 (1998).

131. V. Pavelic, L. R. Tanbakuchi, O. A. Oyehara, and P. S. Myers: *Weld. J.*, **48**, 295s (1969).

132. P. Sahoo, M. M. Collur, and T. DebRoy: *Metall. Trans. B*, **19B**, 967 (1988).

133. A. Khan and T. DebRoy: *Metall. Trans. B*, **19B**, 967 (1988).

134. M. M. Collur, A. Paul, and T. DebRoy: *Metall. Trans. B*, **18B**, 733 (1987).

135. T. DebRoy, S. Basu, and K. Mundra: *Journal of Applied Physics*, **70**, 1311 (1991).

136. T. Hong, W. Pitscheneder, and T. DebRoy: *Science and Technology of Welding and Joining*, **3**, 33 (1998).

137. K. Mundra and T. DebRoy: *Metall. Trans. B*, **25B**, 149 (1995).

138. M. Inagaki and H. Sekiguchi: Trans. Natn. Res. Inst. Metals, **2**, 102 (1960).

139. B. E. Launder and B. D. Spalding: *Mathematical Models of Turbulence*, Academic Press, New York, N.Y. 1972.

140. Innovative Research, Inc., Documentation of COMPACT-3D Version 3.1, Minneapolis, Minnesota (1994).

141. L.-E. Svensson, B. Gretoft, Svensson, and H. K. D. H. Bhadeshia: *Scand. J. Metallurgy*, **15**, 97 (1986).

142. H. Zhao and T. DebRoy: Unpublsihed research, Department of Materials Science and Engineering, Penn State, January, 2000.

143. Z. Yang, J. W. Elmer, J. Wong, and T. DebRoy: "Evolution of Titanium Arc Weldment Macro- and Microstructures - Modeling and Real Time Mapping of Phases," Accepted for publication in *Weld. J.*

144. *Aluminum Standards and Data*, 5th ed., The Aluminum Association, New York, NY, 1976.

145. *Aluminum*, ed. by K. R. Van Horn, ASM, 1976.

CHAPTER 3

MATHEMATICAL MODELING

In this chapter, the models developed in the present study, the three dimensional turbulent heat transfer and fluid flow model, hereafter called the 3D turbulent model, and a three dimensional Monte Carlo technique based grain growth simulation model, hereafter called the 3D MC model, are described. The definition of the models, governing equations, boundary conditions, and the solution techniques of each model are provided. In addition, the phase transformation models used in the present thesis are also discussed. Finally, the procedure for integrating these models for systematic prediction of the weldment macro- and microstructures is presented.

3.1 Three Dimensional Turbulent Heat Transfer and Fluid Flow Model

The 3D turbulent model is developed based on a previous laminar model.[1] The validity of this model has been discussed in chapter 2 and it was noted that the effect of turbulence on the heat transfer and fluid flow in the weld was previously considered through the introduction of spatially independent enhanced viscosity and thermal conductivity in the laminar model. These enhanced viscosity and thermal conductivity were selected based on experience and their values were assumed to be constant in the entire weld pool. For improved understanding of the transport phenomena in the weld pool, quantitative calculation of the enhanced viscosity and thermal conductivity from fundamentals is needed. In the present study, this need was fulfilled by incorporating the widely used K-ε turbulence model[2] in the calculation of heat transfer and fluid flow in the weld pool.

In many welding cases, the heat source moves with a constant velocity. Thus, when viewed in a fixed coordinate system (x, y, z), the welding problem is unsteady. Some efforts[3,4] have been made to investigate the heat transfer and fluid flow using

governing equations formulated in this coordinate system. It was found that the solution of the conservation of mass, momentum, and energy in this coordinate system requires a large number of grids for accurate representation of the moving, time-dependent position of the heat source and the spatial variation of the heat flux. Furthermore, very small time steps are needed to ensure the accuracy and stability of the solution. Therefore, the computation time is very large for adopting this fixed coordinate system.

3.1.1 Model Definition

In the present investigation, a coordinate system which moves with the heat source is adopted. In other words, the three-dimensional convection in the weld pool is solved in the coordinated system attached to the heat source as shown schematically in Fig. 3.1. In this moving coordinate system, the problem can be treated as quasi-steady-state, which means that the temperature and velocity fields are independent of time. This assumption is valid when the welding velocity is constant and the workpiece is relatively long. Under such conditions, the heat source and the molten metal under the heat source are fixed in space, and the material enters and leaves the computational domain at the welding velocity.

Due to symmetry along vertical plane passing through the welding direction, only half of the workpiece is taken as the simulated domain in the model as shown in Fig. 3.2. The Cartesian coordinate system is used in the model with the origin located at the point on the top surface of the weldment and directly below the heat source. The heat input comes from the arc for GTA welding or the combination of the arc and the metal droplets for GMA welding. In the present model, the driving forces for fluid flow in the weld pool include the surface tension gradient force, the electromagnetic force, and the buoyancy force. The weld pool boundary, or the solid/liquid interface, is unknown and is determined by solving the temperature and velocity fields simultaneously. Turbulent calculation of fluid flow and heat transfer is incorporated into the model. The latent heat for melting/solidification has been taken into account in the model. Finally, heat loss
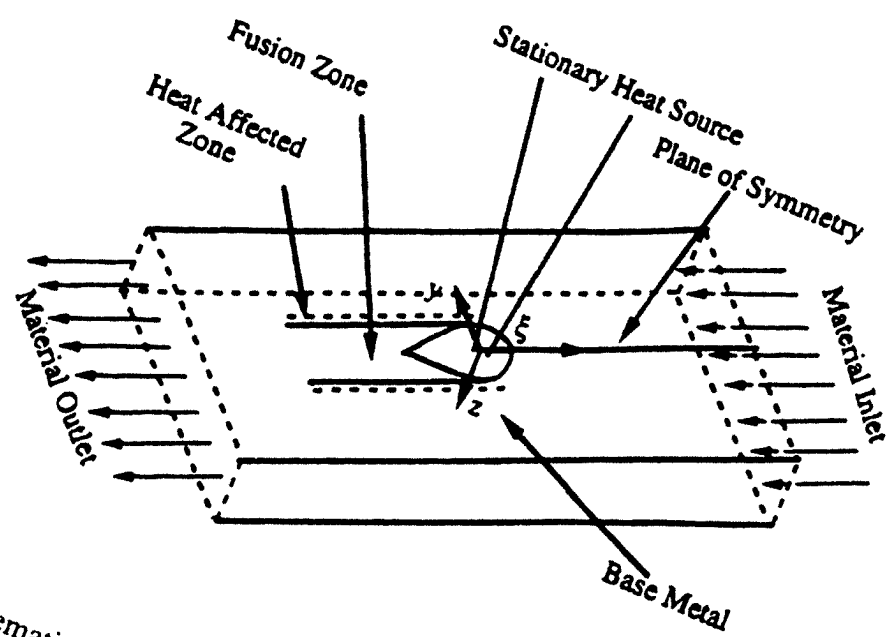
Fig. 3.1: Schematic diagram of the 3D heat transfer and fluid flow model. [1]
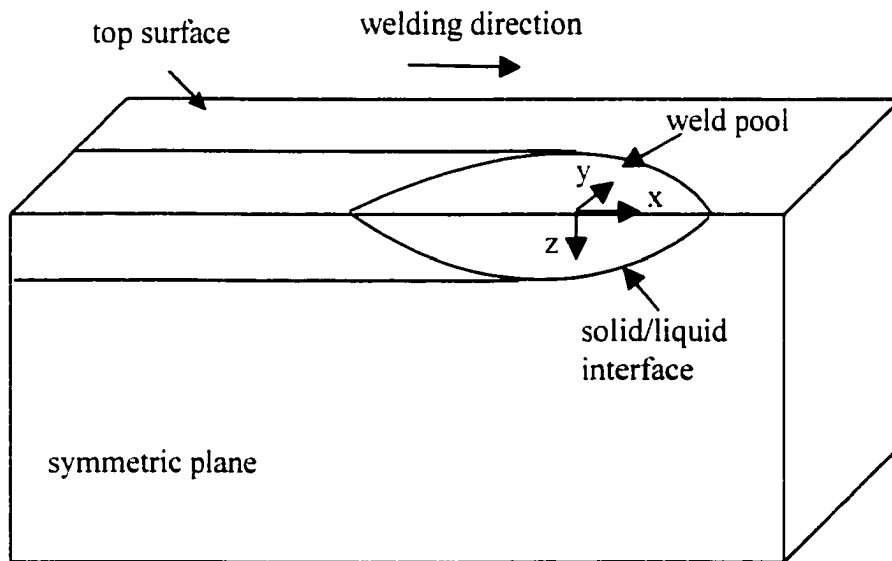
Fig. 3.2: Schematic diagram of the simulated domain in the 3D turbulent heat transfer and fluid flow model. The domain is taken half of the workpiecedue to symmetry in y direction. The length of the domain in x direction is set much larger than the dimension of the weld pool, so that the assumption quasi-steady state heat transfer is valid.

from the plate to its surroundings is calculated considering the combined effects of radiation and convection.

In addition to the assumption of quasi-steady-state, the following assumptions are made in the model:

1. The heat source is assumed to have Gaussian power distribution.

2. As in the majority of the fluid flow calculations including the buoyancy force, the liquid metal is considered incompressible except for the buoyancy force itself.

3. The enthalpy – temperature relationship is assumed be linear in the mushy zone, i.e.. in the region where the solid and liquid phases coexist.

4. The top surface of the weld pool is assumed to be flat.

3.1.2 Governing Equations

3.1.2.1 Conservation Equations of Mass, Momentum, and Energy

The governing equations are first formulated in the moving coordinate system (ξ.y.z.t) attached to the heat source. To treat the convective velocity as the primary unknown in the governing equations. the equations are further modified by subdividing the net velocity and welding velocity into convective and welding velocity components as following:

$$V' = V + V_s \qquad (3.1)$$

where V' is the velocity at any point. V is the convective component of the liquid metal velocity. and V_s is the welding velocity. Using equation (3.1), the steady state versions of the modified governing equations can be derived with V as the primary unknown velocity. The conservation equations of mass. momentum. and energy can be expressed as:[1]

$$\nabla \cdot V = 0 \qquad (3.2)$$

$$\rho \nabla \cdot (VV) = -\nabla P + \nabla \cdot (\mu_{eff} \nabla V) + (S_v - \rho \nabla \cdot (V_s V)) \qquad (3.3)$$

$$\rho \nabla \cdot (Vh) = \nabla \cdot \left(\frac{k_{eff}}{C_p} \nabla h \right) + S_1 + S_h - \rho \nabla \cdot (V_s h) \qquad (3.4)$$

where ρ is the density. P is the effective pressure, C_P is the specific heat, S_V is the source term that takes into account the combined effect of buoyancy force, electromagnetic force, and Marangoni stress, h is the enthalpy, S_h is the source term that takes into account the heat input from the welding source and the convective and radiative heat loss. S_l is the source term that accounts for latent heat of melting and convective transport of latent heat. μ_{eff} is the effective viscosity. and k_{eff} is the effective thermal conductivity.

3.1.2.2 Incorporation of K - ε Turbulent Model

An important component in the present model is the incorporation of K - ε model[2] to calculate the turbulent fluid flow and heat transfer in the weld pool in three dimensions with a moving heat source. A detailed description of the K - ε model was given by Launder and Spalding.[2] Only the salient features of the model are presented here.

The effects of turbulence on the fluid flow and heat transfer were included in the model through the use of effective viscosity and thermal conductivity. The effective viscosity and thermal conductivity can be expressed as:

$$\mu_{eff} = \mu_t + \mu \qquad (3.5)$$

$$k_{eff} = k_t + k \qquad (3.6)$$

where μ_t and k_t are the turbulent values. and μ and k are the molecular values. Unlike the molecular viscosity and thermal conductivity. which are physical properties, the turbulent viscosity and thermal conductivity are properties of both the fluid and the flow system. The turbulent viscosity was calculated by:

$$\mu_t = \frac{C_\eta \rho K^2}{\varepsilon} \qquad (3.7)$$

where C_η is an empirical constant equal to 0.09. K is the turbulent kinetic energy, and ε is the dissipation rate of turbulent kinetic energy. Under steady state condition, the value of

turbulent viscosity can be determined through the solution of the equations of conservation of K and ε as following:

$$\rho\left(V_x\frac{\partial K}{\partial x} + Vy\frac{\partial K}{\partial y} + Vz\frac{\partial K}{\partial z}\right) = \frac{1}{\sigma_k}\left\{\frac{\partial}{\partial x}\left[\mu_t\frac{\partial K}{\partial x}\right] + \frac{\partial}{\partial y}\left[\mu_t\frac{\partial K}{\partial y}\right] + \frac{\partial}{\partial z}\left[\mu_t\frac{\partial K}{\partial z}\right]\right\}$$
$$+\mu_t G_k - \varepsilon \tag{3.8}$$

$$\rho\left(V_x\frac{\partial \varepsilon}{\partial x} + V_y\frac{\partial \varepsilon}{\partial y} + V_z\frac{\partial \varepsilon}{\partial z}\right) = \frac{1}{\sigma\varepsilon}\left\{\frac{\partial}{\partial x}\left[\mu_t\frac{\partial \varepsilon}{\partial x}\right] + \frac{\partial}{\partial y}\left[\mu_t\frac{\partial \varepsilon}{\partial y}\right] + \frac{\partial}{\partial z}\left[\mu_t\frac{\partial \varepsilon}{\partial z}\right]\right\}$$
$$+\frac{\varepsilon}{K}\left(C_1 G_k - C_2\rho\varepsilon\right) \tag{3.9}$$

where σ_k, σ_ε, C_1 and C_2 are empirical constants with corresponding values being 1.0, 1.3. 1.44. and 1.92. respectively:[2] $\mu_t G_k$ is the turbulent counterpart to the viscous dissipation. The symbol of G_k is given in Cartesian-tensor notation and calculated by:

$$G_k = 2\left\{\left[\frac{\partial V_x}{\partial x}\right]^2 + \left[\frac{\partial V_y}{\partial y}\right]^2 + \left[\frac{\partial V_z}{\partial z}\right]^2\right\} +$$
$$\left\{\left[\frac{\partial V_x}{\partial y} + \frac{\partial V_y}{\partial x}\right]^2 + \left[\frac{\partial V_x}{\partial z} + \frac{\partial V_z}{\partial x}\right]^2 + \left[\frac{\partial V_y}{\partial z} + \frac{\partial V_z}{\partial y}\right]^2\right\} \tag{3.10}$$

where V_x, V_y, and V_z are the components of the convective velocity V in the x, y, and z directions. The turbulent thermal conductivity is related to the turbulent viscosity by the turbulent Prandtl number,[2.5] $Pr_t = C_p\mu_t / k_t = 0.9$. Thus, the spatial distribution of viscosity and thermal conductivity of the liquid metal could be calculated from the turbulence model.

3.1.3 Boundary Conditions

The calculations were carried out in a Cartesian coordinate system. Only half of the workpiece was considered since the weld pool is symmetrical along the vertical plane that passes through the welding direction. The boundary conditions for mass, momentum, and energy equations are described below.

3.1.3.1 Boundary Conditions for Mass and Momentum Equations

Along the vertical plane of symmetry (y=0 plane), the boundary conditions for the velocity components were defined as:

$$\frac{dV_x}{dy} = 0 \tag{3.11}$$

$$V_y = 0 \tag{3.12}$$

$$\frac{dV_z}{dy} = 0 \tag{3.13}$$

where V_x, V_y, and V_z are the components of the convective velocity V in the x, y, and z directions. The z-component of the velocity, V_z, was defined to be zero at the top surface. The x and y components of the velocity vector on the top surface (z = 0 plane) were determined by the Marangoni stress and were defined as:

$$-\mu_{eff} \frac{dV_x}{dz} = f_l \frac{d\gamma}{dT} \frac{dT}{dx} \tag{3.14}$$

$$-\mu_{eff} \frac{dV_y}{dz} = f_l \frac{d\gamma}{dT} \frac{dT}{dy} \tag{3.15}$$

where $d\gamma/dT$ is the temperature coefficient of surface tension and f_l is the liquid fraction, which is assumed to vary linearly with temperature in the mushy zone. The velocity in the solid region was set to be zero.

3.1.3.2 Boundary Conditions for Energy Equation

On the top surface, the heat exchange between the heat source and the surface of the sample, and the radiative and convective heat loss to the surroundings were described as:

$$J_h(\xi, y, z)_{z=0} = \frac{Q\eta}{2\pi r_b^2} e^{\left[-\frac{(\xi^2 + y^2)}{2r_b^2}\right]} - \varepsilon_1 \sigma \left(T(\xi, y, z)_{z=0}^4 - T_g^4\right)$$
$$- h_c \left(T(\xi, y, z)_{z=0} - T_g\right) \tag{3.16}$$

where Q is the power input, η is the welding absorption coefficient, r_b is the arc radius, $T(\xi,y,z)z=0$ is the local weld pool surface temperature, ε_1 is the emissivity, σ is the stefan-Boltzmann constant, h_c is the heat transfer coeffcient, and T_g is ambient temperature. In equation (3.16), the first term the represents the Gaussian distribution of heat source. The second and the third terms consider the radiative and convective heat loss, respectively. At the plane of symmetry (y=0), the gradient of the enthalpy was defined as:

$$\frac{dh}{dy} = 0 \qquad (3.17)$$

At other surfaces of the system, the enthalpy was described by setting the temperature equal to the ambient temperature.

3.1.3.3 Boundary Conditions for K and ε

For GTA welding, the boundary conditions for the turbulent kinetic energy, K, and its dissipation rate, ε, at the vertical symmetry plane were defined as: $\partial K/\partial y = 0$ and $\partial\varepsilon/\partial y = 0$. Similarly, at the top free surface the boundary conditions for these variables were defined as: $\partial K/\partial z = 0$ and $\partial\varepsilon/\partial z = 0$. At the solid-liquid interface, the values of K and ε were taken to be zero. For GMA welding, the boundary conditions for K and ε at the vertical symmetry plane and the solid-liquid interface are the same as those for GTA welding. However, at the top surface, the turbulence kinetic energy, K, was assumed to be 5 percent of the mean kinetic energy in the present calculation. This boundary condition was commonly used in similar flow system.[6] The value of ε was determined by the following equation:[5]

$$\varepsilon = \frac{K^{3/2}}{fL} \qquad (3.18)$$

where f is a constant equal to 0.3, and L is the characteristic length of the weld pool (e.g. the depth of the weld pool).

3.1.4 Solution Technique and Implementation

3.1.4.1 Numerical Scheme

The control-volume-based computational method of Patankar,[7] implemented[5] in COMPACT-3D, is used for the numerical solution of the governing equations. The computational domain is divided into control volumes. The basic construction of the control volumes and the grid is shown in Fig. 3.3(a). It should be pointed out that only one plane in the control volume, xy-plane, is shown here for the sake of clarity. In Fig. 3.3(a), the solid lines are the grid lines, and the dashed lines denote the boundaries of the control volumes. The dots are the grid points, which are located in the center of the basic control volumes. The values of the scalar variables such as enthalpy are stored at the grid points. A typical control volume is shown as the shaded area in Fig. 3.3(a). This type of control volumes are called "main" control volumes and are used for solving scalar variables in the calculation.

For numerical stability in the fluid flow calculations, a grid system called "staggered grid".[7] is used to store the vector variables such as velocity components (V_x, V_y and V_z) and body forces. In the "staggered grid" system, the velocity components V_x, V_y and V_z are stored at the interface locations rather than at the grid points, as shown in Fig. 3.3(b). In general, a velocity component normal to each interface is stored at the center of the interface. From Fig. 3.3(b), it can be noted that each velocity component is staggered in its own direction. As a result of using "staggered grid" system, the control volumes used for deriving the discretization equations for momentum are also staggered. For the sake of clarity, only x-y plane of the control volume for the discretization of momentum equations is presented here, as shown as the shaded area in Fig. 3.4(a) and (b). In comparison with the "main" control volumes shown in Fig. 3.3(a) and (b), the momentum control volumes are displaced such that one set of interfaces pass through the grid points. In general, a typical control volume for $V_x(i, j, k)$, as shown in 3.4(a), is made of one half contributions from the "main" control volumes around (i, j, k) and (i-1, j, k). Similarly, the control volume for $V_y(i, j, k)$, as shown in Fig. 3.4(b), is composed of the halves of the main control volumes around (i, j, k) and (i, j-1, k). Discretization equations
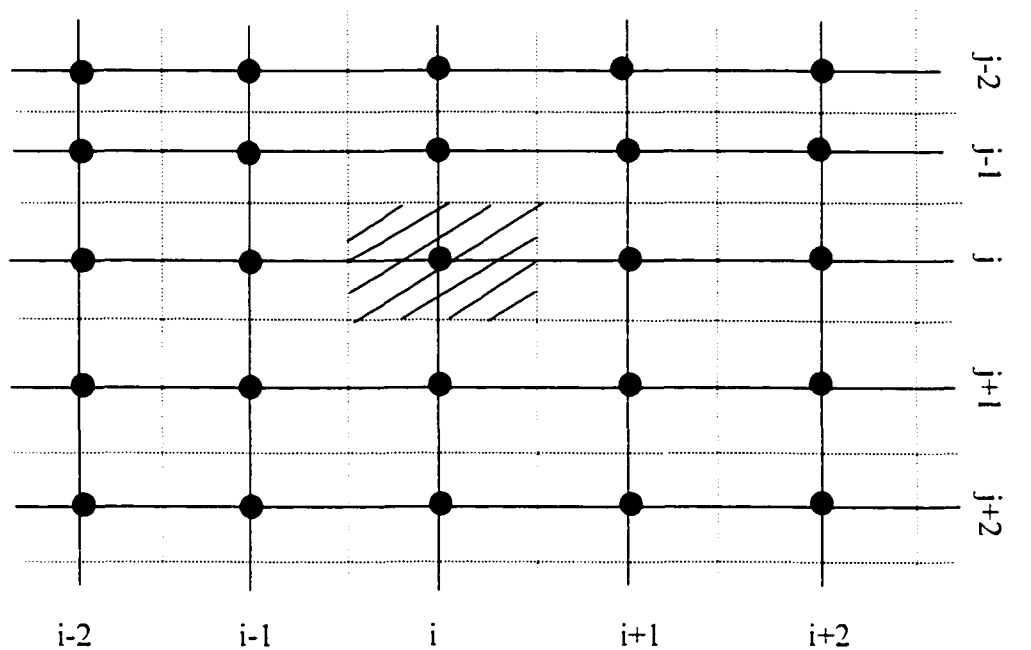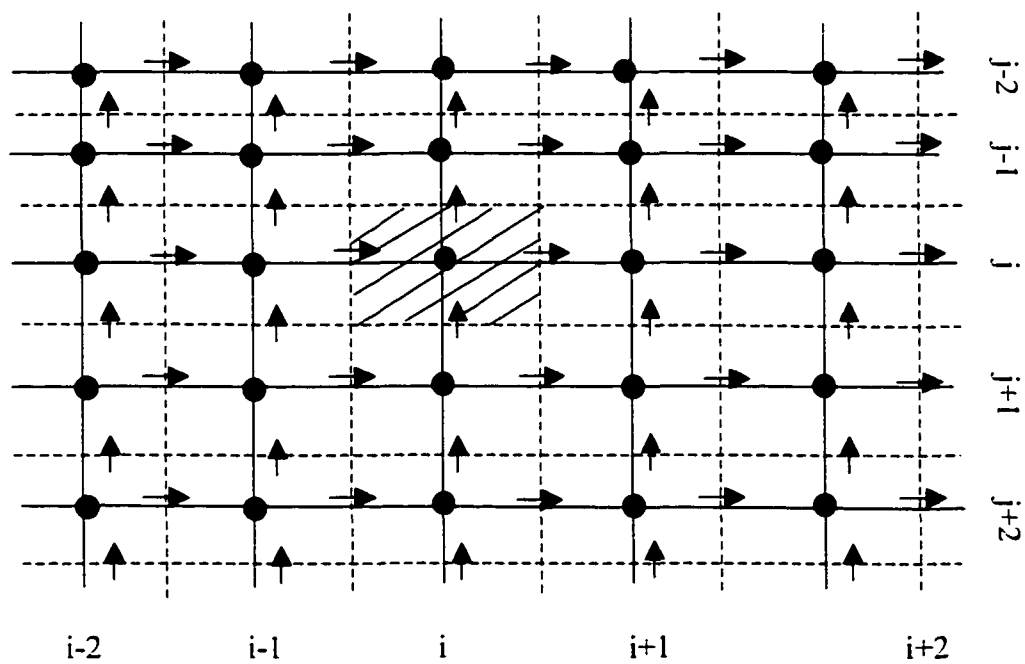
Fig. 3.3: (a) Control volumes and grid points in xy plane; (b) staggered locations for the velocity components in xy plane.
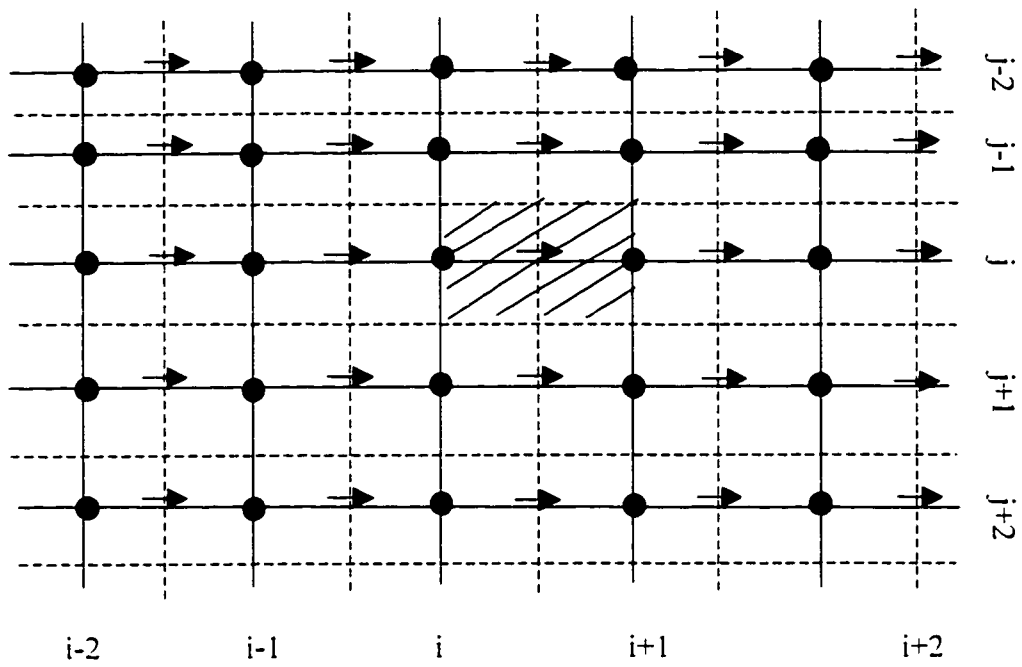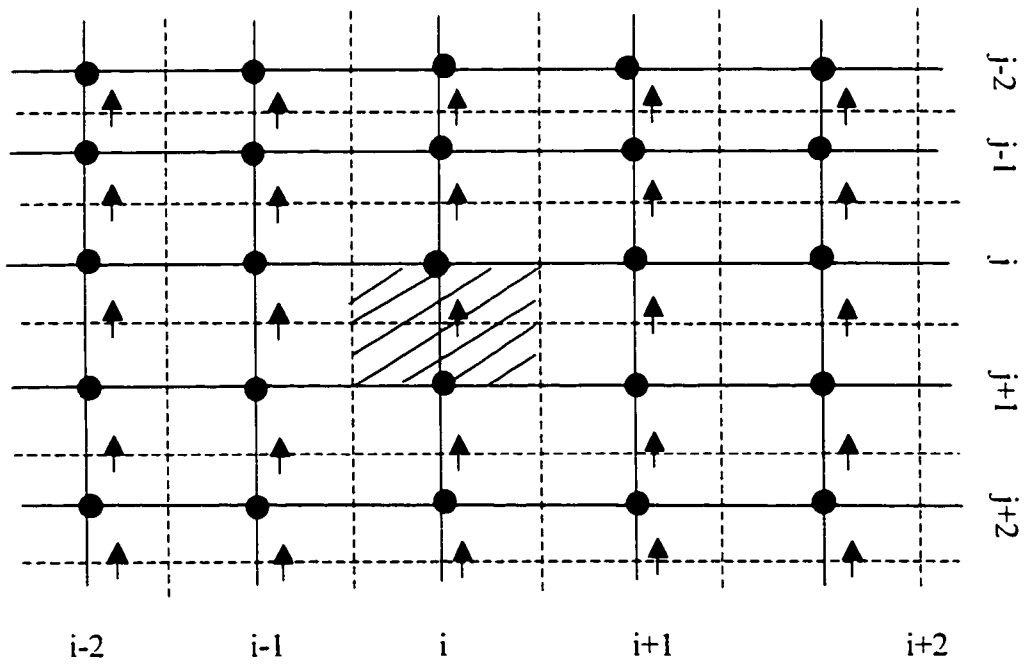
Fig. 3.4: XY plane in the control volumes[5] for the momentum equations.
(a) x - direction momentum, and (b) y - direction momentum.

for specific variables are formulated by integrating the corresponding conservation equations spatially nonuniform grids are used for the maximum resolution of variables. For example, finer grid spacing is used near the heat source and coarser grid spacing is adopted as the distance from the heat source increases.

3.1.4.2 Numerical Stability and Accuracy

For a coupled turbulent heat transfer and fluid flow problem, many physical quantities to be solved are interlinked and nonlinear. During the course of calculation of temperature and velocity fields, the values of temperature and velocity may oscillate or even drift continuously. Such divergence of the variables must be avoided. In the present calculation, a scheme called "underrelaxation" is employed to promote convergence. This scheme is suitable for both dependent variables (e.g. enthalpy, velocity, turbulent kinetic energy, and its dissipation rate) and auxiliary variables (e.g. turbulent thermal diffusivity and turbulent viscosity). The following underrelaxation procedure was used in the calculations.

$$a_p \Phi_p = \sum a_{nb} \Phi_{nb} + b \tag{3.19}$$

as

$$(a_p + i)\Phi_p = \sum a_{nb} \Phi_{nb} + b + i\Phi_p^* \tag{3.20}$$

where a_p is the discretization coefficient at grid point P, Φ_p is the unknown variable to be solved, a_{nb} are the discretization coefficients of neighbor grid points, Φ_{nb} are the values of the unknown variable at the neighbor grid points, Φ_p^* is the value of Φ_p in previous iteration step, b is a constant term in discretization equation, and i is the so-called inertia. Further, the inertia is chosen as

$$i = [(1-\alpha)/\alpha]a_p \tag{3.21}$$

where α is the relaxation factor. No underrelaxiation is introduced when α equals to unity. As α gets closer to zero, the changes in ϕ from iteration to iteration are greatly slowed down.

In the calculation, the formula for underrelaxing an auxiliary variable such as the turbulent viscosity, μ_t, is expressed as

$$\mu_t = \alpha \mu_t^{new} + (1-\alpha)\mu_t^{old} \tag{3.22}$$

where α is the relaxation factor, μ_t^{new} is the new value of turbulent viscosity, and μ_t^{old} is its value in the previous iteration step. In the same manner, the value of turbulent thermal diffusivity can be underrelaxed. This type of underrelaxiation serves to temporarily weaken the links between different variables. For example, if turbulent viscosity is underrelaxed, the changes in the turbulence parameters cannot strongly influence the velocity components.

Since the solution procedure is iterative, it should be repeated a number of times to obtain the converged solution. However, the computation of the fully converged solution of the linear discretization equations is often not desirable because the discretization coefficients are only tentative and must be updated from the freshly computed values of the given variable and other variables. In the present study, the iterative procedure was made until the following convergence criterion was satisfied:

$$\frac{\sum_p |\Phi - \Phi^{old}|}{\sum_p |\Phi|} < 0.001 \tag{3.23}$$

where $\sum_p$ denotes summation over all grid point P. ϕ is the variable to be solved, and ϕ^{old} is its value in the previous iteration step. In addition, two other quantities, SMAX and RSMAX, can be used to monitor the approach to convergence. The symbol of SMAX is the largest absolute value of the coefficients of the pressure-correction equation used in COMPACT-3D. The symbol of RSMAX is a dimensionless form of SMAX, which is obtained by dividing SMAX by the largest mass flow rate across any control-volume face. The quantities of SMAX and RSMAX were automatically calculated by COMPACT-3D and can be output in the calculation to judge the satisfaction of the continuity equation.

Appropriate selection of the underrelaxation parameters is a critical issue for achieving converged results, because the variables are interrelated in the coupled heat transfer and fluid flow calculation. The primary variables in the present calculation include enthalpy (h), three velocity components (V_x, V_y, V_z), pressure (P), turbulent

kinetic energy (K), and the dissipation rate of turbulent kinetic energy (ε). Since these variables are interrelated and the solid/liquid interface of the weld pool is updated for each iteration before convergence, it is very difficult to get converged results by using constant underrelaxation parameters and directly applying turbulent model. As an alternative approach, four steps are taken in the present study for calculation of temperature and velocity fields in the weld pool of both low alloy steels and commercially pure titanium. The iteration numbers and the values of underrelaxation parameters in all the four steps are listed in Tables 3.1 and 3.2 for welding of steel and titanium, respectively.

The first step is to get converged results by running laminar model before turbulent calculation. In this step, the turbulent kinetic energy, K, and its dissipation rate, ε, are not solved. Consequently, the turbulent viscosity, μ_t, and the turbulent thermal diffusivity, k_t, are zero. In the laminar calculation, the values of the underrelaxation parameters can be set to be large for quickly converged results. From Table 3.1, it can be observed that the values of both SMAX and RSMAX became very small after 200 iteration in the first step for steel weldments. After obtaining converged results form laminar model, three additional steps are taken for turbulent calculation, in which the underrelaxation parameters change from small to large values. At the beginning of the turbulent calculation (step 2), the underrelaxation parameters for the variables are taken as small values, specifically for the relaxation parameters of velocity, turbulent kinetic energy K, and its dissipation rate ε. This prevents large oscillation in the calculated velocity and pressure fields. After 50 iterations in step 2, another 50 iterations were undertaken in step 3, in which the underrelaxation parameters were some more moderate. After the transition stages (step 2 and step 3), the values of underrelaxation parameters in the turbulent calculation were set to be large in step 4 for final converged results. For calculation in steel welds, 300 hundred iterations were undertaken in the fourth stage to get converged results. As shown in Table 3.1, the values of SMAX and RSMAX were very small after 300 iterations in the fourth stage. In fact, the values of temperature and velocity remained constant at monitoring locations in the weld pool.

In contrast, fewer iterations (200 iterations) in the fourth stage were necessary in titanium welds to get converged results, as shown in Table 3.2. This is because the Marangoni stress (surface tension gradient force) is a main cause of oscillation in the weld pool. The absolute value of $d\gamma/dT$ of steel (-0.43 N/m·K) is larger than that of titanium (-0.26 N/m·K). Thus, the magnitude of oscillation in steel weld pool was larger than that in titanium. Consequently, more iterations were needed for converged results in steel welds.

The computation of heat transfer and fluid flow was carried out in IBM RS6000 model 39H workstation. When using a 56×30×25 grid system, it took about 50 seconds and 70 seconds for each iteration in laminar and turbulence calculations, respectively. As shown in Tables 3.1 and 3.2, there were totally 600 iterations in the four steps for calculation in steel welds and 500 iterations for titanium welds. Consequently, it took about ten and half hours for a complete run in steel welds and about eight and half hours for that in titanium welds.

3.1.5 Calculation of Thermal Cycles

After the numerical solution of the momentum and energy equations (e.g. equations 3.3 and 3.4), a steady state temperature field can be obtained. At any given location (x, y, z) in the weldment, the temperature variation with time can be expressed as:

$$T(x,y,z,t_2) = \frac{Ts(\xi_2,y,z) - Ts(\xi_1,y,z)}{\xi_2 - \xi_1} V_s(t_2 - t_1) + T(x,y,z,t_1) \qquad (3.24)$$

where $Ts(\xi_2, y, z)$ and $Ts(\xi_1, y, z)$ are the steady state temperatures at co-ordinates (ξ_2, y, z) and (ξ_1, y, z), respectively. $\xi_2 - \xi_1$ is the distance traveled by the arc in time (t_2-t_1), V_s is the welding speed, and $T(x,y,z,t_2)$ and $T(x,y,z,t_1)$ are the temperatures at times t_1 and t_2, respectively.

Table 3.1: Numerical parameters used in calculation of heat transfer and fluid flow for steel welds.

Steps		Step 1	Step 2	Step 3	Step 4
Number of iterations		200	50	50	300
Under-relaxation parameters	velocity	0.7	0.1	0.5	0.7
	pressure	0.6	0.6	0.6	0.7
	enthalpy	0.99	0.6	0.85	0.95
	latent heat	0.8	0.6	0.6	0.8
	turbulent kinetic energy	0	0.1	0.6	0.8
	dissipation rate of turbulent kinetic energy	0	0.1	0.6	0.8
	turbulent thermal diffusivity	0	0.8	0.8	0.8
	turbulent viscosity	0	0.3	0.3	0.3
Accuracy	SMAX	9.6×10^{-4}	1.6×10^{-2}	8.7×10^{-2}	1.0×10^{-3}
	RSMAX	7.8×10^{-3}	7.1×10^{-1}	1.5×10^{-1}	8.1×10^{-3}

Step 1: laminar calculation; Step2: turbulent calculation with very small underrelaxation parameters; Step3: turbulent calculation with intermediate underrelaxation parameters; Step4: turbulent calculation with large underrelaxation parameters.

Table 3.2: Parameters used in the heat transfer and fluid flow calculation for commercially pure titanium

Steps		Step 1	Step 2	Step 3	Step 4
Number of iterations		200	50	50	200
Under-relaxation parameters	velocity	0.7	0.1	0.5	0.7
	pressure	0.6	0.6	0.6	0.7
	enthalpy	0.99	0.6	0.85	0.95
	latent heat	0.8	0.6	0.6	0.8
	turbulent kinetic energy	0	0.1	0.6	0.8
	dissipation rate of turbulent kinetic energy	0	0.1	0.6	0.8
	turbulent thermal diffusivity	0	0.8	0.8	0.8
	turbulent viscosity	0	0.3	0.3	0.3
Accuracy	SMAX	6.2×10^{-4}	6.7×10^{-2}	8.3×10^{-2}	8.5×10^{-4}
	RSMAX	7.2×10^{-3}	2.1×10^{-1}	4.1×10^{-1}	9.8×10^{-3}

Step 1: laminar calculation; Step2: turbulent calculation with very small underrelaxation parameters; Step3: turbulent calculation with intermediate underrelaxation parameters; Step4: turbulent calculation with large underrelaxation parameters.

3.1.6 Modeling Finger Penetration in GMA Welding

The special weld geometry from GMA welding, "finger penetration", has been modeled in the present thesis. The metal droplets are responsible for the characteristic pool shape with "finger penetration". Depending on the welding conditions, the metal transfer mechanism can be roughly classified into three modes:[18] sub-threshold (<200 A), globular (200-250 A), and streaming (>250 A). The streaming mode is associated with a self-induced magnetic field, which exerts a strong radially constrictive force. This force suppresses the normal droplet mode and constricts the molten tip into a taper from which small droplets transfer at high frequency and velocity across the arc. The overheated metal droplets transfer their excess heat to the molten pool.

In the present study, the heat transfer from the metal droplets was simulated by considering the existence of a cylindrical volumetric heat source in the weld pool. This method was originally proposed by Lancaster[19] and then modified by Kumar et al.[20] The dimensions of the cylindrical volumetric heat source were calculated using the parameters such as the drop size, shape, velocity, and frequency. Fig. 3.5(a) and (b) schematically show the calculated cylindrical volumetric heat source in Lancaster's[19] and Kumar's[20] models, respectively. The depth of the cylindrical cavity resulting from the impact of the drops can be estimated from the following relation based on the conservation of energy:[19]

$$h = \left(-\frac{2\gamma}{a\rho g} + \sqrt{\left[\left(\frac{2\gamma}{a\rho g}\right)^2 + \frac{av_d^2}{6g}\right]}\right) \tag{3.25}$$

where h is the estimated depth of the cavity caused by the impact of metal droplets, γ is surface tension, ρ is the density of liquid metal, g is acceleration due to gravity, a is the diameter of the droplet, and vd is the droplet velocity.

The cavity tends to fill between the impingement of the two successive droplets. One method to approximate the time to fill the cavity (and hence the droplet rate required to maintain it) is to consider acceleration of a slug of liquid, equal in volume to that of the

cavity, into the weld pool. The effective depth can be calculated as (h-x), where x is the distance traveled by the center of mass of the slug, using the following expression based on the conservation of energy:[19]

$$x = \left(h + \frac{2\gamma}{a\rho h}\right)\left\{1 - \cos\left[\left(\frac{g}{h}\right)^{1/2} t\right]\right\}$$

(3.26)

According to Kumar et al.[20] the droplets mix completely in the weld pool below the cavity in a cylindrical region having both the radius and height equal to the diameter of drops. Thus, the effective depth of the volumetric heat source can be calculated as (h - x + a). where a is the droplet diameter. The diameter of the droplets was estimated using the following equation:[19]

$$R_d = \frac{\pi(R_d + R_e)}{1.25n^2\left(1 + \frac{\mu_0 I^2}{\pi^2(R_e + R_d)\gamma}\right)^{1/2}}$$

(3.27)

where R_d and R_e are the radius of the droplet and electrode. respectively. n is the ratio of the drop length and diameter. μ_0 is the permeability of free space. I is the current. and γ is the surface tension.
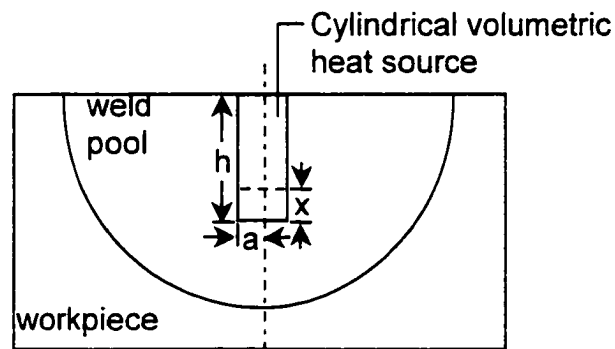
(a)
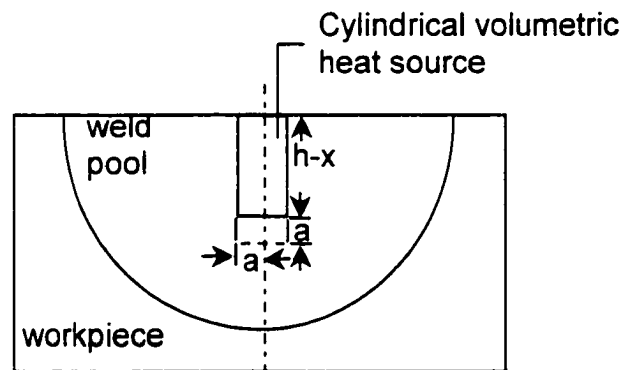
(b)

Fig. 3.5: Schematic of the models for heat input by transferring droplets: (a) Lancaster's model.[19] in which the effective length of the volumetric heat source is h-x: (b) Kumar's model.[20] in which the effective length is h-x+a. The symbol a is the diameter of the metal droplet. The values of h, x, and a can be obtained from equations (3.25), (3.26), and (3.27).

3.2 Three Dimensional Monte Carlo Grain Growth Simulation Model

In the present study, a 3D MC model has been developed to simulate grain growth in the whole HAZ around the weld pool by considering the spatial variations of temperature and thermal cycles in this region. Knowledge of the steep temperature gradient and the thermal cycles at various locations in the HAZ is critical for quantitative simulation of grain growth in this region. In the present investigation, the 3D MC model is coupled with the 3D turbulent model for grain growth simulation in the HAZ. The 3D turbulent model provides not only thermal cycles at various locations for simulation of grain growth but also the geometry of the HAZ, which is used to determine the domain for MC grain growth simulation.

3.2.1 Simulation of Grain Growth in Three Dimensions

The basic methodology for MC simulation of grain growth has been described in chapter 2 and not repeated here. In the present 3D MC model, the grains are mapped onto a discrete three dimensional grid system. Each of the grid points is assigned a random orientation number between 1 and Q, where Q is the total number of grain orientations. The value of Q is taken to be 48 in the present investigation, since it is known[8] that the grain growth exponent becomes almost independent of Q when its value is larger than 30. Values of the local interaction energy are calculated by considering a shell of 26 grid points consisting of the first (6 sites), second (12 sites), and third (8 sites) nearest neighbors, as shown in Fig. 3.6. The new attempted orientation is limited to one of the 26 nearest-neighbors rather than all possible orientations in the system. This is because the grain boundary migration only results from the process that atoms close to the grain

● Site considered ● First shell ● Second shell Third shell
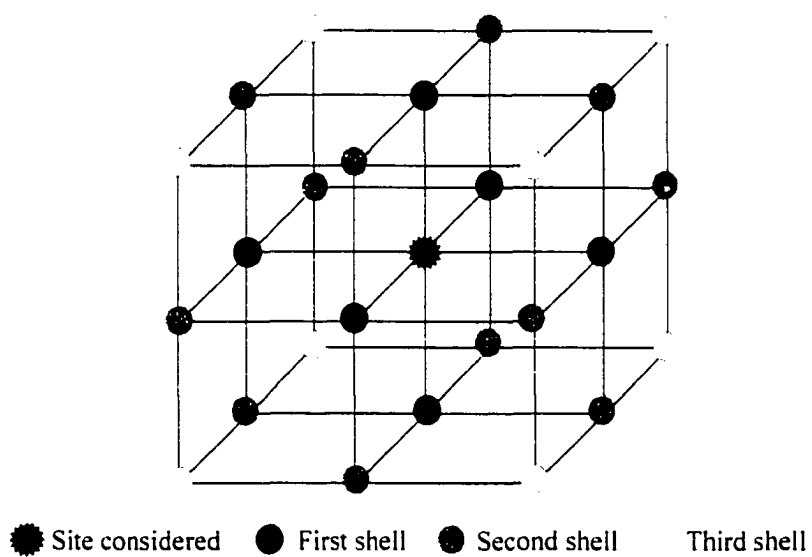
Fig. 3.6: The 26 neighbors in the three nearest shells.

boundary jump into the nearest grain interior. The soundness of this method has been justified in the literature.[9,10]

The grain boundary energy is specified by defining an interaction between the 1st, 2nd, and 3rd 26 nearest-neighbor lattice sites. The change of local interaction energy, ΔE, is the difference before and after the change of grain orientation. Based on equation (2.33), the vlaue of ΔE can thus be calculated as following:

$$\Delta E = J \sum_{i=1}^{26} \left(\delta_{S_i S_0} - \delta_{S_i S_n} \right)$$

(3.28)

where J is a positive constant which sets the scale of the grain boundary energy, δ is the Kronecker's delta function, S_0 is the original orientation number, S_i are the orientation numbers of its nearest neighbors, S_n is a new orientation number. The sum is taken over all 26 nearest neighbors. The kinetics of grain boundary migration are simulated by selecting a site randomly and changing its orientation to one of the nearest neighbor orientations based on energy change due to the attempted orientation change. Successful transitions at the grain boundaries to orientations of nearest neighbor grains thus corresponds to boundary migration.

3.2.2 Grain Growth Kinetics from MC Simulation under Isothermal Conditions

Before simulation of the grain growth under non-isothermal conditions. the dimensionless grain growth kinetics from the present 3D MC model under isothermal conditions needs to be established. As discussed in chapter 2, an empirical relation between the simulated grain size and the MC simulation time can be obtained from the MC simulation as following:

$$L = K_1 \times \lambda \times \left(t_{MCS} \right)^{n_1}$$

(3.29)

where L is the dimensionless simulated grain size measured by mean grain intercepts, λ is the discrete grid point spacing in the MC technique, t_{MCS} is the MC simulation time or the number of MC simulation iteration steps, and K_1 and n_1 are the model constants,

which are obtained by regression analysis of the data generated from MC simulation. The simulated grain growth kinetics described in equation (3.29) depends only on the grid system such as the dimensions (2D or 3D), the total number of grid points in the simulation domain, and the lattice type (triangular or square in 2D, simple cubic in 3D). The simulated grain growth kinetics is independent of material properties and temperature-time history. The simulated mean grain size (L) and the MC simulation time (t_{MCS}) in this equation are dimensionless quantities.

To apply the MC technique for grain growth simulation in the HAZ, an appropriate kinetic model is needed to relate the dimensionless quantities such as the Monte Carlo simulation step, t_{MCS}, and the grid spacing, λ, to the real time and grain size. Depending on the nature of the problem, different kinetic models[11] can be used to establish this relation. These kinetic models are the Atomistic Model, the Grain Boundary Migration (GBM) Model, and the Experimental Data Model (EDM). Detail description of these models has been presented in chapter 2 and are not be repeated here.

3.2.3 Application of MC Simulation Technique in the HAZ of Real Welds

The values of Monte Carlo simulation steps, t_{MCS}, at various locations in the HAZ are calculated by incorporation of the calculated thermal cycles from the 3D turbulent model into a selected kinetic model. For example, the Grain Boundary Migration (GBM) model[11] will be used in the present study to establish the relation between the t_{MCS} and the real time for simulation of grain growth in the HAZ of commercially pure titanium. The algorithm and the governing equation in the GBM model has been described in chapter 2. The values of t_{MCS} at various locations can be calculated by equation (2.42) by considering the effects of the thermal cycles and material properties. The higher the temperature or the longer the time period for grain growth at a site, the higher the value of t_{MCS} is expected at that site.

The t_{MCS} variation at different locations cannot be directly applied in the MC algorithm because the t_{MCS} is a measure of time in the MC algorithm. To solve this problem, a concept of site selection probability is used in the present model. The site selection probability varies depending on the time-temperature history at any given location. The larger the t_{MCS} at a site, the higher the corresponding site selection probability, $p(r)$:

$$p(r) = \frac{t_{MCS}}{t_{MCS}^{max}} \qquad (3.30)$$

where t_{MCS} is the MC simulation time at any site in the region and t_{MCS}^{max} is the maximum value of the MC simulation time in the computational domain. Both tMCS and t_{MCS}^{max} can be calculated from equation (2.42) from the calculated thermal cycles at the corresponding locations. The t_{MCS} variation can thus be transformed into the variation of site selection probability and applied in the 3D MC model.

In the present study, the selection of the domain for MC simulation of grain growth in the HAZ is based on the calculated temperature field from the 3D heat transfer and fluid flow model. In order to achieve efficient simulation of grain growth, two factors need to be considered in selecting the simulation domain. First, all the essential geometric features of the HAZ should be included in the simulated domain. On the other hand, the calculation domain should be kept as small as possible because simulation of grain growth in the whole HAZ region requires extensive calculations. Two domains in the weldment are selected in the present study. The first domain is selected as the dashed block shown in Fig. 3.7(a) to simulate real-time grain structure evolution in the HAZ around the weld pool. The second domain is selected as the thin dashed block shown in Fig. 3.7(b) to focus on simulation of the final grain structure in the HAZ. Assuming that the second domain moves from the heating edge of the HAZ to the cooling edge of the HAZ, the final grain structure in the HAZ can be simulated by considering the whole thermal history.
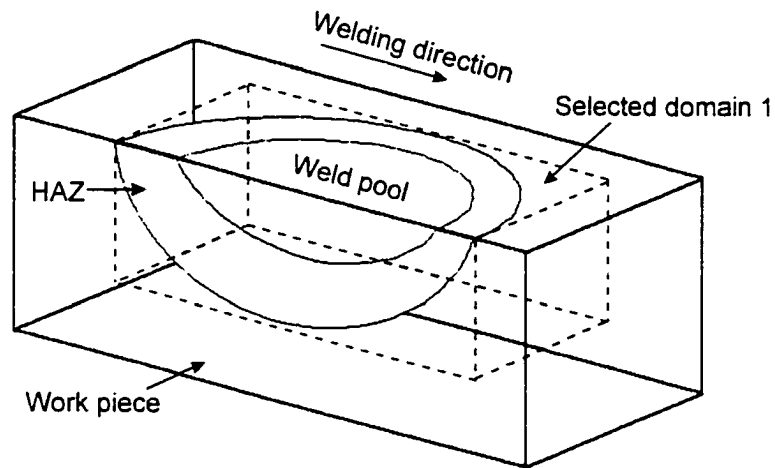
(a)
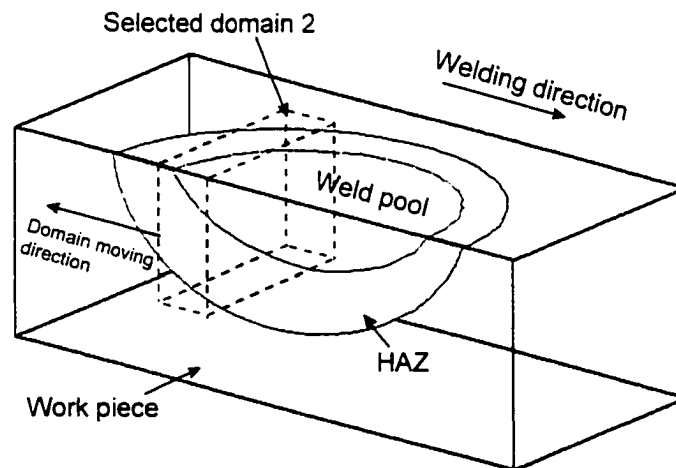
(b)

Fig. 3.7: simulated domains for MC grain growth simulation. (a) selected domain 1 for simulation of real time grain growth; (b) selected domain 2 for simulation of final grain structure in the HAZ.

3.2.4 Numerical Scheme

First, the MC simulation time, t_{MCS}, and the corresponding site selection probability, Pr, at various locations in the HAZ are calculated by equation (2.42) and equation (3.30), respectively. As discussed in the previous section, the effect of the temperature-time history and the material properties on the grain growth in the HAZ are eventually considered in the simulation by various values of Pr at different locations. After the site selection probability at each site in the HAZ is determined, the Monte Carlo simulation algorithm is than used to simulate grain growth. Fig. 3.8 shows the flow chart of the simulation procedure in the present 3D Monte Carlo model. A brief description of each step is given here. The variables used in Fig. 3.8 are indicated within brackets.

(1) The important variables necessary to run the MC model are defined first. These variables include the maximum number of grid points in the x, y, and z directions (imax, jmax, kmax), the total orientation number (iqmax), the value of J/kBT (ajkt) used for calculating the probability when the interaction energy change is positive, total Monte Carlo simulation steps or time (imcmax), and the spacing of the intercept used for measuring mean grain size (ispace).

(2) The values of the orientation transition probability at different positive energy levels are evaluated by the Boltzmann-type probability ($P= exp(-\Delta E/kBT)$). The higher the positive energy level, the lower the value of orientation transition probability. Since 26 neighbors are considered in the present 3D model, there are totally 26 possible positive energy levels.

(3) The site selection probability at each site of the simulation domain is defined. The selection probability at each site is determined from its time-temperature history. The higher the peak temperature and the longer the time for grain growth at a site, the higher the value of the site selection probability at that site. In this manner, the time-temperature dependent grain growth kinetics is incorporated in the MC simulation.

(4) A random orientation between 1 and iqmax is assigned to each site.

(5) After all initial definitions, the simulation of grain growth begins. A site (ix,iy,iz) is randomly selected and its orientation is noted as ior0.

(6) The 26 nearest neighbors of the selected site are located, and their corresponding orientations are determined.

(7) After knowing the orientations of the 26 neighbors, the local interaction energy before reorientation (E0) is calculated by equation (2.32) for isotropic grain boundary.

(8) Randomly pick up a site from the 26 neighbors and note its orientation as ior2.

(9) Calculate the local energy after the attempted reorientation (E1) from equation (2.32) if isotropic grain boundary is considered. At this time, the original orientation (ior0) used for Si in equation (2.32) is replaced by the randomly picked new orientation (ior2).

(10) The change of energy due to the attempted reorientation is calculated by subtracting E1 by E0. If the change of energy is less or equal to zero, the orientation change from ior0 to ior2 is accepted. Otherwise, the reorientation can only be accepted with a probability. The value of this probability is determined by its positive energy level using equation (3.28).

(11) During each MC step, the number of randomly selected site should equal to the number of the total grid points in the simulated domain. If the number of the selected site is less than the number of the total grid points, the procedure from step (5) to step (10) will be repeated. Otherwise, the value of the MC step will be updated by adding 1.

(12) The mean grain size change were calculated after a certain predetermined number of MC steps.

(13) The simulation of grain growth is terminated when the number of MC step reaches the total MC steps (imcmax).

(14) The orientation at each site is written in a file for grain structure visualization.

Input data (imax,jmax,kmax,iqmax,ajkt,imcmax,ispace)

Define transition probability for different positive interaction energy levels

Evaluate the probability for selecting a site based on time-temperature history of the site

Assign a random orientation (1~iqmax) to each site

One MC step

Count MC time steps (i)

Randomly select a point (ix,iy,iz) in the lattice and note its orientation as ior0

Find nearest neighbors of the selected site

Calculate local interaction energy before reorientation (E0)

Randomly pick up a site from the neighbors and note its orientation as ior2

Calculate local interaction energy (E1) after the attempted reorientation ior2

Yes   E1-E0<=0 ?   No

Change initial orientation (ior0) to the attempted orientation (ior2)

Accept the reorientation with a probability (p)

Yes   Number of sites visited < imax*jmax*kmax

No

Calculate mean gain size every sveral MC steps

i>imcmax ?   No

Yes

Write orientation values in a file for visualization

End

Fig.3.8: Flow chart of the 3D MC model.

3.3 Models for Calculation of Phase Transformations

3.3.1 Calculation of Phase Transformations in the Weld Metal of Low Alloy Steels

The final weld metal microstructure in low alloy steels is dominantly determined by the austenite decomposition process within the temperature range 1073 to 773 K. During cooling of the weld metal, allotriomorphic ferrite is the first phase to form from the decomposition of austenite in low alloy steels. It nucleates at the austenite grain boundaries and grows by a diffusional mechanism. As the temperature decreases, diffusion becomes sluggish and displacive transformation is kinetically favored. At relatively low undercoolings, plates of Widmanstatten ferrite forms by a displacive mechanism. At further undercoolings, bainite nucleates by the same mechanism as Widmanstatten ferrite and grows in the form of sheaves of small platelets. Acicular ferrite nucleates intragranularly at inclusions and is assumed to grow by the same mechanism as bainite in the present model.[12-14]

In the present study, Bhadeshia's phase transformation model[12-14] was coupled with the thermal cycles from the 3D heat transfer and fluid flow model to predict the evolution of microstructure in the fusion zone of low alloy steels. The principles and algorithms of the phase transformation model[12-14] have been described in detail in section 2.2.3 of chapter 2 and are not repeated here. From the phase transformation model, the Time-Temperature-Transformation (TTT) diagrams were calculated by equation (2.19). The calculated TTT diagrams can then be transformed to Continuous-Cooling-Transformation (CCT) diagrams based on Scheil's additive rule as given by equation (2.20).

In the original model, the cooling rate within the austenite decomposition temperature range, i.e. from 1073 K to 773 K, in the weld metal of low alloy steels was previously calculated using an empirical equation. The disadvantage of using this empirical equation has been discussed in chapter 2. In the present investigation, the cooling rates for phase transformation calculation were calculated from the quasi-steady temperature field predicted by the 3D turbulent heat transfer and fluid flow model, as

given by equation (3.24). The phase transformations during austenite decomposition in the weld metal of low alloy steels can thus be calculated from fundamental principles by the coupling of the phase transformation model with the heat transfer and fluid flow model.

In the present thesis, the weld metal microstructural evolution in two types of steels, i.e. HSLA-100 steel and C-Mn steeels, were predicted by the model. The effect of chemical composition on the phase transformations in the weld metal were explained by the calculated TTT diagrams. The predicted CCT diagrams for both types of steels were used to understand the weld metal microstructural evolution during continuous cooling. The phase volume fractions in the weld metal of C-Mn steels with different chemical compositions were calculated.

3.3.2 Calculation of Overall Phase Transformation Kinetics

For low alloy steels, some phase transformation models are available for prediction of the microstructure in the FZ and the HAZ. However, adequate kinetic models are not available to calculate phase transformations in many other metal/alloy systems. Under these conditions, the overall phase transformation kinetics can be described by the Johnson-Mehl-Avrami (JMA) equation.[15,16] The JMA equation was originally proposed to describe the isothermal phase transformation kinetics of reactions controlled by the nucleation and growth mechanism. The JMA equation under isothermal conditions can be expressed as:[17]

$$f = 1 - \exp\{-[k(T)(t - t_0)]^n\} \tag{3.31}$$

where f is the transformed phase volume fractions, $k(T)$ is a temperature dependent constant, t is the time, t_0 is the initial time for transformation, and n is a numerical exponent whose value is determined by the nucleation mode and the dimensions for growth. It is a constant independent of temperature, provided there is no change in the

nucleation mechanism. However, k(T) depends on both the nucleation and growth rates, and is therefore highly sensitive to temperature:[17]

$$k(T) = k_0 \times \exp\left(-\frac{\Delta G(T)}{k_B T}\right) \qquad (3.32)$$

where $\Delta G(T)$ is the total activation energy for nucleation and growth, and k_0 is a pre-exponential constant. Since heterogeneous nucleation is assumed in the JMA equation, the values of k(T), $\Delta G(T)$ and k_0 are usually determined by isothermal experiments.

During welding processes, phase transformations occur under the condition of continuous heating and cooling. The JMA equation can be modified for the non-isothermal kinetics.[17] The proposed method used the discretization of the time dependence of the temperature. i.e. approximation of the continuous temperature-time curves by many isothermal steps, each of them obeying the isothermal JMA-kinetics. The detailed procedure to derive the modified JMA equation is available in the literature.[17] The final expression for the transformed fraction obtained from m subsequent isothermal steps can be expressed as: [17]

$$f(t(T)) = 1 - \exp\left\{-\left[\sum_{l=0}^{m-1} k(T_0 + l\Delta T)\Delta t\right]^n\right\} \qquad (3.33)$$

where f(t(T)) stands for the transformed phase fraction under non-isothermal conditions. Δt is the time step. ΔT is the temperature change corresponding to each Δt, T_0 is the initial temperature. k is a temperature dependent constant. and m is the total number of the subsequent isothermal steps. In order to use equation (3.33), the temperature dependence of the transformation rate k(T) and the exponent n have to be specified.

In the present investigation, the modified JMA equation will be used to calculate the overall phase transformation kinetics of the $\alpha \rightarrow \beta$ transition in commercially pure titanium. The extents of the $\alpha \rightarrow \beta$ transition at various locations in the HAZ will be predicted by incorporating of the corresponding calculated thermal cycles into the modified JMA equation.

3.4 Modeling Procedure

To systematically predict weldment macro and microstructures, the mathematical models described in the previous three sections need to be coupled. Fig. 3.9 shows the flow chart of the integration of these models. Starting from the calculation heat transfer and fluid flow in the weld pool, the temperature and velocity fields and the thermal cycles can be obtained. From the calculated temperature fields, the geometries of the FZ and the HAZ can be predicted. By coupling the calculated thermal cycles with the phase transformation models and the 3D MC model, the microstructural evolution, i.e. the change of phase volume fractions and grain size, can be predicted.

The 3D turbulent heat transfer and fluid flow model can be adjusted for different welding processes and different materials by changing the welding parameters, boundary conditions, and the thermo-physical properties of material. Similarly, the 3D MC model can be applied for different materials as long as the physical properties necessary for the grain growth calculations are known. The phase transformation model may need to change depending on the material investigated.

To check the capability of the mathematical models, these models will be applied to predict the weldment macro and microstructures in different materials under various welding conditions in the next two chapters. The predicted results will be compared with the corresponding experimental results.
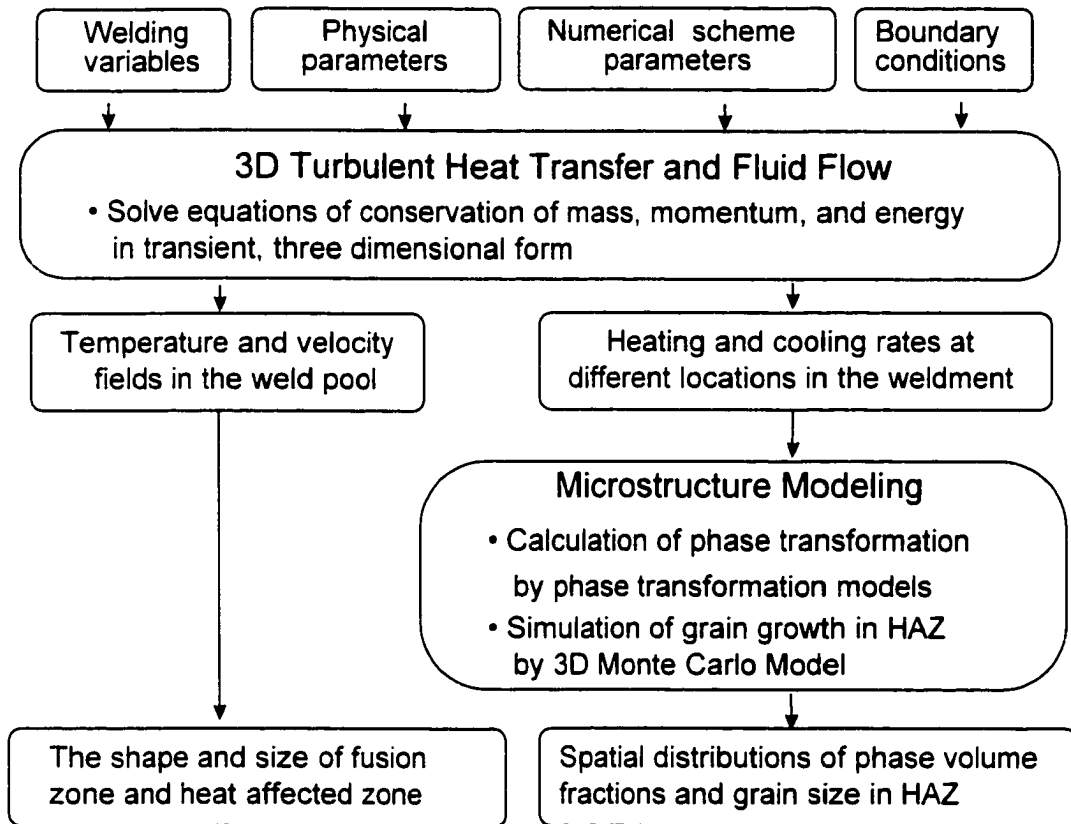
Fig. 3.9: Flow chart of the modeling approach.

3.5 References

1. K. Mundra, T. DebRoy, and K. Kelkar: *Numerical Heat Transfer*, Part A, **29**, 115 (1996).

2. B. E. Launder and B. D. Spalding: *Mathematical Models of Turbulence*, Academic Press, New York, N.Y, 1972.

3. T. Zacharia, S. A. David, J. M. Vitek, and T. DebRoy:. *Metall. Trans. B.*, **21B**, 600 (1990).

4. C. Chan, J. Mazumder, and M .M. Chen: *Metall. Trans. A*, **15A**, 2175 (1984).

5. Innovative Research, Inc.. Documentation of COMPACT-3D Version 3.1. Minneapolis, Minnesota (1994).

6. W. M. Pun and D. B. Spalding: *Heat Transfer Section Report*, No. HTS/76/2, Imperial College London, 1976.

7. S. V. Patanker: Numerical Heat Transfer and Fluid Flow, Hemisphere, New York (1980).

8. M. P. Anderson, D. J. Srolovitz, G. S. Grest, and P. S. Sahni: *Acta Metall.*, **32**, 783 (1984).

9. B. Radhakkrishnan and T. Zacharia: *Metall. Mater. Trans. A*, **26A**, 167 (1995).

10. X. Song and G. Liu: *Scripta Materialia*, **38**, 1691 (1998).

11. J. Gao and R. G. Thompson: *Acta Metall.*, 1996, vol. 44, pp. 4565-4570.

12. H. K. D. H. Bhadeshia and L. -E. Svensson: in *Mathematical Modeling of Weld Phenomena*, ed. by H. Cerjak and K.E. Easterling, p. 109, Institute of Materials (1993)..

13. H. K. D. H. Bhadeshia: in *'Recent Trends in Welding Science and Technology'*, ed. by S. A. David and J. M. Vitek, p. 189, ASM INTERNATIONAL, Materials Park, OH (1990).

14. H. K. D. H. Bhadeshia, L. -E. Svensson, and B. Gretoft: *Acta metall.*, **33**, 1271 (1985).

15. W. A. Johnson and R. F. Mehl: *Trans. Am. Inst. Min. Engs.*, **135**, 416 (1939).

16. M. Avrami: *J. Chem Phys.*, **9**, 177 (1941).

17. P. Kruger: *J. Phys. Chem. Solids*, **54**, 1549 (1993).

18. D. N. Shackleton and W. Lucas: *Weld. J.*, **53**, 537s (1974)..

19. J. F. Lancaster: *The Physics of Welding*, Pergamon Press, New York, NY (1984).

20. S. Kumar and S. C. Bhaduri: *Metall. Trans. B*, **25B**, 435 (1994).

21. L.-E. Svensson, B. Gretoft, Svensson, and H. K. D. H. Bhadeshia: *Scand. J. Metallurgy*, **15**, 97 (1986).

CHAPTER 4

PREDICTION OF MACRO AND MICROSTRUCTURES
IN HSLA-100 AND C-Mn STEEL WELD METALS

In this chapter, the macro and microstructures in the weld metal of low alloy steels are modeled. In particular, two types of steels, i.e. HSLA-100 steel and C-Mn steel, are investigated. The HSLA-100 steel has a good combination of strength, toughness, and weldability. In the past decade, some investigations have been undertaken on the welding of this steel[1-4] or steels with similar composition.[5-8] However, most of previous studies focused on characterization of the microstructures in the weldment. In contrast, very little effort has been made to understand the evolution of the weld metal microstructures from fundamental theories. The purpose of this study is to understand the macro and microstructural evolution in this steel based on mathematical modeling from the fundamentals of transport phenomena and phase transformation theory. Specifically, the special weld geometry from GMA welding, "finger penetration", and the effect of cooling rate on the microstructure in this steel are investigated. The predicted shape and size of the FZ and the HAZ, cooling rates, and the phases present in the weld metal are compared with corresponding experimental results.

The C-Mn steel is selected in this study to examine the capability of the model for quantitative prediction of microstructure in the weld metal. Specially, the effect of chemical composition on the weld metal microstructure is predicted and the phase volume fractions are quantitatively calculated. Since sufficient experimental data[9-11] are available for C-Mn steel, no experiments were conducted in the present study for this steel. In the present investigation, the welding conditions, chemical composition, and the phase volume fractions in the weld metal for C-Mn steel were adopted from experimental work by Svensson and Gretoft.[9]

4.1 Macro and Microstructures in the Weld Metal of HSLA-100 Steel

4.1.1 Experimental Procedures

The HSLA-100 steel welds were made by Blackburn at the Naval Surface Warfare Center. Bead-on-plate welds were deposited using the gas-metal-arc (GMA) welding with 95% argon - 5% carbon dioxide shielding gas at a flow rate of 50 cubic feet per hour. The electrode wire with a diameter of 1.6 mm was fed at a rate of 122 mm/s. Welds were fabricated on 2 inch thick HSLA-100 steel plates at 405 A and 31.3 V. Different cooling rates were obtained by changing the welding velocity and keeping the other variables constant. The temperature of weld metal was measured by Chromel-Alumel thermocouples, which were plunged into the trail of the solidifying weld pool. The cooling rates were determined from the slope of the temperature versus time plots. The welding parameters are shown in Table 4.1.

Table 4.1: Welding process parameters for HSLA-100 steel

GMA. Current: 405A. Voltage: 31.3V, no preheat.

Weld No.	Welding Velocity (mm/sec)	Heat Input (kJ/mm)
1	3.22	3.94
2	4.02	3.15
3	5.29	2.40

* Shielding gas: 95% argon - 5% carbon dioxide, flow rate: 50 cubic feet per hour, and electrode wire was fed rate: 122 mm/s.

The chemical compositions of the HSLA-100 plate and the welding wire were provided by Naval Surface Warfare Center. The chemical compositions of the HSLA-100 plate and the welding wire are listed in Table 4.2. The chemical compositions of the weld metals were determined at Penn State using the spectrometric method with the exception of oxygen and nitrogen, which were determined by vacuum fusion analysis. The weld metal compositions for different welding conditions are given in Table 4.3. The specimens for microstructure examination were initially etched with a 4% aqueous picric

Table 4.2: Compositions of HSLA-100 steel plate and the welding wire (in wt%)

	HSLA -100 plate	Welding wire
C	0.034	0.075
Mn	1.18	1.38
Si	0.25	0.32
Ni	3.51	1.80
Mo	0.18	0.33
Cr	0.047	0.11
Cu	1.25	0.011
Al	0.035	0.004
Ti	0.01	0.021
V	0.001	<0.002
Nb	0.039	0.001
B	<0.005	0.003
O	0.0009	0.012
N	0.005	0.0078
P	0.008	<0.002
S	0.002	0.002

Table 4.3: Weld bead compositions of HSLA-100 steel (in wt%)

Weld No.	1	2	3
C	0.045	0.050	0.039
Mn	1.07	1.07	1.09
Si	0.21	0.20	0.20
Ni	2.36	2.28	2.31
Mo	0.22	0.24	0.24
Cr	0.069	0.063	0.068
Cu	0.69	0.79	0.72
Al	0.015	0.019	0.017
Ti	0.013	0.011	0.010
V	0.001	0.001	0.001
Nb	0.019	0.020	0.016
B	0.0010	0.0016	<0.0005
O	0.032	0.031	0.025
N	0.015	0.018	0.012
P	<0.004	0.006	0.008
S	0.001	0.002	<0.001

acid solution, followed by a Nital solution (2.5% nitric acid dissolved in amyl alcohol). The microstructures obtained under different welding conditions were examined using both optical microscopy and scanning electron microscopy (SEM). Energy-dispersive spectrometry (EDS) was used to qualitatively analyze the major elements in the inclusion particles in the weld metal.

4.1.2 Mathematical Modeling

The 3D turbulent heat transfer and fluid flow model was used for the calculation of the temperature and velocity fields, the geometries of the FZ and the HAZ, and the thermal cycles. The thermophysical data used for the calculation of the fluid flow and heat transfer for HSLA-100 steel are presented in Table 4.4. The calculated thermal cycles

Table 4.4: Data used for the calculation of velocity and temperature fields in HSLA-100 steel welds[40,41]

Physical property	value
Liquidus temperature (K)	1782
Solidus temperature (K)	1742
Density of liquid metal (kg/m3)	7200
Viscosity of liquid (kg/m.s)	6.0×10^{-3}
Thermal conductivity of solid (J/m.s.K)	27.1
Thermal conductivity of liquid (J/m.s.K)	83.6
Specific heat of solid (J/kg.K)	702.0
Specific heat of liquid (J/kg.K)	806.7
Latent heat of melting (J/kg)	267.6×10^3
Temperature coefficient of surface tension (N/m.K)	-0.43×10^{-3}
Coefficient of thermal expansion (1/K)	1.0×10^{-5}
Enthalpy of segregation (J/mol)	-1.66×10^6

were coupled with a phase transformation model[12-14] to predict the microstructure in the weld metal. The special weld geometry from GMA welding, "finger penetration", was modeled by inserting a cylinder volumetric heat source in the weld pool. This algorithm has been described in detail in section 3.1.6. The data used for the calculation of the volumetric heat source under the present welding conditions are given in Table 4.5. The calculated dimensions of the cylindrical volumetric heat source using equations (3.25) and (3.26) in chapter 3 are given in Table 4.6.

Table 4.5: Data used for the calculation of the volumetric heat source

γ surface tension	1.2 N/m
ρ density of liquid metal	7200 kg/m^3
g acceleration of gravity	9.8 m/s^2
a diameter of droplet	2R$_d$
v_d droplet velocity	5.5 m/s
R$_e$ radius of electrode	1.6 x 10^{-3} m
n ratio of the droplet length and diameter	3.5 (estimated)
μ_0 the permeability of free space	1.257 x 10^{-6} henry/m
I current	405 A
t time interval between two successive drops	1/840 (s)

* R$_d$ is the radius of the droplet, which can be estimated using equation 3.27.

Table 4.6: The calculated dimensions of cylindrical volumtric heat source

Welding parameters								Volumetric heat dimensions	
Voltage (V)	Current (A)	Wire feed rate (mm/s)	Wire diameter (mm)	Drop radius (mm)	Drop velocity (m/s)	Drop frequency (per sec)	h-x (mm)	Radius (mm)	Height (mm)
31	405	112	1.6	0.4	5.5	840	4.6	0.8	5.4

The total energy absorbed by the workpiece in the GMA welding process consists of two parts: energy transfer from the arc and energy transported from the metal droplets. The former is the product of the voltage, current, and the efficiency of the process (approximately 8873 J/s). The energy transported by the droplets was assumed to be uniformly distributed in the cylindrical cavity. Under the conditions of the present experiments, the droplets carry an energy of 2050kJ/Kg at a temperature[18] of 2673K. From the wire feed rate and the diameter of the wire, the volume of the metal droplets is estimated to be 22.5×10^{-8} m^3/s corresponding to a droplet delivering rate of 1.73×10^{-3} kg/s. Thus the energy transported by the metal droplets is approximately 3550 J/s, which accounts about 40% of the total energy absorbed by the workpiece. This amount is comparable with the values reported by Mundra et al.[37]

4.1.3 Results and Discussions

4.1.3.1 Temperature and Velocity Fields

Fig. 4.1 shows the computed temperature and velocity fields in three dimensions for the HSLA-100 steel welds from GMA welding. The thermophysical data used for the calculation of the fluid flow and heat transfer for HSLA-100 steel are presented in Table 4.4. In this figure the temperature field is indicated by contour lines, and the velocity field is represented by the arrows. The general features of the calculated temperature field are consistent with the results reported in the literature.[19] In front of the heat source, the temperature gradient is greater than that behind the heat source. The high temperature gradient results in slightly greater liquid metal velocities in front of the heat source than behind the heat source. On the surface of the weld pool, the liquid metal moves from the center to the periphery. This is expected for a metal with a very low concentration of surface active elements (e.g. low sulphur and free oxygen contents) which results in a negative temperature coefficient[20] of surface tension $d\gamma/dT$. The peak temperatures and maximum velocities calculated from the calculations are given in Table 4.7.
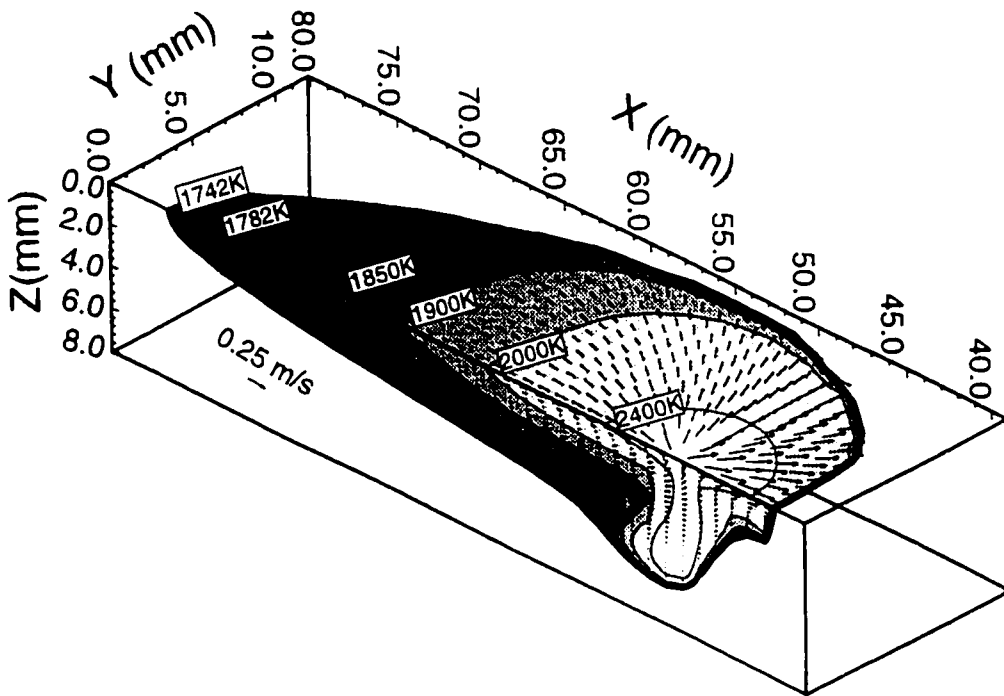
Fig. 4.1: Calculated temperature and velocity fields in weld 3 of HSLA-100 steel. Welding conditions: GMA, 405 A, 31.3 V, 5.29 mm/s, no preheat. Other welding parameters are given in Table 4.1.

Table 4.7: Calculated peak temperatures and maximum velocities for HSLA-100 steel from GMA welding

Weld #	Tpeak (K)	Umax (cm/s)	Vmax (cm/s)	Wmax (cm/s)
1	3007	49.6	53.5	12.5
2	2810	45.8	50.6	11.2
3	2723	43.3	45.8	10.8

* Symbols Tpeak. Umax. Vmax. and Wmax represent the peak temperature and the maximum velocities in x, y. and z directions. respectively.

The distributions of turbulent viscosity, thermal conductivity, kinetic energy, and dissipation rate in the weld pool are shown in Fig. 4.2. These quantities are affected by the fluid motion in the weld pool. It can be observed that the maximum values of these variables lie in the middle of the weld pool. and that the values decrease progressively from the center to the periphery. This is expected since the circulation of the molten metal is most intense near the surface and the level of turbulence decreases progressively as the fluid approaches the solid surface. A very thin layer known as a "laminar sublayer" exists near the solid surface. in which the role of turbulence is negligible and the laminar flow dominates. The maximum dimensionless viscosity (μ_t/μ) and thermal conductivity (k_t/k) values were found to be 18 and 4.5. respectively. The calculated dimensionless viscosity (μ_t/μ) and thermal conductivity (k_t/k) values as well as their spatial distribution patterns are comparable with those reported in the literature.[21,22] Compared to unity, the values of these ratios are very high, which indicates that the dissipations of heat and momentum in the weld pool are significantly aided by turbulence. In most previous research on the simulation of heat transfer and fluid flow in the weld pool, the viscosity and thermal conductivity values were arbitrarily enhanced by a constant factor. The computed turbulent viscosity and thermal conductivity values presented here clearly show that these quantities vary strongly depending on the location within the weld pool.
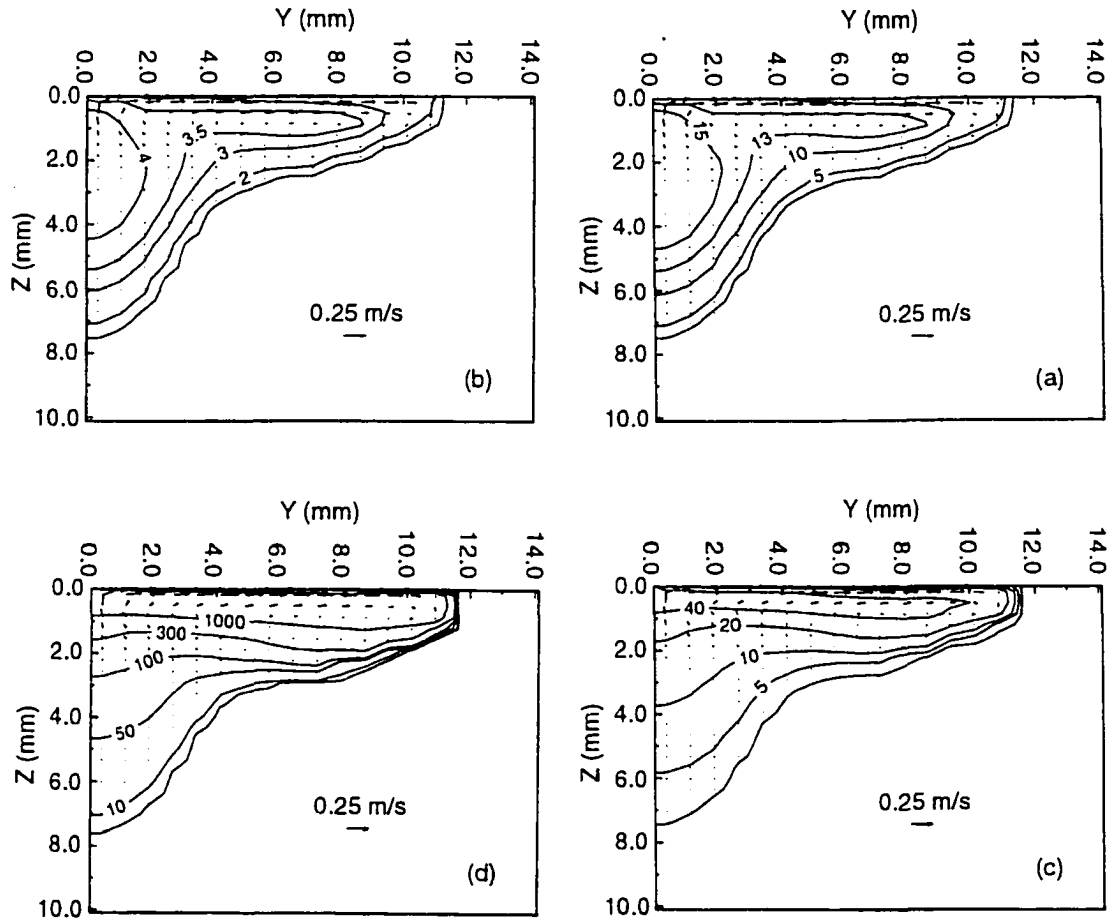
Fig. 4.2: Distribution of turbulent variables in the weld pool of weld 1. (a) dimensionless viscosity, μ_t/μ; (b) dimensionless thermal conductivity, k_t/k; (c) turbulent kinetic energy $(m^2/s^2 \times 10^{-4})$; (d) dissipation rate of turbulent kinetic energy $(m^2/s^3 \times 10^{-4})$. Welding conditions: GMA, 405 A, 31.3 V, 3.22 mm/s, no preheat. Other welding parameters are given in Table 4.1.

Therefore. accurate calculations of temperature and velocity fields must utilize an appropriate turbulence model.

4.1.3.2 Geometry of the FZ and the HAZ

The geometry of the fusion zone (FZ). mushy zone, and heat-affected zone (HAZ) can be predicted from the calculated temperature field as shown in Fig. 4.3. The boundary of the FZ is determined by the liquidus temperature (1782K). The mushy zone is the region between the liquidus and solidus temperatures. i.e., 1782K and 1742K. respectively. The geometry of the HAZ can also be determined from the eutectoid temperature (Ae1). which is known to be about 873K for HSLA-100 steel.[23] From Fig. 4.3. it is observed that the width of the FZ. the depth of the "finger" penetration. and the shapes of both the FZ and the HAZ predicted by the model agreed well with the corresponding experimental results. As the welding velocity increases. the heat input per unit length decreases. Therefore. the depth of "finger penetration" and the width of the FZ decrease as the welding velocity increases. As a consequence of the "finger" penetration in the fusion zone. the shape of HAZ in GMAW weld also exhibits specific features. In the middle of the weld pool. a "finger" shape was formed. On the surface of the weld pool. the liquid metal flows outward. which resulted a wide and shallow weld pool if no "finger penetration" existed. In combination. the weld pool is wide on the surface and deep in the middle part. Consequently. the middle part of the HAZ is much thicker than those at top and bottom parts.

Both the calculated and experimental fusion zone and HAZ dimensions are presented in Table 4.8. Since the shape of the HAZ in GMAW weld is irregular, measurements of the widths at the top (W_T), middle (W_M), and bottom (W_B) of the HAZ were compared with the corresponding theoretically calculated values in Table 4.8. The symbols W_T, W_M, and W_B are defined in Fig. 4.3. From Table 4.8, it is observed that the differences between the calculated and experimental sizes are small. The agreement between the calculated and experimental geometry indicates that the geometric features of the fusion zone and HAZ in GMAW welds can be satisfactorily calculated from the model.
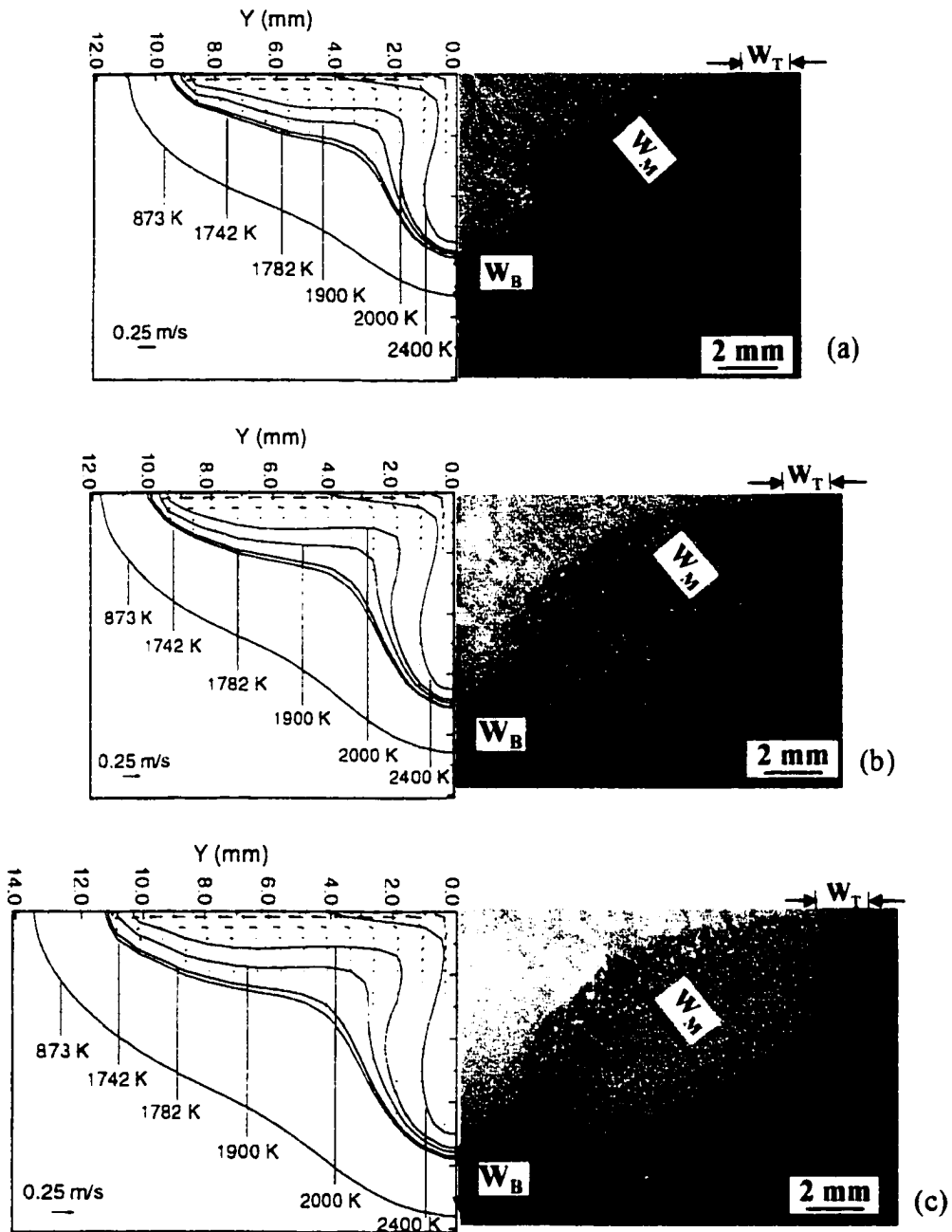
Fig. 4.3: Comparison of the calculated and experimental geometry of the FZ and the HAZ. (a) weld 3: 2.4 kJ/mm; (b) weld 2: 3.15 kJ/mm; (c) weld 1: 3.94 kJ/mm. Symbols W_T, W_M, and W_B are the widths at the top, middle, and bottom of the HAZ. Welding conditions are presented in Table 4.1.

Table 4.8: Comparison of the calculated and experimental FZ and HAZ dimensions

Zone	Weld No.	Dimension	Experimental results (mm)**	Calculated results (mm)
FZ	Weld 1	width	21.8 + 1.2	23.0
		depth	7.3 + 1.6	7.8
	Weld 2	width	20.8 + 1.4	21.9
		depth	7.0 + 1.1	7.2
	Weld 3	width	18.0 + 1.3	19.1
		depth	6.0 + 1.1	6.3
HAZ	Weld 1	WT	1.8 + 0.3	2.1
		WM	4.7 + 0.4	4.0
		WB	1.6 + 0.2	1.8
	Weld 2	WT	1.6 + 0.2	1.7
		WM	4.0 + 0.3	3.4
		WB	1.4 + 0.1	1.5
	Weld 3	WT	1.5 + 0.2	1.5
		WM	3.5 + 0.3	3.0
		WB	1.1 + 0.1	1.2

* W_T, W_M, and W_B are the widths at the top, middle, and bottom of the HAZ as indicated in Fig. 4.3.

** Three cross sections were measured for each weld.

In the present study, the boundary condition for turbulent kinetic energy, K, on the top surface of weld pool was assumed to 5% of the mean kinetic energy, which was based on the value in the literature for calculations of flow system with free surface.[38] The magnitude of turbulent kinetic energy on the free surface is around this value. To check the variation of turbulent kinetic energy at the top surface of the weld pool on the final calculated results, another set of computation was made, in which the top boundary condition for K was set by taking 2.5% of the mean kinetic energy. The computed results obtained by assuming 2.5% and 5% of the mean kinetic energy were compared in Table 4.9. It was found that the differences in the calculated results for these two cases were very small. Since small variation of the turbulent kinetic energy at the top surface did not cause significant change in the calculated results, 5% of the mean kinetic energy was taken for the calculations in all the GMA welds in the present study.

Table 4.9: Comparison of the calculated results by assuming different turbulent kinetic energies (5% and 2.5% of mean kinetic energy) on the top surface in the weld pool of weld 3

		2.5% of mean kinetic energy	5.0% of mean kinetic energy	Difference (%)
Temperature and velocity fields	Tpeak (K)	2761	2723	1.3
	Umax (mm/s)	44.2	43.3	2.0
	Vmax (mm/s)	46.4	45.8	1.3
	Wmax (mm/s)	10.9	10.8	1.0
Geometry	Depth (mm)	6.2	6.3	1.6
	Width (mm)	19.2	19.1	0.5
	Length	34.5	34.3	0.6

* Symbols Tpeak, Umax, Vmax, and Wmax represent the peak temperature and the maximum velocities in x, y, and z directions, respectively.

4.1.3.3 Thermal Cycles

The calculated thermal cycles at different locations are shown in Fig. 4.4. The final microstructure is affected by the cooling rate within the austenite decomposition temperature range, which is usually between 1073K and 773K for low alloy steels. It has been proven that the cooling rate in the fusion zone is almost independent of position at temperatures well below the melting point.[24] Thus, the cooling curve at location b in Fig. 4.4 was chosen, and the corresponding cooling rate between 1073K and 773K was taken as the average cooling rate in the fusion zone. The calculated cooling rates for different welding conditions in the temperature range between 1073K and 773K are compared with the experimental cooling curves in Fig. 4.5. The solid and dashed lines represent the experimental and the calculated cooling curves, respectively. The calculated average cooling rates from a temperature of 1073K to 773K were found to be 18.2K/s, 22.2K/s, and 28.6K/s for welds 1, 2, and 3, respectively between 1073 and 773K. The computed times necessary for cooling from 1073K to 773K were found to be 16.5, 13.5, and 10.5 seconds for welds 1, 2, and 3, respectively. The corresponding experimental values for
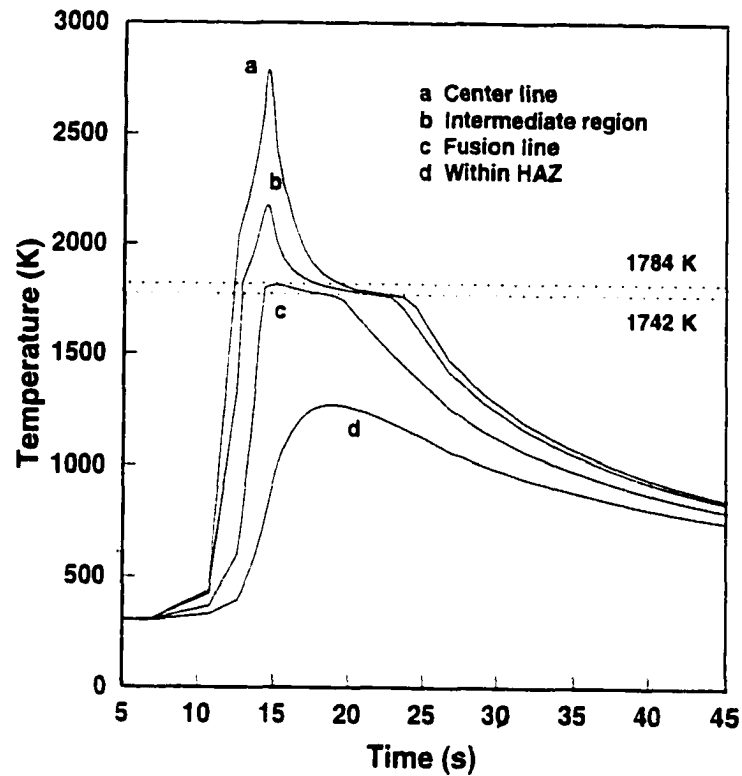
Fig. 4.4: Thermal cycles at different locations of weld 1. Welding conditions:
GMA, 405 A, 31.3 V, 3.22 mm/s, no preheat. Other welding parameters are
given in Table 4.1.
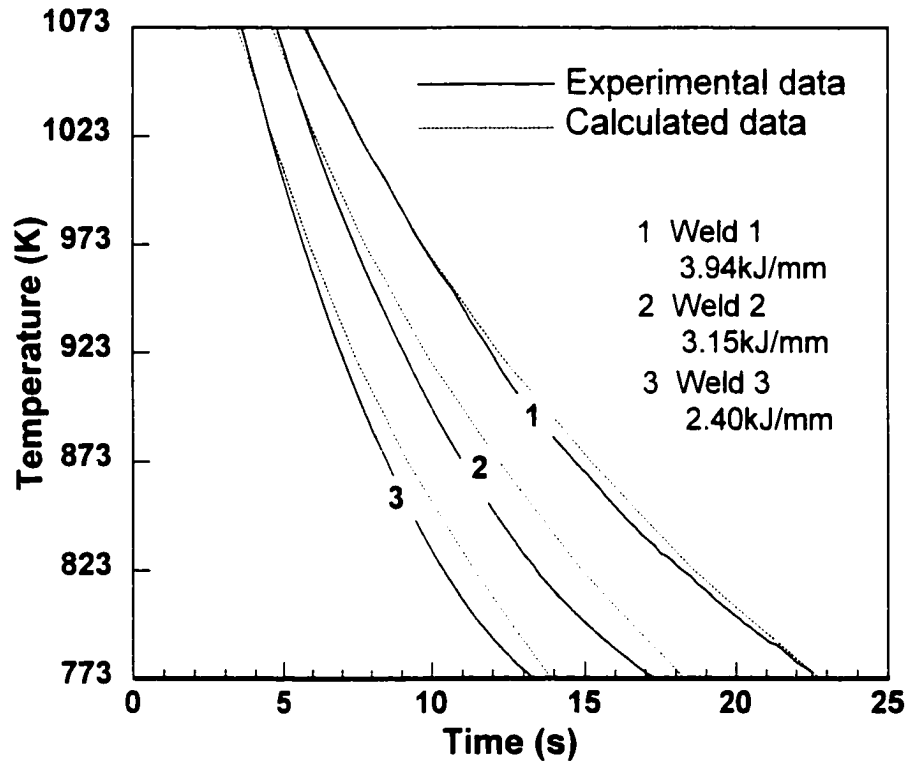
Fig. 4.5: Comparison of the calculated and experimental cooling rates. Welding conditions are presented in Table 4.1. The experimental data were provided by Blackburn.[39]

welds 1, 2, and 3 were found to be 16.3, 12.8, and 10.1 seconds, respectively. Thus, the calculated cooling times agreed well with the experimental results.

4.1.3.4 Microstructures from Experiments

Major Phases in the Weld Metal

The three weld metal microstructures obtained at different heat inputs (i.e. different cooling rates) are shown in Fig. 4.6. Lenticular acicular ferrite (α_a) was found to be the dominant phase in all welds. The morphology of the acicular ferrite can be more clearly observed in the micrographs obtained from high resolution optical microscopy and SEM, both of which are shown in Fig. 4.7 and Fig. 4.8, respectively. From these micrographs, it can be observed that the fine interlocking plates of acicular ferrite are formed within prior austenite grains. The length of the acicular ferrite ranges from 5 μm to 10 μm, and its width is approximately about 2 μm. The acicular ferrite microstructure in the present welds resulted from the combination of appropriate oxygen concentrations (250~320 ppm), moderate titanium and aluminum contents, and the appropriate cooling rate, which are known to be favorable conditions for acicualr ferrite formation.[25,26]

Due to high cooling rates during welding and relatively high alloy element contents in the weld metal, the austenite to ferrite transformations are not expected to go to completion. Some of the austenite remained untransformed, i.e., retained austenite, or subsequently transformed to martensite (M) in the weld metal. This can be seen in Fig. 4.8. The "interstitial spaces" that existed between the acicular ferrite plates are actually the martensite or retained austenite (M/A) constituents. For a quantitative description of the microstructure, Howell[27] differentiated the acicular ferrite microconstituent into two parts: acicular ferrite plates and the "interstitial" M/A constituents. In other word, the acicular plates themselves (a phase) constitute a fraction of the acicular ferrite microconstituent. Based on this concept, a quantitative analysis of acicular ferrite in the weld metal was made by Ryder et al.[28] for the investigated samples. It was found that the acicular ferrite plates constituted approximately 50% of the acicular
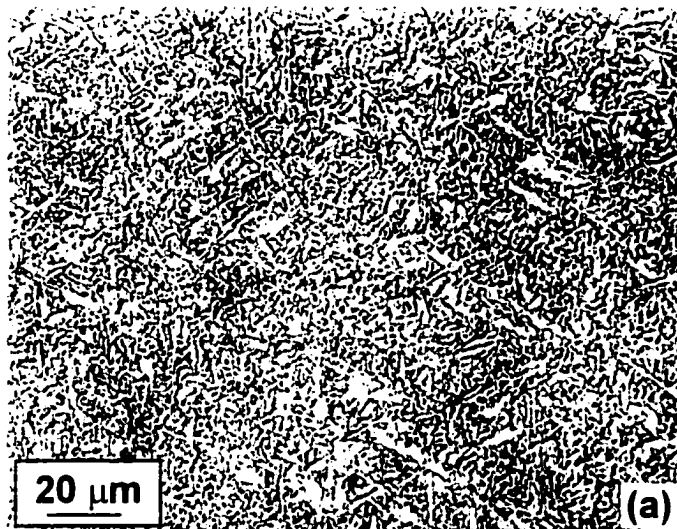
Fig. 4.6(a): weld 1 (3.94 kJ/mm)
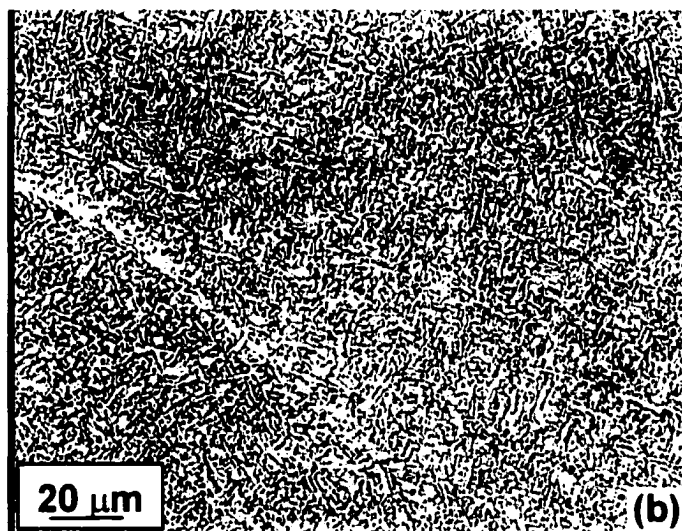
Fig.4.6(b): weld 2 (3.15 kJ/mm)

Fig. 4.6: Optical microstructure in the weld metals obtained from different heat inputs. Welding conditions are presented in Table 4.1.
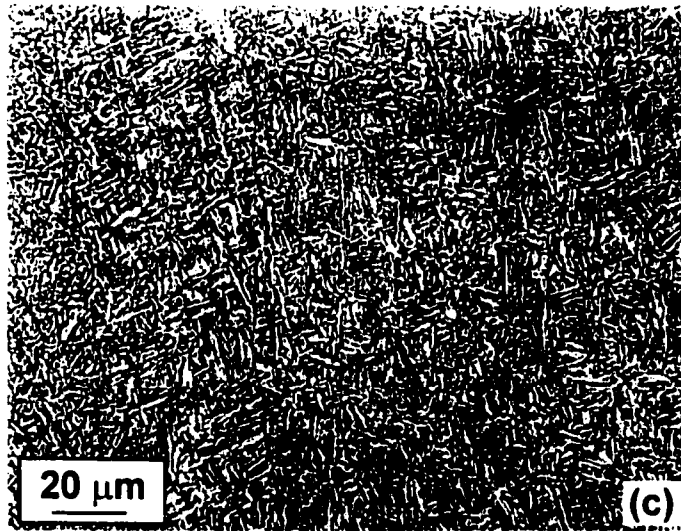
Fig. 4.6(c): weld 3 (2.40 kJ/mm)

Fig. 4.6: Optical microstructure in the weld metals obtained from different heat inputs. Welding conditions are presented in Table 4.1.
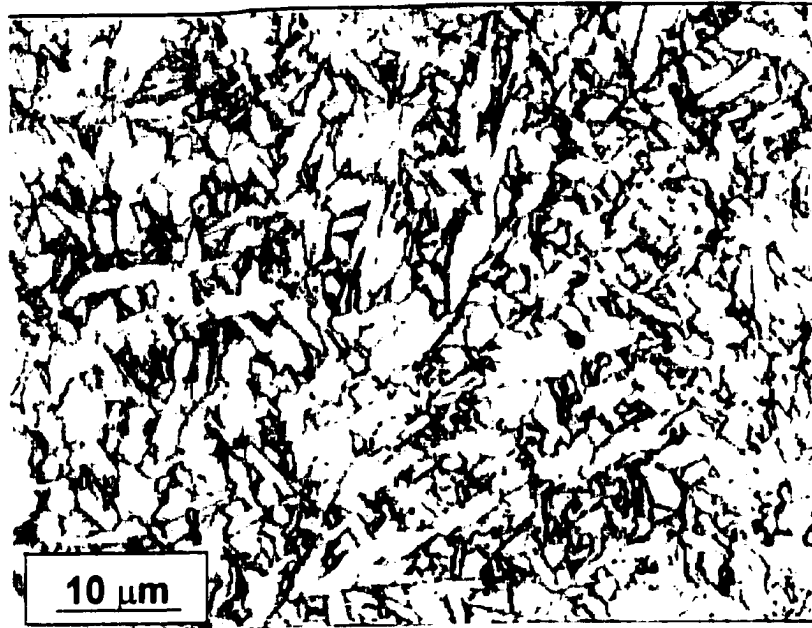
Fig. 4.7: Optical microscopy illustrates the morphology of acicular ferrite in weld 1.
Welding conditions: GMA, 405 A, 31.3 V, 3.22 mm/s, no preheat.
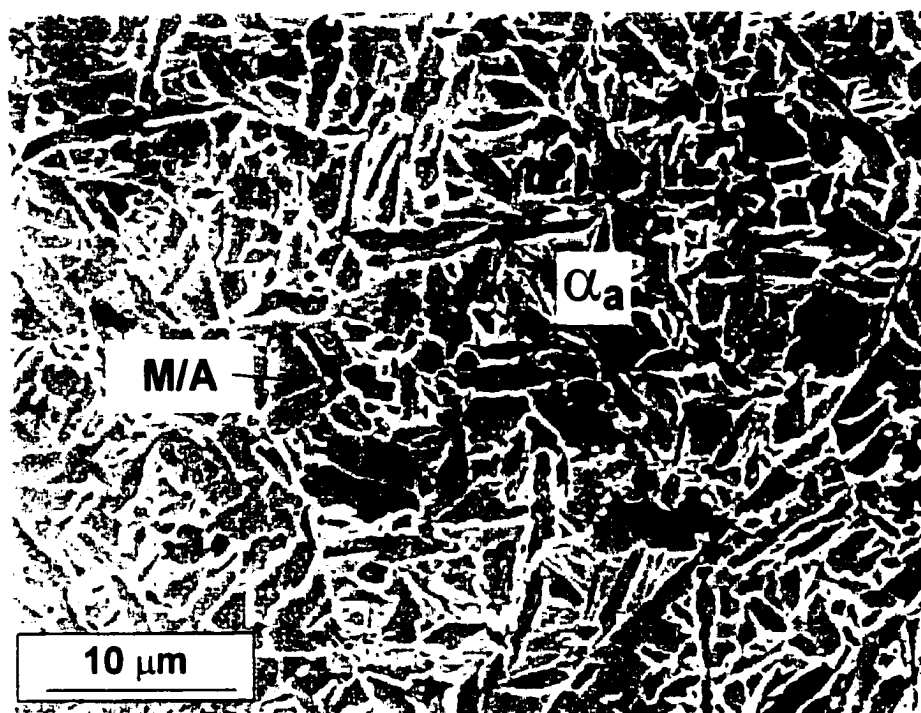
Fig. 4.8: The morphology of acicular ferrite in weld 1 illustrated by SEM. The symbols of M and α_a represent martensite and acicular ferrite, respectively. Welding conditions: GMA, 405 A, 31.3 V, 3.22 mm/s, no preheat.

ferrite microconstituent, with the remaining 50% being the M/A constituent.

Effect of Cooling Rates on the Microstructure

Due to the different cooling rates, microstructural differences among the three welds can also be observed. At relatively higher heat inputs (i.e., slower cooling rate), small amounts of allotriomorphic ferrite (α) and Widmanstatten ferrite (α_w) were observed to form at some of the prior austenite grain boundaries in welds 1 and 2. The allotriomorphic ferrite formed at grain boundaries can be easily identified in the optical microscopy by its very low dislocation densities and the absence of the substructure, as shown in Fig. 4.9(a). In some local regions of welds 1 and 2, a small amount of primary Widmanstatten ferrite was occasionally observed nucleating directly at the prior austenite grain boundaries and growing as sets of parallel plates, as shown in Fig. 4.9(b). The coarse elongated primary Widmanstatten ferrite appears uniformly white, with no evidence of substructure within individual crystals. These individual crystals are separated by thin regions of austenite, which are subsequently retained at ambient temperature or transformed to martentiste. Neither allotriomorphic ferrite nor Widmanstatten ferrite was observed in weld 3, which was produced under relatively lower heat input (i.e., faster cooling rate). In addition, it seems that the size of the acicular ferrite plates also changes with the cooling rate. From Figs. 4.6 (a), (b), and (c), it appears that the higher the heat input (lower cooling rate), the longer and thicker the acicular ferrtie. This observed feature is consistent with previous experimental results.[29] Although no satisfactory theoretical treatment of the kinetics of the acicular ferrite growth has been established, the results here do show that the size of the acicular ferrite plates, like that of banite, increases with transformation temperature. As suggested by Bhadeshia, the activation energy for bainite growth may decrease with temperature.[32] The higher the temperature for bainite transformation, the larger the size of the banite sheaf.
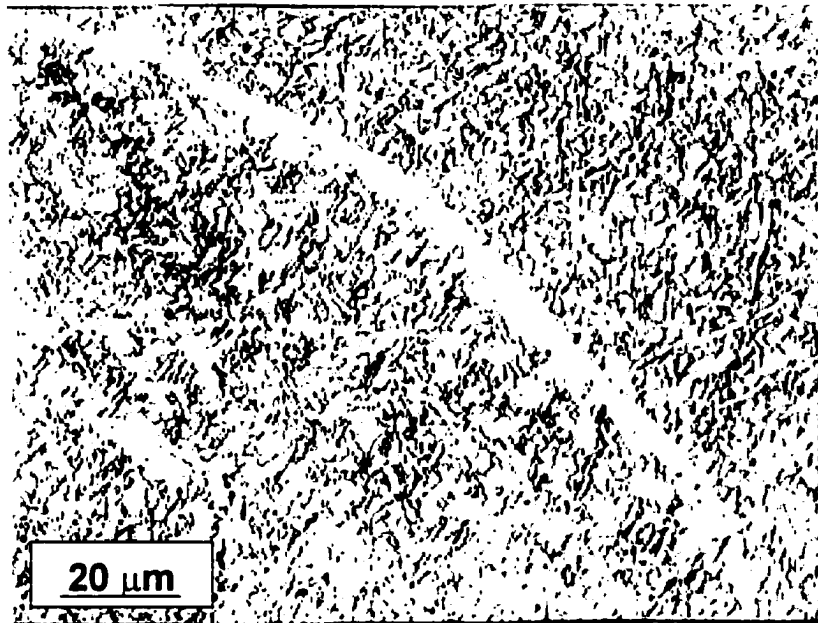
Fig. 4.9: (a) Allotriomorphic ferrite occasionally formed at some prior austenite grain boundary in weld 1. Welding conditions: GMA, 405 A, 31.3 V, 3.22 mm/s, no preheat.
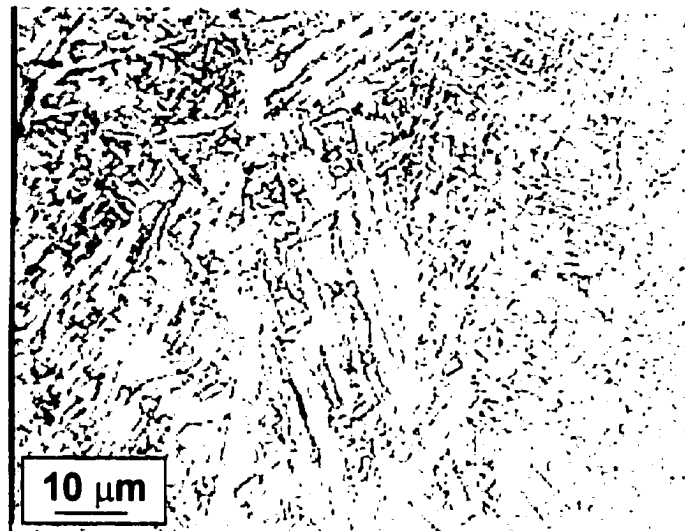
Fig. 4.9: (b)Widmansttaten ferrite in wedge plate shape occasionally formed at some prior austenite grain boundary in weld 2. Welding conditions: GMA, 405 A, 31.3 V, 4.02 mm/s, no preheat.

Fig. 4.10: Acicular ferrite nucleated intragranulary at inclusions within austenite grains; The inclusion particle is a composite with discrete phases: A phase in cubic shape, as indicated by the arrow, is clearly observed in the core of the particle. Welding conditions: GMA, 405 A, 31.3 V, 3.22 mm/s, no preheat.

Inclusion Particles in the Weld Metal

From Figs. 4.8 and 4.9, there is no evidence of nucleation at inclusions for most of the acicular ferrite grains. However, some intragranular inclusion particles do exist as nucleation sites for elongated primary acicular ferrite, as shown in Fig. 4.10. In this figure, it is evident that several elongated primary plates of acicular ferrite nucleated at a single inclusion particle, and then grew along certain crystallographic directions in the austenite. This primary acicular ferrite configuration has also been observed by Ricks et al.[30] Strangwood and Bhadeshia[31] found that these primary acicular ferrite plates probably occur in a Kurdjumov-Sachs (K-S) orientation relationship with the austenite. In the K-S relationship, austenite (fcc) and ferrtie (bcc) appear with the closet-packed planes in each phase, $(111)_{fcc}$ and $(110)_{bcc}$, almost parrallel to each other. From Figs. 4.8 and 4.10, it can also be observed that there are smaller acicular ferrite plates emanating from the primary plates. This phenomenon has been interpreted as evidence that secondary acicular ferrite plates form by intragranular autocatalytic nucleation.[32,33] In autocatalytic nucleation, a one-to-one correspondence between the number of active inclusions and the number of acicular ferrite plates is not expected. The phenomenon of autocatalytic nucleation has also been supported by quantitative metallography,[33] in which the total number of acicular ferrite plates within a region were found to be an order of magnitude larger than the number of inclusion particles.

The major elements in the inclusion particles were examined by energy-dispersive spectrometry (EDS), as shown in Fig. 4.11. It was found that the inclusion particles contained various elements such as Al, Ti, Si, Mn, Fe, and O. Nitrogen is also believed to be in the inclusions, although it is not shown in the EDS map due to the limitation of the EDS method. From the elements in the inclusions, it is suggested that the inclusion particles, which are effective nucleation sites for acicular ferrite formation, consist of a number of discrete phases. These discrete phases in the inclusion particles can be observed in Fig. 4.10, in which a phase with cubic shape is located in the core of the particle and surrounded by other phases. The observed microstructure of the inclusion particle in the present study is consistent with previous results from both experimental[26] and theoretical methods.[32] By using both EDXA and the selected area electron diffraction
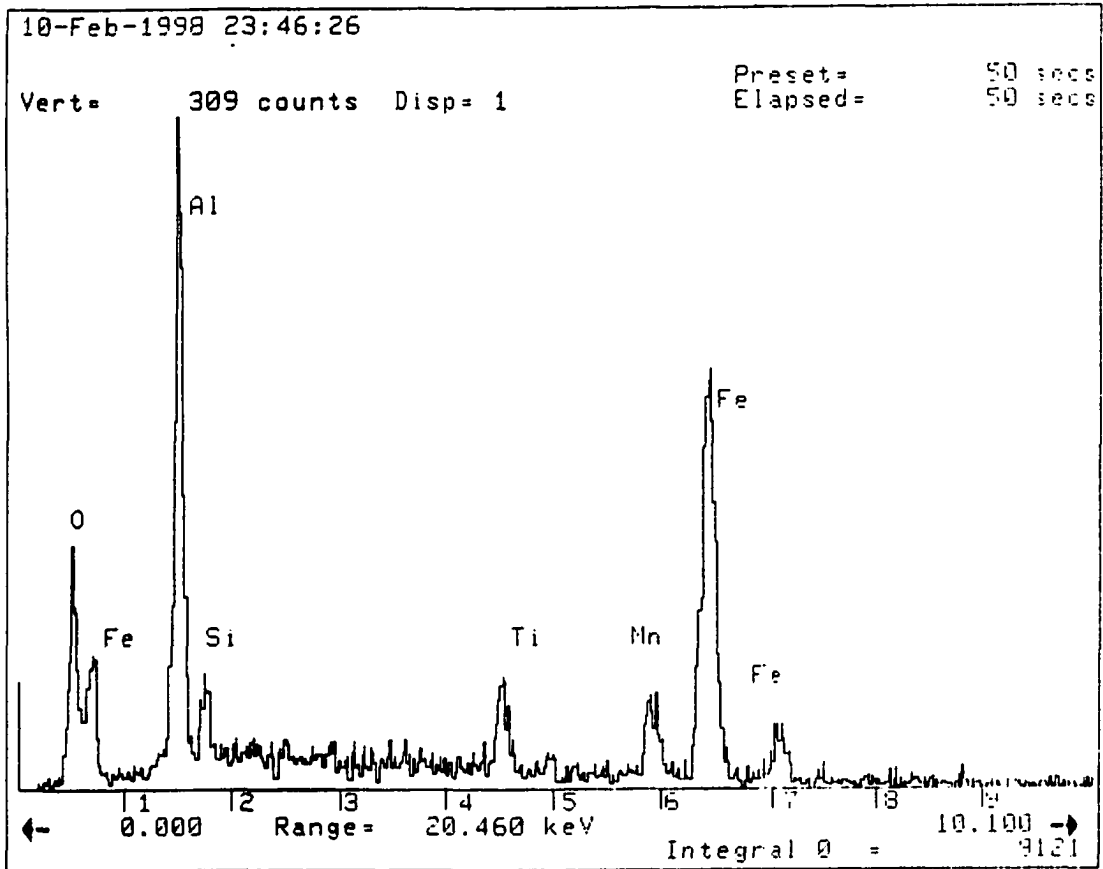
Fig. 4.11: Energy-dispersive spectrometry (EDS) shows elements existed in the inclusion particles. Welding conditions: GMA, 405 A, 31.3 V, 3.22 mm/s, no preheat.

(SAD) method, Barbaro et al.[26] found that the inclusion particles in the arc weld deposits consisted of a titanium nitride phase with a cubic shape in the core. The phase in the core was surrounded by a glassy phase containing manganese, silicon, and aluminum oxides, with a layer of manganese sulphide partly covering the surface of the inclusion particles. Bhadeshia[32] theoretically predicted the microstructure of the inclusion particles in the weld metal by considering both the thermodynamic stability of phases and kinetic factors of the associated chemical reactions. The compound which forms first will be located in the center of the particles, while the elements which are least reactive should be concentrated at the surface of the particles. In the past years, many efforts have been made to identify the most effective inclusion for the nucleation of acicular ferrite. Different theories[26,39] have been proposed on this subject. The results reported here together with some previous work[26] suggest that the inclusion effective for the formation of acicular ferrite is amorphous in nature rather than single compound.

4.1.3.5 Predicted Microstructure from Mathematical Modeling

Calculated TTT Diagrams

The computed TTT diagram of weld 1 is shown as the solid lines in Fig. 4.12. In the following discussions, this TTT diagram will be used to represent the TTT diagrams of all the three welds because of the very close chemical compositions in these three welds. The upper C curve represents the time taken for initiation of the allotriomorphic ferrite formation by diffusional mechanism. The lower C curve represents the Widmanstatten ferrite, acicular ferrite, and bainite, all of which are assumed to form by displacive mechanism in the present used phase transformation model. The horizontal line represents the martensite start temperature. The TTT diagram indicated by solid lines in Fig. 4.12 was calculated by assuming that the weld was chemically homogeneous, i.e., the chemical composition in the bulk region was used for the calculation of this TTT diagram.

However, weld deposits in practice are not chemically homogeneous because nonequilibrium solidification leads to coring. The first solidified regions are depleted of
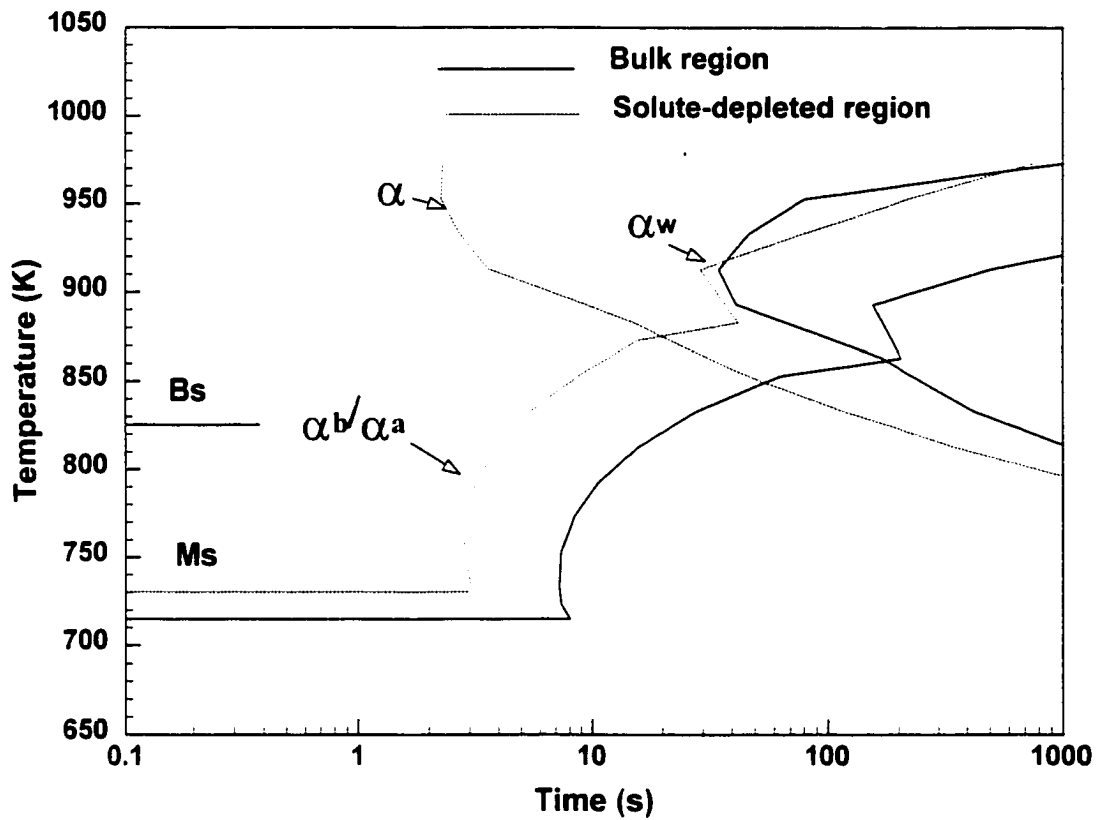
Fig. 4.12: Calculated TTT diagrams for weld 1 from compositiona in bulk and solute-depleted region. The symbols α, α_w, α_a, and α_b represent allotriomorphic ferrite, Widmanstatten ferrite, acicular ferrite, and bainite, respectively. Ms and Bs are the starting temperatures for martensite and bainite, respectively. Welding conditions: GMA, 405 A, 31.3 V, 3.22 mm/s, no preheat.

solute alloying elements and have a lower hardenability. These solute depleted regions will then be first transformed to ferrite during austenite decomposition. The extent of segregation due to solidification can be estimated from the partition coefficient k_i which is the ratio of the concentration of the element i in the δ-ferrite to that in the liquid phase. The partition coefficient used in the model is calculated at the liquidus temperature and the minimum concentration in the solute depleted region is then taken to be $k_i \bar{x}$, where $\bar{x}$ is the average chemical composition in the weld. Due to the rapid cooling rates in the weld metal, diffusion during cooling to ambient temperatures does not lead to significant homogenization of substitutional alloying elements.[33] On the other hand, carbon can be assumed to be homogeneously distributed in the austenite prior to $\gamma \rightarrow \alpha$ transformation because it diffuses much faster than substitutional solutes. The computed equilibrium concentrations of various alloying elements in the solute depleted region for the present weld metal are shown in Table 4.10. The corresponding TTT diagram in the solute depleted region was calculated and shown as dashed lines in Fig. 4.12. Comparing the TTT diagram calculated for the solute depleted region with that calculated for the bulk region, it can be observed that both the upper and lower "C" curves calculated from solute depleted region shift to left. From Fig. 4.12. it can also be observed that the extent of the change in diffusional curve (the upper "C" curve) due to the segregation is much larger than that in the displacive curve (the lower "C" curve). This is because the alloying elements play much more important roles in the diffusion controlled transformations than they act in the displacive transformations.

Table 4.10: Concentrations for calculation of the TTT diagram in solute depleted regions in the HSLA-100 steel welds (wt%)

Weld No.	C	Mn	Si	Ni	Mo	Cr	V
1	0.045	0.80	0.16	1.09	0.11	0.057	0.0007
2	0.050	0.80	0.15	1.05	0.12	0.052	0.0007
3	0.039	0.82	0.15	1.11	0.12	0.056	0.0007

* It should be noted that the carbon contents have been kept as the same as those in the bulk regions considering the redistribution of carbon before austenite decomposition.

Calculated CCT Diagrams

Based on Scheil's additive rule, the calculated TTT diagrams in both bulk and solute depleted regions are transformed to the corresponding CCT diagrams as shown in Fig. 4.13 (a) and (b), respectively. The calculated CCT diagram in the bulk region, as shown in Fig. 4.13(a), shows significant suppression of allotriomorphic ferrite formation. On the other hand, there exists a prominent transformation region within the temperature range intermediate to those of allotriomorphic ferrite and martensite. This region is attributed to acicular or bainite formation. These features are consistent with the experimentally determined CCT diagram of HSLA steels with similar composition,[5,6] as in Fig. 4.14. In contrast, no significant suppression of allotriomorphic ferrite formation is observed in the CCT diagram in the solute depleted region as shown in Fig. 4.13(b). This is because the contents of alloying elements in the solute depleted region are much lower than those in the bulk region.

Predicted Weld Metal Microstructure

Since the phase transformations first take place in the solute depleted region,[12] where lower hardenability exists due to low content of alloying elements, the CCT diagram in this region should be used for prediction of the initiation times of various phase transformations. To predict the microstructural evolution in the three welds investigated, the corresponding calculated cooling curves were imposed on the calculated CCT diagram as shown in Fig. 4.15. It was found that the cooling curves for all the welds intercepted with the displacive curve. Thus, acicular ferrite and bainite were expected to form in all the three welds. Since the diffusional curve had only interceptions with the cooling curves of welds 1 and 2 and not with the cooling curve of weld 3, allotriomorphic ferrite was expected to form in welds 1 and 2 but not in weld 3. Even in weld 1 and 2, the amounts of allotriomorphic ferrite should be very small, because their cooling curves can only intercept the diffusional curve very narrowly. In addition, significant amounts of retained austenite and martensite are expected in the all the three welds, since the cooling curves intercept the lower C curve (displacive curve) at temperatures not too far from the martensite start temperature (Ms). Thus, time for the formation of acicular ferrite or bainite is limited and some untransformed austenite will be retained or subsequently
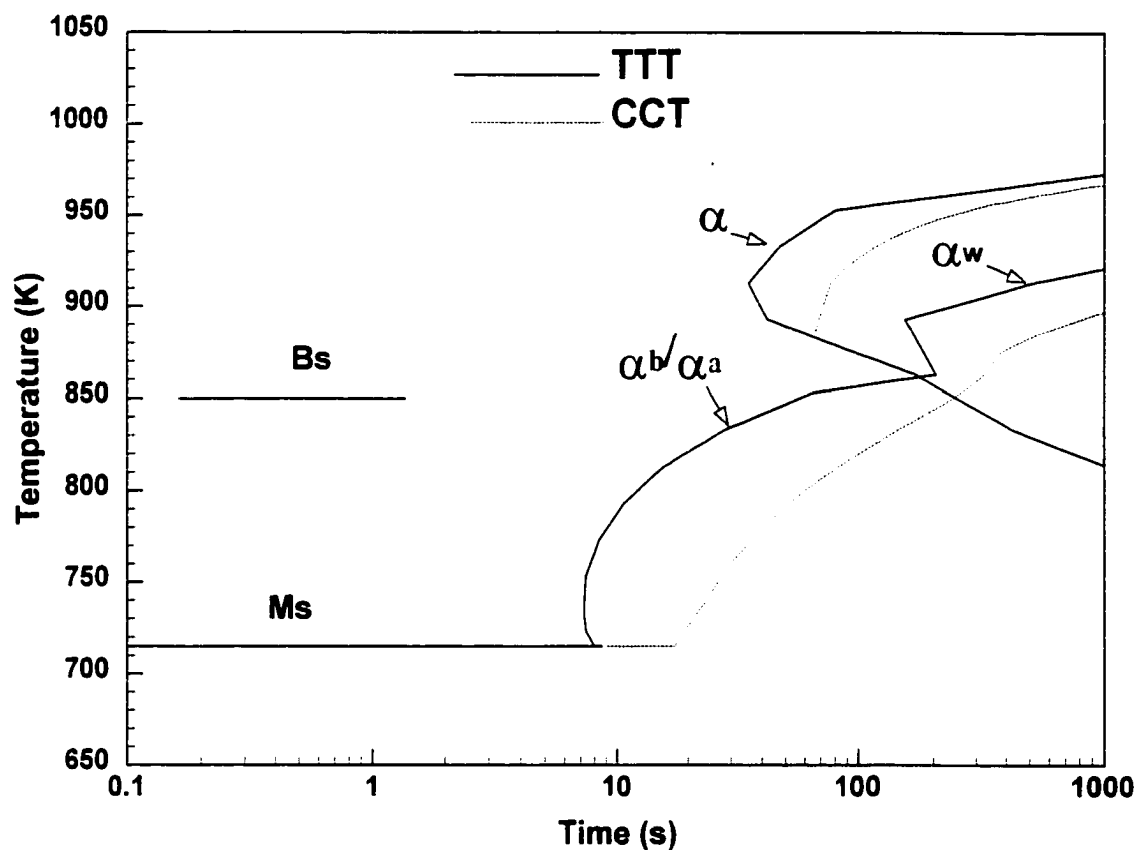
Fig. 4.13: (a) Comparison of the TTT and CCT diagrams for weld 1 in bulk region. The symbols α, α_w, α_a, and α_b represent allotriomorphic ferrite, Widmanstatten ferrite, acicular ferrite, and bainite, respectively. Ms and Bs are the starting temperatures for martensite and bainite, respectively. Welding conditions: GMA, 405 A, 31.3 V, 3.22 mm/s, no preheat
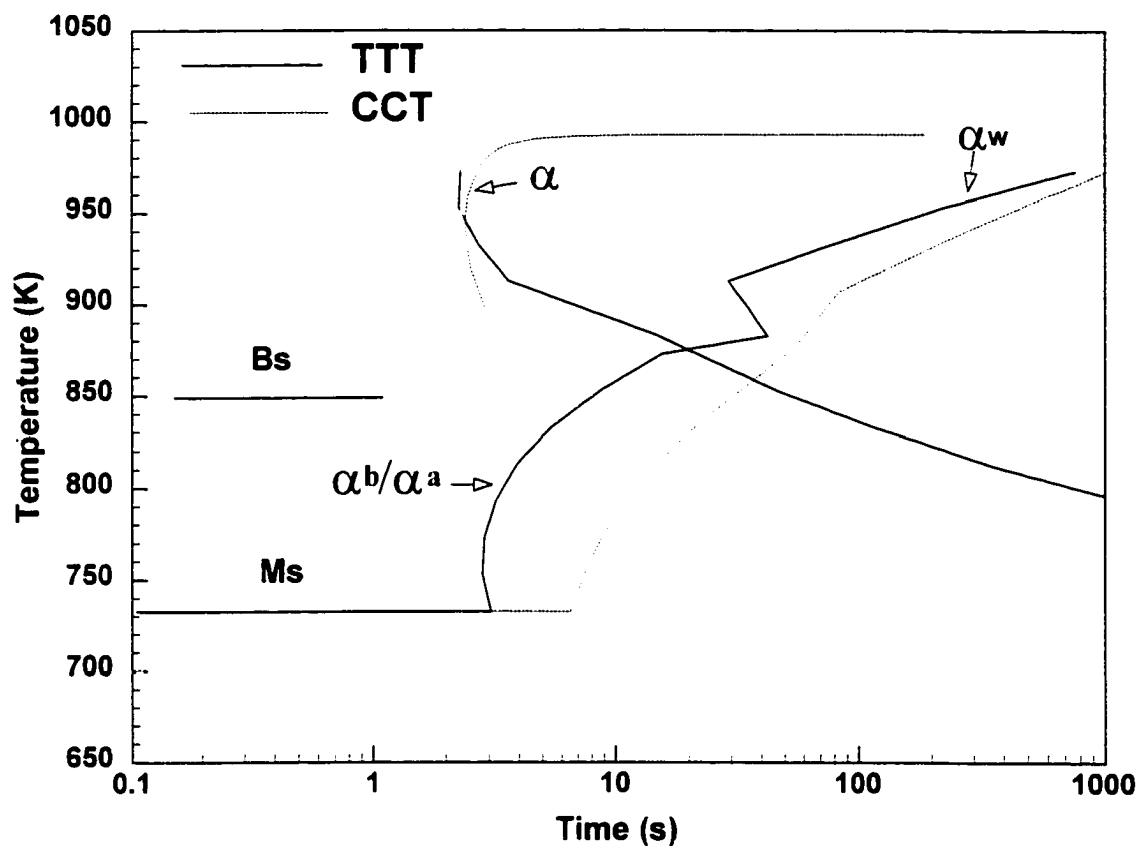
Fig. 4.13: (b) Comparison of the TTT and CCT diagrams for weld 1 in solute depleted region. The symbols α, αw, αa, and αb represent allotriomorphic ferrite, Widmanstatten ferrite, acicular ferrite, and bainite, respectively. Ms and Bs are the starting temperatures for martensite and bainite, respectively. Welding conditions: GMA, 405 A, 31.3 V, 3.22 mm/s, no preheat.
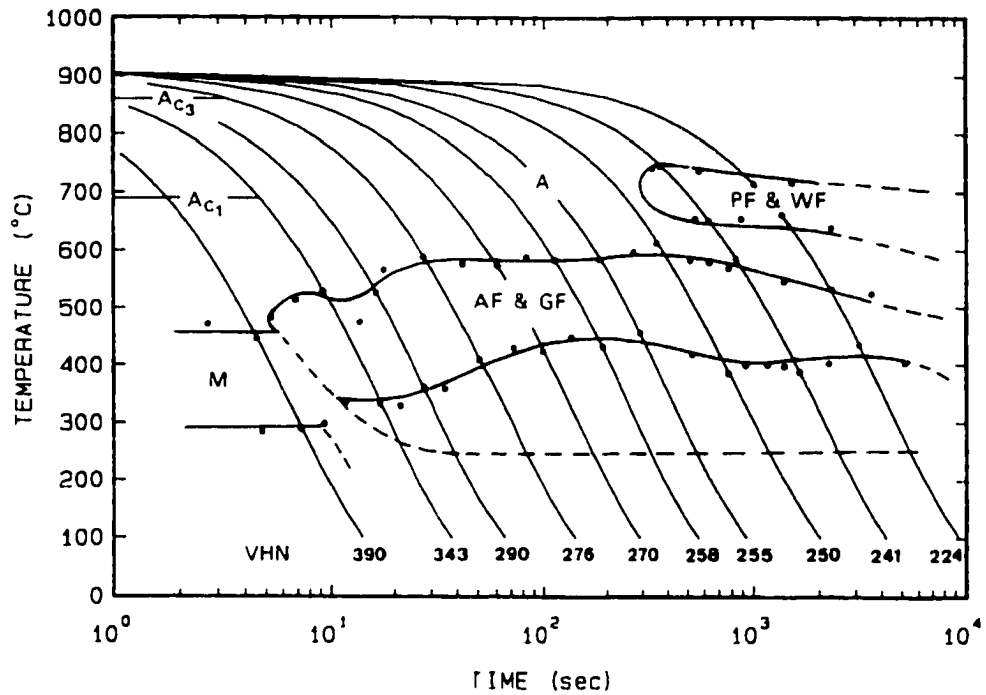
Fig. 4.14: Continuous-cooling-transformation diagram of HSLA steel[6] containing (wt%):
0.06 C, 0.35 Si, 1.45 Mn, 1.25 Cu, 0.97 Ni, 0.72 Cr, 0.42 Mo, 0.04 Nb; A = Austenite, PF
= Polygonal ferrite, WF = Widmanstatten ferrite, AF = Acicular ferrite, GF = Granular
ferrite, M = Martensite.
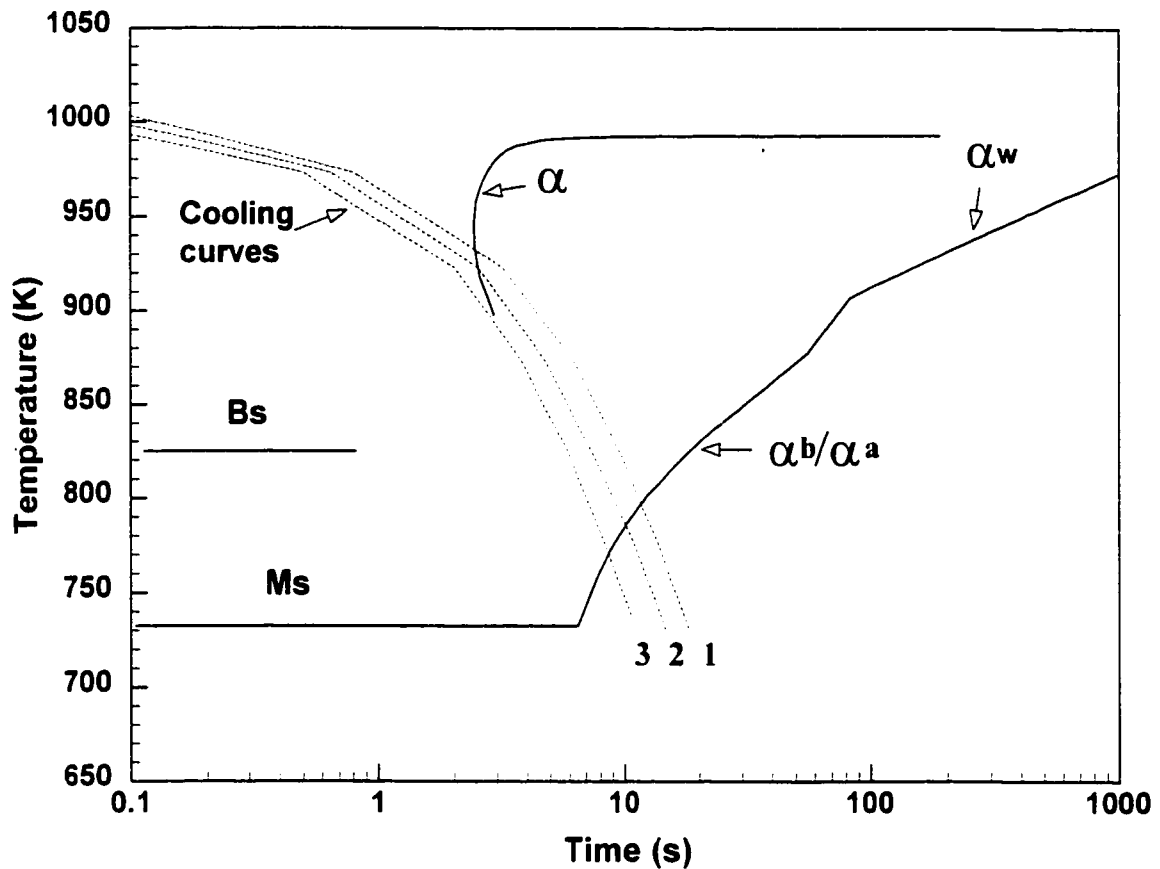
Fig. 4.15: Prediction of microstructure from the calculated CCT diagrams and the cooling rates. The symbols α, α_w, α_a, and α_b represent allotriomorphic ferrite, Widmanstatten ferrite, acicular ferrite, and bainite, respectively. Ms and Bs are the starting temperatures for martensite and bainite, respectively. The symbols of 1, 2, 3 represent calculated cooling rates in welds 1, 2, and 3, respectively.

transformed to martensite. Since the theory for calculation of the nucleation and growth rates of acicular ferrite is not well established, quantitative calculation of acicular ferrite in high strength low alloy steels from fundamentals cannot be done at present. Consequently, the volume fraction of martensite in the investigated HSLA-100 welds cannot be estimated from the present model. However, quantitative experimental results from Ryder et al.[28] showed that around 50% martensite and retained austenite (M/A) constituents existed in the weld metal investigated.

Through the comparison of the predicted and experimental results above, it can be concluded that the predicted microstructures in the welds investigated are consistent with the corresponding observed microstructures.

4.2 Quantitative Prediction of C-Mn Steel Weld Metal Microstructure

4.2.1 Experimental Conditions and Results[9]

Svensson et al.[9] studied the effects of carbon and manganese on the C-Mn weld metal microstructure experimentally. They made bead on plate welds by manual metal arc welding. All welds were made in accordance with ISO2560, with a current of 180 A, voltage 23 V, welding speed 4 mm/s, and a maximum interpass temperature of 523 K. Since the coefficient of the arc heat transfer is normally 80% for manual metal arc welding,[35] the heat input was then around 1 kJ/mm. Different carbon and manganese contents in the weld metal were obtained by changing the electrode coatings. The weld metal compositions, experimentally determined austenite grain size, and the volume fractions of various phases in the weld metal are taken from their paper[9] and reproduced in Tables 4.11 and 4.12, respectively.

Table 4.11: Chemical compositions of the selected C-Mn steel welds[9]

Weld No.	C	Si	Mn	P	S	Al	Ti	N	O
1	0.030	0.45	0.78	0.010	0.013	0.009	0.014	95	336
2	0.059	0.34	0.77	0.010	0.010	0.007	0.011	66	306
3	0.059	0.33	1.09	0.010	0.008	0.007	0.010	64	310
4	0.059	0.30	1.44	0.010	0.006	0.007	0.009	65	305
5	0.065	0.33	1.83	0.010	0.003	0.007	0.009	76	291
6	0.090	0.41	0.78	0.010	0.013	0.003	0.014	36	421
7	0.089	0.35	1.18	0.010	0.011	0.008	0.012	73	404
8	0.088	0.37	1.59	0.010	0.011	0.003	0.012	77	491
9	0.12	0.43	0.86	0.014	0.011	0.005	0.015	54	329

* all contents in weight percent except for the contents of N and O in ppm.

Table 4.12: Experimentally determined austenite grain size and phase volume fractions in the weld metal of C-Mn steels[9]

Weld No.	Austenite Grain size* (μm)	Phase volume fractions (vol. %)		
		V_α	V_w	$V_a + V_m$
1	65	60	29	11
2	71	40	36	24
3	65	33	36	31
4	60	30	25	45
5	48	28	11	61
6	45	35	32	33
7	45	34	28	38
8	45	27	22	51
9	36	28	21	51

* Mean lineal intercept measured normal to length axis of grains. The symbols V_α, V_w, V_a, and V_m represent the volume fractions of allotriomorphic ferrite, Widmanstatten ferrite, acicular ferrite, and microphases.

4.2.2 Results and Discussions

4.2.2.1 Temperature and Velocity Fields

The thermo-physical data used for calculation of heat transfer and fluid flow are given in Table 4.13. The calculated temperature and velocity fields in the weld sample are shown in Fig. 4.16. The general features of the calculated temperature field are consistent with that presented previously in Fig. 4.1 for GMA welding of HSLA-100 steel. In front of the heat source, the temperature gradient is greater than that behind the heat source. The high temperature gradient results in slightly greater liquid metal velocities in front of the heat source than behind the heat source. At the surface of the weld pool, the liquid metal moves from the center to the periphery because of the negative temperature coefficient of surface tension $d\gamma/dT$. The calculated peak temperature in the weld pool is 2402 K. The calculated maximum velocities in x, y, z directions 34.1 cm/s, 37.1 cm/s, and 8.3 cm/s, respectively. Both the peak temperature and the maximum velocities in this case are lower than those in the HSLA-100 steel cases

as given in Table 4.7 in the previous section. This is expected since the heat input in this case is much lower than those in the HSLA-100 steel cases.

Table 4.13: Data used for the calculation of velocity and temperature fields in C-Mn steel welds[40,41]

Physical property	value
Liquidus temperature (K)	1780
Solidus temperature (K)	1742
Density of liquid metal (kg/m3)	7200
Viscosity of liquid (kg/m.s)	6.0×10^{-3}
Thermal conductivity of solid (J/m.s.K)	27.1
Thermal conductivity of liquid (J/m.s.K)	83.6
Specific heat of solid (J/kg.K)	702.0
Specific heat of liquid (J/kg.K)	806.7
Latent heat of melting (J/kg)	267.6×10^3
Temperature coefficient of surface tension (N/m.K)	-0.43×10^{-3}

4.2.2.2 Weld Geometry

The shape and size of the fusion zone, mushy zone (solid-liquid two-phase zone) and heat affected zone can be determined from the calculated temperature profile at different locations in the weld, as shown in Fig. 4.17. The fusion zone boundary was determined from the liquidus temperature (1780K) isothermal surface in the computed temperature field. The mushy zone corresponds to the region located between the solidus temperature (1742K) and liquidus temperature isotherms. The heat affected zone boundary was approximately estimated from the Ae1 temperature, i.e. the phase boundary between (α+γ) and α, which is around 873K in low alloy steels.
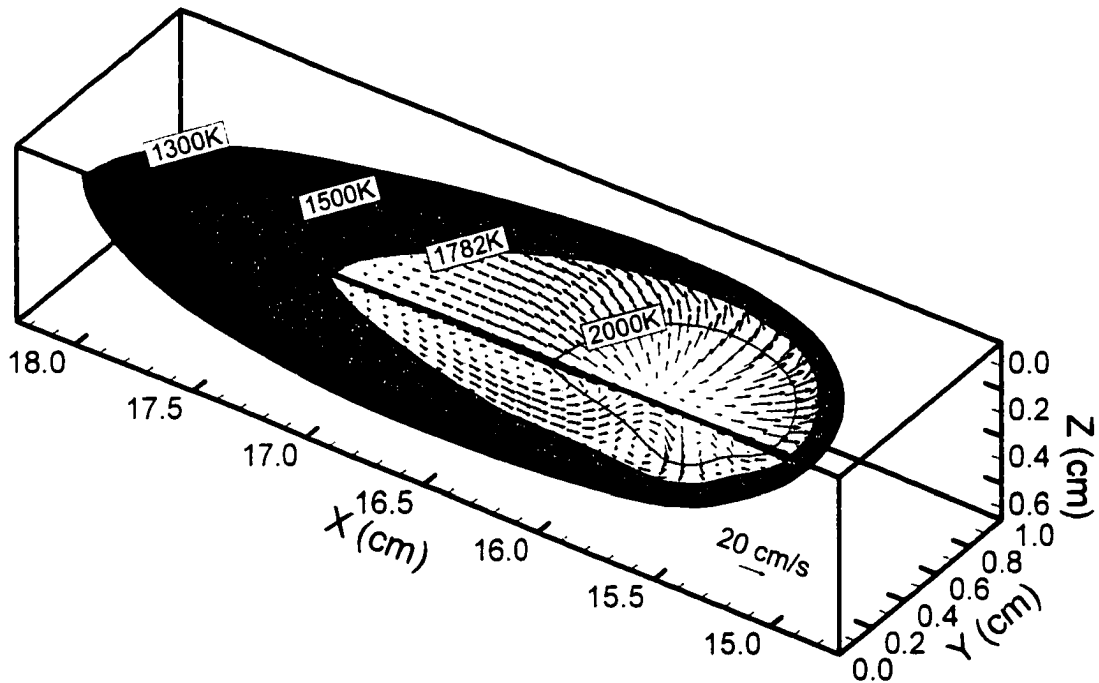
Fig. 4.16: Calculated temperature and velocity fields in the weld pool of manual metal arc welding of C-Mn steels. Welding conditions: 180 A, 23 V, 4 mm/s, interpass temperature equal to 523 K.
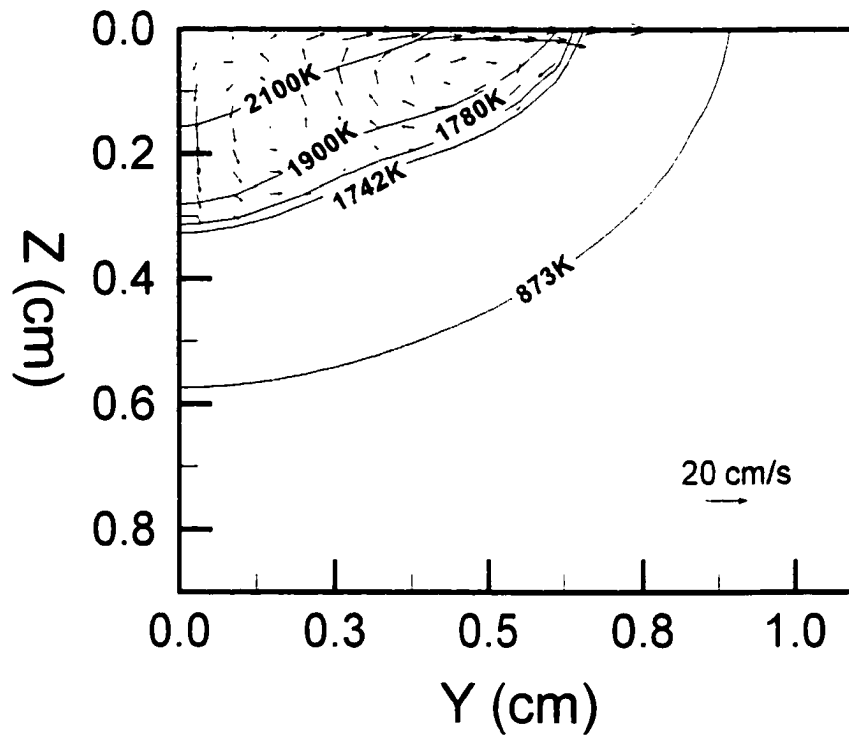
Fig. 4.17: Calculated temperature profiles in the cross section directly under the heat source during manual metal arc welding of C-Mn steels. Welding conditions: 180 A, 23 V, 4 mm/s, interpass temperature equal to 523 K.

4.2.2.3 Calculated Cooling Rates

The cooling rate in the weld metal was calculated from two different methods in this study. One set of cooling rate was numerically calculated by the heat transfer and fluid flow model. The other set of cooling rate was calculated by the empirical equation proposed by Svensson et al,[35] which has been discussed in chapter 2.

The cooling rates between 1073 - 773 K (800 - 500 °C) at different locations calculated by the 3D model are compared with that from the empirical equation (equation 2.28) in Fig. 4.18. It is observed that the cooling rates in the fusion zone calculated by the 3D model are somewhat faster than that obtained from the empirical equation. The time cooling from 800 - 500 °C, $\Delta t_{8/5}$, is usually used to characterize the cooling rate during austenite decomposition. Under the investigated welding conditions, the values of $\Delta t_{8/5}$ from the 3D model and the empirical equation were found to be 10.1 s and 13.8 s, respectively. Although the experimental value of $\Delta t_{8/5}$ for the present welding conditions is not available, the experimental value of $\Delta t_{8/5}$ under somewhat similar welding conditions has been measured by Evans,[36] in which the welding current, voltage, and interpass temperature were 170 A, 21 V, and 513 K, respectively. Although the welding speed was not reported in Evans's experiment, the heat input was reported to be around 1 kJ/mm, which is roughly same as that in the present welding conditions. The value of $\Delta t_{8/5}$ was measured to be 8 s in Evans's experiment. Since the values of the welding current, voltage, and interpass temperature for the present welds are a little bit higher than those in Evan's experiment, the corresponding value of $\Delta t_{8/5}$ for the present welds should be a little larger than 8 s. Thus, the value calculated from the 3D model (10.1 s) seems reasonable while the value from the empirical equation (13.8 s) seems somewhat larger than the actual value. Fig. 4.18 also shows that the difference in the cooling rates at different locations in the fusion zone within the temperature range 1073 - 773 K is small.

4.2.2.4 Calculated TTT Diagrams

The calculated TTT diagrams for different carbon and manganese contents are shown in Fig. 4.19(a) and (b), respectively. The upper and the lower "C" curves in the diagram represent the initial time for the diffusional transformation (e.g. the formation of
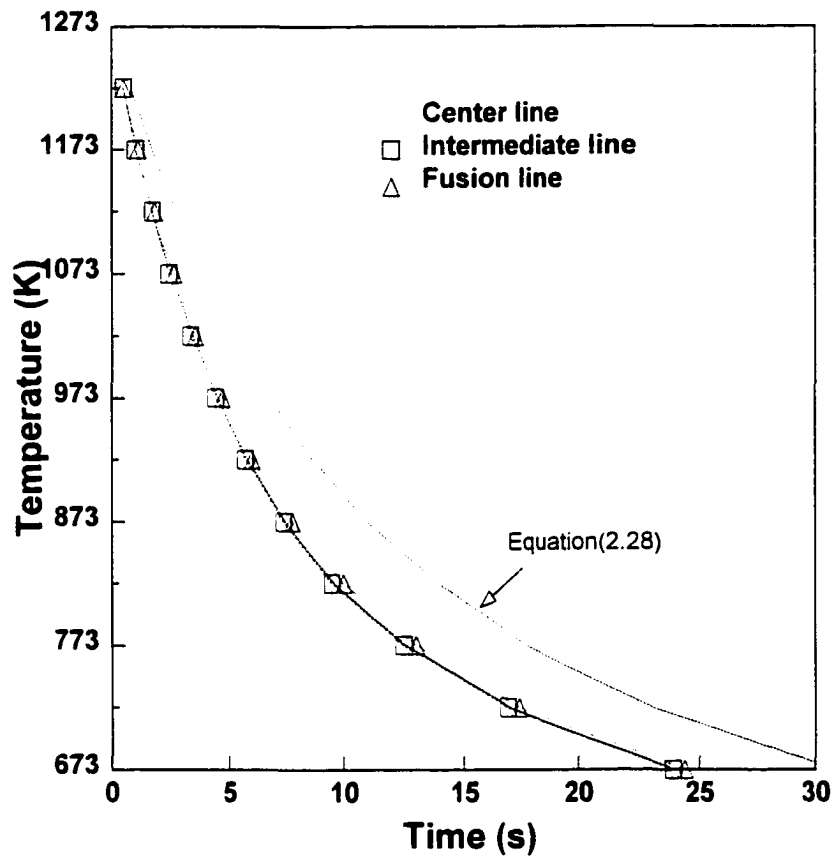
Fig. 4.18: Comparison of calculated cooling rates from 3D model and cooling rate from empirical equation. Welding conditions:[9] manual metal arc welding, 180 A, 23 V, 4 mm/s, 523 K interpass temperature.
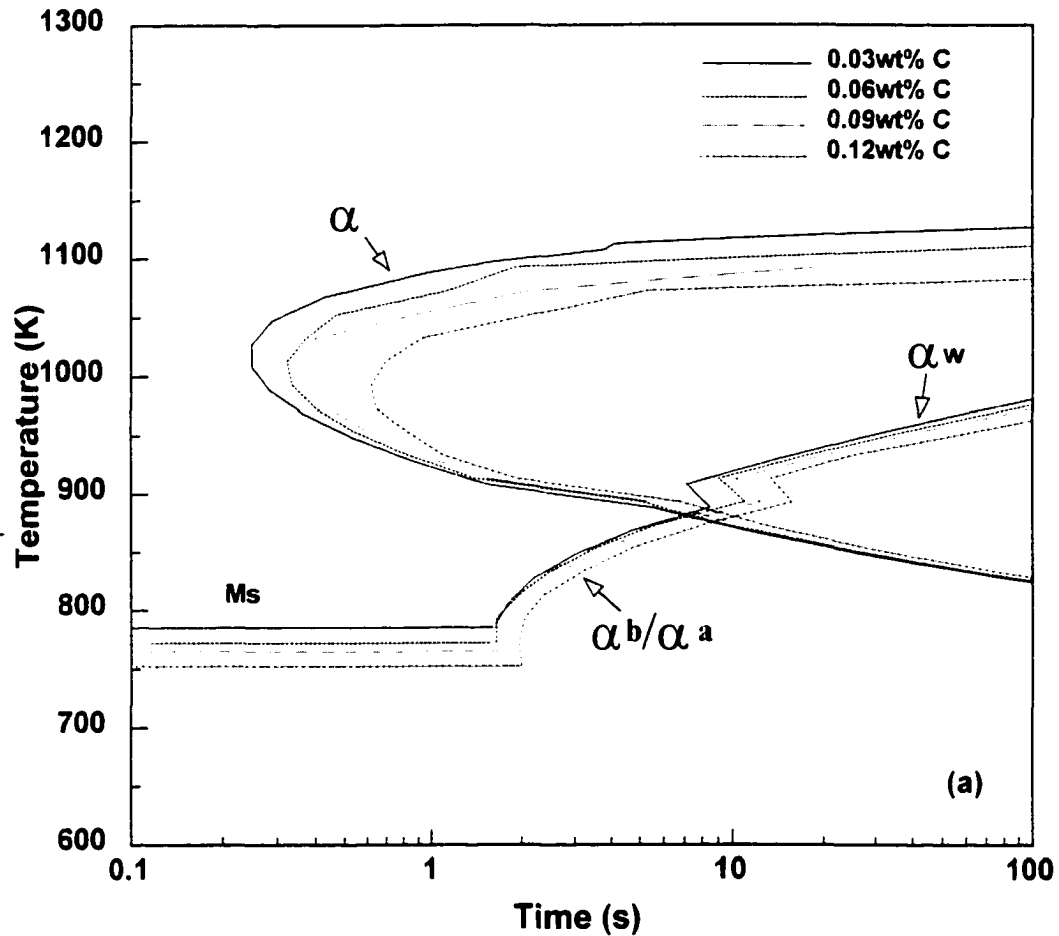
Fig. 4.19: (a) Calculated TTT diagrams of alloys with different carbon contents. The symbols α, α_w, α_a, and α_b represent allotriomorphic ferrite, Widmanstatten ferrite, acicular ferrite, and bainite, respectively. Ms is the starting temperature for martensite.
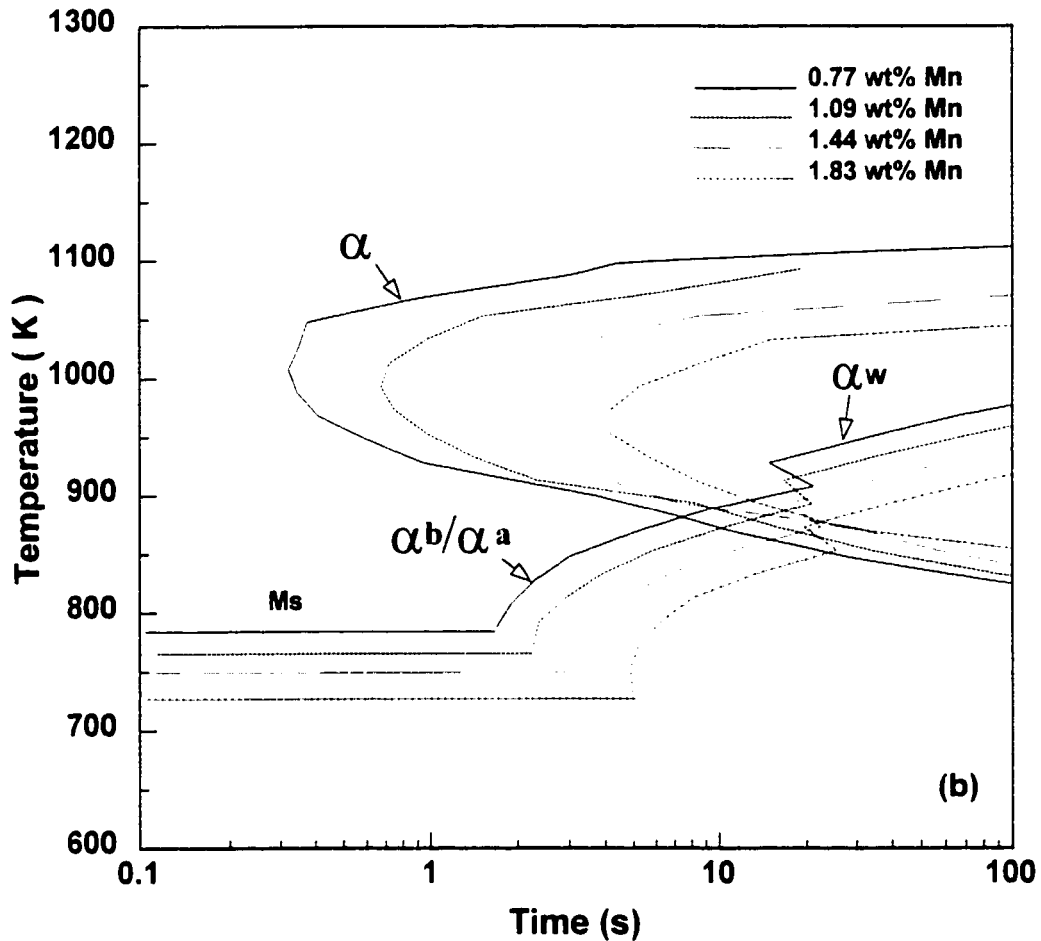
Fig. 4.19: (b)Calculated TTT diagrams of alloys with different manganese contents. The symbols α, α_w, α_a, and α_b represent allotriomorphic ferrite, Widmanstatten ferrite, acicular ferrite, and bainite, respectively. Ms is the starting temperature for martensite.

allotriomorphic ferrite) and that of the displacive transformation (e.g. the formation of Widmansttaten, acicular ferrite or bainite), respectively. The horizontal lines represent the martensite start temperatures. The symbols of α, α_w, α_a, and α_b represents allotriomorphic ferrite, Widmanstatten ferrite, acicular ferrite and bainite, respectively. From Fig. 4.19(a) and (b), it is clear that both the upper and the lower "C" curves shift to the right and the Ms temperatures decrease as the carbon or the manganese contents increase. This is expected because both carbon and manganese can promote the hardenability of the steel significantly. The calculated values of the solidus temperature of the $(\alpha+\gamma)/\gamma$ phase boundary (Ae3), Widmanstatten ferrite start temperature, the bainite start temperature (Bs), and the martensite start temperature (Ms) are given in Table 4.14.

Table 4.14: Calculated temperatures for various transformations in C-Mn steels.

Weld No.	Ae3 (K)	Ws (K)	Bs (K)	Ms (K)
1	1130	1073	943	808
2	1117	1053	931	797
3	1102	1033	916	782
4	1084	1013	901	766
5	1062	993	882	745
6	1108	1033	919	784
7	1087	1013	901	765
8	1069	993	884	747
9	1094	1013	905	768

* The symbols of Ae3, Ws, Bs, ans Ms represent the the solidus temperature of the $(\alpha+\gamma)/\gamma$ phase boundary, Widmanstatten ferrite start temperature, the bainite start temperature, and the martensite start temperature, respectively.

Table 4.15 Calculated chemical compositions in the solute depleted region of the selected C-Mn steel welds (%).

No	1	2	3	4	5	6	7	8	9
C	0.030	0.059	0.059	0.059	0.065	0.090	0.089	0.088	0.12
Si	0.32	0.24	0.24	0.21	0.24	0.29	0.25	0.26	0.31
Mn	0.59	0.58	0.82	1.08	1.37	0.59	1.18	0.89	0.65

As discussed previously in chapter 4, it is the solute depleted region that will be first transformed to ferrite during austenite decomposition. The calculated compositions in the solute depleted regions of the investigated welds are given in Table 4.15. In this case, welds 2 and 5 were selected to compare the calculated TTT diagrams in solute depleted region with those in the bulk region. The alloying content in weld 5 is larger than that in weld 2. The major alloying elements in solute depleted region of weld 2 are (wt%): C: 0.059, Si: 0.24, and Mn: 0.58; The corresponding composition in weld 5 is (wt%): C: 0.065, Si: 0.24, and Mn: 1.37. Fig. 4.20(a) and (b) show the comparison of the calculated TTT diagrams in the solute depleted region and those in the bulk region in the selected two welds. As expected, the calculated TTT diagrams in the solute depleted region shift to left in both welds due to lower alloying content and consequently lower hardenability in these regions. Furthermore, the difference between the TTT diagram of the solute depleted region and that of the bulk region in weld 5 is much larger than that in weld 2. This is because the alloying content in weld 5 is much higher than that in weld 2. Consequently, the extent of alloying element segregation in weld 5 is larger than that in weld 2.

4.2.2.5 Calculated CCT Diagrams

The "additive rule" was used to convert the TTT diagram to CCT diagram. Fig. 4.21(a) and (b) show typical CCT diagrams which were converted from TTT diagrams of weld 5 in the bulk region and the solute depleted region, respectively. The CCT diagrams were represented by dash lines in the figures. The cooling curve calculated from the 3D model was imposed on the CCT diagram to predict the microstructural evolution in the weld during continuous cooling. According to the CCT diagram in the bulk region as shown in Fig. 4.21(a), neither upper C curve (diffusional curve) nor lower C curve (displacive curve) has been intercepted by the cooling curve. This indicates that no allotriomorphic ferrite (α), Widmanstatten ferrite (α_w), and acicular ferrite (α_a)/bainite (α_b) will be formed, and 100% martensite is expected in this weld. The experimental results, shown in Table 4.12, indicate otherwise. The volume fractions of allotriomorphic
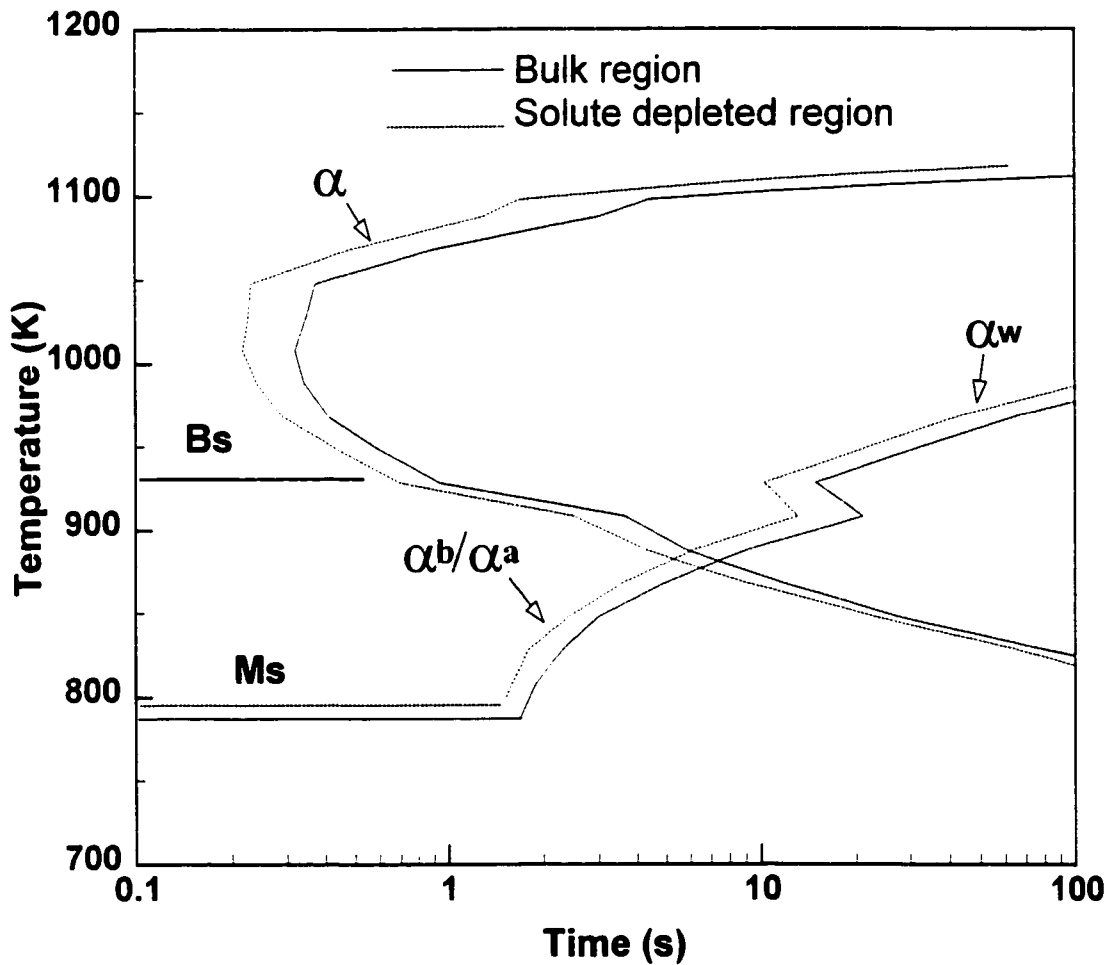
Fig. 4.20: (a) Comparison of TTT diagrams of solute depleted region and bulk region in weld 2. The symbols α, α_w, α_a, and α_b represent allotriomorphic ferrite, Widmanstatten ferrite, acicular ferrite, and bainite, respectively. Ms and Bs are the starting temperatures for martensite and bainite, respectively. Composition in solute depleted region (%): 0.059 C, 0.24 Si, and 0.58 Mn.Composition in bulk region (%): 0.059 C, 0.34 Si, and 0.77 Mn.
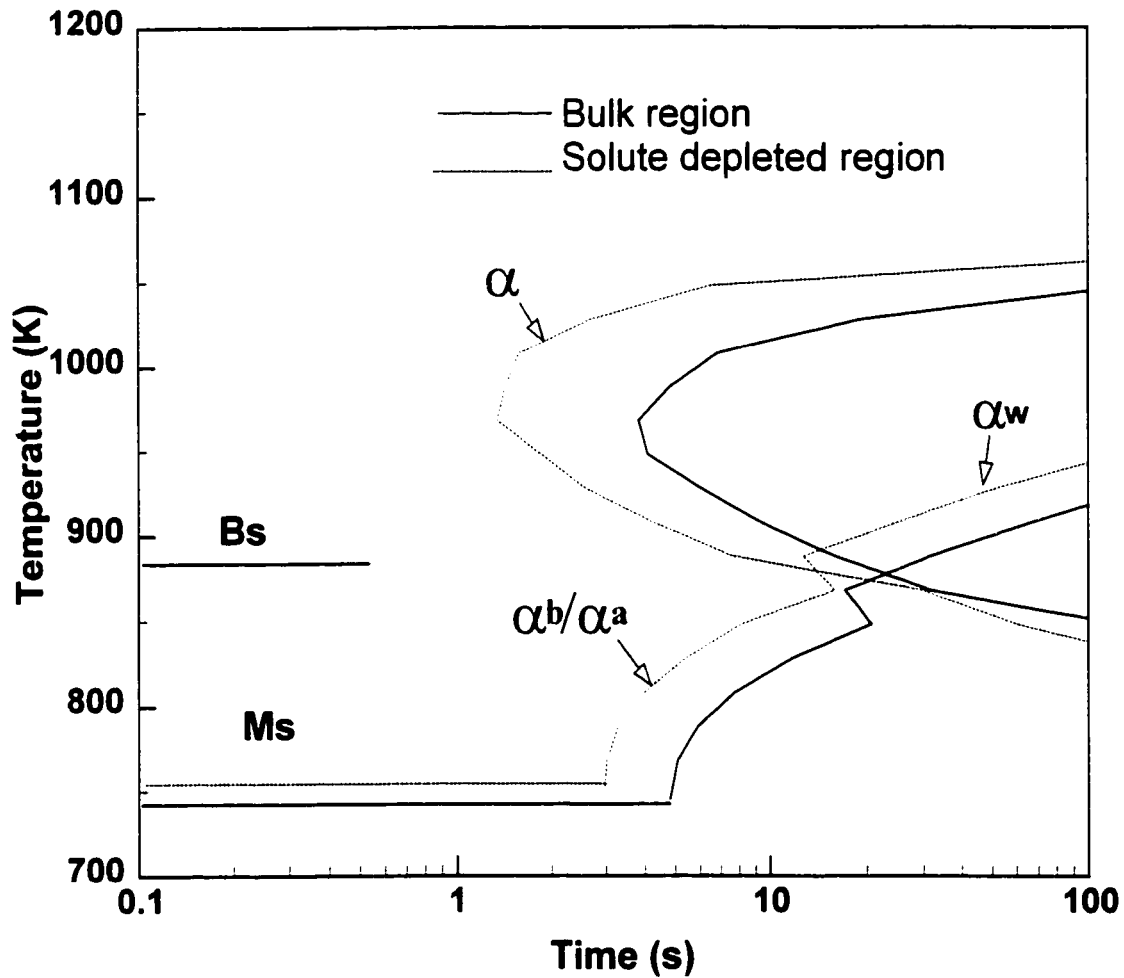
Fig. 4.20: (b) Comparison of TTT diagrams of solute depleted region and bulk region in weld 5. The symbols α. α_w, α_a, and α_b represent allotriomorphic ferrite, Widmanstatten ferrite, acicular ferrite, and bainite, respectively. Ms and Bs are the starting temperatures for martensite and bainite, respectively. Composition in solute depleted region (%): 0.065 C, 0.24 Si, and 1.37 Mn. Composition in bulk region (%): 0.065 C, 0.33 Si, and 1.83 Mn.
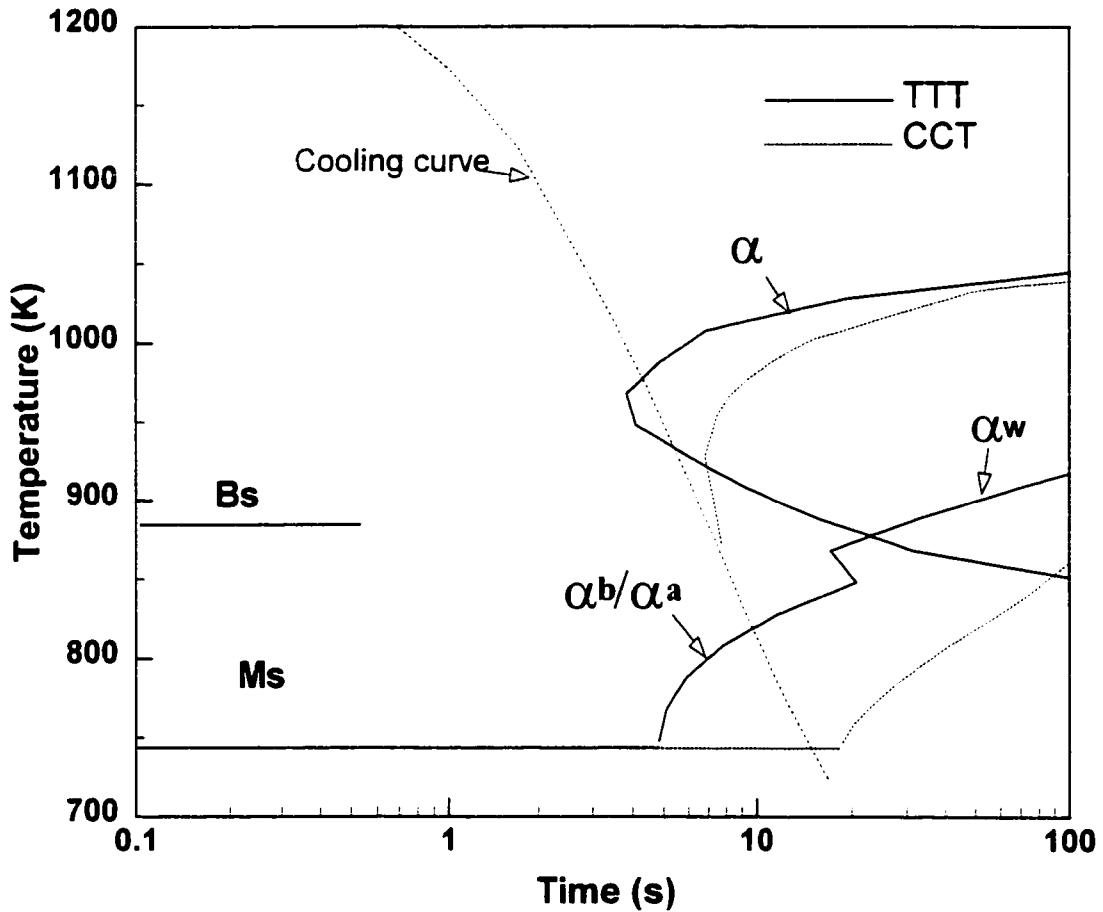
Fig. 4.21: (a) Comparison of CCT and TTT diagrams in the bulk region of weld 5. The symbols α, α_w, α_a, and α_b represent allotriomorphic ferrite, Widmanstatten ferrite, acicular ferrite, and bainite, respectively. Ms and Bs are the starting temperatures for martensite and bainite, respectively. Composition in bulk region (%): 0.065 C, 0.33 Si, and 1.83 Mn. The cooling curve was calculated from the 3D model.
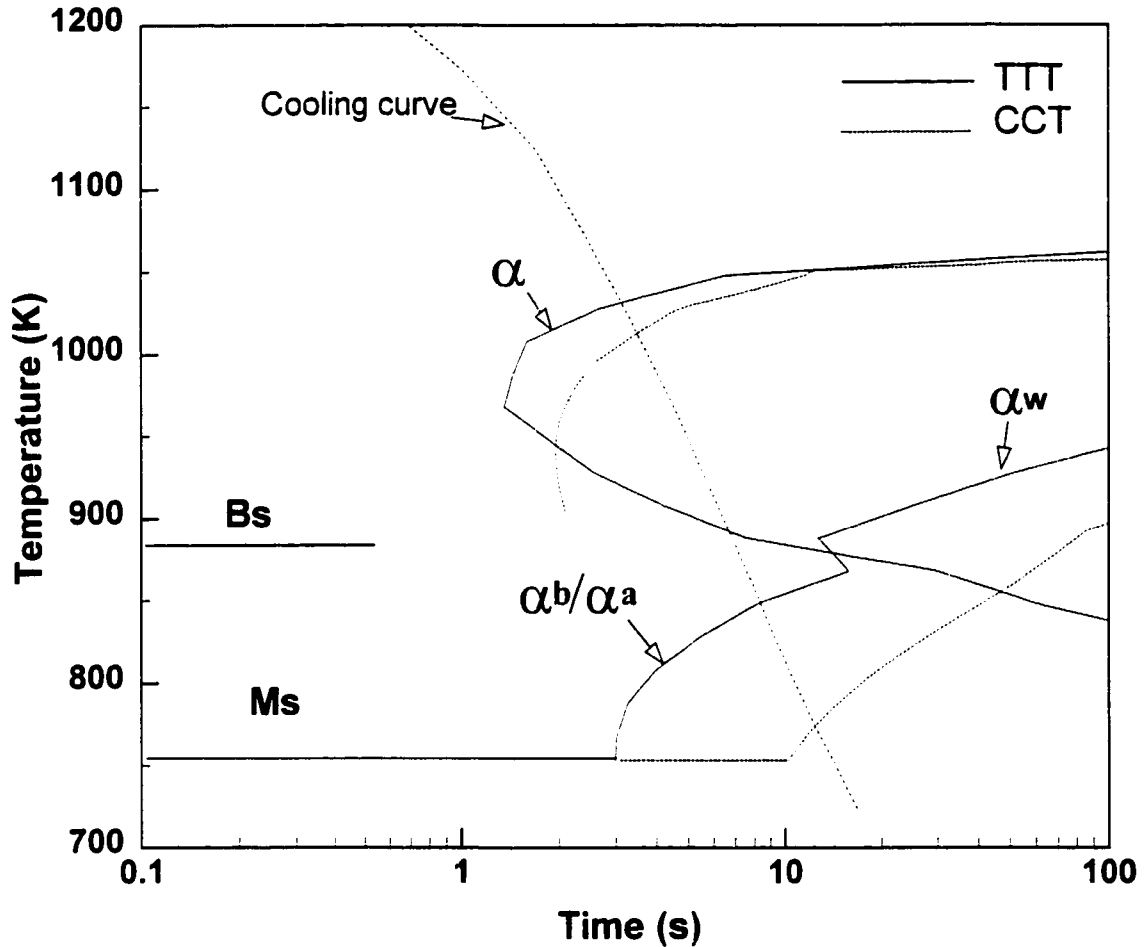
Fig. 4.21: (b) Comparison of CCT and TTT diagrams in the solute depleted region of weld 5. The symbols α, α$_w$, α$_a$, and α$_b$ represent allotriomorphic ferrite, Widmanstatten ferrite, acicular ferrite, and bainite, respectively. Ms and Bs are the starting temperatures for martensite and bainite, respectively. Composition in solute depleted region (%): 0.065 C, 0.24 Si, and 1.37 Mn. The cooling curve was calculated from the 3D model.

ferrite and Widmanstatten ferrite in this weld were experimentally determined to be 0.28 and 0.11. respectively. Therefore, the CCT diagram calculated from the composition in the bulk region cannot explain the weld metal microstructural evolution. On the other hand, the weld metal microstructure can be well explained by the CCT diagram considering solute depletion, i.e., the segregation of alloying elements during solidification. According to the CCT diagram in the solute depleted region as shown in Fig. 4.21(b), the cooling curves intercept both the upper and the lower C curves. Thus, various phases such as allotriomorphic ferrite (α), Widmanstatten ferrite (α_w), and acicular ferrite (α_a)/bainite (α_b) are expected in this weld.

4.2.2.6 Phase Volume Fractions

To quantitatively calculate the phase volume fractions in the weld metal, the two sets of cooling rates calculated from the 3D numerical model and the empirical equation.[35] respectively, were coupled with the Bhadeshia's phase transformation model.[12-14] The calculated phase volume fractions from using these two sets of cooling rates are compared with the experimental data in Table 4.16. The symbols V_α, V_w, V_a and W_m in Table 4.16 represent the volume fractions of allotriomorphic ferrite. Widmanstatten ferrite, acicular ferrite, and microphases. In general, the calculated phase volume fractions from both cooling rates are comparable with the experimental results, as shown in Fig. 4.22(a) and (b). The data points are scattered around the ideal line, in which the calculated volume fractions are equal to the corresponding experimental data. By comparing the experimental data with those obtained using cooling rate from the 3D model, it was found that the average differences in the values of V_α, V_w, and V_a+W_m were 26.0%, 32.0%, and 15.0%, respectively. By using cooling rate from empirical equation, the average differences in the values of $V\alpha$, Vw, and $Va+Wm$ were found to be 49.7.%, 34.0%, and 29.6.%, respectively. Thus, the phase volume fractions predicted by using cooling rate from the 3D model are better than those predicted by using cooling rate from the empirical equation.

It should be noted that the calculated values of V_α are always higher than the experimental values. This is because soft impingement, i.e. the retardation of growth

Table 4.16: Comparison of calculated volume fractions using model (A) and empirical equation (B) with experimental volume fractions[9](C).

Weld	V_α			V_w			$V_a + V_m$		
	A	B	C	A	B	C	A	B	C
1	77	91	60	8	2	29	15	7	11
2	44	52	40	38	35	36	18	13	24
3	41	49	33	28	27	36	31	24	31
4	39	43	30	28	25	25	33	33	45
5	35	43	28	23	21	11	42	35	61
6	45	53	35	26	24	32	29	23	33
7	38	45	34	24	22	28	38	33	38
8	32	38	27	15	14	22	53	49	51
9	46	55	28	19	18	21	35	28	51

* The symbols V_α, V_w, V_a, and V_m represent the volume fractions of allotriomorphic ferrite, Widmanstatten ferrite, acicular ferrite, and microphases.

kinetics due to the overlap of carbon concentration fields near several particles, was ignored in the calculations. Consequently, the parabolic thickening rate constant for allotriomorphic ferrite, α_1 in equation (2.21), was overpredicted by the transformation model. This overprediction can be easily understood from equation (2.22), in which the value of α_1 was calculated. Since the overlap of carbon concentration fields was not considered, the value of the weighted average diffusivity of carbon in austenite, $\overline{D}$ in equation (2.22), was higher than the actual value. As a result, the calculated value of α_1 was higher than the actual value and the model overpredicted the volume fraction of allotriomorphic ferrite. Because the cooling rate calculated from the 3D heat transfer model is higher than that from empirical equation,[35] the calculated time for allotriomorphic ferrite formation in the former is shorter than that in the latter. Therefore, the calculated value of V_α by using the cooling rate from the 3D heat transfer model is lower than that obtained by using the cooling rate from the empirical equation.
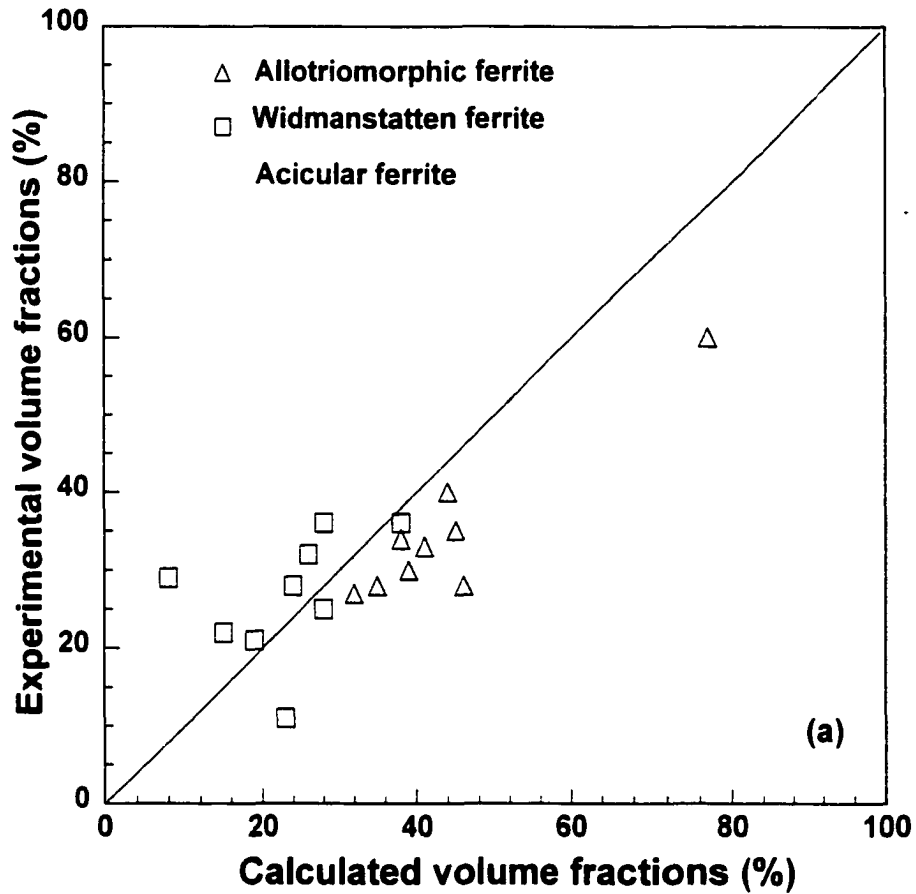
Fig. 4.22: (a) Comparison of the calculated phase volume fractions with the experimental results by using cooling rate from the 3D model. Welding conditions: manual metal arc welding, 180 A, 23 V, 4 mm/s, 523 K interpass temperature.
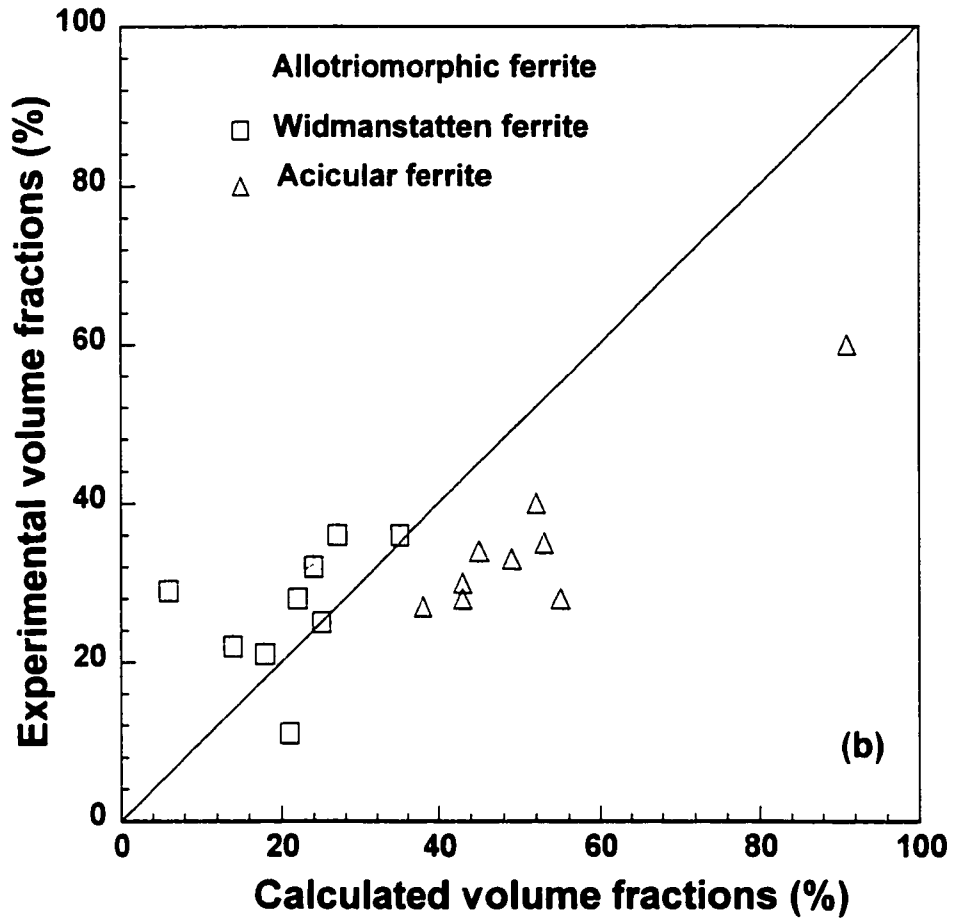
Fig. 4.22: (b) Comparison of the calculated phase volume fractions with the experimental results by using cooling rate from empirical equation.[35] Welding conditions: manual metal arc welding, 180 A, 23 V, 4 mm/s, 523 K interpass temperature.

4.3 Summary and Conclusions

The macro- and microstructures in the HSLA-100 and C-Mn steel weld metals were modeled by coupling a heat transfer and fluid flow model with a well tested phase transformation model. The temperature and velocity fields, the cooling rates, and the shape and size of the FZ and the HAZ were calculated from the heat transfer and fluid flow model. The TTT and CCT diagrams were calculated from the phase transformation model. The microstructures in the investigated steels were examined by coupling the calculated cooling rates with the CCT diagrams. The following conclusions can be made through this study.

For HSLA-100 steel:

(1) The values of effective viscosity and effective thermal conductivity in the weld pool of GMA welding were spatially distributed rather than constants. The high computed values of turbulent viscosity and thermal conductivity indicated that the transport of heat and momentum in the weld pool was significantly aided by turbulence.

(2) "Finger penetration", a unique weld geometric feature in GMA welding, could be satisfactorily predicted by the present model. Fair agreement was achieved between the calculated shape and size of the FZ and the HAZ and the corresponding experimentally observed values.

(3) The calculated cooling rates from the model agreed fairly well with the experimental results. The calculated cooling rates coupled with computed CCT diagrams were used to predict the microstructures in the weld metal of HSLA-100 steel.

(4) The HSLA-100 steel weld metal consisted predominantly of acicular ferrite with small amounts of bainite. Small amounts of allotriomorphic and Widmanstatten ferrites were also observed at high heat inputs. The observed microstructures can be qualitatively predicted from the computed the cooling rates and CCT diagrams.

For C-Mn steels:

(1) The temperature and velocity fields in three dimensions, the cooling rates, and the shape and size of the fusion zone and heat-affected zone were calculated from the heat transfer and fluid flow model. Compared to the cooling rates from an empirical equation, the cooling rates from the model were closer to the experimental data.

(2) The effects of chemical composition on the weld metal microstructure of C-Mn steels can be quantitatively predicted by coupling the thermal model with the available phase transformation model. The phase volume fractions in the welds with different carbon and manganese contents were quantitatively calculated. The calculated phase volume fractions by using cooling rate from the heat transfer and fluid flow model were found in better agreement with the experimental results than those obtained by using the cooling rate from an empirical equation.

The above agreements between the calculated and experimental results in both HSLA-100 and C-Mn steels indicate significant promise for understanding macro- and microstructures of steel welds from the combination of the fundamental principles of transport phenomena and phase transformation theory.

4.4 References

1. J. M. B. Losz and K. D. Challenger: *Recent Trends in Welding Science and Technology*, ed. by S. A. David and J. M. Vitek, p. 229, ASM INTERNATIONAL, Materials Park, OH (1990).

2. R. W. Fonda, G. Spanos, and R. A. Vandermeer: *Trends in Welding Research*, ed. by S. A. David and J. M. Vitek, p. 277, ASM INTERNATIONAL, Materials Park, OH (1995).

3. D. G. Howden, L. Zhang, R. S. Green, K. Smapath, J. H. Devletian, and D. Singh: *International Trends in Welding Science and Technology*, ed. by S. A. David and J. M. Vitek, p. 359, ASM INTERNATIONAL, Materials Park, OH (1993).

4. G. Spanos, R. W. Fonda, R. A. Vandermeer and A. Matuszeski: *Metall. and Maters. Trans. A*, **26A**, 3277 (1995).

5. A. D. Wilson, E. G. Hamburg, D. J. Colvin, S. W. Thomposon, and G. Krauss: *Proceedings of microalloying 88, World Materials Congress*, p. 259, ASM INTERNATIONAL, Materials Park, OH (1988).

6. S. W. Thomposon, D. J. Colvin, and G. Krauss: *Metall. Trans. A*, **21A**, 1493 (1990).

7. R. P. Martukanitz, P. R. Howell, and W. A. Pratt: *International Trends in Welding Science and Technology*, ed. by S. A. David and J. M. Vitek, p. 271, ASM INTERNATIONAL, Materials Park, OH (1993).

8. D. J. Abson: *Welding in the world*, **27**, 76 (1989).

9. L.-E. Svensson, and B. Gretoft: *Weld. J.*, **73**, 454s (1994).

10. G. M. Evans: *Weld. J.*, **62**, 313s (1983).

11. G. M. Evans: *Weld. J.*, **59**, 67s (1980).

12. H. K. D. H. Bhadeshia and L. -E. Svensson: in *Mathematical Modeling of Weld Phenomena*, ed. by H. Cerjak and K.E. Easterling, p. 109, Institute of Materials, UK (1993).

13. H. K. D. H. Bhadeshia: in *'Recent Trends in Welding Science and Technology'*, ed. by S. A. David and J. M. Vitek, p. 189, ASM INTERNATIONAL, Materials Park, OH (1990).

14. H. K. D. H. Bhadeshia, L. -E. Svensson, and B. Gretoft: *Acta metall.*, **33**, 1271 (1985).

15. J. F. Lancaster: *The Physics of Welding*, Pergamon Press, New York, NY (1984).

16. S. Kumar and S. C. Bhaduri: *Metall. Trans. B*, **25B**, 435 (1994).

17. D. N. Shackleton and W. Lucas: *Weld. J.*, **53**, 537s (1974)..

18. G. W. Tichellar, G. Jelmorini, and G. J. P. M. Vander Henvel: *Droplet Temperature Measurement in Arc Welding*, IIW Document 212-411-77, 1977.

19. S. Kou and Y. H. Wang: *Metall. Trans. B*, **17A**, 2271 (1986).

20. P. Sahoo, T. DebRoy, and M. J. McNallan: *Metall. Trans. B*, **19B**, 483 (1988).

21. R. T. C. Choo and J. Szekely: *Weld. J.*, **73**, 25s (1994).

22. K. Hong, D. C. Weckman, and A. B. Strong: *Trends in Welding Research*, ed. by H. B. Smartt, J. A. Johnson and S. A. David, p. 399, ASM INTERNATIONAL, Materials Park, OH (1996).

23. A. D. Wilson, E. G. Hamburg, D. J. Colvin, S. W. Thomposon, and G. Krauss: *Proceedings of microalloying 88, World Materials Congress*, p. 259, ASM INTERNATIONAL, Materials Park, OH (1988).

24. L.-E. Svensson, B. Gretoft, Svensson, and H. K. D. H. Bhadeshia: *Scand. J. Metallurgy*, **15**, 97 (1986).

25. D. J. Abson: *Welding in the world*, **27**, 76 (1989).

26. F. J. Barbro, P. Krauklis and K. E. Easterling: *Materials Science and Technology*, **5**, 1057 (1989).

27. P. R. Howell: 5th International Conference on Trends in Welding Research, ASM International, in press (1998).

28. J. Ryder, Z. Yang, T. DebRoy, and P. R. Howell: "Microstructural Science", 26, International Metallography Society Conference Proceedings, Ottawa, (1998).

29. Y. Horri, M. Wakabayashi, S. Ohkita, and M. Namura: *Nippon Steel Technical Report*, **37**, 1 (1988).

30. R. A. Ricks, G. S. Barritte, and P. R. Howell: *J. Mater. Sci.*, **17**, 732 (1982).

31. M. Strangwood and H. K. D. H. Bhadeshia: in Advances in Welding Research, ed. S. A. David, p. 209, ASM International, Metals Park, OH (1987).

32. H. K. D. H. Bhadeshia: *Bainite in Steels*, Institute of Materials, UK (1992).

33. B. Gretoft, H. K. D. H. Bhadeshia, and L. -E Svensson: *Acta Stereologia*, **5**, 365 (1986).

34. A. Duncan: "Guide to the examination of ferritic steel weld metals" in IIW Doc. IXJ-123-87.

35. L.-E. Svensson, B. Gretoft, Svensson, and H. K. D. H. Bhadeshia: *Scand. J. Metallurgy*, **15**, 97 (1986).

36. G. M. Evans: "Effect of interpass temperature on the microstructure and properties of C-Mn all-weld-metal deposits", in IIW Doc. II-A-460-78.

37. K. Mundra, J. M. Blackburn, and T. DebRoy: *Science and Technology of Welding and Joining*, **2**, 174 (1997).

38. W. M. Pun and D. B. Spalding: *Heat Transfer Section Report*, No. HTS/76/2, Imperial College, London, 1976.

39. J. M. Blackburn: Private communication, March 1996, Naval Surface Warfare Center, Annapolis, MD.

40. *Smithells metals reference book*, 6th edn, ed. by E. A. Brandes, Butterworth, London, 1983.

41. K. Mundra, T. DebRoy, and K. Kelkar: *Numerical Heat Transfer*, Part A, **29**, 115 (1996).

CHAPTER 5

MODELING OF WELD GEOMETRY, PHASE DISTRIBUTION, AND GRAIN STRUCTURE IN THE HAZ OF COMMERCIALLY PURE TITANIUM

5.1 Introduction

The purpose of the study reported in this chapter is to systematically model the weld geometry, the phase distributions, and the grain structure in the HAZ of GTA welded commercially pure titanium. Recently, a spatially resolved X-ray diffraction (SRXRD) technique using synchrotron radiation has been developed to study the phase transformations *in situ* in the HAZ during welding of commercially pure titanium.[1-4] A real-time phase distribution map in the HAZ of titanium weld was established by Elmer et al[1-2] using this unique technique. The real-time map provides phase distribution information and direct evidence of phase transformation kinetics in the HAZ, which cannot be obtained by traditional experimental methods.

For quantitative understanding of the results from the real-time experiments, mathematical modeling is needed. Mathematical modeling combined with the real-time experimental results is effective in studying the kinetics and the mechanisms of phase transformations during welding. Furthermore. the spatial phase distribution map in the HAZ determined by experimental methods is specific for a given set of welding conditions. In the absence of modeling work, when the welding parameters change, a new set of time consuming experiments need to be undertaken to obtain the phase distribution map. In contrast, the phase distirbution maps under various welding conditions can be predicted based on mathematical model by using the kinetic data from previous study.

Pure titanium has two phase transitions:[5] the allotropic transformation α(hcp) $\leftrightarrow$ β(bcc) in the solid state at 1155 K and the melting/solidification transition β(bcc) $\leftrightarrow$ L (liquid) at 1941 K. The α(hcp) $\leftrightarrow$ β(bcc) phase transformation in titanium can occur by

classical nucleation and growth mechanism,[6,7] massive,[6-9] or martensitic[8] mechanisms. The $\beta \rightarrow \alpha$ phase transformation has been studied under continuous cooling conditions in pure titanium. Ti-O alloys, dilute titanium, and some other titanium based binary alloys. Cormier et al[6] studied the kinetics of the $\beta \rightarrow \alpha$ phase transformation in both pure titanium and Ti-O alloys by recording the electrical resistance and the temperature during quenching the samples. They found that the $\beta \rightarrow \alpha$ transition took place by a classical nucleation and growth mechanism (e.g. thermally activated process) at cooling rates less than 3000 K/s. The martensitic transformation mechanism (e.g. athermal process) can only take place[6] at cooling rates larger than 3000 K/s. According to Cormier's results, interstitial oxygen at concentrations up to 1.2 at.% has no significant effect on the kinetics of transformation. Debuigne et al[39] suggested that the $\beta \rightarrow \alpha$ phase transformation takes place by classical nucleation and growth mechanism rather than martensitic transition mechanism based on dilatometry results.

Data on the $\alpha \rightarrow \beta$ transformation in titanium during heating is scarcer than that of the $\beta \rightarrow \alpha$ transformation that occurs during cooling. Recently, Elmer et al[1-4] investigated both the $\alpha \rightarrow \beta$ transformation during heating and the $\beta \rightarrow \alpha$ transformation during cooling in the heat affected zone of commercially pure titanium weldment by using spatially resolved X-Ray diffraction (SRXRD) method. For the commercially pure titanium investigated in their study, the transformation from α (hcp) phase to β (bcc) phase was found to occur at 1158 ± 5 K due to the presence of oxygen, iron, and other impurities.[1] On the other hand, the transition temperature from β (bcc) phase to α (hcp) phase was identified to be[1] 1188 ± 5 K. Fig. 5.1 shows the real-time phase distribution map[1] in the HAZ of commercially pure titanium. As the material approaches and then moves away from the heat source, a series of changes take place in the HAZ and result in several sub regions as following: (1) the annealed and recrystallized α-Ti zone (α_{AR}); (2) the completely recrystallized α-Ti zone (α_{RG}); (3) partially transformed α-Ti zone (β_L), where the α-Ti and β-Ti coexist; (4) single β phase region (β); and (5) back-transformed α-Ti (α_{BT}). Determination of the phase boundaries existing between these regions can not only provide phase distribution information, but also important phase transition
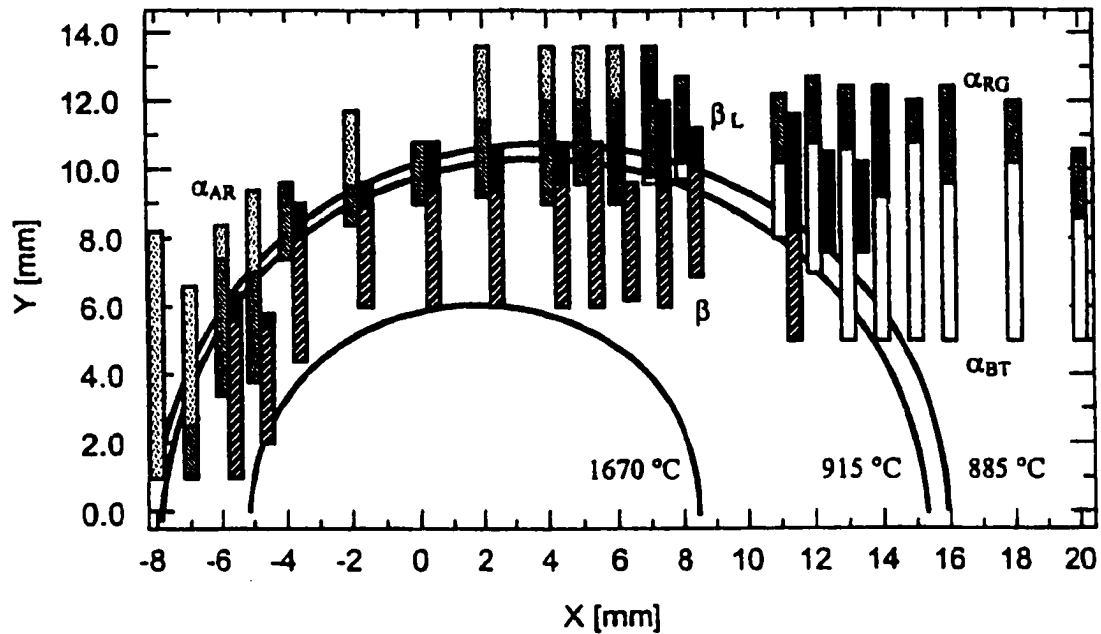
Fig. 5.1: Real-time phase distribution map in the GTA welded commercially pure titanium by using spatially resolved X-ray diffraction (SRXRD) technique.[1] The annealed and recrystallized α-Ti, α_{AR}, is shaded with small dots; The recrystallized α-Ti, α_{RG}, is shaded with right diagonal striples; The back-transformed α-Ti α_{BT}, is shaded with solid white; The single β phase region, β, shaded with left diagonal striples; The symbol of β_L, shaded with solid black is the β-Ti that coexists with α-Ti in low amount.

kinetics data, which can be used to identify possible phase transformation mechanisms. For example, the kinetic data of the $\alpha\rightarrow\beta$ transition during heating are scarce and its transformation mechanism is uncertain. Elmer et al[1-4] evaluated the kinetics for both the $\alpha\rightarrow\beta$ transition during heating and the $\beta\rightarrow\alpha$ transition during cooling in titanium from experimental phase distribution map. The average time for $\beta\rightarrow\alpha$ transition at various locations was estimated to be about 0.91 seconds. The $\beta\rightarrow\alpha$ transition was thought to occur via a massive transformation.[1] On the other hand, the minimum time for the $\alpha\rightarrow\beta$ transition during heating was estimated to be about 1.81 seconds. Since oxygen stabilizes the α phase to higher temperatures, it was suggested that the $\alpha\rightarrow\beta$ transition during heating was probably controlled by the long range diffusion of oxygen.[1]

5.2 Modeling Task in This Study

The purpose of this study is to predict the weld geometry, phase distributions, and the grain structure in the HAZ of the commercially pure titanium. Knowledge of temperature field and thermal cycles is a prerequisite for quantitative understanding of the weld geometry, the phase transformations, and the grain growth at various locations in the HAZ. In this study, the 3D turbulent heat transfer and fluid flow model will be used to calculate the temperature field and thermal cycles. For the sake of comparison, a laminar model will also be used to calculate the temperature field and the corresponding weld geometies. The nature of the flow in the weld pool under various welding conditions will be examined.

The phase boundaries of the $\alpha/(\alpha+\beta)$, the $(\alpha+\beta)/\beta$, and the β/L (liquid) in the HAZ of titanium welds will be identified. As a first effort to model the phase transitions in titanium, only the $\alpha\rightarrow\beta$ transition during heating will be considered in the present study. This is not only because of its uncertain transformation mechanism but also the uniqueness of the kinetic data obtained from the SRXRD technique. These kinetic data are very difficult to obtain by traditional methods because the microstructures that form during heating are subsequently altered by the transformations that take place during

cooling. The calculated rates of α to β phase transformation assuming different phase transformation mechanisms are compared with the corresponding experimental results to identify the mechanism of this transformation.

In addition to the real-time phase distribution, one objective of the present study is to establish a real-time 3D grain structure map in the HAZ. The spatial distribution of grain size in the entire HAZ will be modeled by coupling the 3D Monte Carlo (MC) model with the 3D heat transfer and fluid flow model. The capability of the 3D MC model for quantitative prediction of the spatial grain size distribution in the entire HAZ will be tested for various welding conditions. The simulated grain structure will be compared with the corresponding experimental results.

5.3 Experimental Procedure

5.3.1 Welding and Real -Time Determination of Phases

The welding and Spatially Resolved X-Ray Diffraction (SRXRD) experiments were conducted by Dr. J. W. Elmer and Dr. J. Wong at Lawrence Livermore National Laboratory.[1-4] A schematic diagram of the experimental setup is shown in Fig. 5.2. Grade 2 commercially pure titanium bar of 10.2 cm diameter was welded by gas tungsten arc (GTA) welding. The composition of the as received bar was (in wt%): 0.14% Fe, 0.17% O, 0.03% Al, 0.02% Cr, 0.08% C, 0.001% H, 0.014% N, 0.02% Ni, 0.005% V, and 0.004% Si. GTA welds were made at a constant power of 1.9 kW (100 A, 19 V), and extra high purity helium (99.999%) was used as both the welding and shielding gas. The titanium bar was rotated at a constant speed below the fixed electrode.

In the present study, four welds at different heat inputs were examined. Different heat inputs were obtained by changing the welding speed while keeping other parameters unchanged. The welding conditions of the four welds are listed in Table 5.1. The weld geometries and the grain size distributions in the HAZ of the four welds can be used to

validate the model results. The SRXRD experiment by Elmer et al[1-2] was only done on weld 2 since considerable work is needed for the real-time measurements.

Table 5.1: Weld conditions for GTA welding of commercially pure titanium

Weld Number	Speed (mm/s)	Current (A)	Voltage (V)	Energy per length (kJ/mm)
1	0.5	108	18.2	3.9
2	1.0	108	18.5	2.0
3	2.0	108	19.0	1.0
4	4.0	108	19.8	0.5

* No preheat for all of the welds.

The SRXRD experiments were performed by Drs. Elmer and Wong[1-4] on the 31-pole wiggler beam line, at Stanford Synchrotron Radiation Laboratory (SSRL) with Stanford Positron-Electron Accumulation Ring (SPEAR) operating at an electron energy of 3.0 GeV and an injection current of about 100 mA. The focused monochromatic synchrotron beam (8.5 keV) was passed through a 180 μm tungsten pinhole to render a 200 μm beam on the sample at an incident angle of about 25°. Additional details about the synchrotron beam are available in the literature.[12] The welding assembly was mounted to a translation stage driven by a stepper motor with 10 μm precision and placed inside the environmental chamber to prevent oxidation of titanium during welding. Spatial mapping of the phases in the HAZ was performed using the translation stage to manipulate the weld (welding torch and workpiece) with respect to the fixed x-ray beam in order to probe discrete regions around the weld. Movements perpendicular to the centerline of the weld were controlled by a computer and were achieved by direct translation of the workpiece with respect to the x-ray probe. A typical SRXRD run consisted of gathering 40 diffraction patterns at 200 μm apart along a pre-determined path to span a range of 8 mm through the HAZ.
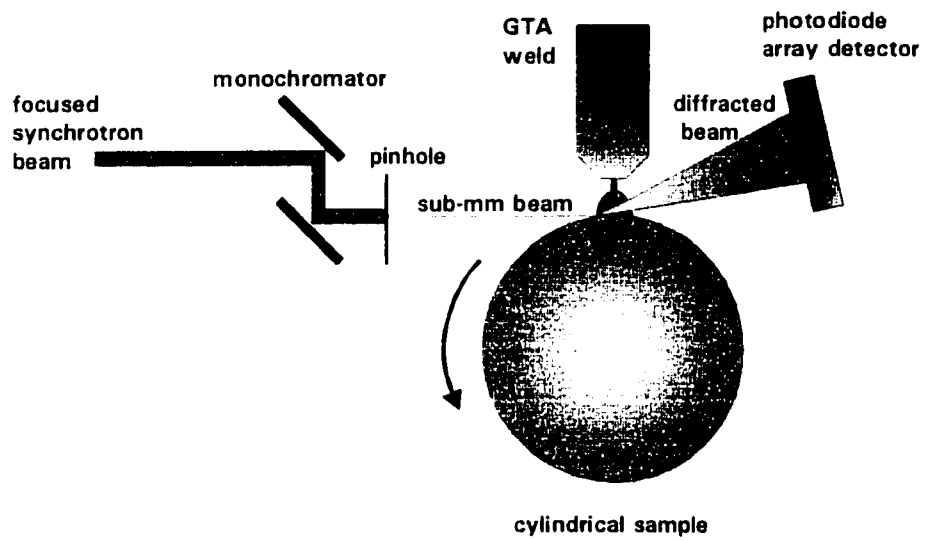
Fig. 5.2: Experimental setup.[1]

SRXRD data were taken by Drs. Elmer and Wong during welding by positioning the beam at a fixed location with respect to the welding electrode and collecting data for 6 s per diffraction scan while the bar rotated under the torch at a constant speed.[1-4] Up to 40 scans were taken during one revolution of the weld around the cylinder by incrementally jogging the weld in 200 μm steps to new locations at 6 s intervals. In this way a series of x-ray diffraction patterns were collected for a given weld along a direction perpendicular to and away from its centerline, and thus spanning an 8mm range through the HAZ. Results of the sequential linear x-ray diffraction measurements made perpendicular to the welding direction were combined to construct a phase transformation map around the liquid weld pool. Additional details about the welding procedure are available in the literature.[1-4]

5.3.2 Material Characterization

Optical metallography was performed by the author on post-weld samples using conventional polishing and etching techniques. Etching was performed in a chemical bath of 15 parts lactic acid, 5 parts nitric acid and 1 part hydrofluoric acid. To quantitatively describe the grain size gradient in the HAZ, the mean grain sizes at various distances from the fusion line were measured using lineal intercept method[13] by placing test lines parallel to the fusion line. Due to significant grain size gradient in the HAZ, different magnifications in the range of 20× to 100× were used depending on the locations from the fusion line to ensure accurate grain size measurements.

5.4 Mathematical Modeling

5.4.1 Calculation of Temperature Field and Thermal Cycles

The temperature fields and thermal cycles under various welding conditions were calculated by the 3D turbulent heat transfer and fluid flow model. The model has been described in detail in chapter 3. The physical dimensions of the solution domain were

32.0 (length) × 6.3 (width) × 5.1 (thickness) cm³. A 56x30x25 grid system was used in the calculations. Spatially non-uniform grids were used for maximum resolution of variables. Finer grids were used near the heat source. The minimum grid spacing was 0.005 cm directly below the weld pool surface. The thermo-physical properties of the titanium for calculation of the heat transfer and fluid flow are given in Table 5.2. The geometries of the FZ and the HAZ can be predicted based on the calculated temperature field. The calculated thermal cycles at various locations in the HAZ were used for modeling phase transformations and grain growth.

Table 5.2: Data used for the calculation of velocity and temperature fields in titanium welds[1,44]

Physical property	value
Liquidus temperature (K)	1941
Solidus temperature (K)	1941
Density of liquid metal (kg/m³)	4100
Viscosity of liquid (kg/m.s)	5.2×10^{-3}
Thermal conductivity of solid (J/m.s.K)	28.0
Thermal conductivity of liquid (J/m.s.K)	28.0*
Specific heat of solid (J/kg.K)	700.0
Specific heat of liquid (J/kg.K)	800.0
Latent heat of melting (J/kg)	292.6×10^{3}
Temperature coefficient of surface tension (N/m.K)	-0.26×10^{-3}
Thermal expansion coefficient (K⁻¹)	1.7×10^{-6}

* Estimated since no values were available for these data in the literature.

5.4.2 Modeling Phase Transformations in the HAZ

5.4.2.1 Possible Mechanisms

As stated earlier, the α↔β phase transformation in titanium can occur by classical nucleation and growth,[6,9] massive,[6-9] or martensitic[9] mechanism. These mechanisms

compete with one another and the mechanism that is ultimately responsible for the phase transformation depends on the purity of the titanium, its microstructure, and the thermal processing conditions. The martensitic phase transformation occurs only at high rates, and has been reported[6] to take place at cooling rates in excess of 3000K/s. This cooling rate far exceeds those encountered in conventional arc welds and precludes this mechanism. Massive transformations in titanium have been reported to occur at cooling rates similar to those of martensitic transformations,[6] but also at cooling rates which are well within the realm of arc welding.[7] Conventional nucleation and growth phase transformations with long range solute partitioning occur only at low cooling rates and are generally believed to occur with much slower kinetics than massive transformations.[8, 9]

In previous investigation,[1-4] SRXRD was used as an in-situ experimental technique to map the phases that exist around an arc weld in commercially pure titanium. This phase map contains data on the $\alpha \rightarrow \beta$ transformation kinetics in the form of spatial displacements of the product phase with respect to the thermodynamic transformation isotherm. Experimental results[1-4] showed that the $\alpha \rightarrow \beta$ transformation during heating took place with slower rate than the $\beta \rightarrow \alpha$ transformation during cooling. From the SRXRD measurements, the $\beta \rightarrow \alpha$ transformation was estimated[1] to occur with an interface velocity of 100 μm/s, which is consistent with measured interface velocities of massive transformation in dilute titanium alloys.[7] Since massive $\beta \rightarrow \alpha$ transformations during cooling of titanium and titanium alloys have been well documented by other investigators,[6-9] this mechanism was assumed to be responsible for the $\beta \rightarrow \alpha$ transformation during cooling in titanium arc welds. The $\alpha \rightarrow \beta$ transformation, on the other hand, was estimated by the SRXRD measurements to occur at rates more consistent with long range diffusional growth,[3] but a thorough investigation of this mechanism was not performed. Since the $\alpha \rightarrow \beta$ transformation has not been documented nearly as well as the $\beta \rightarrow \alpha$ transformation in the available literature, the transformation kinetics need to be studied in more detail. Here, the isotherms calculated from the turbulent fluid flow and heat transfer model are utilized as an input to a modified JMA kinetic model to study the possible rate controlling step for the $\alpha \rightarrow \beta$ phase transformation.

The principal impurities in the grade 2 titanium are O (0.17 wt. %) and Fe (0.14 wt.%). In the previous study,[1-2] the presence of Fe-rich bcc/omega phase particles distributed throughout the grains was observed in the starting titanium microstructure.[3] These pre-existing particles may provide growth sites for the $\alpha \to \beta$ transformation and also tie up much of the Fe impurities.[1] Therefore, it is likely that the $\alpha \to \beta$ transformation during arc welding takes place by a growth-dominated mechanism whereby nucleation of the β phase is not necessary. Since the $\alpha \to \beta$ transformation could be controlled either by diffusion of titanium or oxygen atoms across the α/β interface, or oxygen atoms long range diffusion, each of these possible scenarios will be modeled to determine which is the most likely to control the $\alpha \to \beta$ transformation rate. The following three mechanisms are considered here: I - an interface controlled mechanism with titanium short-range diffusion (across the α/β interface), II - an interface controlled mechanism with oxygen short-range diffusion (across the α/β interface), and III- a long range solute partitioning mechanism with oxygen diffusion.

5.4.2.2 Calculation of the Phase Transformation

The JMA equation is suitable for describing the kinetics of reactions controlled by the nucleation and growth mechanism.[14-15] Therefore, this equation is applicable to describe the $\alpha \to \beta$ transition in titanium for all the mechanisms assumed in the above three scenarios. To calculate the kinetics of the $\alpha \to \beta$ transition under non-isothermal conditions in the HAZ, a modified JMA equation,[16] equation (3.33), was adopted in the present study. The description of this modified JMA equation was given in chapter 3.

In order to use equation (3.33), the temperature dependence of the transformation rate k(T) and the exponent n have to be specified. The values of k(T) and n are dependent on the transition mechanism assumed. If the transport of Ti atoms across the interface is considered to be the limiting step, the activation energy of the titanium self-diffusion could be taken as the value of $\Delta G(T)$ in equation (3.32) to calculate k(T). If the transport of oxygen atoms across the interface is considered to be the limiting step, the activation energy of the oxygen diffusion in titanium could be taken as the value of $\Delta G(T)$. In both

cases, it is assumed that the pre-existing Fe-stabilized bcc/omega phase particles[1,2] provide a sufficient density of growth sites so that nucleation of β particles from the matrix is not required. Under these zero-nucleation rate conditions, a value of n = 1.5 can be assumed for the JMA nucleation mode exponent for long range diffusion and n = 3.0 can be assumed for interface controlled growth.[11]

The kinetic data used in the JMA model is summarized in Table 5.3 for three different scenarios. In all three mechanisms, the pre-exponential constant k_0 in equation (3.32) took the same value. This value was estimated from the experimental data in the literature[35] and was found to be 2.18×10^6. For the purpose of this paper, k_0 will be taken to be a constant for the $\alpha \rightarrow \beta$ transformation since the temperature dependence of k_0 is not known for titanium and also it is believed that the temperature dependence of k_0 can be considered to be small[17] compared to the exponential term in equation (3.32).

Table 5.3: Kinetic data used for the calculation of the $\alpha \rightarrow \beta$ phase transformation for different proposed mechanisms.

Scenarios	Assumed mechanisms	n	K_0	ΔG (kJ/mole)
I	Titanium short range diffusion (interface controlled)	3.0	2.18×10^6	152.7 (ref. 19)
II	Oxygen short range diffusion (interface controlled)	3.0	2.18×10^6	138.2 (ref. 29)
III	Oxygen long range diffusion	1.5	2.18×10^6	138.2 (ref. 29)

5.4.3 Modeling Grain Growth in the HAZ

The grain growth in the HAZs of the welds was simulated by coupling the 3D Monte Carlo model with the 3D heat transfer and fluid flow model. As discussed in chapter 2, different kinetic models can be used for establishing the Monte Carlo

simulation step (t_{MCS}) with real time-temperature kinetics. These kinetic models include Atomistic Model, Grain Boundary Migration (GBM) Model, and Experimental Data Base (EDB) Model. The Atomistic Model is not suitable for the present simulation since the size of the simulated domain is considerably larger than the atomic scale. In addition, the EDB model can not be used in this study because the isothermal grain growth data for the commercially pure titanium are insufficient. The experimental data for isothermal grain growth in the β-phase region of the commercially pure titanium were limited to two temperatures (1000 °C and 1100 °C) in the literature.[30] Therefore, the Grain Boundary Migration Model (GBM) was used in present study to establish the relation between the t_{MCS} and the real time. In the GBM model, the grain growth is assumed to obey parabolic relationship, i.e., the grain growth exponent is taken as the ideal value of 2.0. The soundness of using the GBM model to simulate grain growth in commercially pure titanium can be justified by the available isothermal grain growth kinetic data in the literature, in which the grain growth exponent was found[30] to be approximately 2.0 in the β-Ti phase region within the temperature range from 1000 °C to 1100 °C.

The algorithm and the governing equation in the GBM model has been described in chapter 2. The values of t_{MCS} at various locations can be calculated using equation (2.42) by considering the effects of the thermal cycles and material properties. In the present simulation, the initial β-Ti grain size, L_0, was assumed to be equal to the α-Ti grain size after recrystallization[1] (25μm). Although this assumption does not consider the grain size change due to the α→ β transformation, it sets an upper limit to the starting β-Ti grain size since the size of the daughter phase is less than that of the parent phase. The value of activation energy for grain growth usually ranges from 1/2 to 2/3 of that for bulk diffusion.[18] Here we approximately take 2/3 of the activation energy of Ti atom bulk diffusion[19] (153.0 kJ/mol) as the value of that for grain growth. The grain boundary energy has been assumed to be a constant and independent of temperature.[20-24] The data of titanium grain boundary energy is not available in the literature, but was estimated to be 0.75 J/m^2 as indicated by the procedure given in appendix I. The value of Vm can be calculated based on the density and atomic weight of titanium. The activation entropy for grain boundary migration, ΔS_a, can be assumed[23] to be equal to the entropy of fusion of

the material, ΔS_f. The value of ΔS_a for titanium[25] is 7.21 $J \cdot mol^{-1} \cdot K^{-1}$. The data used for the modeling grain growth are listed in Table 5.4.

Table 5.4: Data used for the calculation of the grain growth kinetics in single β phase region[1,23,25]

Initial average grain size, L_0	25 μm
Activation energy for grain growth, Q	1.02×10^5 J/mol
Grain boundary energy, γ	0.75 J/m^2
Accommodation probability, A	1.0
Average number per unit area at grain boundary, Z	2.0×10^{19} atoms$\cdot m^2$
Atomic molar volume, V_m	1.1×10^{-5} $m^3 \cdot mol^{-1}$
Activation entropy, ΔS_a	7.21 $J \cdot mol^{-1} \cdot K^{-1}$
Avagadro's number, N_a	6.02×10^{23} mol^{-1}
Planck's constant, h	6.624×10^{-34} $J \cdot s$
Lattice point spacing, λ	50 μm in the first grid system $\quad$ 25 μm in the second grid system

5.5 Results and Discussions

5.5.1 Calculated Temperature Distributions and Flow Patterns

An example of the computed temperature and velocity fields in the weldment is shown in Fig. 5.3. The general features of the calculated temperature field are consistent with the results reported in the literature[26] and those predicted in the previous chapter. In front of the heat source, the temperature gradient is greater than that behind the heat source. The high temperature gradient results in slightly greater liquid metal velocities in front of the heat source than behind the heat source. On the surface of the weld pool, the liquid metal moves from the center to the periphery. This is expected for a metal with a very low concentrations of surface active elements (e.g. very low sulphur and low free oxygen contents) which results in a negative temperature coefficient of surface tension
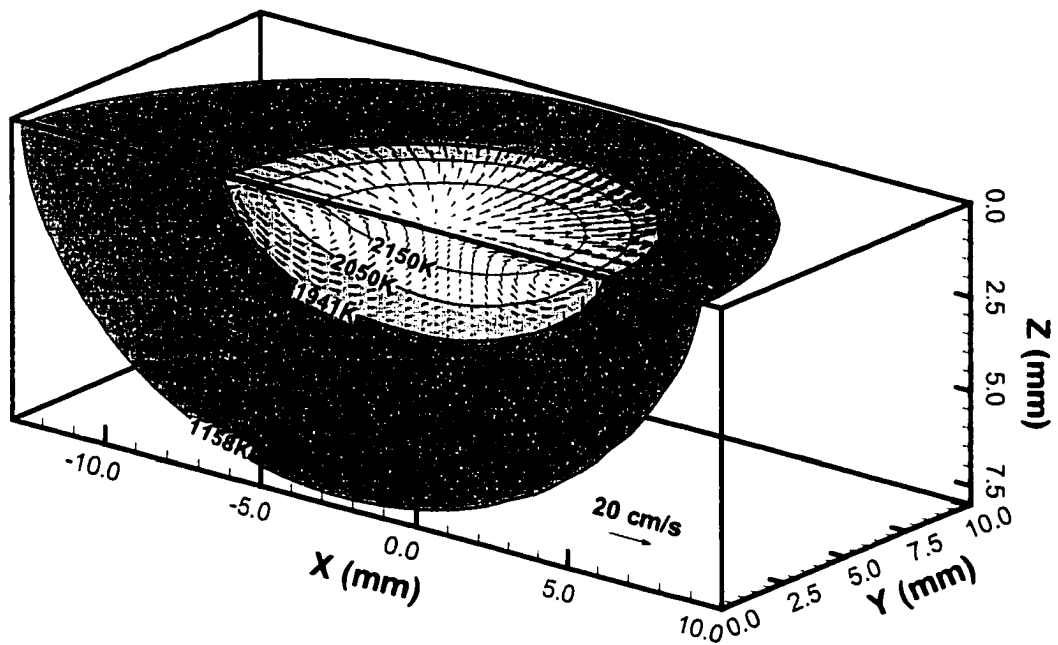
Fig. 5.3: Calculated temperature and velocity fields in three dimensions in weld 2. Welding conditions: GTA, 100A, 19V, welding speed: 1.1 mm/s.

dγ/dT. As the result of the outward fluid flow and heat transfer on the surface, the weld pool is wide and shallow.

The distributions of turbulent viscosity, thermal conductivity, kinetic energy, and dissipation rate in the weld pool are shown in Fig. 5.4. These quantities are determined by the fluid motion in the weld pool. Since the welding current is not high under the present welding conditions, the electromagnetic force is weak and surface tension is the dominant force. Therefore, the circulation of the molten metal is most intense near the surface and the level of turbulence decreases progressively as the fluid approaches the solid surface. It is interesting that the maximum values of these variables do not lie in the middle of the weld pool. This is because the distributions of these variables are determined by the flow system and the maximum velocity gradient does not occur in the middle in the weld pool. The surface velocities are low near the center because of the symmetry. The maximum dimensionless viscosity (μ_t/μ) and thermal conductivity (k_t/k) values were found to be 13.5 and 4.0, respectively. The calculated dimensionless viscosity (μ_t/μ) and thermal conductivity (k_t/k) values and their spatial distribution patterns are comparable with those reported in the literature.[27-28] The high values of these ratios indicate that the dissipations of heat and momentum in the weld pool are significantly aided by turbulence.

In Table 5.5, the calculated temperatures and velocities from the turbulent model are compared with the results calculated by assuming laminar fluid flow in the weld pool. It can be observed that both the peak temperatures and the maximum values of the velocities are considerably lower for the turbulent calculations because of more efficient transport of heat. Although the peak temperatures in the weld pool were not experimentally measured, the peak temperatures obtained from the laminar model are much higher than the values reported by Kraus[31] for similar heat input for the welding of steels.
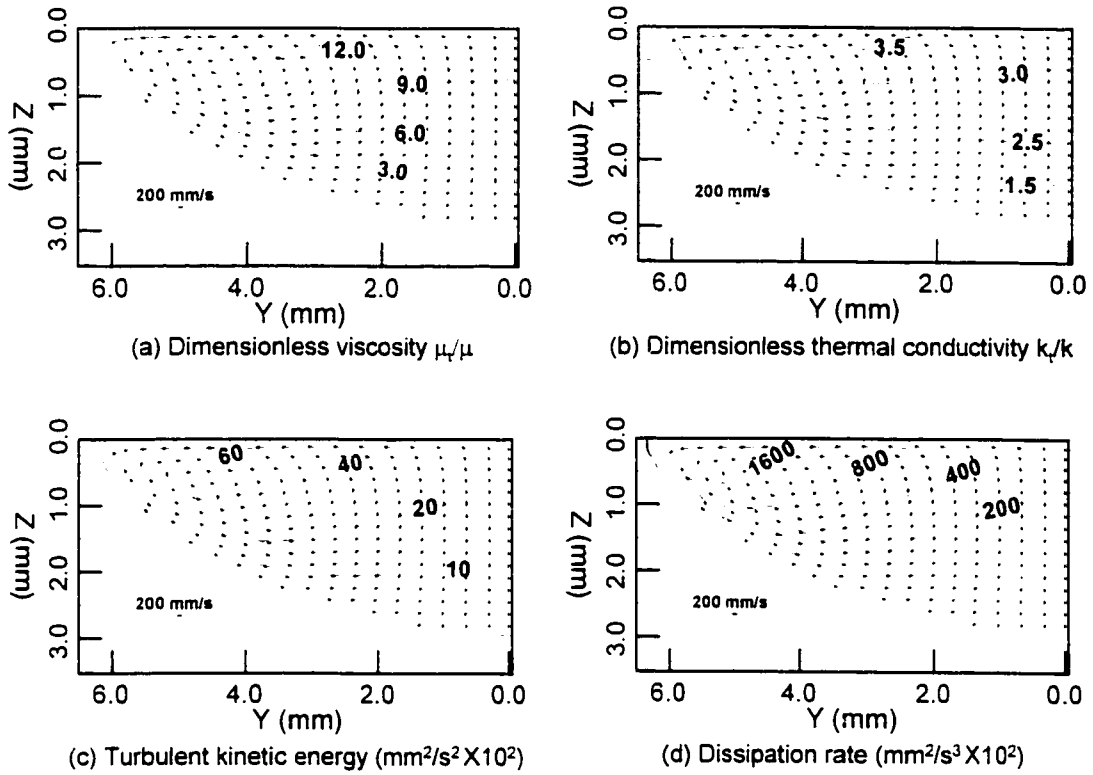
Fig. 5.4: Spatial distribution of turbulent variables in the weld pool.

Table 5.5 Comparison of temperatures and velocities from laminar and turbulent models

	Laminar model				Turbulent model			
Weld #	Umax	Vmax	Wmax	Tpeak	Umax	Vmax	Wmax	Tpeak
1	36.5	102.5	14.0	2795	22.4	69.4	8.4	2429
2	29.7	86.7	11.5	2702	20.5	43.8	6.2	2295
3	25.8	59.1	7.9	2632	17.8	41.3	5.0	2207
4	23.5	55.6	5.7	2581	16.3	37.5	4.5	2144

5.5.2 Calculated Geometries of the FZ and the HAZ

A typical calculated geometry is compared with the corresponding experimental results in Fig. 5.5. The calculated geometry of the fusion zone is determined by the titanium liquidus temperature[5] (1941K). Since the starting temperature for the annealing and recrystallization of α-Ti is not known, the geometry of the HAZ cannot be exactly predicted. However, the β phase containing region (e.g. the $\alpha+\beta$ phase area and the single β phase area) in the HAZ can be predicted. This region exists between the α/β transition isotherm[5] (1155K) and the liquidus temperature (1941K). If we temporarily call the β phase containing region as the HAZ, then its width can also be predicted. From Fig. 5.5, it can be observed that the calculated geometries of both the FZ and the HAZ are comparable with the experimental results under the specified welding condition. From Fig. 5.5, it can also be observed that the widths of the HAZ at various locations are different. The width of the HAZ on the top surface is relatively less than that below the weld pool. Likewise, Fig. 5.6 shows the comparison of the calculated geometry with the experimental results for other heat inputs. It can be observed that the calculated dimensions are comparable with the experimental data under various welding conditions.
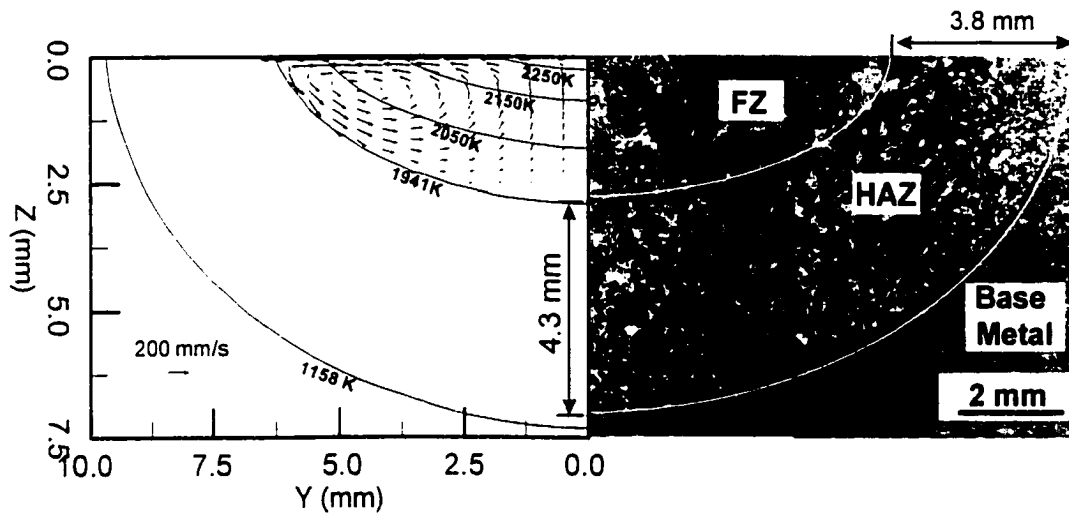
Fig. 5.5: Comparison of the calculated (at location x = 0) and experimental geometies of the FZ and the HAZ of weld 2. The width of the HAZ varies with location. The width of the HAZ on the top surface is less than that at the bottom of the HAZ The micrograph in this figure is provied by Dr. J. W. Elmer.

(a)

(b)

(c)
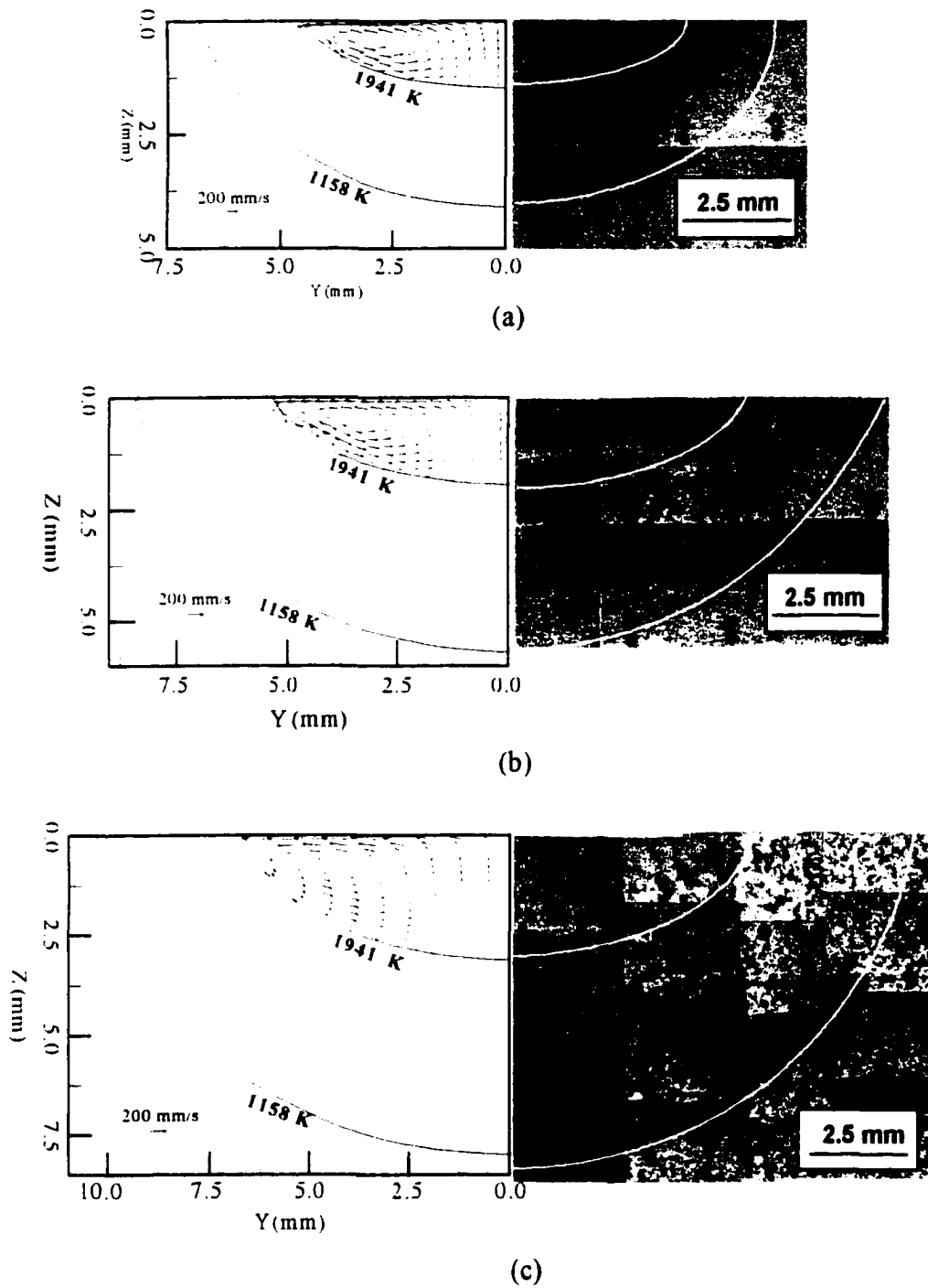
Fig. 5.6: Comparison of the calculated and experimental geometries under different heat inputs. (a) weld 4; (b) weld 3; and (c) weld 1.

In contrast, there are significant differences between the experimental geometries and those calculated by assuming laminar heat transfer and fluid flow in the weld pool. Fig. 5.7 shows the comparison of the experimental geometries with those calculated from laminar calculations in two cases. It is obvious that the weld pool depths calculated from laminar calculation are much shallower than the actual values.

The weld pool geometries calculated from both turbulent and laminar models are compared with the experimental data in Table 5.6. It is found that the differences between the calculated dimensions from the laminar model and the experimental data are much larger than those between the turbulent model and the experimental results

Table 5.6 Comparison of the calculated weld pool dimensions from laminar and turbulent model with the experimental results.

Weld No.	Laminar model				Turbulent model				Experimental	
	Depth		Width		Depth		Width		Depth (mm)	Width (mm)
	D (mm)	Diff (%)	W (mm)	Diff (%)	D (mm)	Diff (%)	W (mm)	Diff (%)		
1	1.8	43.7	14.7	10.5	3.4	6.3	13.6	2.3	3.2±0.2	13.3±0.3
2	1.6	40.7	14.1	17.5	2.8	3.7	12.2	1.6	2.7±0.2	12.0±0.3
3	1.4	22.2	12.3	16.0	1.9	5.6	10.8	1.9	1.8±0.2	10.6±0.2
4	1.0	16.7	9.9	22.2	1.5	25.0	9.1	12.3	1.2±0.2	8.1±0.2

* The symbols D, and W represent the depth and width of the calculated weld geometry. The symbol Diff represents the relative difference between the calculated values and the corresponding experimental data expressed in percentage.

except for weld 4, in which the calculated depth from laminar model is closer to the actual weld depth. This suggests that the nature of the flow in the weld pools of welds 1, 2, and 3 is turbulent. In weld 4, the calculated depth from laminar model (1.0 mm) is
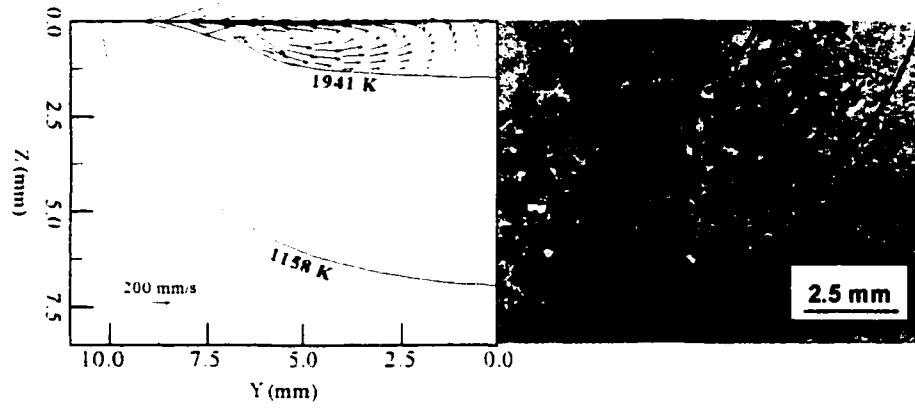
(a)
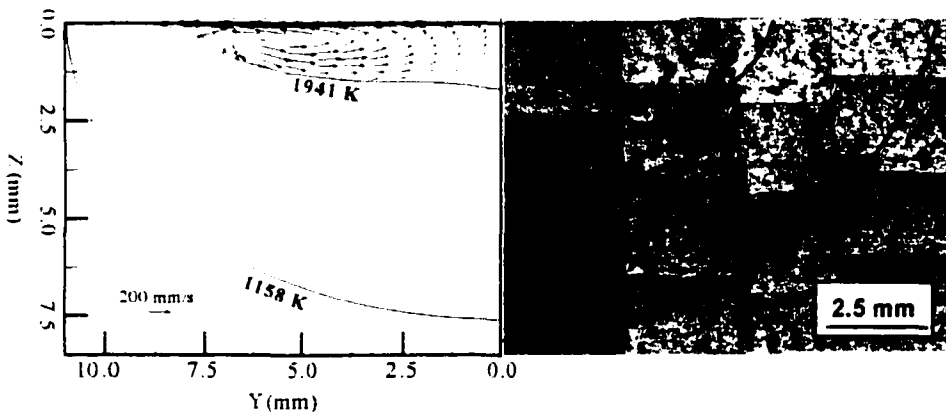
(b)

Fig. 5.7: Comparison of the calculated geometries from the laminar model and experimental results. (a) weld 2 and (b) weld 1.

relatively closer to the actual weld depth (1.2 mm) compared to that from the turbulent model (1.5 mm). In contrast, the difference (22.2%) between the calculated width from laminar model and the actual weld width in this weld is larger than that from the turbulent model (12.3). Therefore, it is difficult to say which mechanism, turbulent or laminar, is dominant in weld 4 by comparing the geometries. But at least, the results indicated that the effect of turbulence in weld 4 was much smaller than in the other three welds and this effect is consistent with low heat input used in weld 4.

5.5.3 Spatial Distribution of Phases

The calculated isotherms of α/β (1158K) and β/liquid (1941K) phase transitions were imposed on the experimentally determined phase distribution map as shown in Fig. 5.8(a). Thus, the calculated isotherms matched the phase distribution map very well. This means that the phase boundaries of $\alpha/(\alpha+\beta)$ and β/liquid can be satisfactorily predicted by the calculated temperature. The $(\alpha+\beta)/\beta$ phase boundary lies at the locations where α-Ti totally transformed to β-Ti, as indicated by the arrows in Fig. 5.8(b). The prediction of the $(\alpha+\beta)/\beta$ phase boundary needs the knowledge of both thermal cycles and the kinetics of the transformation, and therefore cannot be predicted by the thermal model alone.

To predict the locations of the $(\alpha+\beta)/\beta$ phase boundary, a series of lines parallel to the welding direction were selected as shown in Fig. 5.8(b). These lines pass through the locations where the $(\alpha+\beta)/\beta$ phase boundary has been experimentally determined. As the material approaches the heat source, the $\alpha \rightarrow \beta$ transition at different locations begins when the monitoring locations reach the α/β isotherm (1158K). The extent of $\alpha \rightarrow \beta$ phase transformation along these lines were calculated by a combination of the calculated thermal cycles and the modified JMA equation (3.29) as described in chapter 3. The calculated thermal cycles experienced by the material moving along these lines are shown in Fig. 5.9. From this figure, the peak temperatures and the time periods above the α/β isotherm along these lines can be obtained. The further away from the welding center
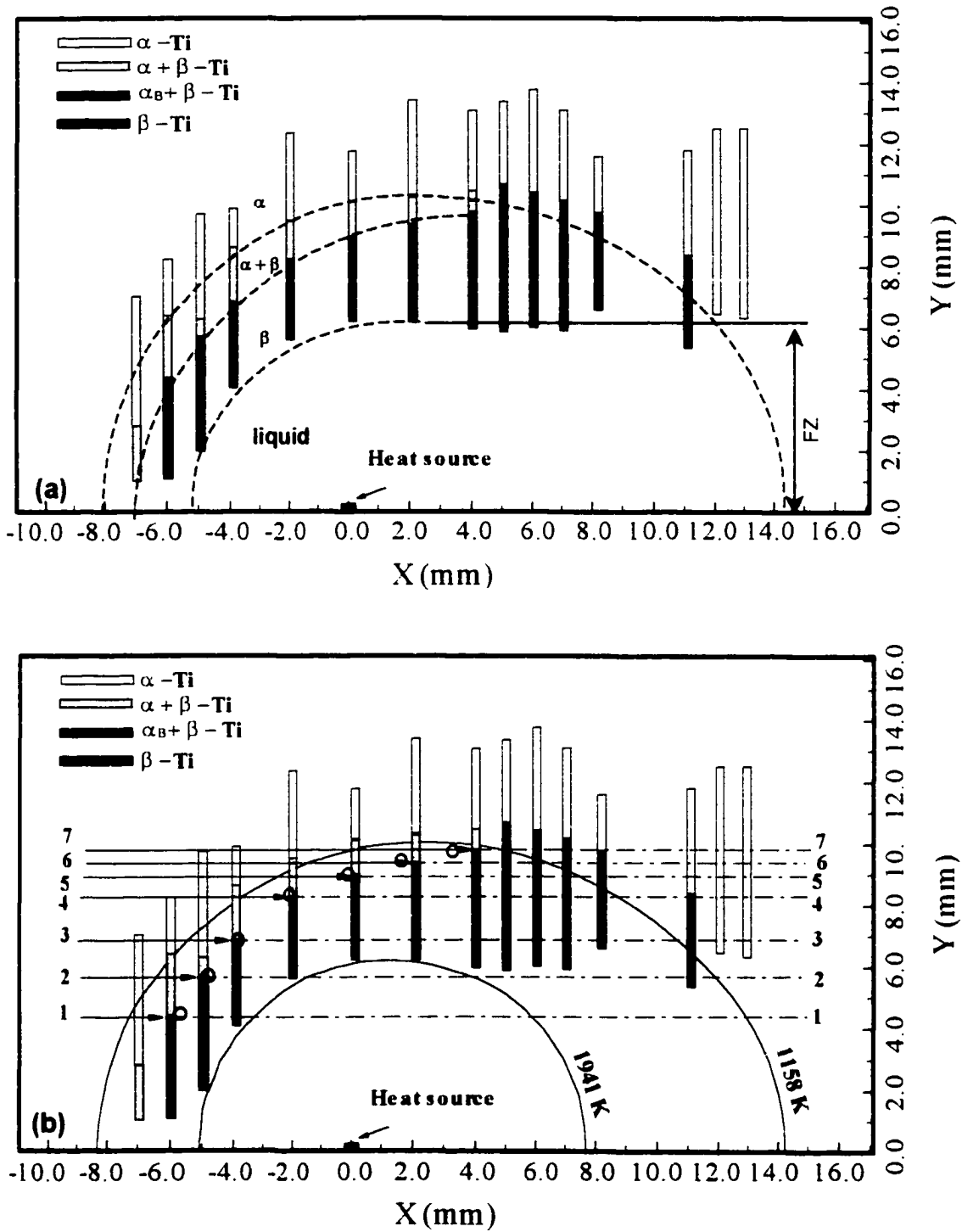
Fig. 5.8: (a) Real time phase distribution map from SRXRD data; (b) Calculated phase transition isotherms on the phase distribution map. Distances from welding center line: 1 - 4.2 mm; 2 - 5.8 mm; 3 - 6.6 mm; 4 - 8.2 mm; 5 - 8.8 mm; 6 - 9.2 mm; 7 - 9.6 mm.
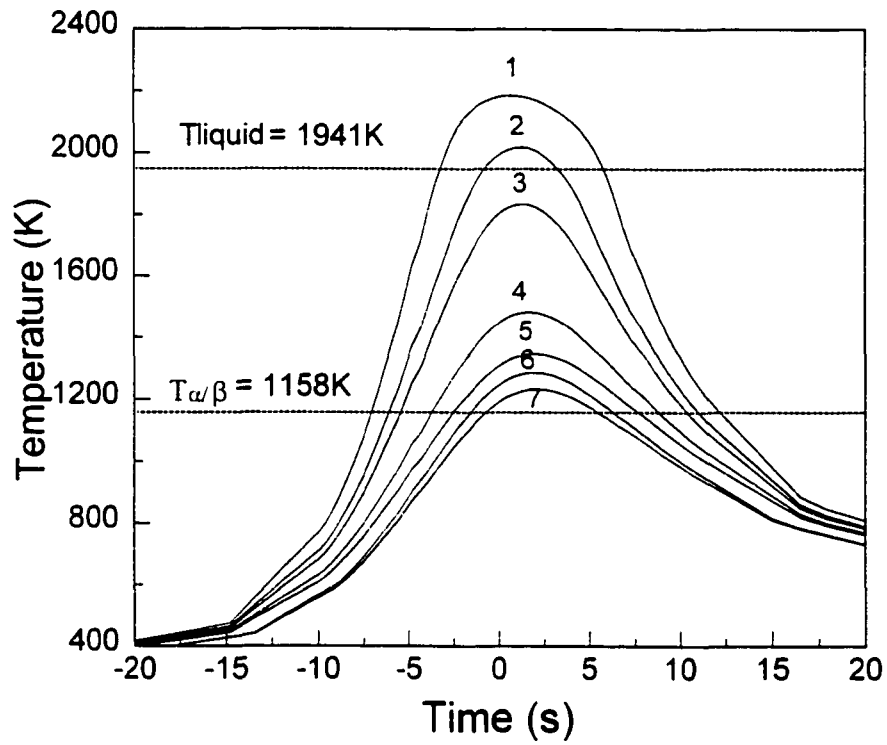
Fig. 5.9: Calculated thermal cycles at different locations. Distances from welding center line: 1 - 4.2 mm; 2 - 5.8 mm; 3 - 6.6 mm; 4 - 8.2 mm; 5 - 8.8 mm; 6 - 9.2 mm; 7 - 9.6 mm.

line. the lower the temperature and the shorter the time period above the α/β transformation temperature. The peak temperatures and the time periods above the α/β isotherm along these lines are given in detail in Table 5.7. It can be observed that the peak temperatures along lines 1 and 2 were higher than the melting point of titanium (1941 K). Thus, the material at these locations were melt during welding. At the location of 6.6 mm to the welding center line, the total time above the α/β isotherm (1158K) was calculated to be 16.6 s, while the corresponding time at the location of 9.6 mm to the welding center line was only 7.1 s. These temperature-time data at various locations will be used for the determination of the spatial distribution of phases.

Table 5.7: Calculated peak temperatures and overall times over the α/β isotherm at the seven different locations

Location No	1	2	3	4	5	6	7
Distance* (mm)	4.2	5.8	6.6	8.2	8.8	9.2	9.6
Tpeak (K)	2186	2019	1835	1483	1347	1287	1233
$t_{total}(s)$	20.0	18.1	16.6	13.1	10.6	9.0	7.1

* Distance here indicates the distance from the location to the weld center line; t_{total} here represents the total time above the α/β isotherms which includes both the heating time and the cooling time.

After knowing the thermal cycles along the lines parallel to the welding direction. the extents of phase transformation along these lines can be calculated from equation (3.29). Different assumed transition mechanisms were exmined to predict the $(\alpha+\beta)/\beta$ phase boundary by taking the corresponding values of n and $\Delta G(T)$ presented in Table 5.3. For each mechanism, the times for the completion of the $\alpha \rightarrow \beta$ transformation along these lines were calculated. The calculated reaction times for all of the mechanisms are shown in Table 5.8. The time for the completion of the $\alpha \rightarrow \beta$ transformation along a line parallel to the welding direction can also be obtained experimentally from the phase

distribution map. In this way, the time was calculated by dividing the distance (between the α/β isotherm and the experimentally determined location of the $(\alpha+\beta)/\beta$ phase boundary along this line) by the welding speed.

Table 5.8: Comparison of the calculated and experimental times necessary for the completion of $\alpha \rightarrow \beta$ transformation at different locations

Locations		1	2	3	4	5	6	7
Times from phase distribution map (s)		1.25	1.45	1.60	1.91	2.26	3.05	3.91
Calculated times under different conditions (s)	Mechanism I	1.20	1.35	1.51	1.75	2.14	2.62	3.36
	Mechanism II	0.85	0.93	1.02	1.12	1.28	1.50	1.65
	Mechanism III	1.12	1.30	1.45	1.65	1.95	2.24	2.62

To identify the possible mechanism for the $\alpha \rightarrow \beta$ transformation, the calculated times for each assumed mechanism were compared with the times determined from the experimental phase distribution map, as shown in Fig. 5.10. It was found that the times from the phase distribution map agreed well with the calculated times from mechanism I, in which the $\alpha \rightarrow \beta$ transition was assumed to be controlled by the transport of Ti atoms across the interface. The calculated times from mechanisms III, in which the transition was assumed to be controlled by oxygen long range diffusion, are also approximately comparable with the experimentally determined times. Significant discrepancies exist between the experimental determined times and the calculated times from mechanisms II, in which the transition was assumed to be controlled by the transport of oxygen atoms across the interface. Through the comparison of the calculated times with the experimentally determined times, it seems that the $\alpha \rightarrow \beta$ transition is most likely controlled by the transport of Ti atoms across the interface.
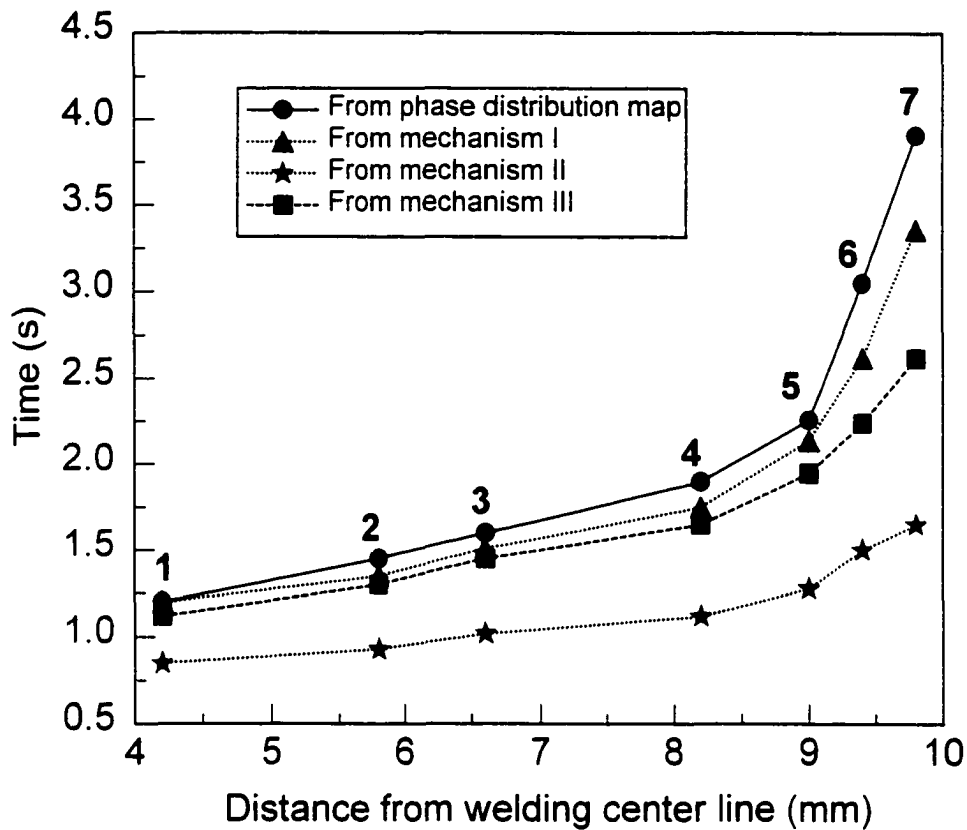
Fig. 5.10: Comparison of times needed for the completion of the $\alpha \to \beta$ transformation from JMA equation and from phase distribution map. Different mechanisms assumed for the application of JMA equations are given in Table 3. Distances from welding center line: 1 - 4.2 mm; 2 - 5.8 mm; 3 - 6.6 mm; 4 - 8.2 mm; 5 - 8.8 mm; 6 - 9.2 mm; 7 - 9.6 mm.

By adopting the mechanism that the $\alpha \rightarrow \beta$ transformation was controlled by the transport of Ti atoms across the interface, the locations of the $(\alpha+\beta)/\beta$ phase boundary along the lines parallel to the welding direction were predicted. The transformed volume fractions of α phase along the lines were calculated by equation (3.29) and shown in Fig. 5.11 (a). Depending on the thermal history experienced, the times for the completion of the $\alpha \rightarrow \beta$ transformation along these lines were different. As expected, the further the line away from the welding center line, the longer the time for the completion of the transformation. This trend can be more clearly observed by comparing the times needed for the $\alpha \rightarrow \beta$ transformation along different lines as shown in Fig. 5.11(b). After obtaining the reaction times along these lines, the distances between the transformation starting points and the transformation finishing points can be calculated by multiplying the welding speed with the calculated reactions times. The starting points are the intercepts of the calculated α/β isotherm with these lines. Thus, the locations of the $(\alpha+\beta)/\beta$ phase boundary along these lines can be determined and shown as the plain circles in Fig. 5.11(b).

5.5.4 Grain Growth in Single β Region

5.5.4.1 Selection of Simulated Domain and Grid Spacing

Since the present study focuses on the simulation of grain growth in single β region, the simlation domain was selected to cover the region in the HAZ containg single β phase. The β phase containing region was identified by the α/β transition temperature isotherm (1158 K). The selection of the domain for MC simulation of grain growth in the HAZ was based on the calculated temperature field from the 3D heat transfer and fluid flow model. As described previously in chapter 3, two simulation domains in the weldment were selected in the present study. The first domain was selected as the dashed block shown in Fig. 5.12(a) to simulate real-time grain structure evolution in the HAZ around the weld pool. This domain covers the region of the HAZ where β grain growth occurs. The length, width, and thickness of the simulation domain were 20 mm, 10 mm
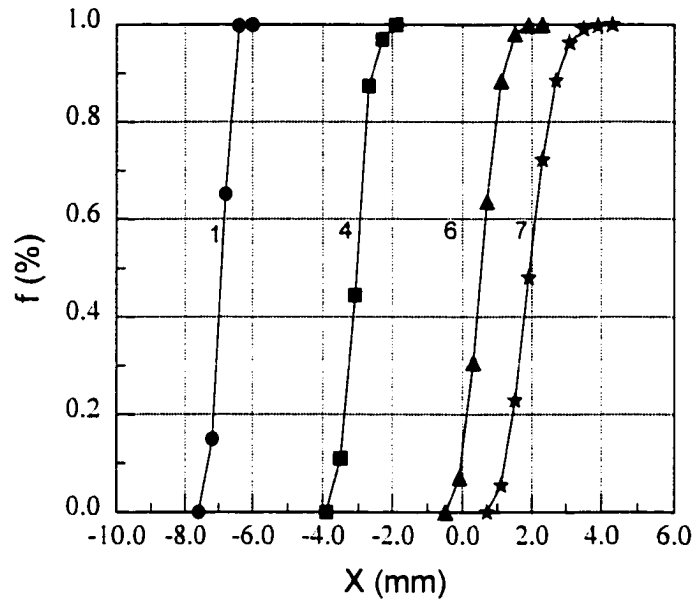
(a)
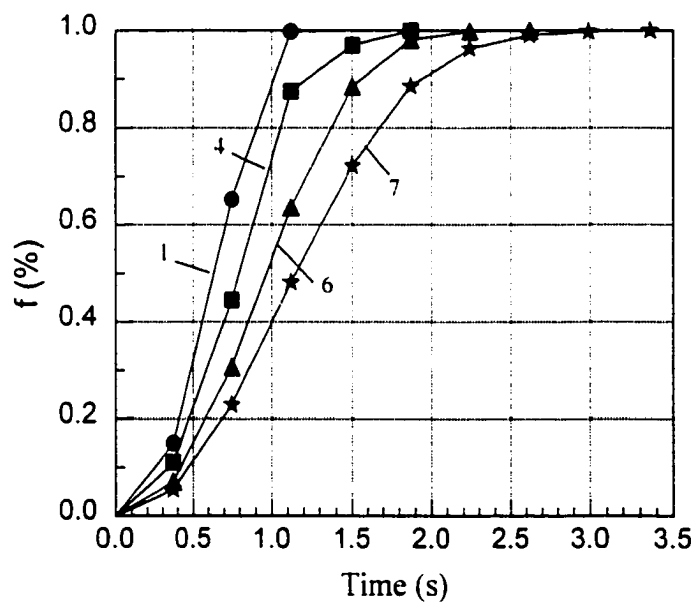
(b)

Fig. 5.11: (a) Calculated β phase transformation along temperature - time profiles given in Fig. 5.8; (b) Calculated times needed for α → β transformation at different lines.
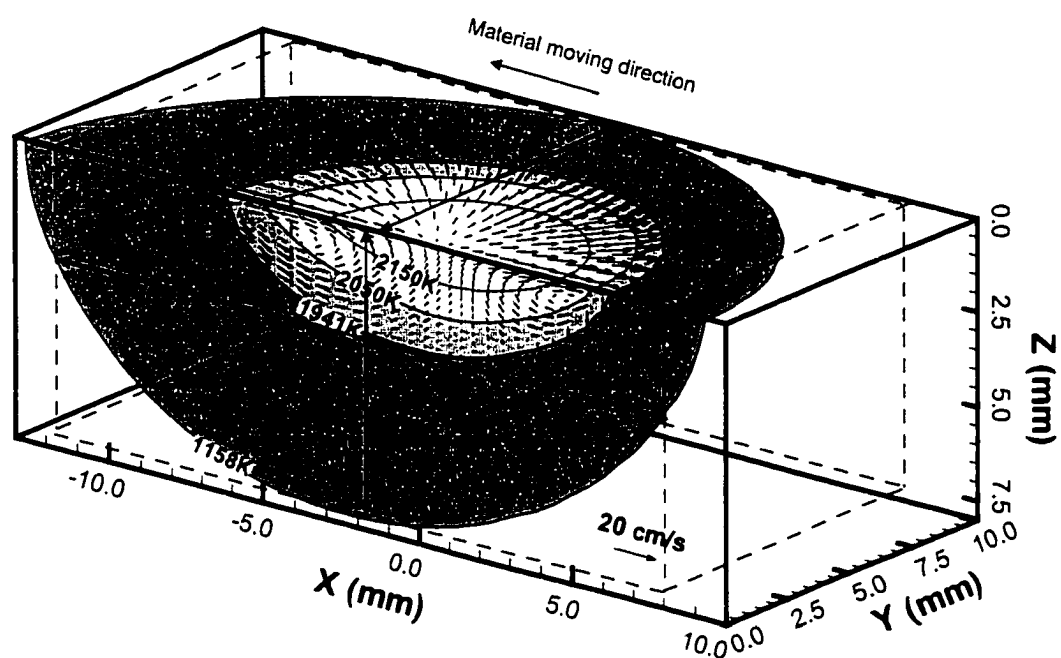
Fig. 5.12(a) Domain selected for simulation of grain structure evolution in the HAZ. The length (L), width (W), and depth (D) of the selected domain are 20mm, 10mm, and 7.5 mm, respectively. The corresponding grid system used for the MC model is 400×200×160.
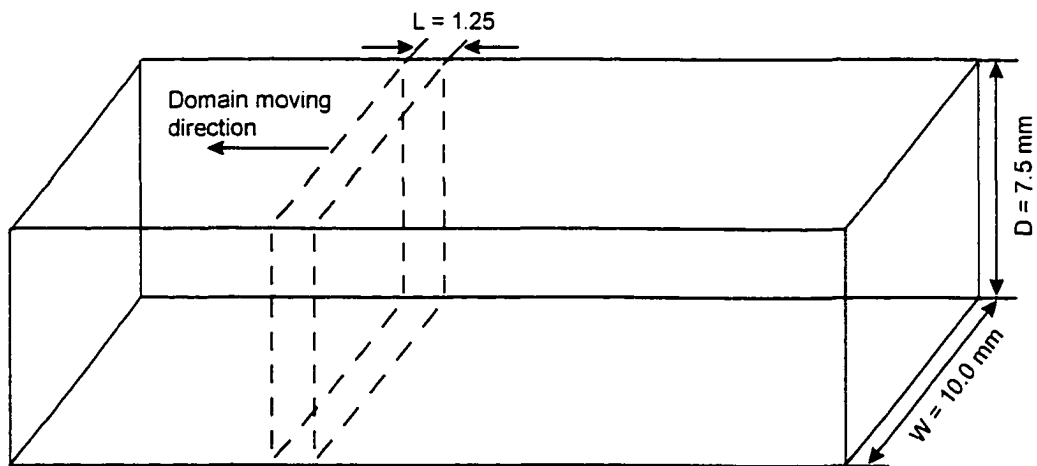
Fig. 5.12(b) Domain selected for simulation of final grain structure in the HAZ. The selected domain is assumed to move from the location where grain growth begins to the location where grian growth ends. The length (L), width (W), and depth (D) of the selected domain are 1.25 mm, 10 mm, and 7.5 mm, respectively. The corresponding grid system used for the MC model is 50X400X300.

and 8.0 mm, respectively. A 400×200×160 grid system was used. Consequently, the spacing of the grid points (λ) in this MC grid system corresponds to an actual distance of 50 μm. This value is twice that of the initial β-Ti mean grain size[1] (25 μm). The soundness of using this grid spacing will be justified later in this section.

The second domain was selected as the thin dashed block shown in Fig. 5.12(b) to focus on simulation of the final grain structure in the HAZ. The grid system used in this domain was 50×400×300, which corresponds the actual domain with the volume of 1.25×10×7.5 mm³. Thus, the spacing of the grid points is 25 μm, which is equal to the initial mean grain size. In this method, the selected domain is assumed to move at the same speed and in the same direction as the workpiece as indicated in Fig. 5.12(b). Assuming that the selected domain moves at a constant velocity for the duration ranging from the beginning to the end of the grain growth in the single β phase region, the resulting final grain structure of the HAZ can thus be simulated by considering the whole thermal history at the corresponding sites.

Theoretically, the grid spacing should be set equal to the initial mean grain size for realistic simulation. However, it requires considerable computer memory if the simulated domain is large or the initial mean grain size is small. For example, the first simulated domain in the present investigation needs to consider the entire β-Ti phase containing region (20×10×8 mm³). This physical domain corresponds to an 800×400×320 or 102.4 million grid points if the grid spacing is set equal to the initial mean grain size (25 μm). The required memory for this grid system considering 100 time steps is beyond the available resources for most modern workstations. Consequently, the grid spacing for the first domain in the present simulation was taken as twice as the initial mean grain size. It should be pointed out that the value of the grid spacing (λ) adopted in the MC simulation will not significantly affect the final grain structure as long as the final grain size are much larger than the grid spacing. This is because the effect of the value of grid spacing (λ) on the grain size has already been considered in determining the Monte Carlo simulation step (t_{MCS}), as given in equation (2.42) in chapter 2. According to equation

(2.42), the larger the value of λ, the smaller the t_{MCS}. In other word, the predicted final grain structures should be almost the same although different values of grid spacing are used.

It should be recognized that grid spacing larger than average initial grain diameter after recrystalization is not suitable for simulation of the grain structure in regions where the grain growth is rather limited. For example. if the final grain size is equal or less than the selected grid spacing, the grain growth process can not be properly simulated. In the titanium welds studied in this thesis, the final grain sizes near the fusion line in the HAZ are 5 to 12 times larger than the grid spacing adopted in the first domain (50 μm). Therefore. this grid spacing is suitable for simulation of grain growth under the present welding conditions. The significant grain size gradients in the HAZ can be effectively simulated by using this grid spacing in the first domain, although the grain growth behavior far away from the fusion line (near the base metal), where the final grain size is less than 50 μm. can not be simulated.

5.4.4.2 Grain Growth Kinetics from MC Simulation under Isothermal Conditions

Fig. 5.13(a) shows the simulated isothermal dimensionless grain growth kinetics for the two grid systems at 1550 K. which is the median of the melting temperature (1941K) and the α/β transition temperature (1158 K). The data used for calculations are presented in Table 5.4. From Fig. 5.13(a), it can be observed that the simulated grain growth kinetics in the two grid systems are actually the same. This is expected since the numbers of the grids in these two systems are very large and both systems use simple cubic lattice. The values of K_1 and n_1, which are used to describe the isothermal grain growth kinetics in equation (3.29), can be obtained from the log-log plot of the simulated grain size (L) vs the MC simulation time (t_{MCS}). Fig. 5.13(b) shows this log-log plot for grid system 400×200×160, in which the solid line is simulation result and the dashed line is the result from linear fit. The values of K_1 and n_1 can be determined from the slope and the intercept of the dashed line, respectively. The values of K_1 and n_1 were determined to be 0.81 and 0.48 from the 3D MC model. The obtained inverse of grain growth exponent
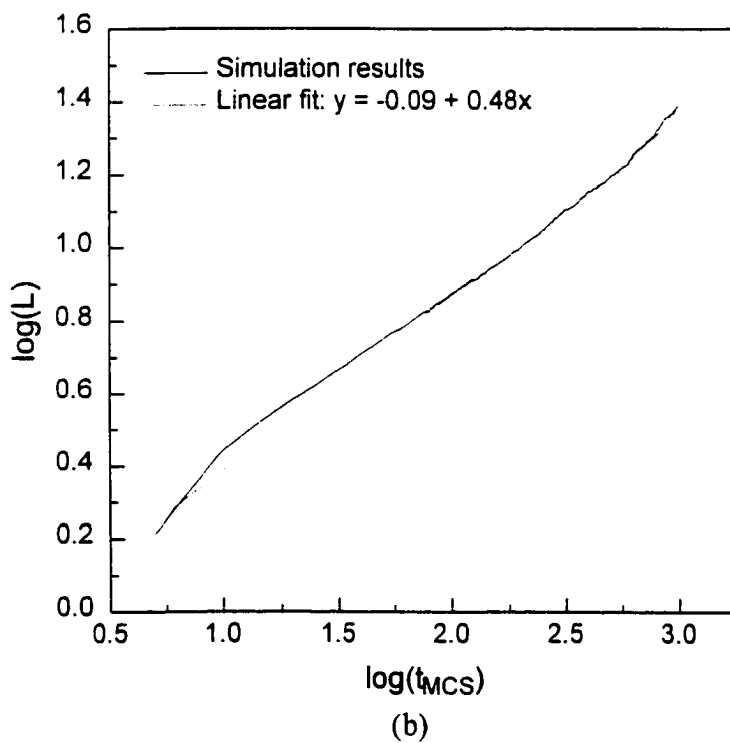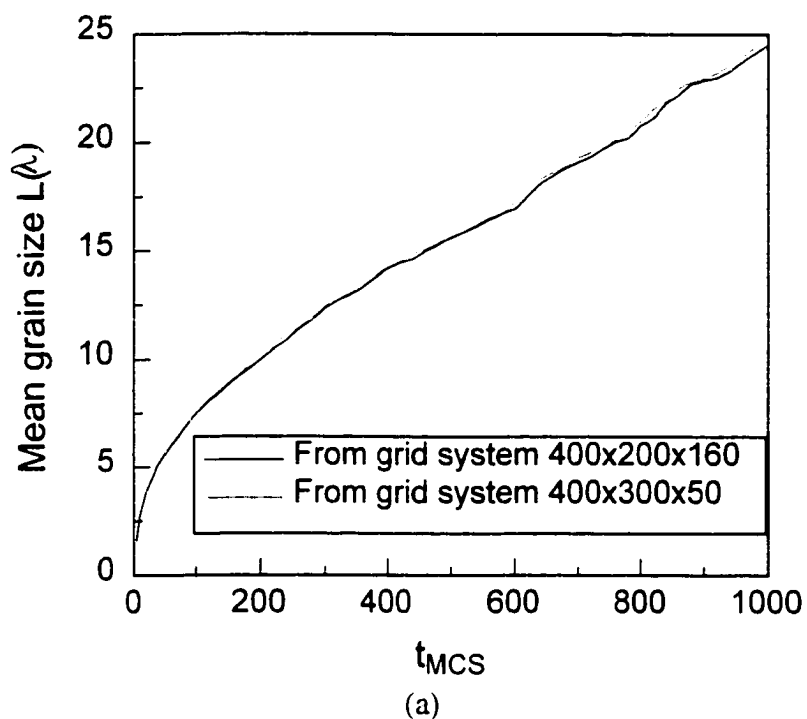
Fig. 5.13: Simulated grain growth kinetics from the MC model. Both of the mean grain size L and Monte Carlo simulation time t_{MCS} are dimensionless quantities in this figure.

(0.48) is comparable with the simulated value (0.46) from 3D MC simulation in the literature.[33] Compared with the value in the literature (0.46), the present value (0.48) is closer to the theoretical limit (0.50) derived by Burke and Turnbull based on grain boundary migration.[32] This is because the grid system used in the present 3D MC model is much finer than that in the literature[33] (50×50×50). K_1 represents the simulated grain boundary mobility. Like the simulated grain size (L) and the MC simulation time (t_{MCS}), K_1 in equation (3.29) is also a dimensionless number. Its value depends on the MC simulation model.

5.5.4.3 Distributions of MC Simulation Step and Site Selection Probability

After knowing the constants K_1 and n_1 of the present 3D MC model, the t_{MCS} at each site was calculated from equation (2.42) by incorporating the corresponding thermal history into the equation. The distribution of the t_{MCS} in the first domain using the 400×200×160 grid system (the first grid system) is shown in Fig. 5.14(a) and (b). From these figures, it can be observed that the maximum value of the t_{MCS} lies at the locations nearest to the fusion line. The t_{MCS} near the fusion zone change drastically due to the steep temperature gradient. This phenomenon is more evident at the edge in front of the weld pool. From Fig. 5.14(a), it can also be observed that the value of t_{MCS} increases as the temperature or time for grain growth at a location increases. This can be easily understood by tracking a specific point in the domain as shown in Fig. 5.14(a). As the material at this location moves from point A to point B, the t_{MCS} at this point will increase. After knowing the spatial distribution of t_{MCS} in the domain, the corresponding distribution of site selection probability, p(r), can be obtained from equation (3.30) as shown in Fig. 5.15(a) and (b). As expected, the spatial distribution of p(r) is similar to that of t_{MCS}.

Figs. 5.16(a) and (b) show the distribution of the t_{MCS} and p(r) in the domain using the 50×400×300 grid system (the second grid system). Compared to the values of t_{MCS} in Fig. 5.16(a) and Fig. 5.14(a), it can be observed that the t_{MCS} in the second grid system is much larger than that in the first system. This is because the grid spacing in the second
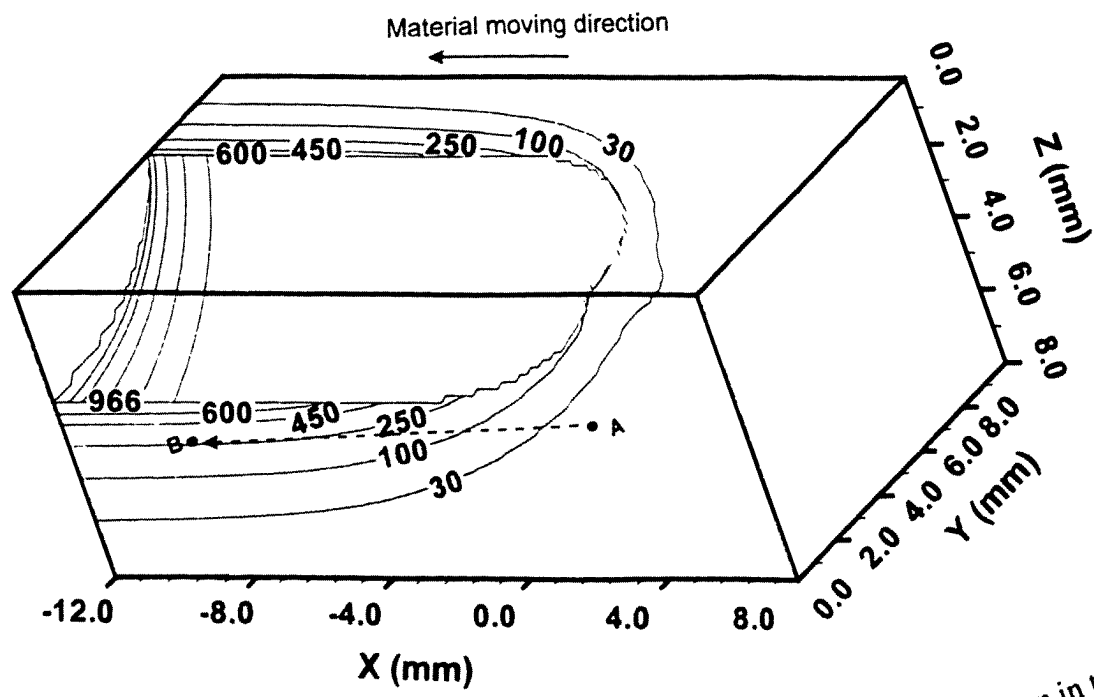
Fig. 5.14(a): Monte Carlo simulation time t_{MCS} spatial distribution in the simulated domain ($20 \times 10 \times 8$ mm^3).
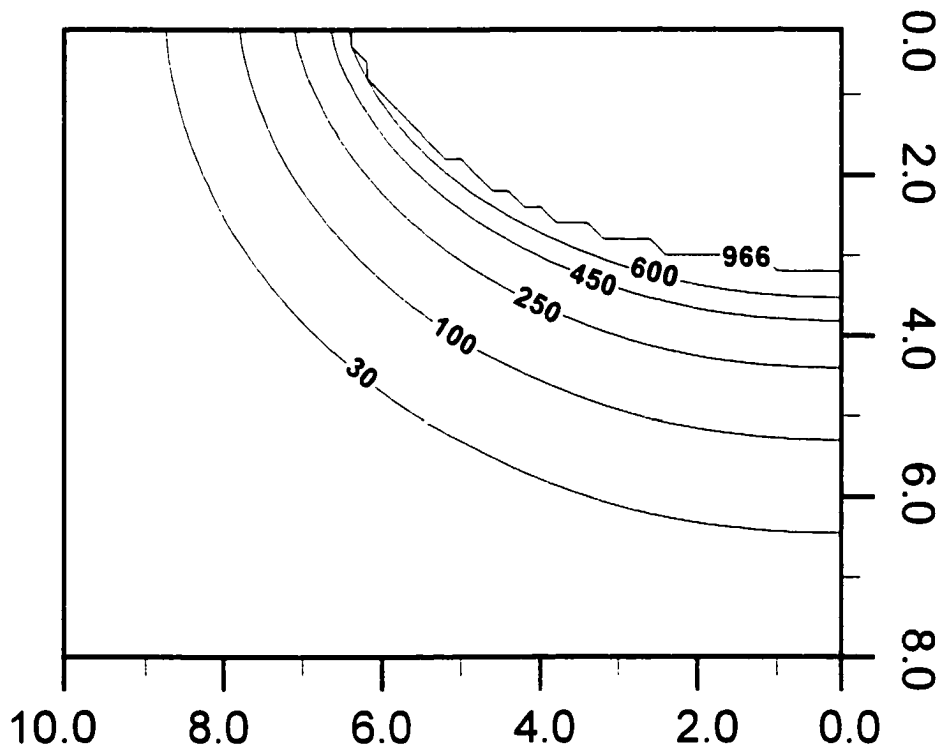
Fig. 5.14(b): Monte Carlo simulation time t_{MCS} spatial distribution
in the cross section of the domain (x = -12.0 mm)
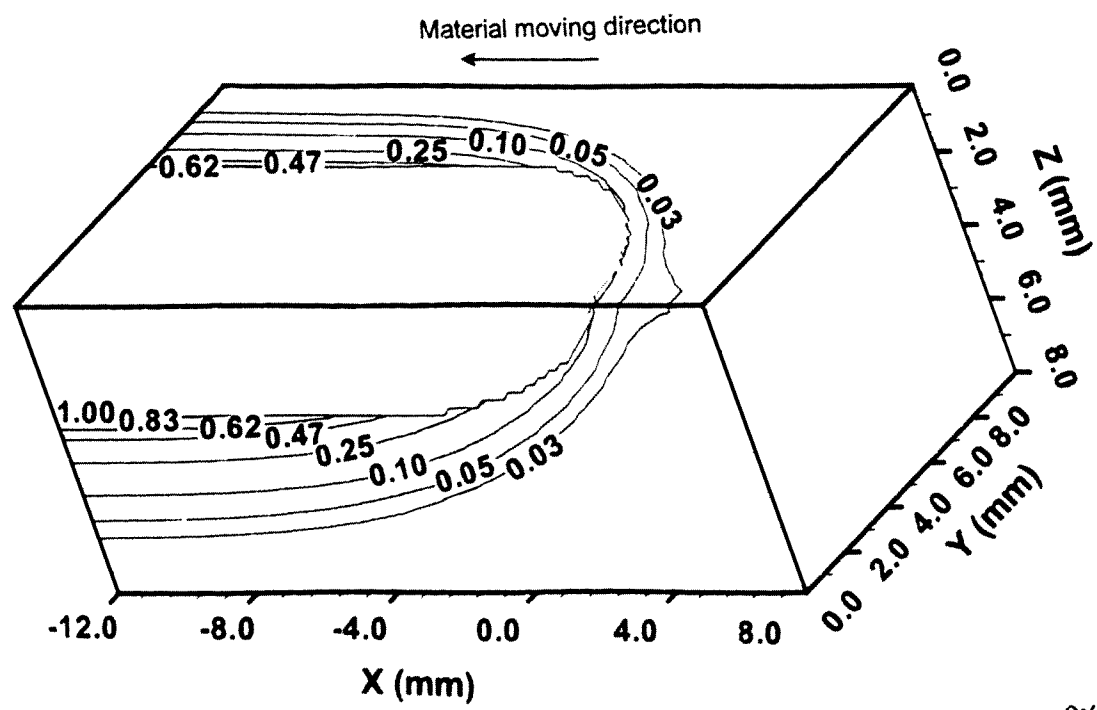
Fig. 5.15(a): Site selection probability spatial distribution in the domain (20×10×8 mm^3)
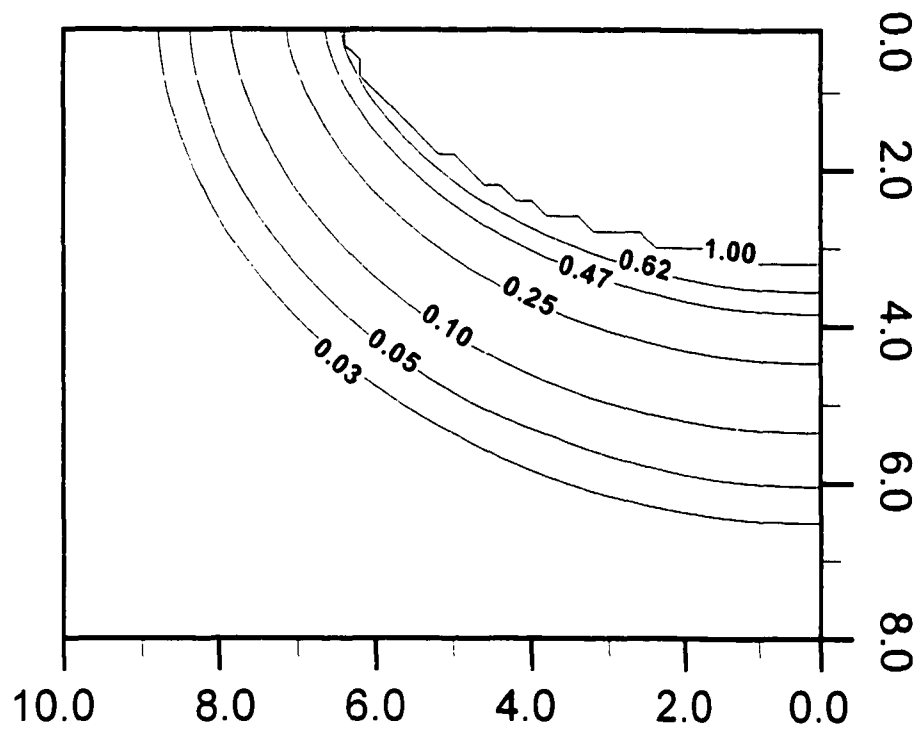
Fig. 5.15(b): Site selection probability spatial distribution in the cross section of the domain (x = -12.0 mm).
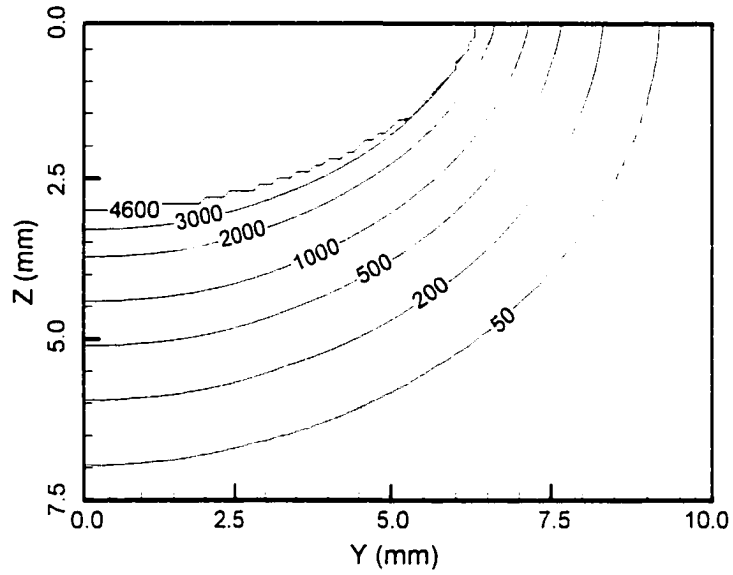
(a)
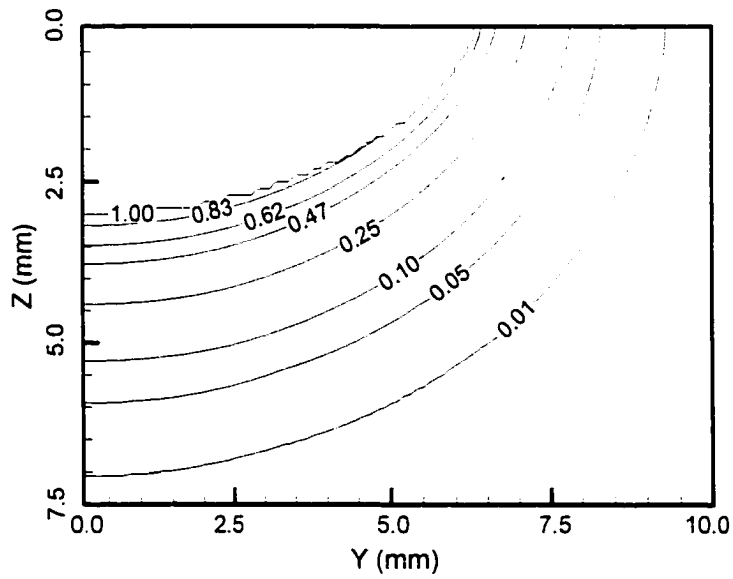
(b)

Fig. 5.16 (a): Monte Carlo simulation time t_{MCS} and (b) site selection probability.

system is only half of that in the first grid system. The finer the grid system, the larger the t_{MCS} needed for achieving the same grain size. After obtaining the p(r) distribution, the temperature time history at each site as well as the material properties can be incorporated into the model by considering the spatial site selection probability distribution in the simulation domain.

5.5.4.4 Simulated Grain Structure in the HAZ

By using the $400 \times 200 \times 160$ grid system (the first grid system), a real-time, three-dimensional map of grain structure distribution around the weld pool was obtained as shown in Fig. 5.17 (a). The heat source is located at x = 0.0. In front of the heat source, the material experiences significant grain growth during heating. This can be clearly observed in both the top surface and the symmetrical vertical plane. Behind the heat source, the β-Ti grains continue to grow until the temperatures reach the β/α transition temperature profile (1158 K), which has been given in Fig. 5.12(a). From the simulated 3D grain distribution map, the grain structure in every location in the whole HAZ around the weld pool can be obtained. For example, the real-time grain size distribution on the top surface and that on the symmetrical vertical plane can be clearly observed as shown in Fig. 5.17 (b) and (c).

In the simulated real-time grain structure map, the thermal effects on grain growth can be effectively illustrated. In the region in front of the weld pool, the extent of grain growth is limited and the grain size is fine due to the very short time for grain growth before the material at these locations melts. At the locations where the material does not melt, the mean grain size becomes coarser with time. In the mean time, the width of the HAZ increases with time. These features can be clearly seen in both the top and side views of the simulated grain structure map shown in Fig. 5.17(b) and (c).

Likewise, the grain structure at any plane in the domain can be viewed by examining the corresponding cross section normal to x, y, or z direction. Fig. 5.18 shows the spatial distribution of grain structure at several cross sections normal to x direction. The dynamic change of grain structure in the HAZ as well as the weld geometry is
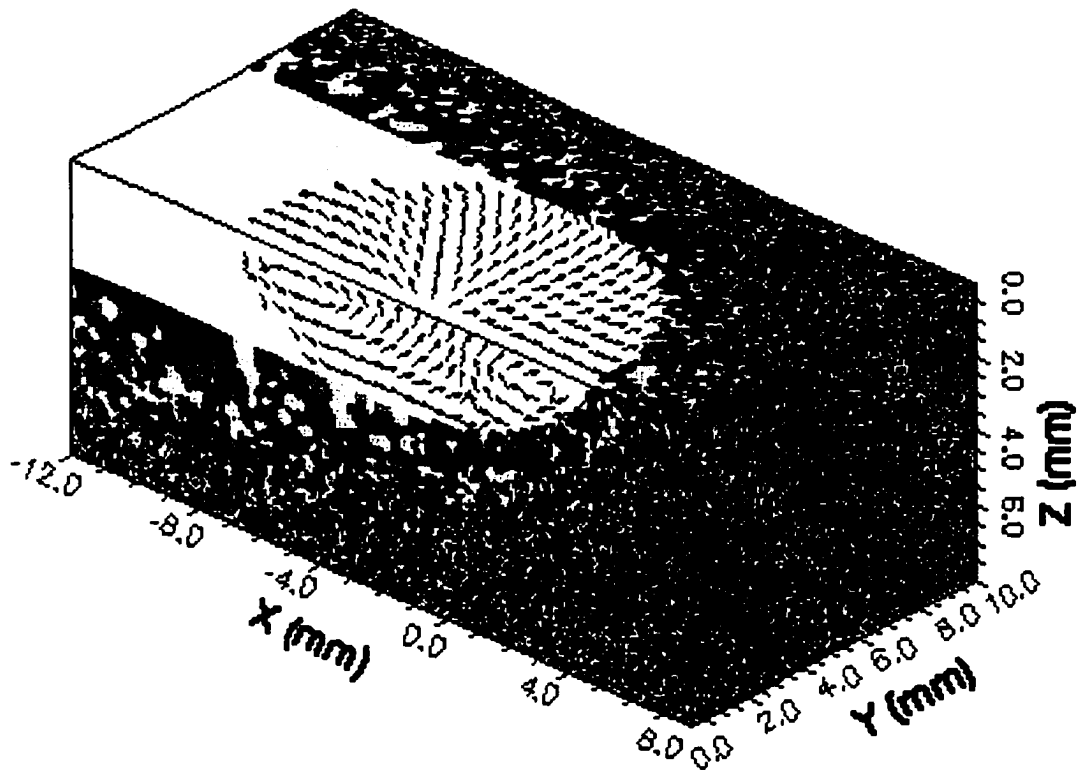
Fig. 5.17(a): Real time mapping grain structure distribution around the weld pool in three dimensions using 400X200X160 grids. The grid spacing is 50 μm.
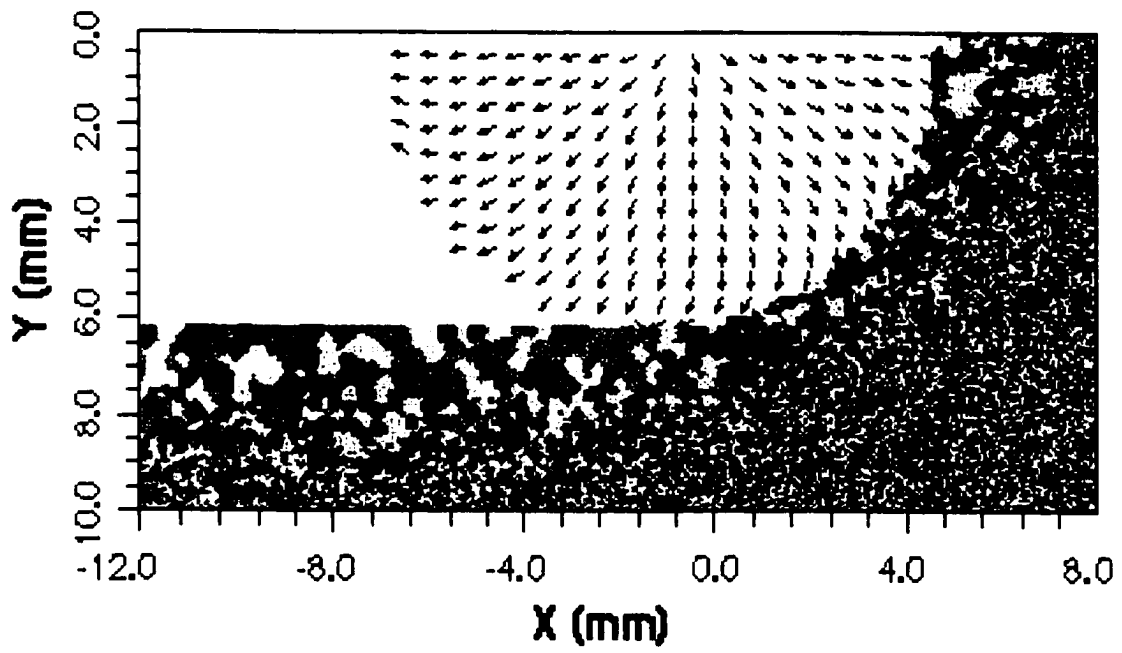
Fig. 5.17(b): Top view of grain structure distribution around the weld pool.
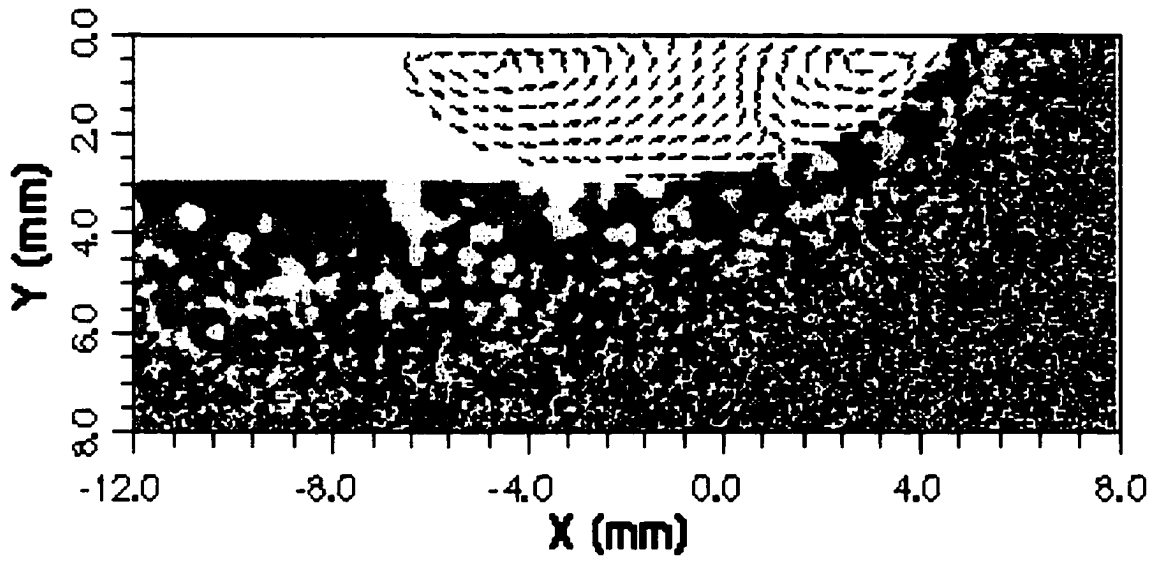
Fig. 5.17(c): Side view of grain structure distribution around the weld pool.
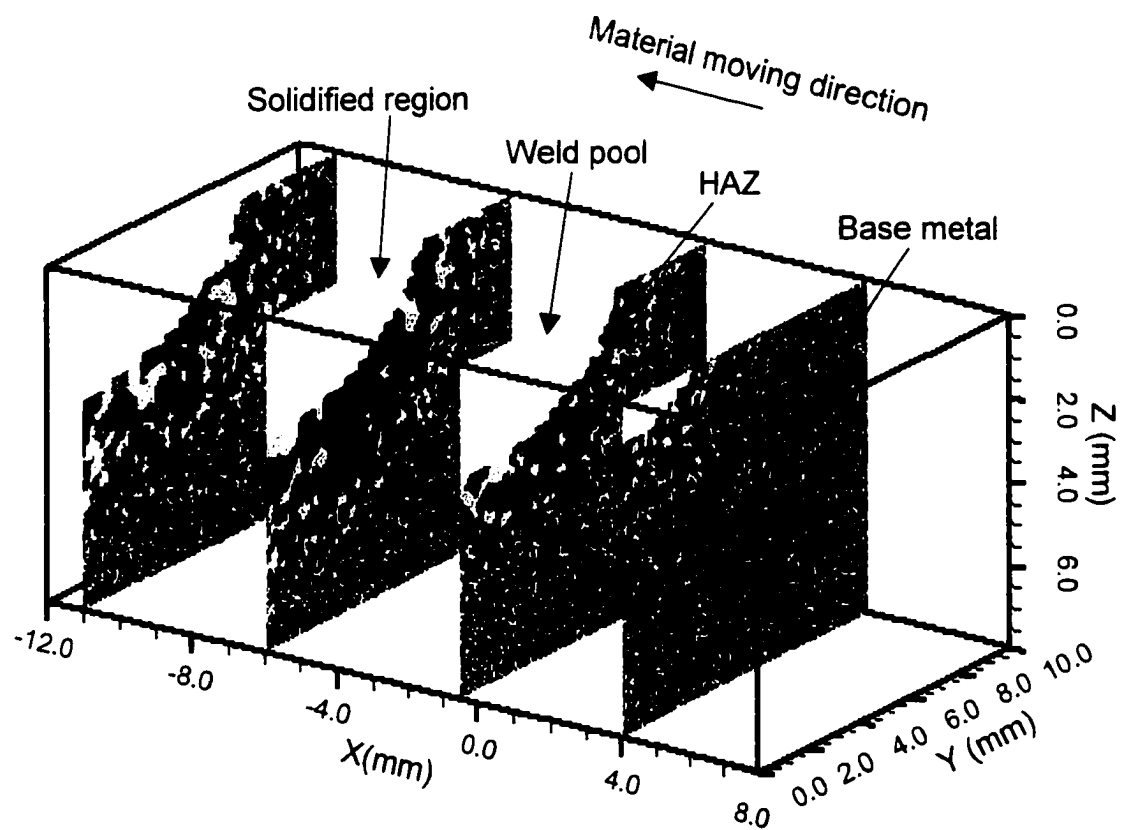
Fig. 5.18: Grain structure evolution as the material approaches and moves away from the heat source (x=0)

effectively illustrated in this figure. For example, the extent of grain growth at the cross section 4 mm ahead of the heat source is limited and only very small portion of material large grains near the weld pool actually melt and the width of the weld pool continues to grow. When the material arrives at the location under the heat source, the size of the weld pool reaches the maximum value. Significant grain growth is observed at this location. After that, the liquid metal begins to solidify and the weld pool shrinks. However, the grain growth in the HAZ continues till some more time when the material moves away from the heat source.

The simulated final grain structure of the HAZ after the completion of welding is shown in Fig. 5.19. Significant spatial grain size gradient is observed in the simulated HAZ structure. The closer a site to the fusion line, the coarser the grain size at that site. This is expected since the grain size change depends on both the temperature and the time period for grain growth. The higher the temperature and the longer the time for grain growth, the larger the final grain size. Furthermore, it can be observed that grain growth on the top surface of the HAZ (along line ab) is not as significant as that in the vertical direction shown by line cd in Fig. 5.19. This is because the thermal cycle at a location on the top surface has lower temperature and shorter time for grain growth than that at the location with the same distance to the fusion line on the central vertical plane of the HAZ. The simulated grain structures under various welding conditions are shown in Fig. 5.20. All the grain structures shown in Fig. 5.20 were simulated using the same grid system (400×300×50). From Fig. 5.20, the effect of heat inputs on the grain size in the weld HAZ can be clearly observed. As the heat input decreases, the extent of grain growth also decreases. Weld 1 has the largest heat input (3932 J/mm) and thus has the largest extent of grain growth in its HAZ. In contrast, grain gowth in weld 4 is limited due to very low heat input (534 J/mm).

To verify the simulated results, the grain size distribution along both lines ab and cd, as shown in Fig. 5.19, were measured in all the welds. The experimental grain size measurement was made after cooling to ambient temperature. It should be pointed that the grain size in the postweld microstructure is not the same as that predicted in the single β phase region due to $\beta \rightarrow \alpha$ transformation occurring during the cooling of the weldment.
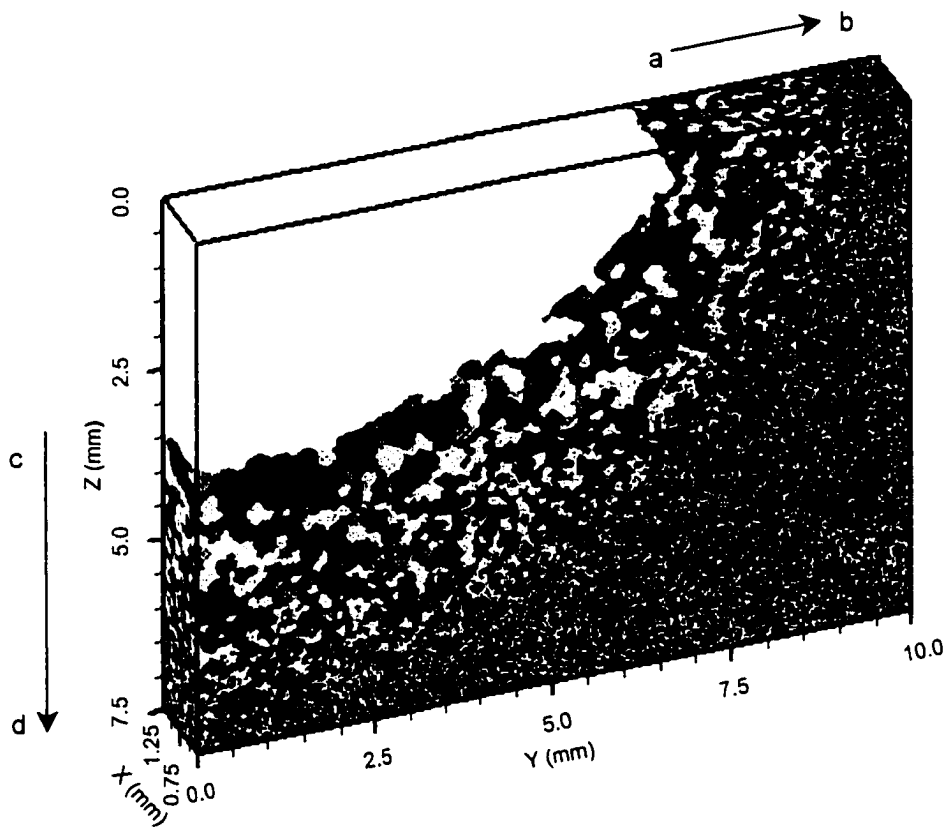
Fig. 5.19: Simulated final grain structure of the HAZ using 50X400X300 grids
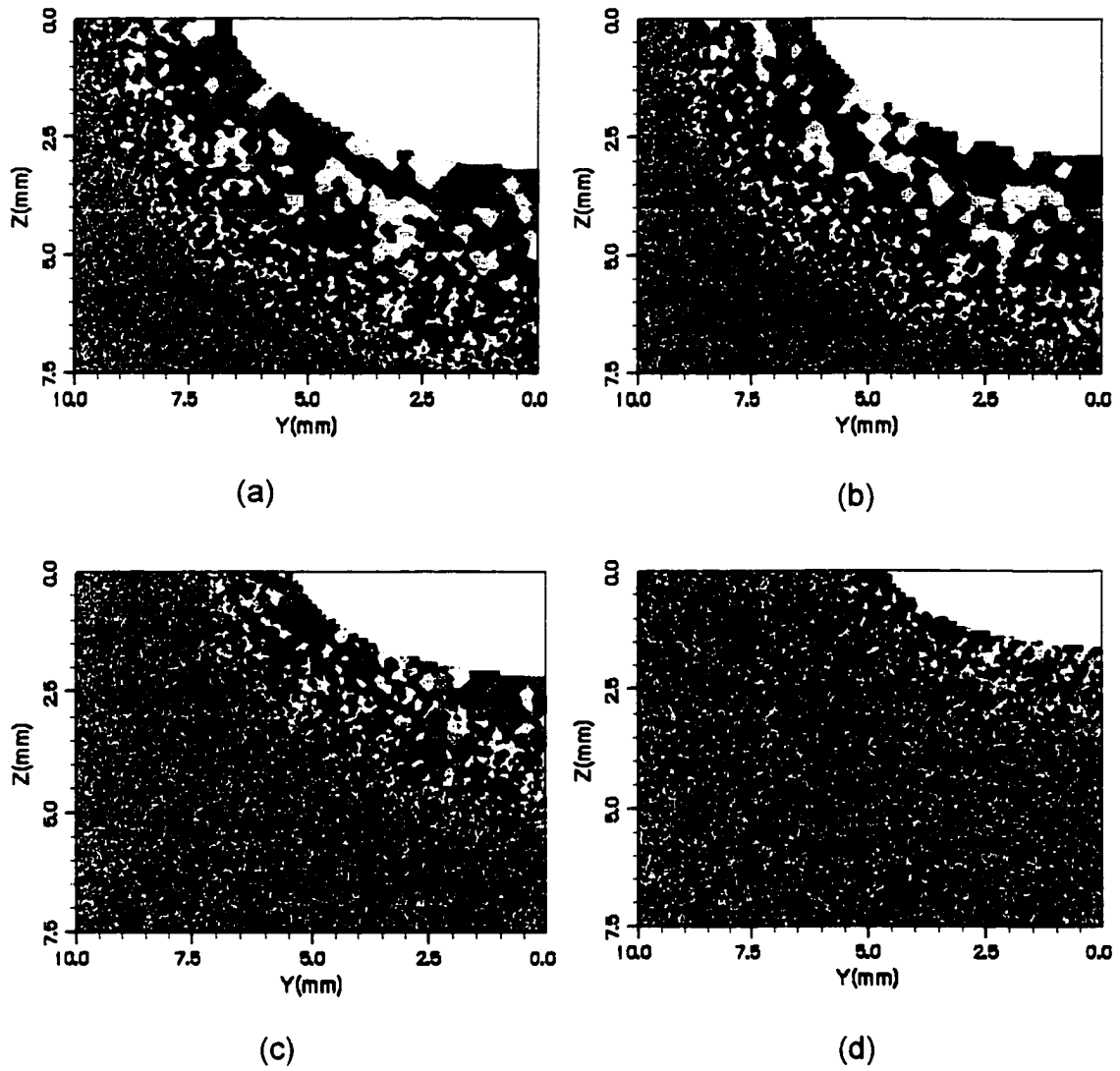
Fig. 5.20: Comparison of the simulated grain structures under various welding conditions. (a) weld 1 (3.9 kJ/mm); (b) weld 2 (2.0 kJ/mm); (c) weld 3 (1.0 kJ/mm); (d) weld 4 (0.5 kJ/mm).

The grain size measurement was based on the prior β grain boundary in the postweld microstructure.

The calculated results for the four welds are compared with the experimental results in Fig. 5.21. It should be noted that lineal intercept method was used in both experimental measurement and theoretical calculation in the present study. It can be observed that the calculated and the experimentally measured grain sizes are comparable in all the four welds. Furthermore, it can be observed the mean grain sizes at various locations along line ab are smaller than the corresponding locations equidistant from fusion plane along line cd in all the welds. For the sake of clarity, the distributions of grain size in the four welds with different heat inputs are compared in Fig. 5.22 (a) and (b). It is obvious that the extent of grain growth increases as the heat input increases. Due to very large heat input in weld 1, the experimental determined grain size near the fusion line on the top surface (along line ab) and the on the vertical plane (along line cd) were found to be 541 ± 17 μm and 591 ± 18 μm, respectively. In contrast, the corresponding experimental values in weld 4 were only 183 ± 19 μm and 242 ± 17 μm, respectively.

As pointed out earlier, one advantage of the present 3D MC simulation is that it can predict the spatial variation of grain size in three dimensions. In Fig. 5.22, the grain size gradients on the top surface and on the vertical plane in all the four welds have been quantitatively presented. For more effective illustration of the spatial distribution of grain size, the grain size gradients along another three directions in the HAZ of weld 2 were calculated from the simulated grain structure and shown in Fig. 5.23. It can be observed that the grain size at the same distance to the fusion line increases progressively in the order from line ab, line 1, line 2, line 3, and line cd. For example, at the distance of 1.5 mm to the fusion line, the mean grain sizes in lines ab, 1, 2, 3, and cd are 176 μm, 196 μm, 217 μm, 242 μm, and 262 μm, respectively.
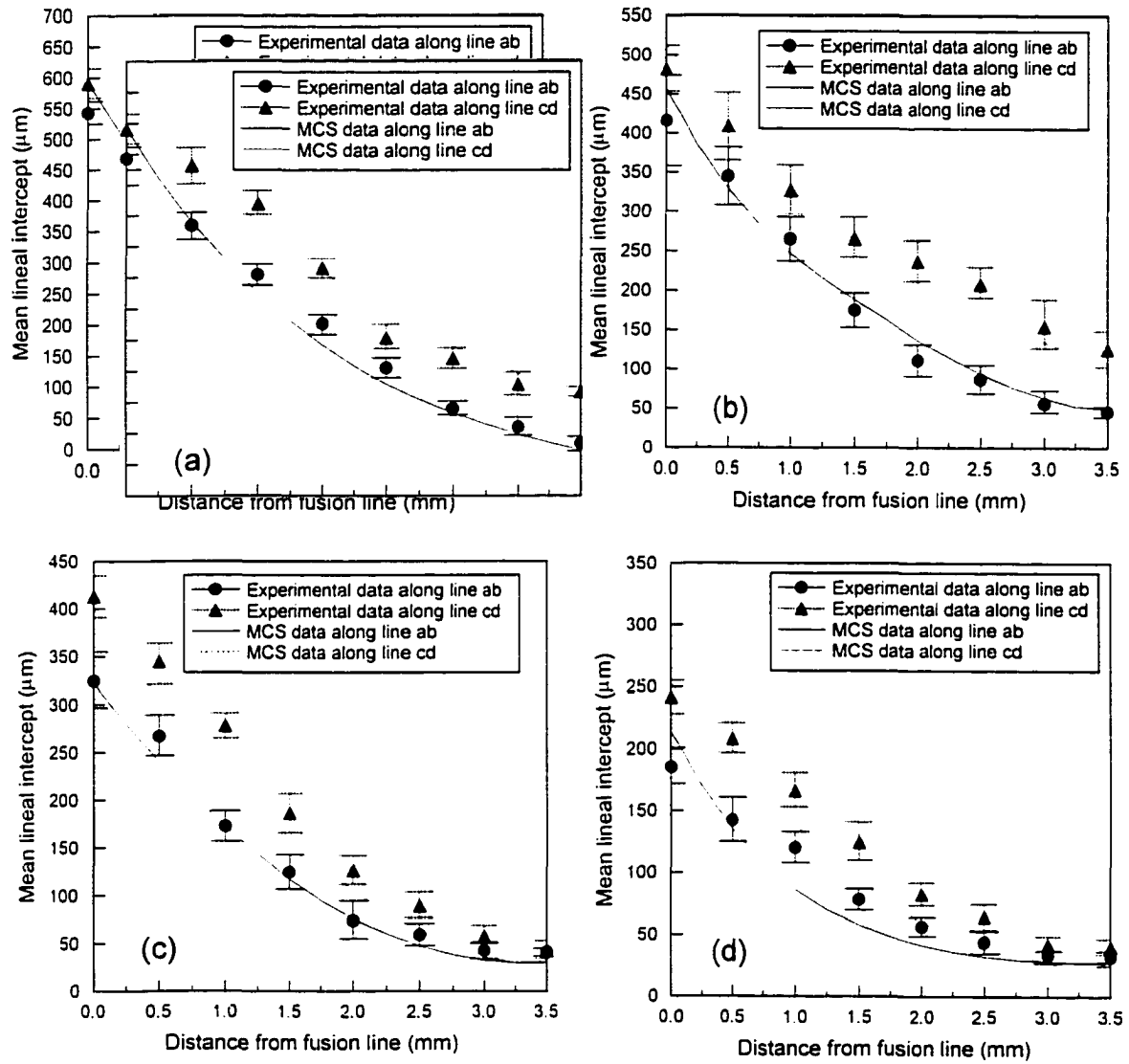
Fig.5. 21: Comparison of the simulated grain structures under various welding conditions. (a) weld 1 (3.9 kJ/mm); (b) weld 2 (2.0 kJ/mm); (c) weld 3 (1.0 kJ/mm); (d) weld 4 (0.5 kJ/mm).
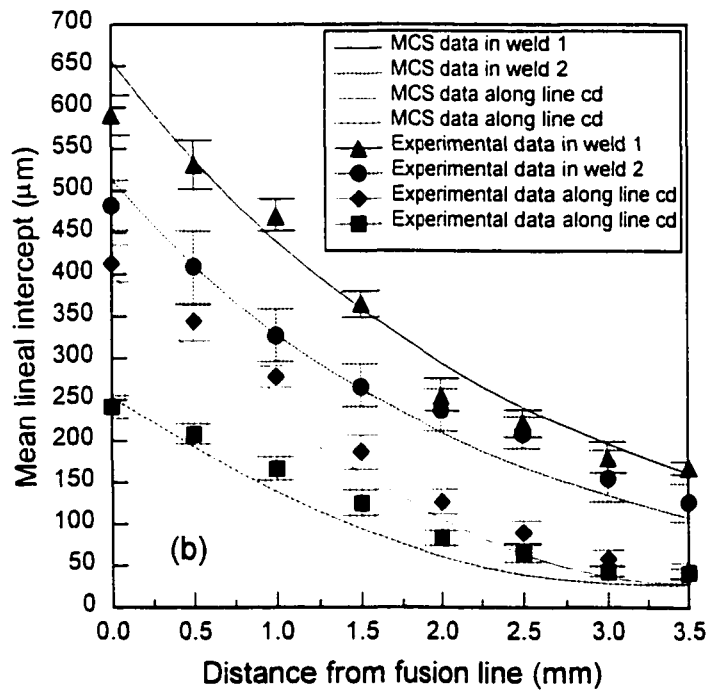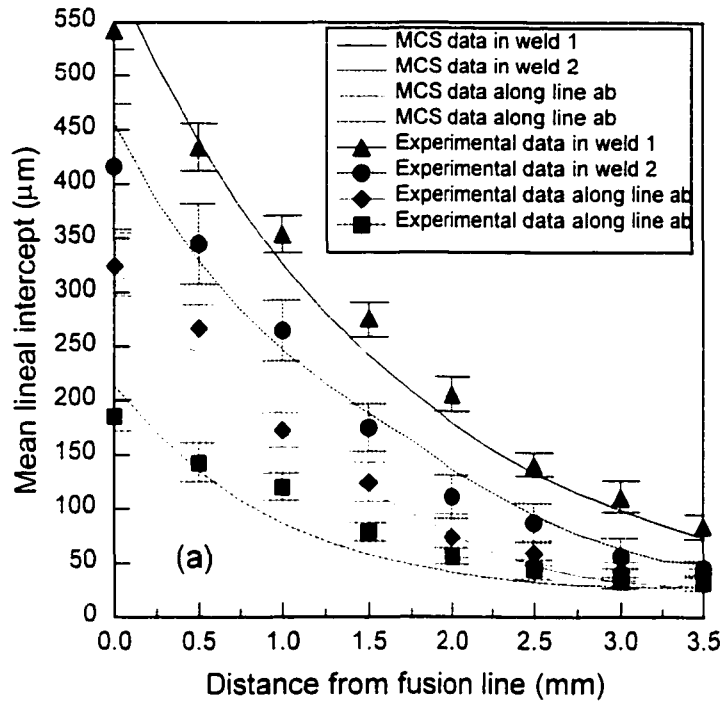
Fig.5. 22: Variation of mean grain size under different heat inputs. (a) along line ab, and (b) along line cd. The heat inputs for the four welds are: (1) weld 1 (3.9 kJ/mm), (2) weld 2 (2.0 kJ/mm), (3) weld 3 (1.0 kJ/mm), and (4) weld 4 (0.5 kJ/mm).
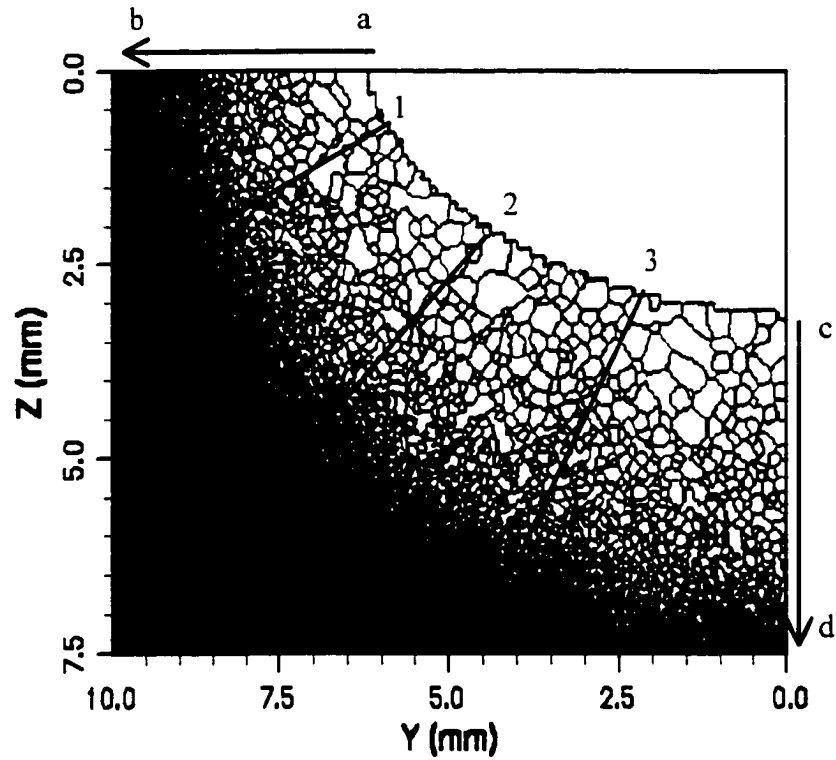
(a)
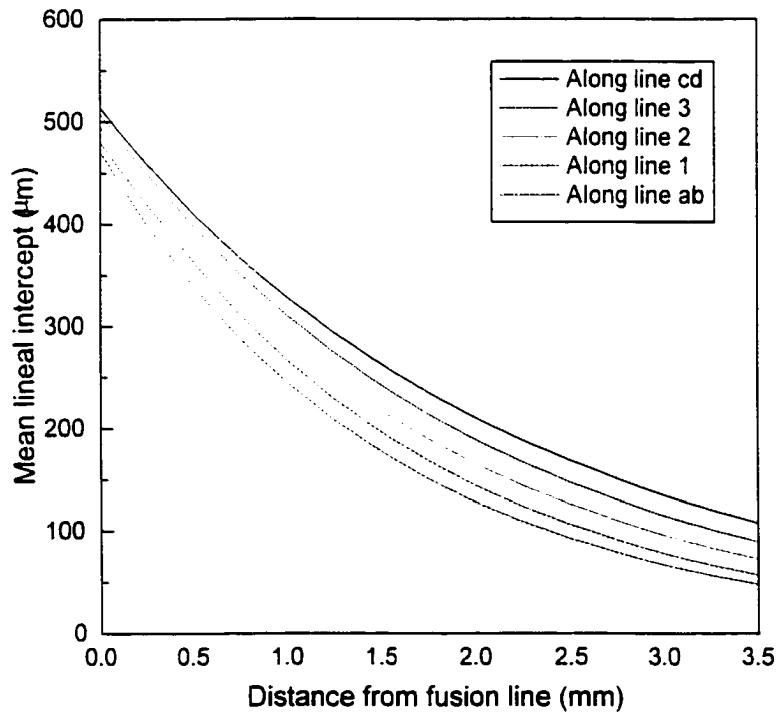
(b)

Fig. 5.23: Spatial distribution of grain size in the HAZ of weld 2. (a) Specified lines for grain size measurement; (b) Grain size gradients along different lines.

5.5.4.5 Grain Size Distribution and Topology in the HAZ

Under isothermal conditions, the grain size distribution and topological information can be obtained by statistics analysis. Some features have been reported on the grain size distribution and topology based on theoretical analysis[34-36] or experimental data.[37,38] For example, the grain size distribution frequency f, when plotted vs $\log_{10}(R/\overline{R})$, peaks at $(R/\overline{R})$ =1, has an upper cut-off around $(R/\overline{R})$ =2.7, and asymptotically approaches zero as $(R/\overline{R})$ tends to zero. In addition, both grain size and topological distributions were found to be time invariant under isothermal conditions,[34] which has been confirmed by MC simulation under isothermal conditions.[21] Although the time invariant features of the grain size and topological distributions can not be examined in the HAZ due to non-isothermal condition and steep temperature gradient in this region, it is still interesting to check some aspects of the grain size distribution and topology in the HAZ.

In the present study, the grain size and topological distributions along three planes parallel to the top surface of weld 2 (2.0 kJ/mm) are studied based on both 3D MC simulated grain structure and experimental data. The planes investigated are: 0.5 mm, 1.5 mm, and 2.5 mm below the weld pool. Figs. 5.24 (a), (b) and (c) show the grain size distributions along the three investigated planes from the 3D MC simulation and experimental results. In these figures, the experimental data are presented by histograms and the data from MC simulation are presented by solid dots. For comparison, the experimentally determined grain size distribution in the base metal is presented in Fig. 5.24 (d). In Figs. 5.24 (a), (b), and (c), it can be observed that the histograms from 3D MC simulations are comparable with those from experimental data.

In all figures, the grain size distributions from both simulation and experimental data exhibit asymmetric peaks at $\log_{10}(R/\overline{R})$ = 0 and has an upper cut-off around $\log_{10}(R/\overline{R})$ = 0.5. This means that most of the grains in the domain have the average grain size and the maximum grain size is about 3.2 times the average grain size. These characteristics of the grain size distribution in the HAZ are consistent with those obtained under isothermal conditions in the literature.[21]
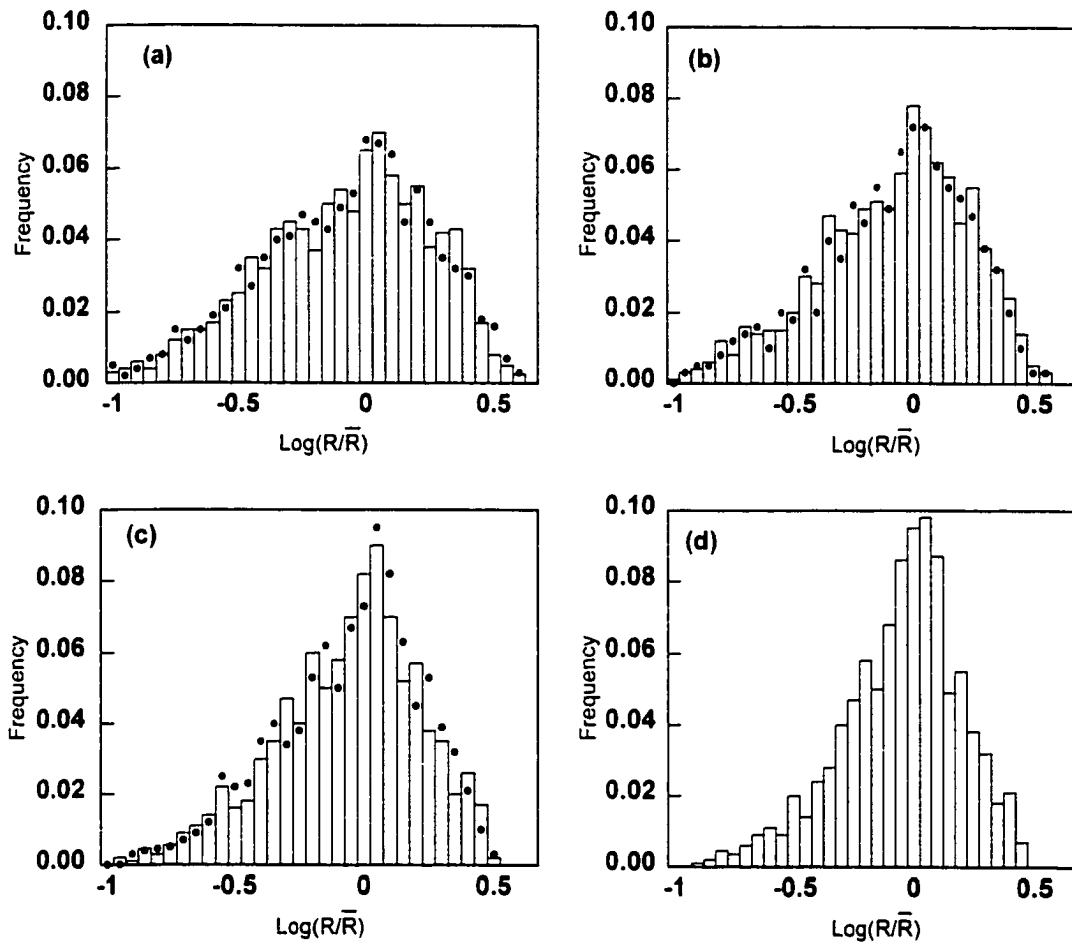
Fig. 5.24: Grain size distributions determined from experimental data (histograms), compared to the results from 3D MC simulation (solid dots) at different locations: (a) 0.5 mm from fusion line; (b) 1.5 mm from fusion line; (c) 2.5 mm from fusion line; (d) base metal.

However, comparing the grain size distributions at the three planes, it can be seen that the peak frequency changes with distance from the fusion zone. The closer the investigated region to the weld pool, the less the magnitude of the peak frequency. The experimental data show that the maximum magnitude of the frequencies at the four locations were found to be 0.071, 0.078, 0.090, respectively. The corresponding value in the base metal was 0.098. The grain size distribution in the plane with a distance of 2.5 mm below the weld pool, as shown in Fig. 5.24 (c), is comparable with that in the base metal as shown in Fig. 5.24(d). In contrast, the grain size distributions at locations 0.5 mm and 1.5 mm below the weld pool, as shown in Figs. 5.24 (a) and (b), are somewhat different form that in the base metal. Compared to that in the base metal, the grain size distributions in Figs. 5.24 (a) and (b), have lower frequency peaks and broader distribution spectrums. This can be clearly observed in Fig. 5.25 (a), in which the grain size distributions in the three planes are shown by polynomial fitting the simulation results. The differences of grain size distributions along these three lines in the HAZ probably result from thermal effect. The closer the investigated plane to the fusion line, the higher the peak temperature experienced by the region. Thus, the grain size distribution in a region closer to the fusion plane is broader and has lower frequency peak.

The grain size distributions from the 3D MC simulation along the three planes are compared with the theoretical distributions shown in Fig. 5.25(b). Three theoretical distributions were proposed by Feltham.[34] Hillert[35] and Louat.[36] From Fig. 5.25 (b), it can be observed that the grain size distributions along the three planes do not fit any of the theoretical distributions. Specially, large difference exists between the results from the 3D MC simulation and Hillert's distribution. In contrast, the results from the 3D MC simulation are comparable with Louat's distribution at the smaller size region. At the larger size region, the results from 3D MC simulation are closer to the Feltham's log-normal distribution. It should be noted that all the three theoretical distributions are derived from isothermal grain growth. All the three authors described a "mean field approach" which deals with the change in size of an isolated grain embedded in an environment representing the average effect of a whole array of grains. According to the "mean field approach" the overall flux, j, of grains is given by:
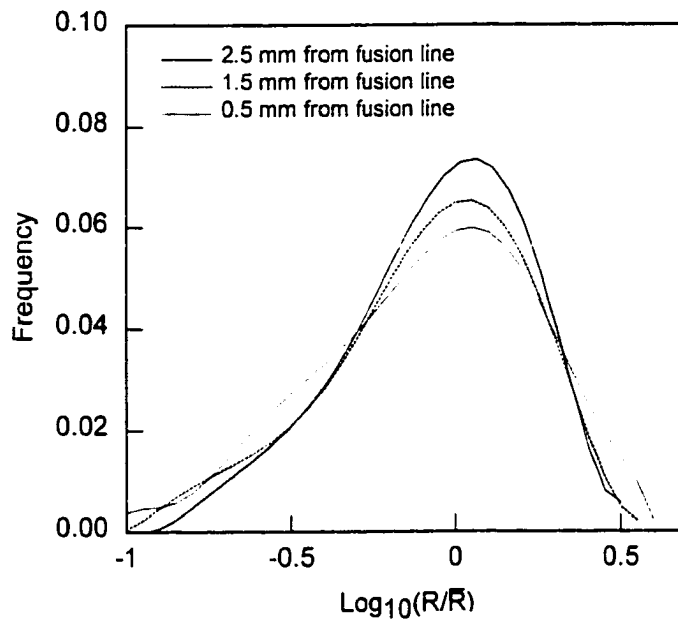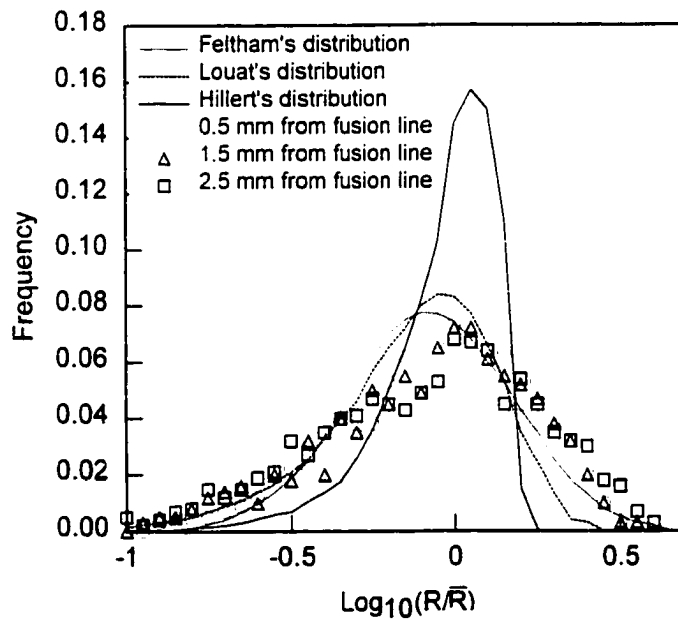
Fig. 5.25: (a) Comparison of the grain size distribution along different lines in the HAZ.

(b) Comparison of the grain size distribution in the HAZ from 3D MC simulation with those from theoretical predictions under isothermal conditions.

$$j = -D\frac{\partial f}{\partial R} + fv \qquad (5.1)$$

where D is the diffusion coefficient which only depends on the specific grain boundary mobility and f is the distribution function which is a function of both R and t. The first term in the above equation refers to a diffusion-like process in which grains larger than $\overline{R}$ get larger due to the "concentration gradient" $\frac{\partial f}{\partial R}$ and the second term refers to a drift velocity v due to the reduction in grain boundary area. The physical basis for the diffusion like process is still not clear.

Feltham[34] and Hillert[35] assumed that the drift due to driving force dominates normal grain growth. Hillert[35] assumed a particular expression for the drift velocity and then solved for f(R,t) and Feltham[34] used an experimentally determined f (assumed to be log-normal) to find velocity. v. Louat[36] on the other hand argued that boundary motion is a random process and the diffusion term is more important than the drift term and considered only the diffusion term to solve for the grain size distribution. From Fig. 5.25(b), it can be observed that the grain size distributions along the three lines do not fit any of the theoretical distributions in the entire region. Specially, large difference exists between the results from the 3D MC simulation and Hillert's distribution. In contrast, the results from 3D MC simulation are comparable with Louat's distribution at the smaller size region. At the larger size region, the results from the 3D MC simulation are more closer to the Feltham's log-normal (Gaussian) distribution. This clearly shows that the "true nature of grain growth lies in between concepts of curvature and random walk"[21] and no term in the equation (5.1) can be neglected under the conditions investigated in this paper.

The grain topology in the HAZ is examined in the sections of the simulated grain structures. i.e., the topological information is analyzed in two dimensions in the present study. In two dimensions, the topology of an individual grain is specified by the number of edges, N_e, or equivalently by the number of vertices. The grain topology is examined by plotting the frequency of occurrence, $P(N_e)$, against the number of grain edges, as

shown in Fig. 5.26 for both the calculated 3D MC results and also the experiments. It can be seen that the calculated results match experimental results very closely. It is also found that the peaks of the frequency of occurrence along all the three planes correspond to the grains with five or six edges. The frequency increases rapidly for a small number of edges and decreases quickly when the number of edges exceeds six in all the three cases. The characteristics of edge distribution in the HAZ obtained here are comparable with those obtained from MC simulation under isothermal conditions.[21]

The observed distribution of grain edge number is consistent with the general topological rule,[40] which tells that that the average edge number of individual grains should be equal to six in a two-dimensional array of grains. This topological rule has also been theoretically derived by Mullins[41] and Neumann.[42] Based on the behavior of individual grains and the uniform boundary model, they obtained a correlation between grain growth kinetics and the topological class of individual grains, which can be expressed as:[35]

$$\frac{dR}{dt} = \frac{M\gamma}{R}\left(\frac{n}{6} - 1\right)$$
(5.2)

where R is the grain size. M is the mobility of the grain boundary, γ is the grain boundary energy, n is the average grain edge number of individual grains. To conserve the total size of the two dimensional system, the sum of $\frac{RdR}{dt}$ over all the grains must be zero. Thus, the average grain edge number of individual grains, n, should be 6 in a two dimensional system. Grains with edges less than six will shrink while grains with edge more than six will grow. Fan and Chen[43] have simulated this temporal evolution of grain edges in detail by using continum field model.
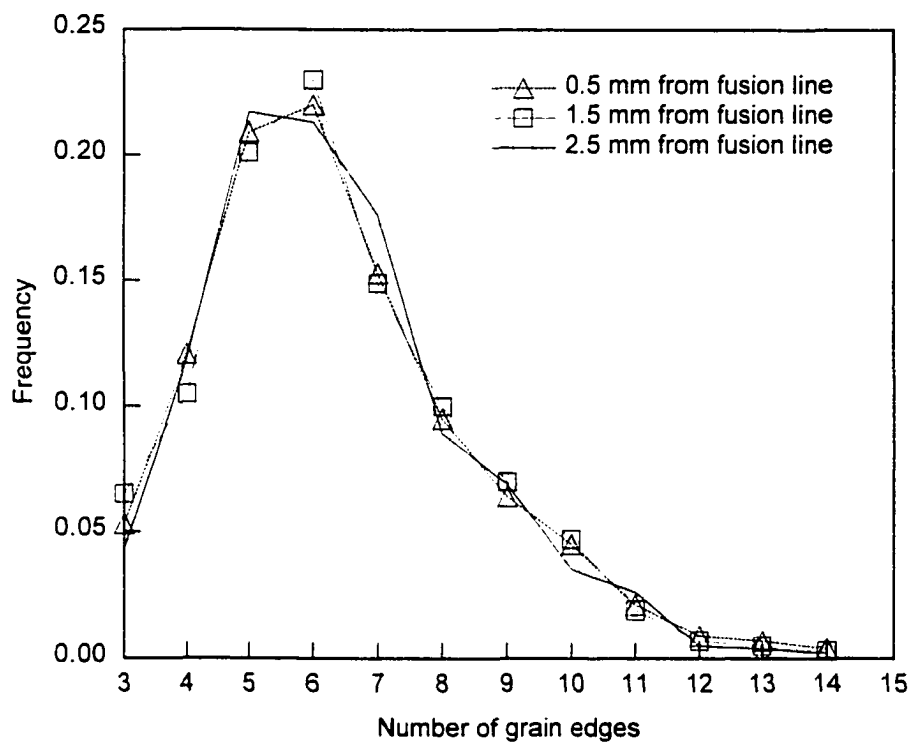
Fig. 5.26: Distribution function for the number of edges per grain plotted against edge class number along three lines in the HAZ.

5.6 Summary and Conclusions

The weld geometry, the phase distribution, and the grain structure in the HAZ of GTA welded commercially pure titanium were systematically modeled based on a combination of both transport phenomena and phase transformation theory. The weld pool geometry under various welding conditions was calculated from both laminar and turbulent models and compared with the experimental data. The calculated phase distribution was compared with the real time phase mapping data obtained by Elmer et al[1-2] using a unique spatially resolved X-Ray diffraction (SRXRD) technique with synchrotron radiation. The grain structures in the HAZs under various welding conditions were simulated and compared with the corresponding experimental data. Through a comparison of the calculated and experimental results, the following conclusions can be made:

1. The weld geometry calculated from the turbulent model is in much better agreement with the experimental data than those predicted from the laminar model. The high computed values of turbulent viscosity and thermal conductivity compared to the corresponding laminar values indicated that the transport of heat and momentum in the weld pool was significantly aided by turbulence. Thus, previous calculations of heat transfer and fluid flow based on the assumption of laminar flow need to be re-examined.

2. The spatial distribution of phases in the weldment can be quantitatively predicted by coupling of the heat transfer and fluid flow model with a phase transformation kinetic model based on a modified JMA equation. The predicted phase boundaries of the $\alpha/(\alpha+\beta)$, $(\alpha+\beta)/\beta$, and the β/liquid in the titanium weldments were in good agreement with the experimental results.

3. The mechanism of the $\alpha \rightarrow \beta$ transition was examined by the comparison of the calculated reaction times from several possible mechanisms with the experimentally determined reaction times. It was found that the $\alpha \rightarrow \beta$ transition was mostly likely controlled by the transport of Ti atoms across the α/β interface.

4. A 3D real-time grain structure map in the entire HAZ around the weld pool was established by coupling the 3D MC model with the calculated thermal cycles from the 3D heat transfer and fluid flow model. The salient features of the grain growth in the HAZ can be effectively illustrated in the map. The grain structure at any plane in the domain can be viewed by examining the corresponding cross section normal to x, y, or z direction.

5. The capability of the 3D MC model to quantitatively predict the spatial distribution of grain size in the HAZ of commercially pure titanium has been tested for various welding conditions. The calculated grain sizes for four heat inputs were comparable with the corresponding experimental results. In particular, it was found that the grain size gradients in the HAZ varied with locations. At the same distance from the fusion line, the mean grain size may be quite different at different locations. For example, the mean grain size at a distance of 1.5 mm to the fusion line on the top surface in weld 2 was found to be 176 μm, while the corresponding location on the symmetrical vertical plane equivalent from the fusion line was 262 μm.

6. The grain size and topological distributions along several lines parallel to the fusion line in the HAZ were studied based on both 3D MC simulated grain structure and experimental data. The predicted grain size distributions are comparable with experimental data. The characteristics of the grain size and topological distributions along the investigated several lines in the HAZ are in general comparable with those obtained under isothermal conditions in the literature. However, the grain size distribution along the line closer to the fusion line is broader and has less frequency peak than that along the line near the base metal.

The above agreements between the calculated and experimental results indicate significant promise for understanding both macro- and microstructures of titanium welds from a combination of the fundamental principles from both transport phenomena and phase transformation theory.

5.7 References

1. J. W. Elmer, J. Wong and T. Ressler: *Metall. Mater. Trans. A*, **29A**, 2761 (1998).

2. J. W. Elmer, J. Wong, M. Fröba, P. A. Waide and E. M. Larson: *Metall. Mater. Trans. A,* , **27A**, 775 (1996).

3. J. Wong, M. Fröba, J. W. Elmer and P. A. Waide: *J. Mater. Sci.*, **32**, 1493 (1997).

4. T. Ressler, J. Wong, and J. W. Elmer: J. Phys. Chem., 1998, vol. 102, 12/10 issue.

5. M. Donachie, Jr: *Titanium A Technical Guide*, p. 177, ASM international, Materials Park, OH (1994).

6. M. Cormier and F. Claisse: *J. Less-Common Metals*, **34**, 181 (1974).

7. M. R. Plichta, H. L. Aaronson, and J. H. Perepezko: *Acta Metallurgica*, **26**, 1293 (1978).

8. T. B. Massalski: in *Phase Transformations*, ASM, 433 (1970).

9. M. Ruch and D. Arias: *Scripta Metallurgica et Materialia*, **24**, 1577 (1990).

10. D. A. Porter and K. E. Easterling: *Phase Transformation in Metals and Alloys*, Chapman & Hall, 1992.

11. J. W. Christian: *The Theory of Transformations in Metals and Alloys*, Edition 1, Part I, Part XII, and Part XV, Pergamon, Oxford, 1965.

12. V. Karpenko, J. H. Kinney, S. Kulkarni, K. Neufeld, C. Poppe, K.G. Tirsell, Joe Wong, J. Cerino, T. Troxel, J. Yang, E. Hoyer, M. Green, D. Humpries, S. Marks, and D. Plate: *Rev. Sci. Instrum.*, 60, 1451 (1989).

13. *Annual Book of ASTM Standards*, 1996, vol. 1, sect. 3, ASTM, West Conshohoken, Pennsylvania.

14. W. A. Johnson and R. F. Mehl: *Trans. Am. Inst. Min. Engs.*, **135**, 416 (1939).

15. M. Avrami: *J. Chem Phys.*, **9**, 177 (1941).

16. P. Kruger: *J. Phys. Chem. Solids*, **54**, 1549 (1993).

17. D. W. Henderson: *J. Non-Cryst. Sol.*, **30**, 301 (1979).

18. D. A. Porter and K. E. Easterling: *Phase Transformation in Metals and Alloys*, Chapman & Hall, London, 1992.

19. N. E. W. de Reca and C. M. Libanati: *Acta Metall.*, **16**, 1297 (1968).

20. M. P. Anderson, D. J. Srolovitz, G. S. Grest, and P. S. Sahni: *Acta Metall.*, **32**, 783 (1984).

21. D. J. Srolovitz, M. P. Anderson, P. S. Sahni, and G. S. Grest: *Acta Metall.*, **32**, 793 (1984).

22. Y. Saito and M. Enomoto: *ISIJ International*, **32**, 267 (1992).

23. J. Gao and R. G. Thompson: *Acta Metall.*, **44**, 4565 (1996).

24. A. Wilson, R. P. Martukanitz, and P. Howell: *"Experimental and Computer Simulation of Grain Growth in HSLA-100/80 Steels During Welding and Cladding"*, to be published in the 5th International Conference on Trends in Welding Research. 1998, Pine Mountain, GA.

25. *Titanium Alloys*, ASM Internationl. Materials Park, OH. 1994.

26. S. Kou and Y. H. Wang: *Metall. Trans. A.* **17A**, 2265 (1986).

27. R. T. C. Choo and J. Szekely: *Weld. J.*, **73**, 25s (1994).

28. K. Hong, D. C. Weckman, and A. B. Strong: *Trends in Welding Research*, H. B. Smartt, J. A. Johnson and S. A. David, eds., p. 399, ASM INTERNATIONAL. Materials Park, OH (1996).

29. D. V. Ignatov, M. S. Model, L. F. Sokyriansky, and A. Ya. Shinyaev: *Titanium Science and Technology*, vol. 4, R. I. Jaffee and H. M. Burte, eds., p. 2535, Plenum Press, New York, 1973.

30. F. X. Gill, D. Rodriguez, and J. A. Planell: *Scripta Metallurgica et Materialia*, **33**, 1361 (1995).

31. H. G. Kraus: *Weld. J.*, **68**, 84s (1989).

32. J. E. Burke and D. Turnbull: *Prog. Met. Phys.*, **3**, 220 (1952).

33. B. Radhakkrishnan and T. Zacharia: *Metall. Trans. A*, **26A**, 167 (1995).

34. P. Feltham: *Acta metall.*, **5**, 97 (1957).

35. M. Hillert: *Acta metall.*, **13**, 227 (1965).

36. N. P. Louat: Acta metall.,**22**, 721 (1974).

37. P. A. Beck, Phil. Mag. Suppl., **3**, 245 (1954).

38. D. A. Aboav and T. G. Langdon: *Metallography*, **2**, 171 (1969).

39. J. Debuigne and E. Etchessahar: "Titanium'92 Science and Technology", ed. F. H. Froes and I. Caplan, p. 739 (1993).

40. C. S. Smith, "Metal Interfaces", p. 65, ASM, Cleveland (1952).

41. W. W. Mullins, J. Appl. Phys., **27**, 900 (1956).

42. J. Von Newmann, "Metal Interfaces", p. 108, ASM, Cleveland (1952).

43. D. Fan and L. -Q. Chen: *Acta mater.*, **45**, 611 (1997).

44. *Smithells metals reference book*, 6th edn, ed. by E. A. Brandes, Butterworth, London, 1983.

CHAPTER 6: CONCLUDING REMARKS

The present thesis have addressed several important issues involved in welding process such as heat transfer and fluid flow in the weld pool, phase transformations in the weld and its HAZ, and grain growth in the weld HAZ. Appropriate modeling heat transfer and fluid flow in the weld pool and kinetics of phase transformations are necessary for prediction of the weld geometry and the microstructure evolution during welding. In the present thesis, the effect of turbulence on the heat transfer and fluid flow in the weld pool has been studied. The rigorously calculated results from the three dimensional thermofluid model indicated that the heat transfer and fluid flow in the weld pool was significantly enhanced by turbulence in many cases, particularly when high heat input was used. Thus, accurate prediction of the weld geometry and thermal cycles in the weldment should consider the effect of turbulence in the weld pool.

The 3D turbulent heat transfer and fluid flow model developed in this thesis was based on a previous laminar model available at Penn State, which has been refined through the past 15 years and applied in different materials such as pure iron, stainless steel, and low alloy steels. In the present study, a 3D turbulent model was developed for the calculation of the weld geometry and thermal cycles in several material systems (e.g. C-Mn steel, HSLA-100 steel, and commercially pure titanium) using GTA and GMA welding. Specially, "finger" penetration, the unique geometric feature of GMA welding, was satisfactorily predicted. The results presented in this thesis suggest that it is necessary to use a comprehensive thermofluid model to describe the transport phenomena in the weld pool when accurate results are sought from mathematical modeling.

Microstructure development is one of the most important and also complicated issue during welding process. In low alloy steel weldments, the weld metal microstructure is a function of both chemical composition and cooling rates. Modeling of steel weld metal microstructure requires accurate cooling rate experienced by the material. Modeling of steel weldment microstructure has now reached a level where it is possible to quantitatively predict the effects of welding variables such as chemical

composition on the phase volume fractions in the weld metal for many low alloy steels. However, phase transformation models can not be applied to welding process unless the thermal cycles are known. In the weldment, the thermal cycles vary with location and are dependent on welding conditions. Accurate knowledge of thermal cycles is a prerequisite for quantitative calculation of the phase transformations. Empirical equations for calculation of cooling rate in the weldment are not flexible to consider either the weldment geometry or the welding variables. Furthermore, such an approach can not calculate the thermal cycles at various locations. In contrast, comprehensive heat transfer and fluid flow models can be used to predict thermal cycles for various weldment geometries under different welding conditions at all locations within the weldment. Thus, coupling of a phase transformation model with the calculated thermal cycles from a comprehensive thermal model is attractive for the prediction of the weld metal microstructural evolution in low alloy steels. In the present thesis, a well tested phase transformation model was coupled with the present thermal model to predict the weld metal microstructure in C-Mn steels and HSLA-100 steel. The results presented in this study show that the effects of chemical composition and cooling rates on the weld metal microstructure can be satisfactorily predicted in these alloys by coupling the CCT diagrams obtained from the phase transformation model and the cooling rates calculated from the comprehensive thermal model.

In the weld HAZ, the kinetics of phase transformations and grain growth vary across the weldment and are functions of both the heating and cooling rates and the maximum temperatures attained during the thermal cycles. Understanding of these welding induced spatial variations of microstructures needs comprehensive modeling and concomitant experiments. The phase transformation rates at various locations in the weld HAZ can be quantitatively calculated by coupling the thermal cycles obtained from the thermal model with an appropriate phase transformation kinetic model. The results from mathematical modeling combined with those from carefully planned experiments can provide insight into the mechanisms of phase transformations that take place during welding processes. This has been illustrated in the present thesis in the study of commercially pure titanium, in which mathematical modeling was combined with real-

time experiments to investigate the phase transformation mechanism in the HAZ. The mechanism of the α-Ti→β-Ti transformation during heating was identified by a comparison of the experimental results with kinetic data obtained from modeling assuming various possible mechanisms.

The grain growth phenomenon in the HAZ is complicated due to the steep temperature gradients and rapid thermal cycling in this region. Previous work on MC simulation of grain growth in the HAZ was limited in two dimensions. Considering the significant change of local thermal and topological environment within the HAZ, simulation of grain growth in two dimensions is not sufficient for understanding of grain growth occurring in three dimensional environment. For a more realistic simulation, a three dimensional Monte Carlo based grain growth simulation model is needed. Furthermore, accurate knowledge of the thermal cycles at various locations in the HAZ are needed to simulate grain growth in the HAZ. The results in the present thesis show that the salient features of the grain growth in the entire HAZ considering the steep temperature gradients and transient thermal cycles can be effectively simulated by coupling a 3D MC model with a 3D thermal model. The results also indicate that the spatial distribution of grain size in the HAZ could be quantitatively predicted by the present modeling approach.

The 3D Monte Carlo model was applied for the simulation of grain growth in commercially pure titanium in the present study. It will be useful to apply the model to other alloy systems such as steels, aluminum alloys, and titanium alloys. The general methodology is straightforward. However, it should be realized that simulation of grain growth in alloy systems should consider these factors that may retard or inhibit grain growth. These factors include solute drag, the presence of second phase particles, and the grain boundary liquidation near the fusion zone. The Grain Boundary Migration (GBM) kinetic model used in the present study for pure titanium is obviously not suitable for all alloy systems. Thus, isothermal experiments need to be undertaken if the kinetic data for grain growth are not available for any important alloy of interest.

The most important feature of this study is its usefulness in understanding trends in macro and microstructure resulting from variations in both welding variables and weld metal chemical composition based on the fundamentals of transport phenomena and phase transformation theory. The results obtained from the mathematical models developed in the present thesis provide not only improved understanding of fusion welding processes from a scientific point of view but also a guideline for practical welding application. Using a reliable comprehensive mathematical model, the conventional trial and error approach for the determination of welding parameters for a given task can be minimized. It is hoped that structurally sound and reliable welds can be designed using phenomenological models without excessive empirical trials.

APPENDIX: ESTIMATION OF GRAIN BOUNDARY ENERGY OF TITANIUM

The grain boundary energies of metals are often found to be roughly 1/3 of their surface free energies.[1] The surface free energy of titanium is not available in the literature. However, the surface free energies of metals are related with their melting points. The higher the melting point, the higher the value of surface free energy.[1] This correlation can be seen in Fig. I.1, which is drawn based on the data available in the literature.[2] By linear fit of the data in Fig. I.1, the surface free energy of titanium near the melting point (1941 K) can be estimated to be about 2.25 J/m^2. If the grain boundary energy of titanium is taken as 1/3 of this estimated surface free energy, its correspondingly value will be 0.75 J/m^2. This estimated grain boundary energy is comparable with those of other metals whose melting points are close to titanium and experimentally measured value are available in the literature. For example, the grain boundary energy[2] of γ-Fe is 0.756 J/m^2.

1. D. A. Porter and K. E. Easterling: *Phase Transformation in Metals and Alloys*, Chapman & Hall (1992).
2. L. E. Murr: *Interfacial Phenomena in Metals and Alloys*, Addison-Wesley (1975).
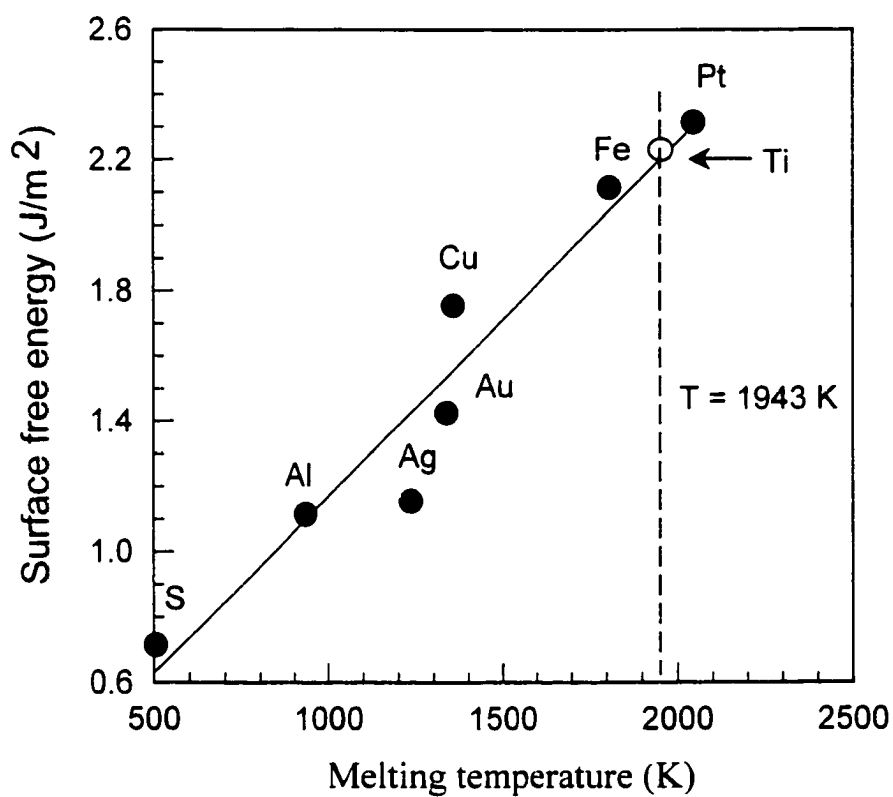
Fig. I.1: Estimation of the surface free energy of titanium based on the data of other metals available in literature.[2]

Vita

Zhishang Yang was born in Hunan province, China, on 18 February 1968. He obtained both Bachelor and Master degrees of Engineering in Metallurgy at University of Science and Technology Beijing (USTB) in 1989 and 1992, respectively. After that, he worked as an instructor at USTB for three and half years. In the spring of 1996, he joined the Pennsylvania State University to pursue doctoral study in Materials Science and Engineering. He is a member of American Welding Society, American Society of Metals, and the Minerals, Metals & Materials Society.

1. Z. Yang and T. DebRoy: "Modeling Macro- and Microstructures of Gas - Metal - Arc Welded HSLA - 100 steel," *Metall. and Mater. Trans. 30B*, 483 (1999).

2. Z. Yang and T. DebRoy: "Prediction of weld metal macro- and microstructures from fundamentals of transport phenomena and phase transformation theory," *Sci. and Tech. of Welding and Joining*, vol. 2, 53 (1997).

3. Z. Yang, J. W. Elmer, J. Wong, and T. DebRoy: "Evolution of Titanium Arc Weldment Macro- and Microstructures - Modeling and Real Time Mapping of Phases," accepted for publication in *Weld. J.*

4. Z. Yang, S. Sista, J. W. Elmer, and T. DebRoy: "Three Dimensional Monte Carlo Simulation of Grain Growth During GTA Welding of Titanium ", submitted for publication.

5. S. Sista, Z. Yang, and T. DebRoy: "Three Dimensional Monte Carlo Simulation of Grain Growth in the HAZ of a 2.25Cr-1Mo Steel Weld ", accepted for publication in *Metall. and Mater. Trans. B*.

6. Z. Yang, J. W. Elmer, J. Wong, and T. DebRoy: "A Combined Modeling and Experimental Study of Microstructural Evolution in Titanium Arc Weldments", to be published in the proceedings of the 1999 ASM Materials Solutions Conference, Cincinnati, Ohio.

7. J. Ryder, Z. Yang, T. DebRoy, and P. R. Howell: "A Quantitative Analysis of the Microstructures Developed in an HSLA 100 Weld Metal," *Microstructural Science*, vol. 26, International Metallographic Society Conference Proceedings, Ottawa, 1998.

8. F. Zhang, Z. Yang, L. Ren, Z. Yu, and R. Zhou, "Determination of Partial Isothermal Section of Ti-Al-Dy Ternary Phase Diagram at 1000 °C,"*Zhongguo Xitu Xuebao*, vol. 14, No. 3, 1996.

9. Z. Yang, F. Zhang, L. Ren, Z. Yu, and R. Zhou, "Effect of RE (Y, Dy) on the Microstructure and Mechanical Properties of TiAl-Base Alloys," *J. of USTB*, vol. 17, No. 5, 1995.

10. Z. Yang, F. Zhang, L. Ren, Z. Yu, and R. Zhou, "Determination of Partial Isothermal Section of Ti-Al- Y Ternary Phase Diagram at 1000 °C," *J. of USTB*, vol. 17, No. 6, 1995.

11. W. Chen, Z. Yang, and R. Zhou, "Reduction Kinetics of Molybdenum Oxide in Slag," *Steel Research*, vol. 64, No. 10, 1993.